Department of Physics and Astronomy

University of Heidelberg

Diploma Thesis

in Physics
submitted by

Radoslav Rusanov

born in Levski, Bulgaria

2011

Measurement of neutral-pion production suppression in Pb–Pb collisions at $\sqrt{s_{\mathrm{NN}}} = 2.76$ TeV with ALICE at the CERN LHC

This diploma thesis has been carried out by Radoslav Rusanov
at the
Physikalisches Institut
under the supervision of
Prof. Dr. Johanna Stachel

Measurement of neutral-pion production suppression in Pb–Pb collisions at $\sqrt{s_{\mathrm{NN}}}$ = 2.76 TeV with ALICE the CERN LHC

In the late fall of 2010 the Large Hadron Collider at CERN started to operate with lead ions for the first time. For one month, the accelerator delivered Pb–Pb collisions at a center-of-mass energy per nucleon pair of $\sqrt{s_{\mathrm{NN}}}$ = 2.76 TeV. The ALICE experiment collected over 30 million minimum-bias events during this time. The measurement of the neutral-pion transverse-momentum spectrum for different centralities is very important for the determination of its production rate. The comparison of the spectra for central and peripheral collisions to the spectrum from proton-proton collisions allows us to study jet quenching for neutral pions via the extraction of the nuclear modification factor R_{AA} and is important for the characterization of the medium created in the collision process. In this work neutral pions are measured by reconstructing converted photons with the central tracking system of the ALICE detector. This alternative method allows the reconstruction of neutral pions with high precision down to much lower transverse momenta compared to the conventional method with calorimeters.

Messung der Unterdrückung der Produktion neutraler Pionen in Blei-Blei-Kollisionen bei $\sqrt{s_{\mathrm{NN}}}$ = 2.76 TeV mit ALICE am CERN-LHC

Im späten Herbst 2010 wurde die Umstellung des LHC am CERN auf Schwerionenbetrieb erfolgreich vollzogen. Einen Monat lang lieferte der Beschleuniger Blei-Blei-Kollisionen bei einer Schwerpunktsenergie pro Nukleonenpaar von $\sqrt{s_{\mathrm{NN}}}$ = 2.76 TeV. Das ALICE-Experiment konnte in dieser Zeit über 30 Millionen Kollisionen aufzeichnen. Für die Bestimmung der Produktionsrate neutraler Pionen in Pb–Pb-Kollisionen bei dieser Energie ist die Messung des π^0-Transversalimpulsspektrums für verschiedene Zentralitäten von großer Bedeutung. Der Vergleich dieses Spektrums aus zentralen und peripären Pb–Pb-Kollisionen mit pp-Kollisionen erlaubt uns die Bestimmung von R_{AA}, welches die Unterdrückung der Teilchenproduktion bei hohen p_{T} beschreibt und dabei zur Charakterisierung des bei der Kollision erzeugten Mediums dienen kann. In dieser Arbeit erfolgt die Messung von π^0-Mesonen mittels Rekonstruktion konvertierter Photonen im zentralen Spurerkennungssystem des ALICE-Detektors. Diese alternative Methode ermöglicht eine Messung mit hoher Auflösung und die Bestimmung des Spektrums bis hin zu viel kleineren Transversalimpulsen verglichen mit der konventionellen Methode mit Kalorimetern.

Contents

List of Figures

1 Introduction

Nature knows four different fundamental interactions: gravitation, electromagnetism, the weak and the strong force. The last three of those are mediated by bosonic particles, which couple to the corresponding charge of the fermionic matter particles. The photon, responsible for the electromagnetic force, couples to the electric charge, the strength of the force is proportional to the charge of the particles involved. A particle without an electric charge, like the neutrino, is 'neutral' and cannot be attracted or repelled by a charged particle via the electromagnetic force. But a neutrino can interact with an electron by the weak force. The weak force, although it is unified with the electromagnetic by the Standard Model, has some significant differences like the very massive mediating particles, the $W^{\pm}$ bosons having electric charges and neutral Z^0 boson which all can couple weakly to each other. The strong or color force which keeps the atomic nucleus together and is responsible for the formation of its constituents, the proton and neutron, and other hadronic particles has also some unique properties. The large coupling constant, falling with rising energy scale, and the fact that the gluons have color charge themselves, leading to gluon-gluon interactions, cause together the confinement of color charge. This phenomenon leads to a unique potential, that rises towards infinity for large distances. This way it is not possible to have a free color-charged particle, so all quarks and gluons are trapped inside color-neutral mesons and baryons. The energy plugged into the separation of two quarks produces new quark/anti-quark pairs out of the vacuum, which then build new color-neutral hadrons together with the original quarks.

Theory nevertheless predicts the existence of a state of matter under given conditions consisting of free quarks and gluons, the Quark Gluon Plasma (QGP). This is possible due to the phenomenon of asymptotic freedom in the strong force which is caused by the weakening of the color charge with decreasing distance between the quarks. The Nobel Prize in Physics 2004 was awarded to David J. Gross, H. David Politzer and Frank Wilczek for the theoretical discovery of this phenomenon [1]. The QGP is expected to be formed at very high temperatures, just like in the early universe, or at very high baryon densities like in the core of neutron stars [2]. In the laboratory we are able to create this state of matter by colliding heavy ions with very high energy in the center-of-mass system ($\sqrt{s_{\mathrm{NN}}} > 10$ GeV) [3, 4]. In such central collisions we have both hot and dense matter. It is very important to study such nuclear collisions, since they give us the possibility to probe the QGP and this way can help us find answers to questions about the formation of the universe.

Suppression of particle production at high transverse momenta is qualitatively a common feature of ultra-relativistic heavy-ion collisions. High p_{T} partons are produced by hard scattering in the early stage of the collision and their production scales therefore from proton-proton to heavy-ion collisions with the number of binary collisions. They then interact with the hot medium, created during the thermo-dynamic evolution of the system and hereby lose energy. The ratio of the yield in heavy-ion collisions to the properly
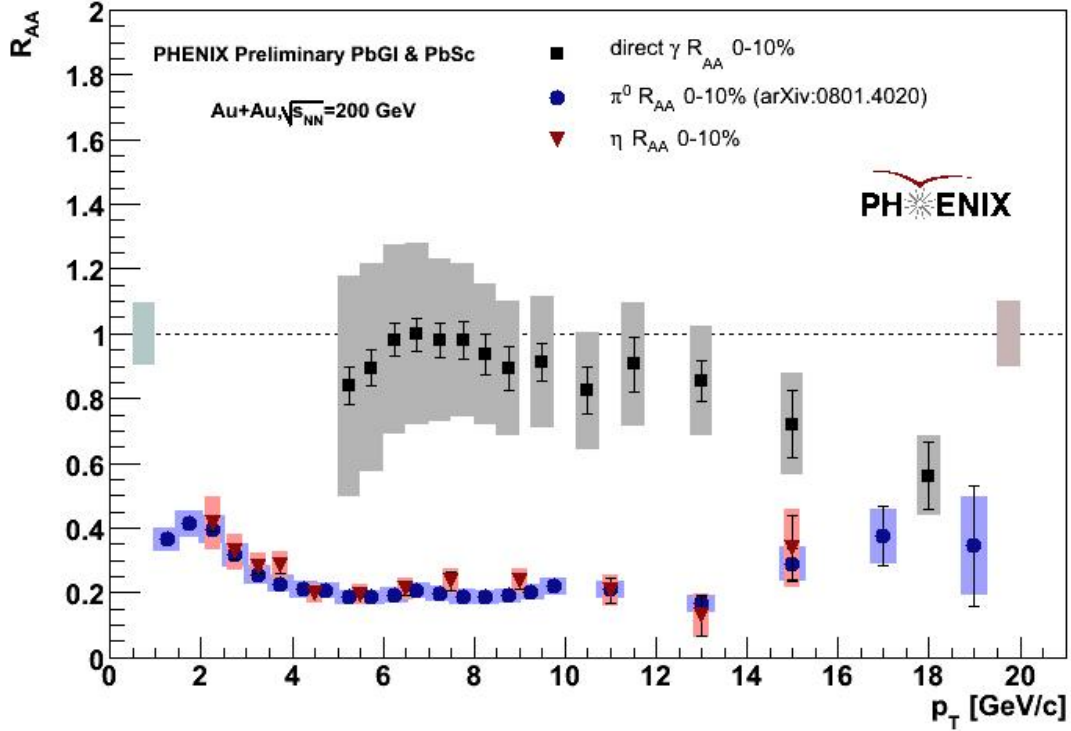
Figure 1.1: π^0, η and direct γ R$_{AA}$ for Au-Au collisions with 0-10% centrality at $\sqrt{s_{NN}} = 200$ GeV [6].

scaled yield in pp collisions, R$_{AA}$, of neutral pions measured by the PHENIX experiment at RHIC for central Au–Au collisions at $\sqrt{s_{NN}} = 200$ GeV shows already a suppression by a factor of up to 5 [5]. A more recent measurement of the PHENIX π^0 R$_{AA}$ is shown in Fig. 1.1 together with the R$_{AA}$ of direct photons and the η meson . But the phenomenon of high-p_T production suppression alone is not an evidence for the formation of QGP.

During the history of heavy-ion experiments three possible observations were considered to be signatures of the QGP formation in a nuclear collision. These are the enhancement of direct photons, created by thermal radiation of the fireball, the J/ψ suppression caused by dissociation of the bound state in the hot medium and the enhancement of strangeness due to the lower mass of free strange quarks if compared to the mass of bound states. The direct photons are predicted to have a rather small production rate and are situated on top of a large π^0 and η decay background. The comparison of the η to π^0 ratio at different transverse momenta in heavy-ion and proton-proton collisions together with their R$_{AA}$ (Fig. 1.1) is important for the characterization of the medium. The exact values can be used to check models that predict particle yields and ratios for a system that has thermalized due to QGP formation [7].

It is therefore of key importance to measure precisely the π^0 and η spectra in both heavy-ion and proton-proton (pp) collisions. The ALICE experiment at CERN's Large Hadron Collider (LHC) is designed to study lead-lead (Pb–Pb) collisions at center-of-mass energies of up to $\sqrt{s_{NN}} = 5.5$ TeV in a very high track-density environment. It also performs very well for pp collisions, giving us the opportunity to measure pp reference data for the

Pb–Pb physics. In ALICE we have the possibility to measure photons not only with calorimeters performing better at high p_{T} due to their energy resolution that follows $\Delta E/E \sim 1/\sqrt{E}$ [8] but also by reconstructing photon conversions in the detector with the central tracking system. The gamma candidates obtained this way can be then combined to pairs resulting into an invariant-mass distribution with peaks at the π^0 and η mass. The use of charged-particle tracks reconstructed in a magnetic field where the momentum resolution is proportional to the absolute value of the momentum ($\Delta p/p \sim p$) [8] above the multiple scattering limit gives this alternative method two main advantages: it can reconstruct the two neutral mesons down to a very low transverse momentum of 0.4 GeV/c and it provides narrow mass peaks, improving the signal to background ratio and therefore the significance and allowing a precise measurement.

2 Theoretical Background

2.1 Standard Model and Neutral Pions

With the construction and operation of various accelerators and colliders starting from the fifties of the last century the number of known particles increased rapidly creating a large "zoo" and requiring an organizational system in order to understand fundamental laws behind the observed phenomena. In the 1960's the Standard Model (SM) of the electro-weak interaction was first proposed and then able to make a series of predictions most of which were proved to be correct by experiments in the following 50 years. The first big success was the observation of neutral currents [9] and the charm quark [10],[11] in 1973 and 1974; the discovery of the $W^{\pm}$ and Z^0 intermediate bosons [12] followed in 1983. The observation of the top quark [13] and the τ neutrino in 1994 and 2000 left the Higgs boson [14] the only SM particle that has not been discovered yet. All these successful predictions show that despite some open issues and problems with the Standard Model it is an extremely good description of the fundamental building blocks of matter and of the interactions between them.

The simultaneous description of the electromagnetic and the weak interactions with a gauge theory lead to the choice of the SU(2)⊗U(1) group. The hypercharge associated to the U(1) group is related to the weak isospin and the electric charge. The theory has four gauge bosons: a triplet coming from SU(2) and a neutral field associated to U(1). The charged bosons of the weak force are created as a mixture of the first two members of the triplet. The Z^0 and the photon are linear combinations of the third boson in the triplet and the neutral field [15]. The "weakness" of the weak force comes not from a small coupling constant but is caused by the large masses of the mediating bosons which are also responsible for the short range of the interaction. Adding the masses "by hand" breaks the gauge invariance explicitly and calls for an extension of the theory to handle this problem. This extension is based on spontaneous symmetry breaking and the Higgs mechanism. Having a charged self-interacting scalar field $\phi = (\phi_1 + i\phi_2)/\sqrt{2}$ with a potential of the following shape: $V(\phi^*\phi) = \mu^2(\phi^*\phi) + \lambda(\phi^*\phi)$ (Fig. 2.1 (right)) we get a continuum of distinct vacua and both the Lagrangian and the vacua are invariant under the global phase transformation: $\phi \rightarrow exp(-i\theta)\phi$. By choosing a vacuum however we cause the symmetry to be spontaneously broken. If we redefine our field so that it becomes suitable for small perturbations around the chosen vacuum we obtain two particles: a scalar field with real and positive mass and a massless scalar boson, a Goldstone boson. The existence of such a particle, however, was not observed by any experiment so far and so the theory needs another modification to escape this problem. The solution is to require that the Lagrangian is invariant under a local transformation $\phi \rightarrow exp[-iqa(x)]\phi$ and not under a global gauge symmetry. This mechanism, called the Higgs mechanism, not only provides a field theory with spontaneous symmetry breaking with no massless Goldstone boson but also has the "nice" feature that the gauge boson(s) become massive

making it the perfect candidate for an electroweak gauge theory [15]. A visualization of the spontaneous symmetry breaking potential described above is shown in Fig. 2.1 (right). The electroweak theory developed to describe the leptonic sector can be extended by adding quarks to the collection of elementary particles and this way the hadronic sector is included. The SM contains six quarks and six leptons as the building blocks of matter and four bosons as force carriers. In Fig. 2.1 (left) one can see all SM elementary particles whose existence has been confirmed with only the Higgs boson missing. The fundamental matter particles as presented below form isospin doublets of the weak interaction ([u,d], [e, ν_e], ...) which is true only for left-handed fermions. Right-handed fermions do not interact weakly. Furthermore no right-handed neutrinos have be observed, although the fact that the neutrino mass is finite [16] suggests the existence of right handed neutrinos.
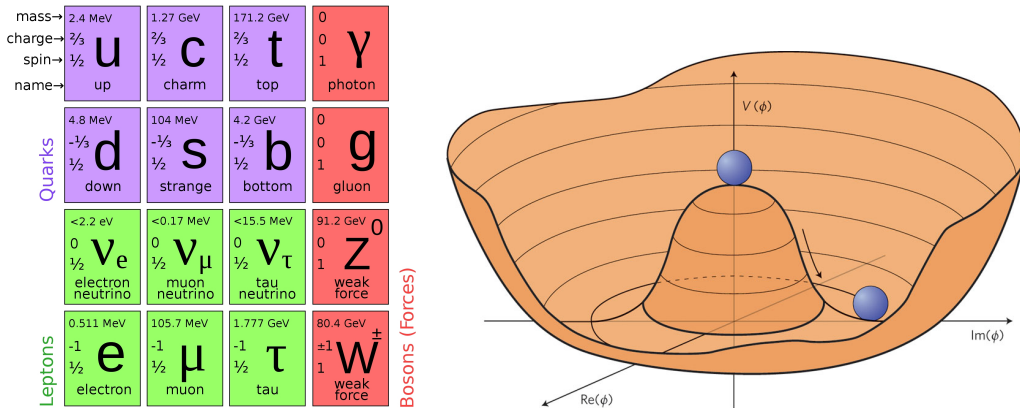
Figure 2.1: The Standard Model particle "zoo" with all matter and force particles (left) [17] and the potential responsible for the spontaneous symmetry breakdown and the mass of the Higgs (right) [18].

The adding of the quarks to the SM leads to its extension by the Quantum Chomo Dynamics (QCD), a SU(3) gauge theory describing the interaction between the quarks. This so called strong or color force is the one with the largest coupling constant of all. It couples to the color charge of the fermions and is mediated by gluons. There are three different color charges (red, green and blue) and three anti-color charges. This results in eight different gluons that have spin 1 and do all carry two color charges, a feature common only to the strong force. This leads to gluon self-interaction and together with other attributes of QCD causes the "confinement" of color charge which means that color charges are always bound and no free colored objects exist. All the quarks are bound within mesons consisting of two quarks or baryons build out of three quarks. The mesons are bosons having spin 0 or 1, the baryons are fermions with spin 1/2 or 3/2.

The three lightest mesons are the pions (π^+, π^- and π^0) which are formed from the two lightest quarks and the corresponding anti-quarks coming from the first generation: the up and down quark. They form an isospin triplet and are actually Goldstone bosons together with the five other light pseudo-scalar mesons generated as an octet by the spontaneous symmetry breaking of chiral symmetry by the confinement of color charge in a QCD sector with 3 flavors of light quarks that are idealized to be massless [19]. The fact that in real QCD the light quarks have masses breaks the chiral symmetry explicitly and causes the mesons that become Pseudo-Goldstone bosons to have masses too. The "smallness" of

these masses compared to other mesons is explained by the fact that the explicit symmetry breaking is small. Pions are naturally created in cosmic showers in the atmosphere but do not reach the surface in large numbers due to their short mean free path. They are also the mediating particles of the forces between the nucleons in a nucleus. In particle collisions they are produced in great numbers. The neutral pion that has a mass of 134.98 MeV/c^2 is a combination of the $u\bar{u}$ and $d\bar{d}$ bound states of quarks which having the same quantum numbers cannot be observed separately but only as a superposition. In pp or Pb–Pb collisions π^0 mesons are created both during the initial interaction and as a decay product of various heavier particles. The main contributions come from the η, ρ and ω mesons. With $c\tau = 25.1$ nm the π^0 meson decays directly at the primary vertex in two γ particles with a branching ratio of 98.8%. The π^0 differential cross-section in pp collisions can be predicted by NLO calculations and then compared to experimental results serving as an important test of pQCD. Such a comparison of the measured π^0 differential cross-section for pp collisions at $\sqrt{s} = 200$ GeV and NLO pQCD is presented in Fig. 2.2 (left) and shows a very good agreement for the KKP fragmentation function over seven orders of magnitude [20].
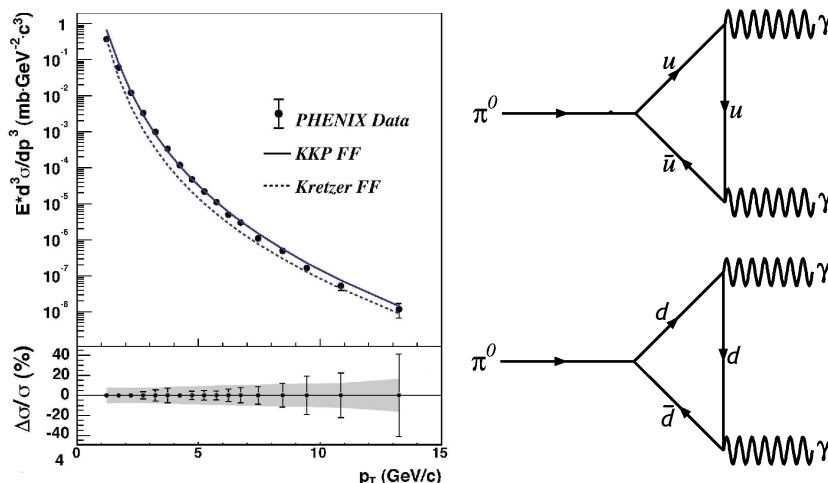
Figure 2.2: Comparison of the measured π^0 cross-section for pp collisions at $\sqrt{s} = 200$ GeV/c and NLO pQCD calculations (left) [20]; Feynman diagrams of the neutral pion decay into two photons (right).

In the same figure (right) the Feynman diagrams of the π^0 decay into two photons are shown. This decay channel is the main one for the neutral pion with a branching ratio (BR) of 98.8% with only one other important channel: the Dalitz decay, where the π^0 decays into a electron-positron pair and a gamma particle with a BR of 1.2%. The two-gamma decay is an electromagnetic process and so the mean life time of the neutral pion is very short ($\sim 8.4 \times 10^{-17}$ s) making it undetectable directly but only reconstructable from its decay products. With a simple calculation it can be shown that the distribution of the π^0 vs its decay asymmetry $\alpha = |E_1 - E_2|/(E_1 + E_2)$ is flat independent from the π^0 momentum. The distribution is not flat any more if we consider only reconstructed mesons at low momenta due to the fact that the detection probability of photons depends on their momenta. This effect can be used to enhance the π^0 signal compared to the combinatorial background.

2.2 pp and Pb–Pb Collisions

There are six major collision systems that are common at particle accelerators: e^+e^-, e^-p, pp (or p$\bar{\text{p}}$), pA, dA and AA. The LHC has already provided pp and AA collisions, so in the following some information on those will be presented. The number of interactions per time interval when two particle beams are colliding is following the formula: $R = \sigma \cdot L$, where σ is the interaction cross-section and L is the luminosity. The luminosity is a measure of the intensity of the beams and extent to which they are focused. It can be calculated by the simple formula: $L = (n_1 \cdot n_2 \cdot f)/A$, where n_1 and n_2 are the numbers of particles per beam bunch, f is the bunch crossing frequency and A is the beam crossing area. The simplification here is that the density distribution over the geometrical beam cross-section is flat. The problem coming from the fact that this is not the case since this distribution has a Gaussian shape can be easily solved by integrating $dL = (\rho_1 \cdot \rho_2 \cdot f) \cdot dA$ over the area A, where $\rho_i = dn_i/dA$ or by using $A = \sigma_x \cdot \sigma_y$ where σ_x and σ_y are the widths of the density distributions [21]. The physical interaction cross-section is linked to the probability for an interaction to happen and depends on the size and inner structure of the colliding particles, the forces involved and the center-of-mass energy. This energy is defined as the total energy in the center-of-mass system. In Fig. 2.3 the dependence of the total pp cross-section on the center-of-mass energy is shown on the left. The rise with $\sqrt{s}$ is caused by Pomeron exchange.
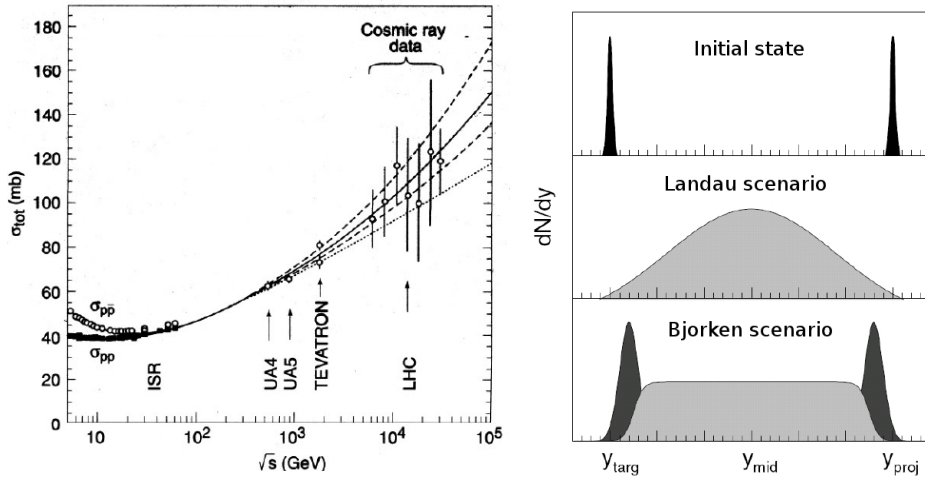
Figure 2.3: The total pp cross-section as function of the center of mass energy (left) and two scenarios of total stopping (Landau) and transparency (Bjorken) for a nucleus-nucleus collision (right).

If we go to ultra-relativistic heavy-ion collisions where the De Broglie wave length is very small compared to the size of the nuclei the process can be considered as a collision of two black discs. The cross-section is determined by the geometrical size and can be calculated with the formula: $\sigma_{inel}^{A+B} \approx \sigma_{geo} = \pi \cdot r_0^2 \cdot (A^{1/3} + B^{1/3})$ where the radii of the nuclei are $R_A \approx r_0 \cdot A^{1/3}$ with $r_0 = 1.2$ fm. There are two regimes for the dynamics of the collision: full stopping of the heavy ions ($\sqrt{s_{NN}} \approx$ 5-10 GeV, Landau) or transparency ($\sqrt{s_{NN}} >$ 100 GeV, Bjorken). In the first case a thermo-dynamical expansion of an initially $2 \cdot R_A/\gamma$ thick cylinder with a radius of R_A is taking place. For the transparency case the created

medium has the form of a long cylinder resulting into a flat rapidity distribution. Both cases together with the initial state are shown in Fig. 2.3 (right).

2.2.1 Collision Centrality and Number of Binary Collisions $\langle N_{coll} \rangle$

The impact parameter b, *i.e.*, the distance between the trajectories of the two nuclei is, next to the center-of-mass energy ($\sqrt{s_{NN}}$), the most important parameter in an AA collision. It is directly related to the mean number of nucleons that take part in the interaction $\langle N_{part} \rangle$ and determines the multiplicity of the event. Those nucleons that do not collide continue to fly along the beam axis, but since the nucleus was wounded it falls apart emitting particles at very small angles that can be detected by a zero degree calorimeter (ZDC) sitting close to the beam pipe but far away ($\sim$100 m) from the vertex. If one combines this information with the number of charged-particle tracks (N_{ch}) produced at pseudo-rapidities further away from the beam axis ($\eta \approx 5$), which is proportional to the total multiplicity, it is possible to determine the centrality of the event. This quantity given in per-cent describes the fraction of events that are more central than the observed one out of the total number of events. In Fig. 2.4 (left) the number of events vs the ZDC energy and the charge in a detector placed at $3.0 < \eta < 3.9$, which is a measure for N_{ch}, is presented together with the centrality definition [22].
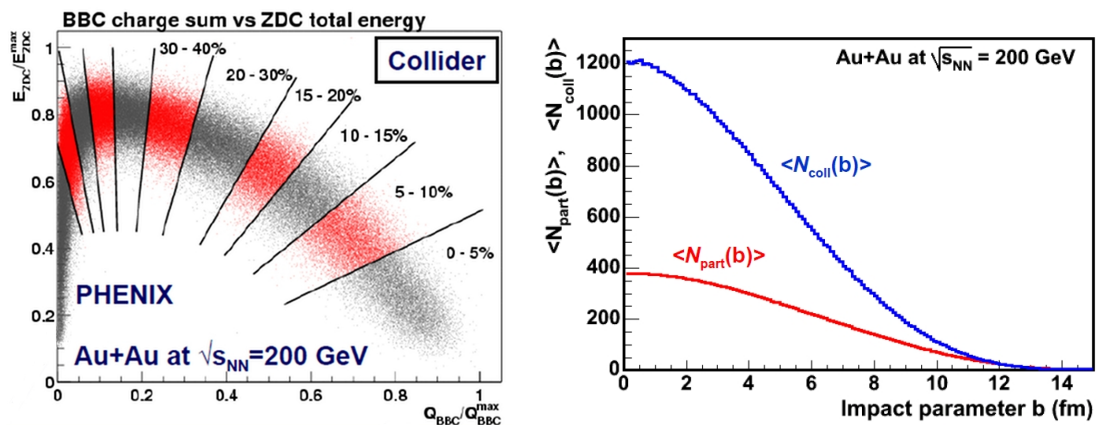
Figure 2.4: Number of events vs ZDC energy and charge in a detector at $3.0 < \eta < 3.9$ (left) [22]; mean number of participants $\langle N_{part} \rangle$ and of binary collisions $\langle N_{coll} \rangle$ vs impact parameter (right) [23].

In a heavy-ion collision hard interactions do not scale with the number of participants. The small cross-section for a hard interaction in a single nucleon-nucleon collision means that the probabilities for a hard scattering are adding up when a nucleon from one of the nuclei is colliding successively with the nucleons from the other nucleus. This is described by the number of binary collisions $\langle N_{coll} \rangle$ with which high-p_T processes scale. This number is usually calculated with a Glauber model assuming that the nucleons travel on straight trajectories and the collision cross-section is constant independently from previous collisions. The inelastic nucleon-nucleon cross-section and a nuclear density profile are used as input. $\langle N_{coll} \rangle$ and $\langle N_{part} \rangle$ from a Glauber model calculation vs the impact parameter are shown in Fig. 2.4 (right) [23].

2.2.2 Quark-Gluon Plasma

The running of the coupling constant α_s of the strong force which is responsible for the confinement of color charge at low energy scales has another, very intriguing consequence: the asymptotic freedom of quarks when they are close enough to each other [1] suggests the existence of a state of matter at high temperatures and densities where the constituents of hadrons are deconfined. This state of matter consisting of free quarks and gluons is called quark-gluon plasma (QGP). Our world is ruled by low temperatures and densities and so the quarks and gluons are imprisoned in hadrons. After its creation by the Big Bang the universe was a hot and dense fireball and so it is thought that the matter was in the form of QGP at some time. The expansion and the resulting cooling led then to the hadronization around 10 μs after the Big Bang. In Fig. 2.5 (left) the phase diagram of QGP spanned by the temperature and the net baryon density is presented where one can see the phase transition region at high temperatures and/or densities together with the crossing points of the Early universe, neutron stars and heavy-ion collisions [24].
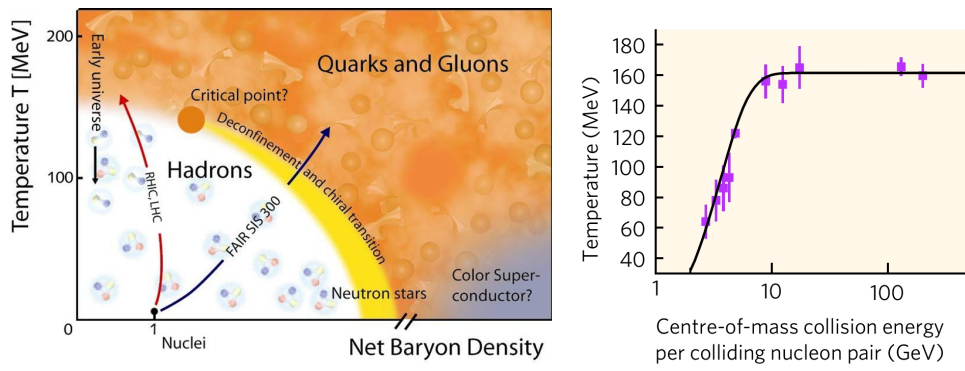
Figure 2.5: Phase diagram of QGP [24]; transition temperature as function of the collision energy [3].

Heavy-ion collisions that have been carried out at sufficiently high energies since the 1980's are the way of creating and studying QGP in the laboratory. The net baryon density is expected to be up to few times smaller than nuclear matter suggesting transition temperatures close to the one of the freeze-out in the Early universe. This temperature has been first estimated to be roughly of the order of 100 MeV [3] and is in good agreement with the limiting temperature for hadronic systems calculated by Ralf Hagedorn in the 1960's. Recent results based on QCD space-time lattice calculations suggest the transition temperature to be between 170 and 190 MeV [3, 25] for different energy normalizations on the lattice. Although facing significant technical problems the extension of the lattice QCD calculations into regions of non-zero net baryon densities shows that the critical temperature drops only very slowly by 2-3% if going to densities expected for nuclear collisions that are three times smaller than those of nuclear matter. In the evolution of a heavy-ion collision that lasts for 10^{-25} s a QGP is supposed to form and then thermalize during a lifetime of order 10^{-22} s. The creation and evolution of QGP during a Pb–Pb collision at $\sqrt{s_{\mathrm{NN}}} = 5.5$ TeV obtained by a simulation is shown in Fig. 2.6. The expanding QGP cools down and hadronizes eventually when it reaches the critical temperature. This means that the temperatures of the hadronic spectra measured at heavy-ion experiments

should be always the same if the collision energy was high enough for QGP formation. Higher energies just heat up the plasma and increase its life time. The experimental results shown in Fig. 2.5 (right) agree with this hypothesis by having a temperature saturation at T $\approx$ 160 MeV at center of mass energies per nucleon pair at ~10 GeV.
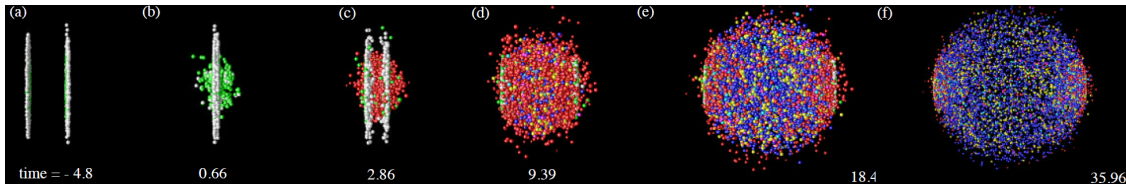
Figure 2.6: A Pb–Pb collision from the initial state (a) through the collision (b), the QGP formation (c) and (d) and the fireball evolution (e) and (f).

Talking about temperatures, phases and phase transitions calls for the existence of "matter" after the collision and not just the creation of a group of particles. The first requirement for the build-up of such a system is a large number of particles out of which it consists. Such numbers are only present in heavy-ion collisions and cannot be reached by far in electron or proton collisions. The other important condition is the achievement of local equilibrium so thermo-dynamical quantities can be defined and relations between them studied. This is only possible if the system lives long enough so a sufficient number of interactions can take place between the particles (order of magnitude five [3]). The first accelerators where the center-of-mass energies are considered to be high enough for a phase transition were operated at the Brookhaven National Laboratory (BNL) in the United States and at CERN in the early 1990's. The SPS at CERN was able to reach, with $\sqrt{s_{NN}} = 17.2$ GeV, energies almost four times higher than in BNL and collected clear evidence for the creation of a new state of matter [26]. The Relativistic Heavy-Ion Collider (RHIC) that followed at BNL with $\sqrt{s_{NN}} = 200$ GeV and the LHC at CERN with energies per nucleon pair of up to 5.5 TeV are able to create systems that live longer and in the case of the LHC will reach temperatures several times higher than the critical one.

An answer to the question about the extent to which the medium created in heavy-ion collisions is "matter"-like can be found if the hadron yields are compared to a model assuming chemical equilibrium at freeze-out. The idea is that all hadronic particles in the final state are formed when the fireball reaches certain values for temperature, volume and baryon chemical potential where a characterization of the system can be done by a grand-canonical ensemble. Results from SPS and RHIC support the equilibrium hypothesis especially if multi-strangeness baryons are taken into account whose yields are in very good agreement with chemical-equilibrium calculations [3]. A consideration of the timescale and the temperature of the fireball and the particle interaction rates in it suggests that an equilibrium cannot be reached in the hadronic phase of the system, especially for the multi-strangeness baryons. It is much more the phase transition and specific processes during the transition like multi-hadron scattering that drive the fireball towards equilibrium [7]. Anisotropic particle production in semi-central collision described by the v_2 coefficient and explained by pressure gradients due to initial shape asymmetries also suggest a hydrodynamical evolution of a system that has quickly reached equilibrium [3].

2.2.3 Strongly Interacting Medium and Nuclear Modification Factor R_{AA}

It is expected that hard interactions where high momentum transfer between partons takes place will occur in nucleus-nucleus collisions just like in pp collisions. Hard interactions do not scale with the number of participating nucleons like the multiplicity but with the number of nucleon-nucleon collisions that are thought to be independent from each other as it was described in subsection 2.2.1. The highly energetic quarks and gluons produced in such interactions can be used to study the properties of the medium created in AA collisions since they are created at an early stage and then interact with their environment. The nuclear modification factor R_{AA} defined as:

$$R_{AA} = (dN_{AA}/dp_{\mathrm{T}})/\left(\langle \mathrm{N_{coll}} \rangle \cdot dN_{pp}/dp_{\mathrm{T}}\right) \tag{2.1}$$

is a measure of the parton energy loss in the medium. If there would be no medium effects and a nuclear collision would be just a superposition of pp collisions we expect the R_{AA} to be exactly 1 for high transverse momenta and below one at lower p_{T} where particle production does not scale with $\langle \mathrm{N_{coll}} \rangle$ yet. The situation would be described by the R_{AA} presented in Fig. 2.7 (left).
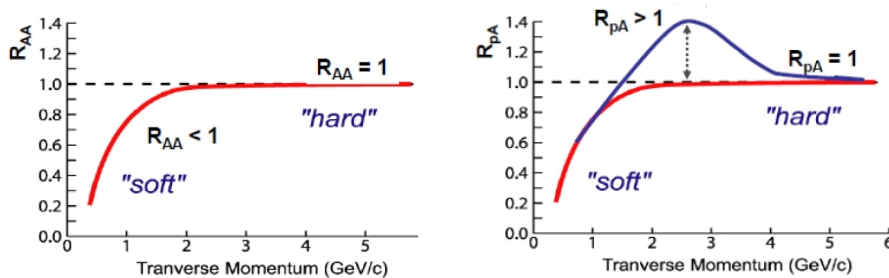
Figure 2.7: The expected R_{AA} & R_{pA} for simple scaling from pp (left) and with Cronin effect (right) [27].

The real R_{AA} is modified by initial and final state effects that do both occur in heavy-ion collisions. If we want to learn about the medium created in such collisions we need to study the initial state effects in order to be able to separate them from the final state effects caused by the medium. The experimental environment to do this are proton-nucleus (pA) collisions since there the spectra are also modified by initial state effects but no or only very little final state effects occur because no hot medium is created. When partons of a nucleon from one of the nuclei transverse the other nucleus inelastic multiple scattering before the actual hard interaction increases its transverse momentum. This effect discovered in the 1970's at Fermilab is called the Cronin effect and leads to an enrichment of the spectrum at intermediate p_{T} and causes the R_{pA} to be larger than 1 in this region. For higher p_{T} the effect is only a negligible fraction of the total transverse momentum and the R_{pA} which can be seen in Fig. 2.7 (right) goes back to 1 [27]. Another initial state effect is the modification of the parton distribution functions if we go from free protons to nucleons in a nucleus that is caused by shadowing and anti-shadowing. There are different parameterizations that describe this modification and are tested experimentally. The quark and anti-quark distribution functions are well understood and the models are tested with Drell-Yan muons that are not affected by medium effects. The gluon distributions can be tested only indirectly and the parameterizations vary within a wide range [27].

One of the effects caused by the medium created in a heavy-ion collision is the collective motion of the partons within the thermo-dynamic expansion of the system. This results in an increase of the (transverse) momenta of the particles since they all get an additional velocity kick. An enrichment of the spectra at low and intermediate p_T takes place which is less important at higher p_T. Therefore, if the energy loss of partons that traverse the medium created in the collision is to be studied, it needs to be done at high transverse momenta where no other effects contribute to the modification of the spectra. There are two energy loss mechanisms: the scattering with other partons that dominates at low energies and the radiation of gluons, *i.e.*, the gluon bremsstrahlung that dominates at high energies [27]. In Fig. 2.8 (left) the radiative energy loss of a parton before fragmentation is shown. The reduction of the energy of the partons translates into a reduction of the (transverse) momentum of the hadrons. Due to the power-law shape of the hadron spectra at high p_T ($dN/dp_T \sim (1/p_T)^n$ with n about 7) even a small energy loss results into a large suppression factor for the yield.
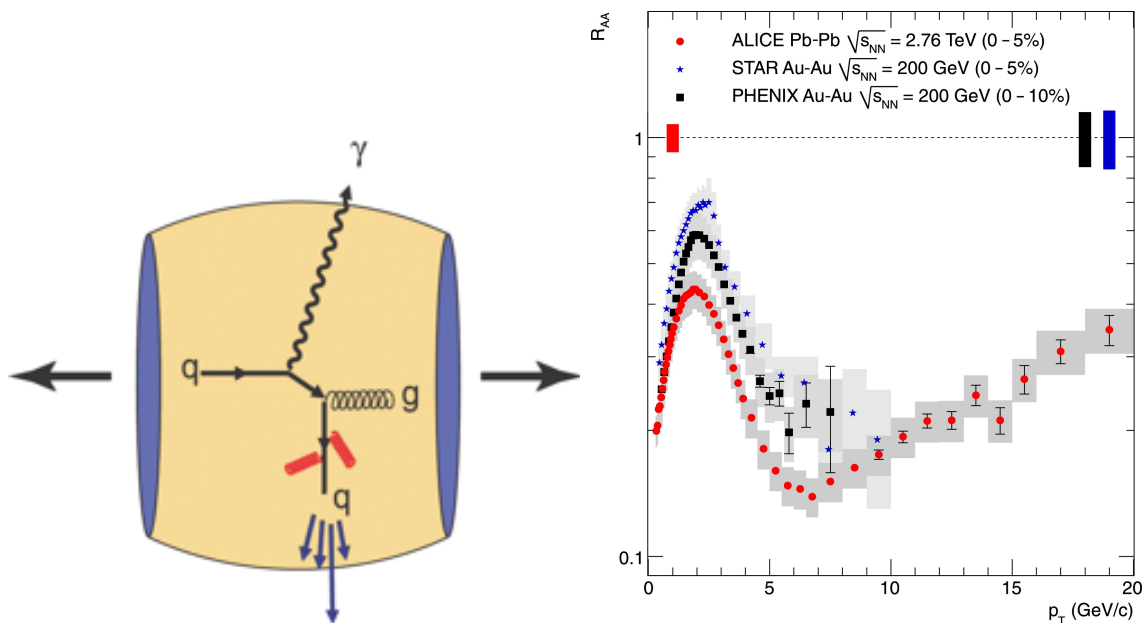
Figure 2.8: Feynman diagram for parton energy loss and direct photon production (left) and the $h^{+/-}$ R_{AA} in ALICE, STAR and PHENIX for different centralities and collision energies (right) [28].

This can be seen in the unidentified charged particle ($h^{+/-}$) R_{AA} for 0-5% centrality measured with ALICE at $\sqrt{s_{NN}} = 2.76$ TeV [28] where a suppression factor of ~ 7 is observed. The mean energy loss $\langle \Delta E \rangle$ by the radiative mechanism for a static medium is proportional to the strong coupling constant α_s, the Casimir factor C_r (3 for gg and 4/3 for qg interactions), the transport coefficient $\hat{q}$ (related to medium characteristics) and the second power of the path length (which comes about due to interactions between the radiated gluons and the medium)[27]. This $\langle \Delta E \rangle \sim \alpha_s C_r \hat{q} L^2$ depends also on the energy of the partons. Two models, a naive but easy to calculate one with $\Delta E \sim E$ and a second one that uses $\Delta E \sim log(E)$ as suggested by QCD [29] are discussed in sub-section 5.2.3 and their parameters are extracted from the measured π^0 R_{AA} for 0-20% centrality.

2.3 Interaction of Photons with Matter

The neutral pion reconstruction method described in this Thesis does not use electromagnetic calorimeters for photon detection but reconstructs the photons that have converted in the detector's material. In this section we will shortly summarize the interactions of photons with matter focusing on the aspects important to this analysis. The kind of interaction that dominates and the strength of the absorption coefficient is strongly dependent on the energy of the incoming electromagnetic radiation. For photons with energies as low as visible light or even infrared the photoelectric effect is the main absorption mechanism. A light quantum is absorbed by an electron in the shell of an atom which is then freed having the difference between the photon energy and its binding energy as kinetic energy or it can be just lifted into a higher shell if the photon energy is not high enough. This effect is dominant up to energies of few tens of keV depending on the material. From there on and up to few MeV the Compton scattering where the photon is absorbed and re-emitted by a quasi-free electron becomes more important. For energies higher than twice the electron mass the creation of an electron/positron pair is possible and quickly becomes the dominant process. Because of energy and momentum conservation such a process can only happen in matter, where the recoil is absorbed by a nucleus. Fig. 2.9 shows the two leading order Feynman diagrams for the pair creation. In Fig. 2.10 (left) the absorption coefficient μ together with its different contributions is shown on the left as a function of the photon energy.
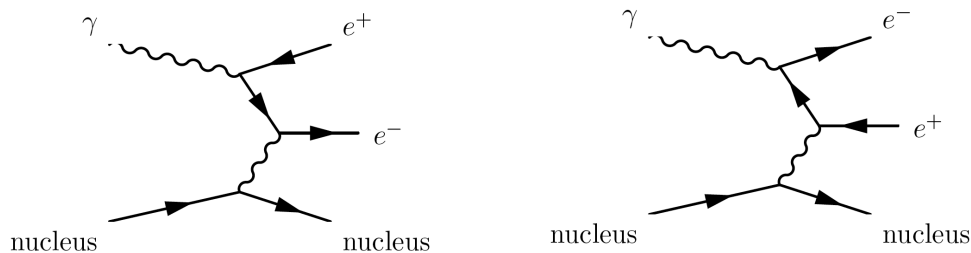
Figure 2.9: The two leading order Feynman diagrams for pair production.

The gamma absorption coefficient describes, in a statistical point of view, the fraction of light that is not absorbed when passing through a d cm thick object according to the law of Lambert-Beer: $I(d) = I_0 \cdot e^{-\mu \cdot d}$ where $I(d)/I_0$ can be also seen as the probability for a single photon to pass through an object of thickness d. The conversion density in a non-homogeneous medium is a measure of the material density distribution in this medium. In Fig. 2.10 (right) one can see the distribution of conversions in the inner part of ALICE reproducing its inner structure (6 ITS layers and the inner parts of the TPC).
The mean conversion probability for high p_T photons in ALICE from the primary vertex to the middle of the TPC at 180 cm is estimated to be between 8% and 9% [30] depending on the exact η cut (0.75-0.9) applied on the photons. For the Pb–Pb analysis ($|\eta| < 0.75$) it is $\sim$8.1%. With the mean free path for a photon defined as $\lambda = 1/\mu$ we obtain that this corresponds to a material budget of $\sim$8.4% of one mean free path by using the law of Lambert-Beer. The electron tracking in our analysis starts for energies higher than few tens of MeV where the energy loss of electrons is already dominated by bremsstrahlung (see
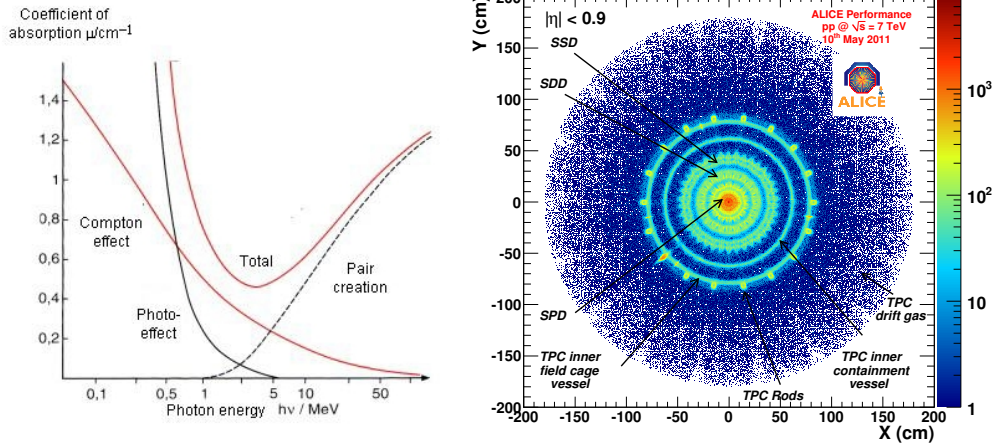
Figure 2.10: Gamma absorption coefficient with its different contributions vs the γ energy (left) [31]; distribution of conversions in of the ALICE detector showing its different components (right) [32].

Fig. 2.11 (left)). The mean electron energy in material decreases following the formula: $E(x) = E_0 \cdot e^{-x/X_0}$, where X_0 is the radiation length after passing of which the electron has lost 63.2% of its original energy. By using the relation $X_0 = \frac{7}{9} \cdot \lambda$ [33] it can be estimated that the electron loses in average only ∼10.3% of its energy while transversing the ALICE material until a radius of 180 cm which would correspond to ∼10.9% of a radiation length. Such low losses for the electron and the low fraction of a radiation length itself which is responsible for multiple scattering gives us the possibility to track electrons down to 50 MeV/c with precise momentum determination. This together with the moderate asymmetry of photon conversions at low energies (see Fig 2.11 (right) where the fraction of the e^+ energy out of the γ energy is shown) allows the reconstruction of photons with p_T down to 100 MeV. On the other hand the low conversion probability reduces the photon statistics by a factor of 12 and makes the analysis dependent on high data statistics. In the case of the π^0 meson where the conversion probability enters quadratically in the reconstruction efficiency the situation is even more critical.
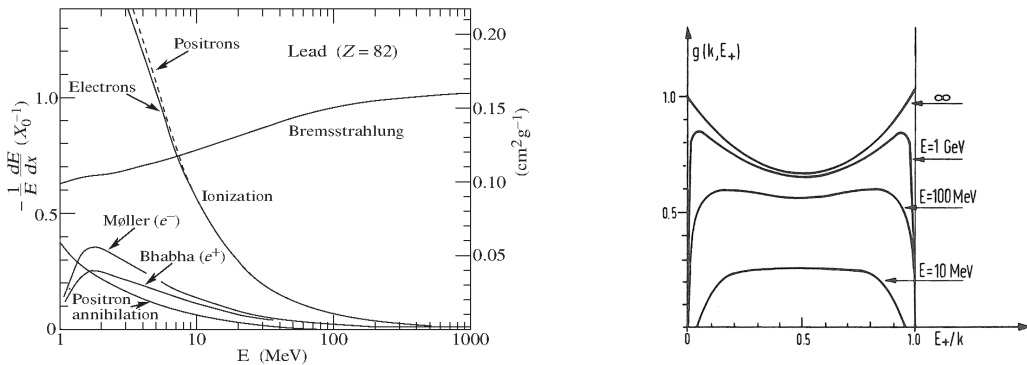
Figure 2.11: The electron energy loss in matter with its different contributions (left) [34] and the distribution of positrons from γ conversions vs their fraction of the γ energy (right) [35].

3 Experimental Setup

3.1 CERN and the Large Hadron Collider

The European Organization for Nuclear Research or in French "Conseil Européen pour la Recherche Nucléaire" (CERN) is one of the world's greatest and most prestigious scientific organizations where thousands of physicists and engineers are working to find answers to some of the most urgent questions about the fundamental laws of physics and the formation of the early universe [36]. In 1952 when the predecessor council was founded and then in 1954 when the organization itself came into life the understanding of the nucleus was one of the major research topics of that time. Today the understanding of matter goes much deeper and CERN's main interest is focused on particle physics searching for the fundamental constituents of matter and the forces acting between them. The organization is financed with money coming for the budget contributions of its member states.
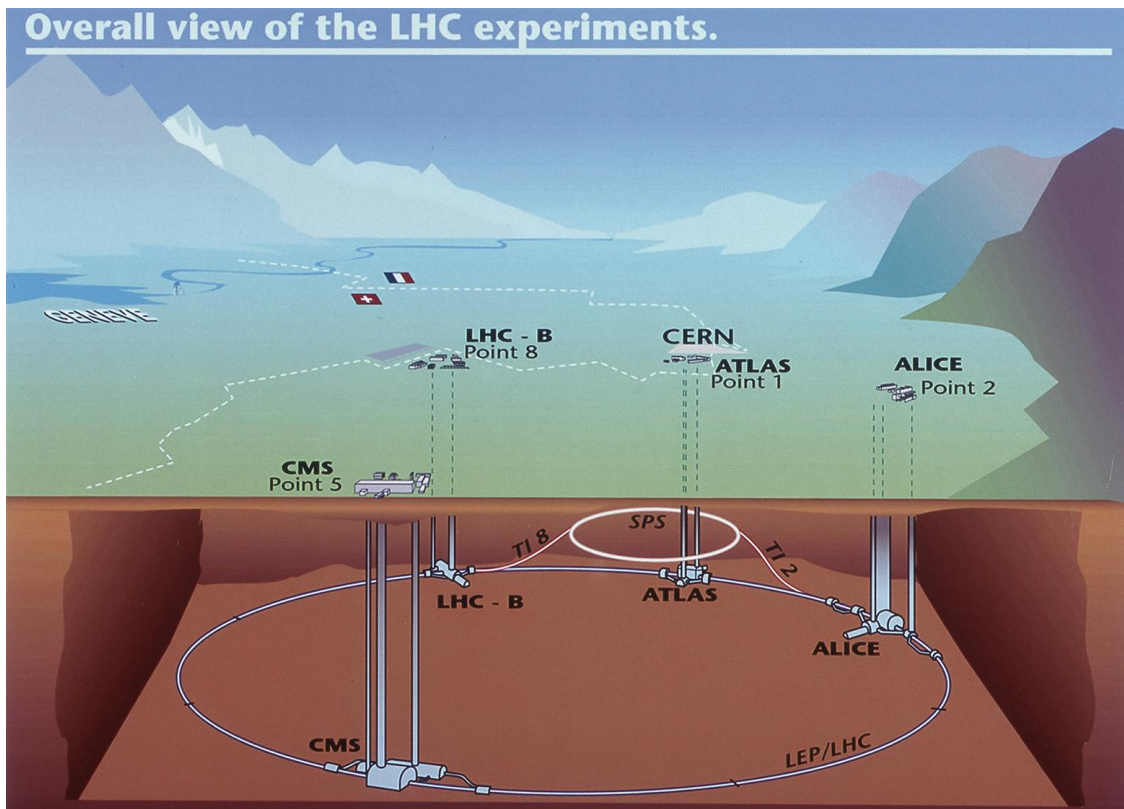
Figure 3.1: CERN's Large Hadron Collider situated under the city of Geneva in Switzerland [37].

Having 21 member states today CERN can look back on a long history of important achievements, significant contributions to the world's science and prizes. In 1984 Carlo Rubbia and Simon Van der Meer received the Nobel Prize in physics for their contributions to the discovery of the $W^{\pm}$ and Z^0 field bosons. Using the first proton-antiproton collider the unification of weak and electromagnetic forces was confirmed. In 1992 Georges Charpak was awarded the Nobel Prize in physics for the development of the multiwire proportional chamber which revolutionized particle detection and was later also used for X-ray imaging in radio-biology increasing the recording speed and this way reducing the radiation doses. In 1989 the World Wide Web was first proposed at CERN by Tim Berners-Lee and in 1991 it was released to the high energy physics community via a CERN program library. Few years later the WWW became one of the most important means of information exchange and presentation world wide still remaining an open standard.
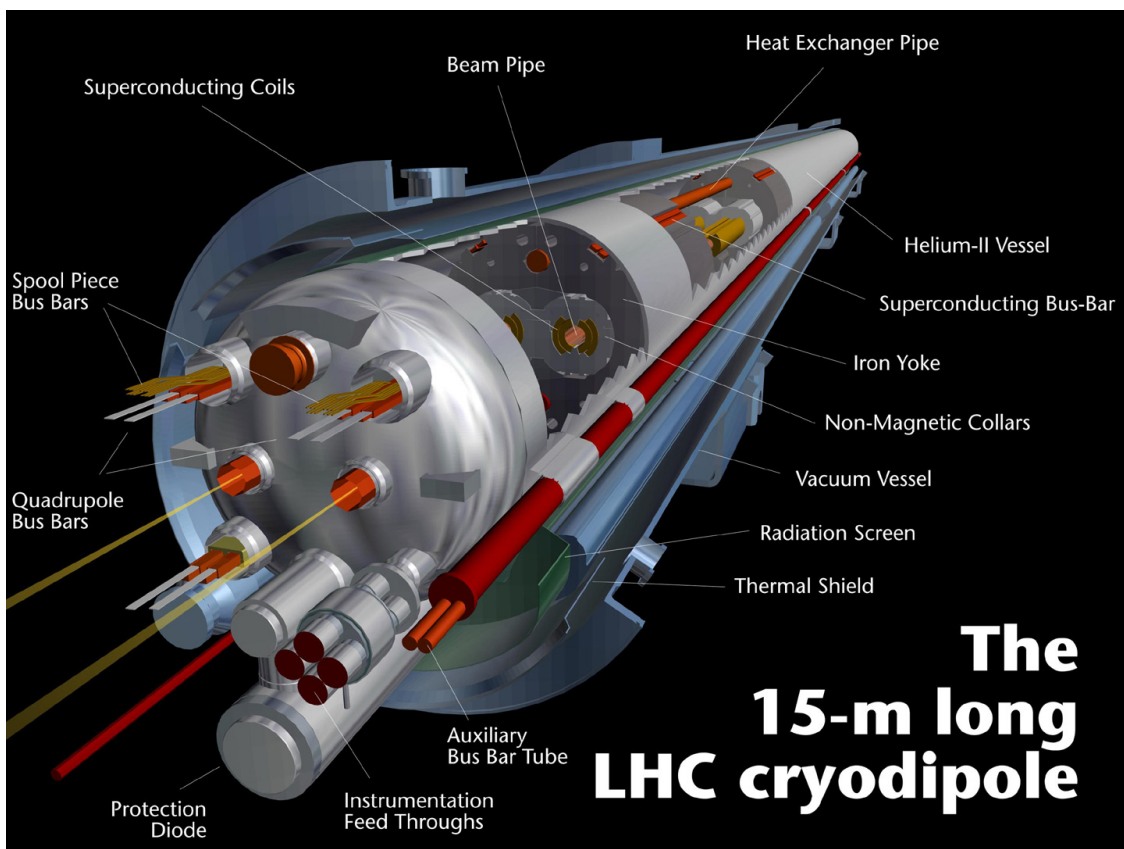
Figure 3.2: One of the 15 m long dipole magnets used to bend particles along the 27 km long circle [38].

The Large Hadron Collider (LHC) is the most recent and largest project of CERN. With a circumference of almost 27 km and running about 100 m below the surface (the exact depth depends on the height of the landscape at the observed position) it is situated under the city of Geneva in Switzerland but also crosses the border into France (see Fig. 3.1). It is a particle accelerator and collider built to be operated with protons and heavy ions like lead (Pb) with the highest energies ever achieved. The LHC will help to gain a better

understanding of fundamental laws of nature and hopefully to discover new physics. One of the main targets in the analysis of the collected collision data is the discovery of the Higgs boson that is responsible for the mass of the particles or the disprove of its existence. Assuming a mass between 115 and 200 GeV/c^2, which is the most probable range, and LHC collision energies it is easier to create a Higgs particle using the see quarks or gluons of a proton rather than its valence quarks since the first are more probable at the needed values of x if one looks at the parton distribution function. This way LHC can do without anti-protons and achieve very high luminosity not being limited by their production rates. Studying the hot and dense medium created in heavy-ion collisions, finding an evidence for the formation of the quark-gluon plasma, a state of matter where quarks and gluons are not confined any more, and describing its properties is another important issue. The higher the collision energy of the two heavy ions the hotter and more dense is the created medium which makes the duration of the QGP phase much longer. There is of course the expectation that new physics will be found in the LHC data giving us the possibility to test Standard Model extension theories or to find new particles and forces.

The LHC mainly consists of dipole magnets which bend the particles around the orbit, quadrupole magnets to shape and focus the beams and acceleration cavities to increase energy per proton from 450 GeV at injection to 7 TeV. Since it is a proton-proton collider and the two particle beams need to circulate in opposite directions the LHC contains two separate beam pipes. These are kept at ultra-high vacuum to reduce the number of interactions between the beam and its environment. The quality of this vacuum is $\sim$10^{-17} bar on a volume of 150 m^3. Having the particles accelerated to such high energies or momenta the magnetic field needed to keep them on track even with the large radius of the LHC is very high, so superconducting magnets that can maintain a 8.3 T field are in use (see Fig. 3.2). These superconducting magnets are filled with liquid helium of -268.7°C (4.5 K) and are then cooled down by refrigerators to -271.3°C (1.9 K), a temperature where helium is super-fluid. Before filled into the magnets the helium is first pre-cooled to -193.3°C (80 K) and then cooled down to -268.7°C (4.5 K) by the refrigerators. The cryogenic system responsible for the LHC cooling is by far the largest in the world.

There are four major experiments that collect data from LHC collisions. ATLAS is one of the two general-purpose detectors out of those four. It consists of an inner detector system for tracking and momentum measurement, electromagnetic and hadronic calorimeters to determine the energy of a large number of particles, a muon spectrometer and a collection of superconducting magnets creating a toroidal field. Its main objective is the search for the Higgs boson, extra dimensions, and new particles that could be the building blocks of dark matter. CMS is the other general-purpose detector which however uses a solenoidal magnetic field. It follows the same scientific goals, but uses different technical implementations. Both detectors have their advantages in different areas and the cross-check of their independent results will ensure the quality of the analysis. ATLAS and CMS are also studying heavy-ion collisions. LHCb is the only forward detector and is designed to study the matter anti-matter asymmetry in the universe that being rather small still created a universe consisting of matter and almost no anti-matter. The analysis of the beauty or bottom quark will play a major role in the LHCb experiment. ALICE is the fourth major detector and was build specifically for the study of heavy-ion collisions. It will be described in detail in the next section.

3.2 ALICE

ALICE (A Large Ion Collider Experiment) [39] is dedicated to the study of strongly interacting matter and the quark-gluon plasma (QGP) created in the extremely high energy density and temperature environment of ultra-relativistic nucleus-nucleus collisions. It is designed to analyze charged and neutral hadrons, electrons, muons and photons that are created in such collisions even at the very high particle densities of a central Pb–Pb event. The ALICE collaboration that build the detector and is now analyzing the data consists of over 1000 physicists from more that 100 institutes in 30 different countries. The detector itself measures $16{\times}16{\times}26$ m^3 and weights around $10\,000$ t. It combines a central barrel part for the measurement of hadrons, electrons and photons and a forward muon spectrometer. The central barrel situated in the large solenoid magnet of the former L3 experiment at LEP covers a pseudo-rapidity range of $|\eta| < 0.9$. The coverage is much larger if only certain (innermost layer of the ITS or the inner half of the TPC) detectors are used. The schematic setup of the ALICE detector with all its sub-detector systems is presented in Fig. 3.3.
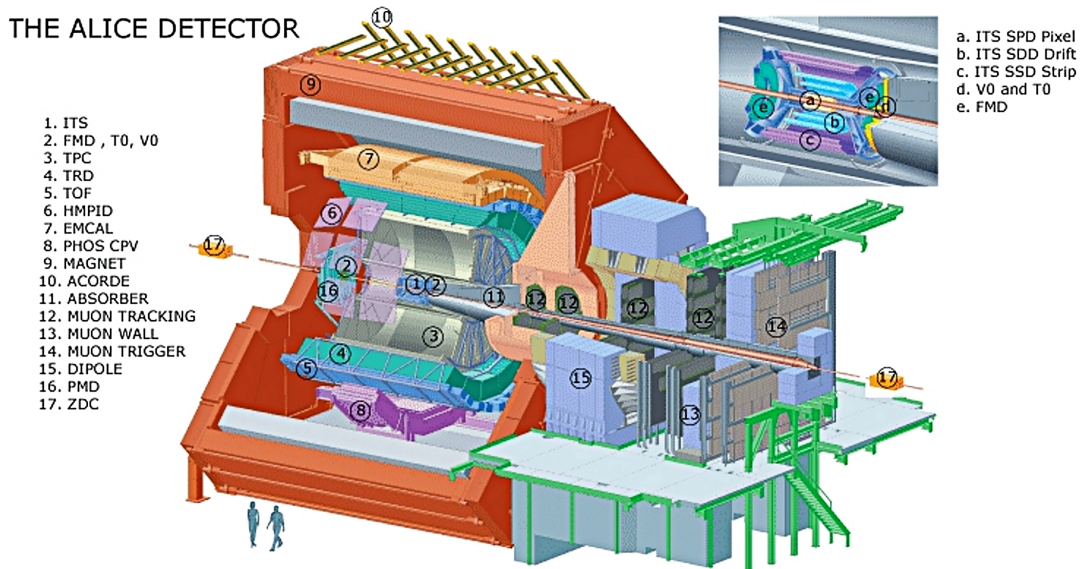
Figure 3.3: A schematic picture of the ALICE detector, one of the major experiments at the LHC [40].

The Inner Tracking System (ITS) situated directly around the beam pipe is responsible for vertex reconstruction and tracking especially at low transverse momenta since low p_T primary tracks do not reach any other parts of the detector. It consists of six layers that use different technologies (silicon pixel, drift and strip detectors). They are surrounded by the cylindrical Time Projection Chamber (TPC), which is a gaseous drift detector able to handle an enormous number of tracks in a single event. The TPC is followed by the Transition Radiation Detector (TRD) which is able to separate electrons from pions at high transverse momenta and helps to improve the momentum resolution for high p_T tracks. The Time Of Flight Detector (TOF) is the most outer detector in ALICE that

covers the full azimuthal range. It is an important tool for particle identification (PID). The Ring Imaging Cherenkov for high momentum particle identification (HMPID) and the two electromagnetic calorimeters PHOS (high-resolution PHOton Spectrometer with limited acceptance centered around $\eta = 0$) and the EMCal (electromagnetic calorimeter with moderate resolutions but large coverage in η positioned opposite to PHOS) do all not cover the full azimuth. The muon detector situated at one side of the central barrel between $2°$ and $9°$ relative to the beam axis consists of absorbers, 14 planes of tracking and triggering detector chambers and an additional dipole magnet. A collection of smaller detectors (ZDC, PMD, FMD, T0 and V0) is used for the measurement of global event observables and triggering. Additionally, cosmic rays can be triggered by an array of scintillators (ACORDE) on top of the L3 magnet.

Being the only dedicated heavy-ion experiment at the LHC, ALICE is a general-purpose detector designed to measure a wide range of observables. Measuring the multiplicity and the zero-degree energy flow allows the determination of the centrality, the impact parameter or the number of participating nucleons of a nucleus-nucleus collision and gives us the possibility to study the modification of specific hard processes in such collisions as a function of those parameters. ALICE, designed to cope with the high track-density environment of a central Pb–Pb collision, operates very well for pp collisions. Therefore it allows us to compare the results mentioned before with pp results obtained by the same detector, this way reducing many systematic uncertainties. The production rates of heavy flavor particles, the fragmentation of jets, the suppression of particle production at high p_{T} and even particle interferometry, all being important analysis issues for the study and description of the QGP, do all need a baseline or reference measurement in pp collisions. Elliptic flow and so-called direct photons are also being investigated with data collected by the ALICE collaboration.

The choice of design for ALICE had two major constraints: the extremely high track density and the rather low interaction rate that were expected for the operation with nuclear beams. Charged-particle multiplicities of up to $\mathrm{d}N/\mathrm{d}\eta = 4000$ had to be taken into account even after the RHIC data has been used for the extrapolation towards LHC energies [39]. At the same time, Pb–Pb collisions should not happen with more than 10 kHz which made possible the use of slow but high-granularity detectors as the silicon drift detector (SDD) and TPC. Since both hard interactions and thermo-dynamical (soft) processes are of great interest for the description of the strongly interacting medium created in an AA collision, the tracking needed to cover a large range of transverse momenta from $\sim$50 MeV/c up to $\sim$100 GeV/c. Three design characteristics of ALICE make this possible: the material thickness being only 13% of a radiation length up to the outer shell of the TPC reduces multiple scattering at low p_{T}; the large tracking level arm of up to 3.5 m allows the measurement even at high momenta; the moderate magnetic field of 0.5 T is well suited to ensure full coverage of the needed p_{T} range. Many of the physics observables depend on the species or mass of a particle and therefore their identification (PID) over a large p_{T} range is very important. ALICE uses a wide range of PID techniques including specific energy loss dE/dx, time-of-flight, Cherenkov and transition radiation, calorimeters, muon filters and the reconstruction of secondary vertices. Although concentrating on mid-rapidity, where the energy density is maximal and baryon density minimal, ALICE still covers a range wide enough to study jet fragmentation and particle decays at low momenta.

3.3 Detectors and Their Role in the Analysis

3.3.1 Tracking with ITS and TPC

There are three detector systems that are responsible for the tracking in the central barrel of ALICE. These are the ITS, the TPC and the TRD, which can be used to improve tracking at high momenta. The inner tracker has three basic responsibilities: the reconstruction of secondary vertexes for heavy flavor and strange particles, PID and tracking for low-momentum primary tracks and improving of the tracking resolution at higher p_T. The TPC is also doing tracking and PID but up to much higher momenta of 100 GeV/c for tracking and 50 GeV/c for PID on the relativistic rise of the dE/dx distribution.
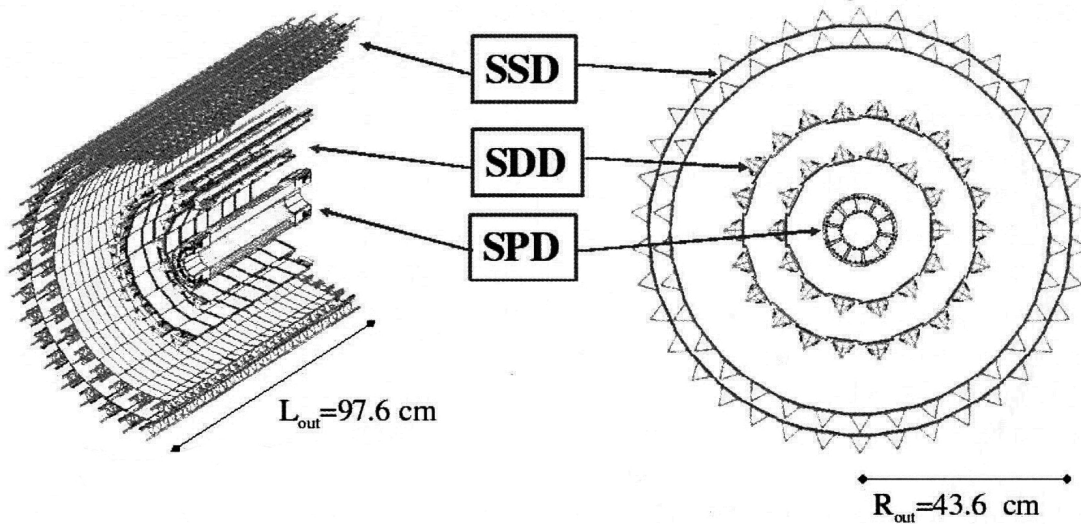
Figure 3.4: The Inner Tracking System (ITS) build up out of 6 layers of silicon detectors [39].

A schematic view of the ITS is shown in Fig. 3.4. It consists of three pairs of cylindrical layers each using a different technology. The four innermost layers are truly 2D devices using silicon pixel (SPD) and drift detectors (SDD). The outer two layers are build of two-sided silicon strips (SSD). The first layer starts directly after the beam pipe at 5 cm outer radius, the last one ends at R = 43.6 cm just before the TPC starts. The number, position and layout (granularity) of the ITS layers were chosen in a way that it can achieve its main objectives: reconstruction of the primary vertex with a precision better than 100 μm and improvement of the TPC tracking. ITS has ~12.6 million readout channels 9.8 million of which are in the first and second layers. This number does not take into account the number of time bins in the SDD which are used to determine the rϕ position of a hit. The pseudo-rapidity range of all layers is $|\eta| < 0.9$ but by taking the first layer only the coverage can be extended to $|\eta| < 1.96$. This creates an overlap with the Forward Multiplicity Detector and allows the measurement of charged-particle densities. The SPD detector consists of a 2D matrix of reverse-biased diodes bump-bonded on a readout chip. This sandwich construct together with the light-weight carbon-fiber

support structure allows to reduce the material budget to ∼1% X_0 per layer. The readout of the SPD is binary: the pre-amplified and shaped signal is compared to a threshold and the digital output level changes if the signal lies above. The SDD detector measuring the rϕ position by the drift time needs a very homogeneous high-resistivity silicon in order to achieve the precision it has. The SDD operates at a HV of -2.4 kV; it has two 35 mm long drift regions separated by the HV cathode. The two layers of the SDD have analog readout just like the SSD detector in order to measure the ionization energy loss of charged particles along their trajectory. The silicon strip detector (SSD) has readout electronics that is AC coupled to the sensor on both sides. The readout has a speed of up to 10 MHz with a power dissipation of 340 μW per channel. To keep it low and constant is crucial in order not to disturb the TPC where the stability of gas temperature is very important for the properly calibrated operation of the detector.
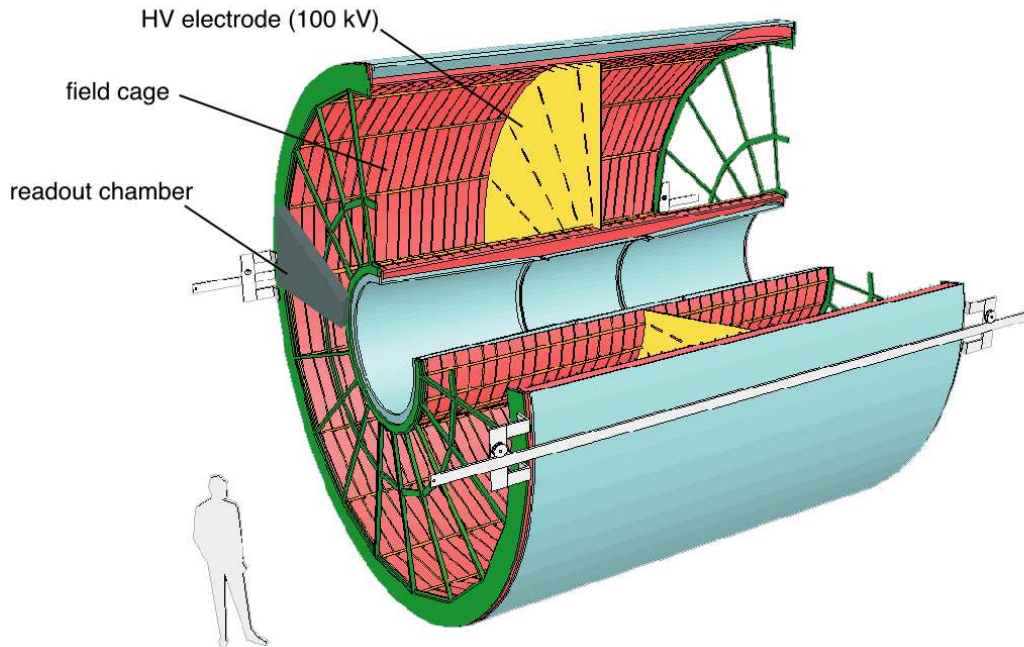
Figure 3.5: The TPC consisting of a gas volume, an electric field cage and readout chambers [41].

The need to handle up to 10 000 tracks within the acceptance range led to the choice of a TPC despite the slow speed and large data volume. The ALICE TPC [42]starts just after the last layer of the ITS having almost the maximum acceptable hit density in its innermost region and has an outer radius of 2.5 m. Being the main tracking detector in ALICE the TPC provides charged-particle momentum measurement, good two-track separation, PID and vertex determination at the mm level. Expecting to have Pb–Pb collisions with up to 8 kHz at the highest LHC luminosity and a large charged particle production the TPC was designed to cope with an occupancy of 15-40% depending on the position relative to the primary vertex. It is expected that the TPC will be able to collect central heavy-ion events with a rate of 200 Hz, where the ion feedback from the gas amplification during

the gate open time starts to distort the tracking. Having very high interaction rates in pp and searching for rare processes only triggered events will be processed by the TPC. But because of the long drift time of 90 μs there will be tracks from up 60 other events together with the tracks of the triggered event assuming a collision rate of 350 kHz. The total charge they cause will be still small compared to a central Pb–Pb event and tracks from the pile-up events can be removed since pointing to a different vertex. A sketch of the TPC design is presented in Fig. 3.5 where one can see its cylindrical shape. The overall size is 5×5×5 m^3 with an active volume of 88 m^3. The gas composition is $Ne/CO_2/N_2$ (85.7-9.5-4.8) [42] in which the ionizations charge is transported over a distance of up to 2.5 m from the HV membrane in the center to the multi-wire proportional chambers in the end caps. The gas mixture was optimized for drift speed, low diffusion and multiple scattering, and aging. It allows high electric fields (400 V/cm) but being a "cold gas" it requires a stable environment (temperature and pressure). The readout at the end plates has an active area of 32.5 m^2 and is segmented into two rings (with 18 sectors each) with different size of the readout pads and wire geometry. The total number of channels is about half a million, they all have analog readout to measure the dE/dx of the tracks.

The reconstruction of the primary vertex is performed using the hits from the SPD detector. For this purpose points that are close in azimuthal angle are combined and the z coordinate of the vertex is obtained by using a linear interpolation. Then in a similar procedure the position of the vertex in the transverse plane is calculated. Here the linear interpolation is not very precise due to the bending in the magnetic field but the results are a good starting point for the tracking algorithms. The position of the vertex is re-calculated using the reconstructed tracks. At the end the spacial resolution in z has a small constant term and a term depending on $dN_{ch}/d\eta$. For pp collision with 6-7 tracks on average the resolution is ∼100 μm in Pb–Pb where the multiplicity is much higher on the 10 μm level.

The TPC uses a Kalman filter for track finding and fitting. The seeding which is very crucial for this procedure is done using the space-point positions from the center of gravity of the clusters. This is done from the outermost pad rows towards the center of the TPC in steps by adding clusters to the current track if they are compatible with its parametrization and then updating the track and going to the next pad row. This is done twice: with and without the primary vertex as a constraint. After this both sets of track candidates are propagated to the ITS again with and without the primary vertex as a constraint. It is also possible to split a TPC track into two separate track candidates if more than one acceptable hit is found in one layer. At the end a decision is taken based on the χ^2 of the candidates. After the ITS tracking the whole method is reversed and the tracks are prolongated back into the TPC trying to remove any outlying clusters using the full available information. After the tracks are matched to the TRD tracklets (optional) and to the TOF space points the refit is done one last time inwards to extract the fit parameters close to the primary vertex. The TPC+ITS tracking efficiency is above 80% at 0.3 GeV/c for pp and goes up to 90% for higher momenta, in central Pb–Pb events it is just few percent lower [39]. Tracks without the primary vertex assumption are used in a subsequent analysis to find charm and beauty particles with a decay length of few hundred μm.

The first step of the reconstruction of strange particles (K_S^0, Λ, ...) or converted photons is done during (on-the-fly V0 finder) or directly after the tracking (off-line V0 finder) by two methods searching for secondary vertexes. Only secondary tracks with large impact

parameter are used here. The distance of closest approach is calculated and if it lies below a certain value and the point of closest approach is before the first measured points of the tracks a so-called V0 candidate is saved. A cut on the pointing angle (angle between the reconstructed V0 momentum and the line between the primary and secondary vertex) can also be applied to ensure higher purity of the selected sample but it must be handled with care because it is a bias against cascade particles. The tracks are refitted and the track parameters are recalculated under the assumption of the secondary vertex for the on-the-fly V0 finder which is possible because at this stage of the analysis the information about hits in the ITS and clusters in the TPC is still available. This improves the position and momentum resolution for the V0 candidate. For the off-line V0 finder this is not possible since it operates after the tracking, which nevertheless gives us the possibility to rerun the finder with modified cuts without repeating the whole reconstruction.

3.3.2 PID with TPC and TOF

The analysis presented in this Thesis uses the PID information from the TPC dE/dx and the TOF detector to improve the purity of the selected electrons and positrons for the gamma reconstruction. ALICE can provide additional track PID by using the ITS dE/dx, the TRD, the EMCal or the HMPID detectors. All the results from different detectors can be combined using the Bayesian method. Here first each detector provides a vector with the probabilities for the track to be of a certain particle type. Then the normalized vectors are combined to an overall probability vector. For the final PID decision the different populations of the particle-species have to be taken into account. This so called a priori probability vector can be obtained either from MC or in an iterative procedure starting with flat a priori probabilities. This method allows the usage of the PID information without knowing the technicalities of the individual detector systems. In our analysis we use MC information to correct the raw yields for efficiency. Because of this we need to insure that the efficiency calculated from MC is properly reproducing the situation in data. Therefore we need much more control over the PID and use a different procedure where we try to cut away from the electron/positron distributions in order to have only a minimal effect on the efficiency but we reject all tracks that cannot be an electron to increase the sample purity and this way also the quality of the analysis.

The dE/dx measurement with the TPC has a resolution of 5.5% in pp, which increases to 6.5% for central Pb–Pb collisions [39]. The mean of 65% of the pad-row samples with the lowest amplitude is used for this measurement. The separation power of the TPC PID is very good for the $1/\beta^2$ region at low momenta, it then goes to zero when the curves cross and increases again because of the relativistic rise of the dE/dx at high momenta. For our analysis we use the TPC to exclude all tracks that are more then +5 or -4 standard deviations (σ) away from the electron/positron line in the dE/dx vs momentum distribution and we additionally exclude tracks close (3σ) to the charged pion line between 0.4 and 5 GeV/c, where electrons and pions are well separated.

The PID gap due to the line crossings in the TPC dE/dx is closed by the TOF detector. It can separate pions from electrons from 0.3 GeV/c up to 0.7 GeV/c, kaons up to 2.5 GeV/c and protons up to 4.5 GeV/c. The precision for the measurement of the arrival time is 80 ps. The detector itself is barrel-shaped and covers the central pseudo-rapidity range in ALICE. It is segmented into 18 sectors in ϕ and each sector in 5 modules in z and situated

between 370 and 400 cm in R. The length of the active area is 741 cm. In Fig. 3.6 (left) one can see the layout of the TOF detector as it is mounted inside the L3 magnet. Multi-gap Resistive-Plate Chambers (MRPC) are used for particle detection. These gaseous detectors are rather simple and allow the use of commercial materials. Reduction of production costs and coverage of large areas can be easily achieved this way. The main advantage of MRPCs is that they have uniform and high electric field over the full sensitive gaseous volume of the chamber. This way any charge produced by transversing charged particles starts an avalanche immediately. This process generates signals at the pick-up
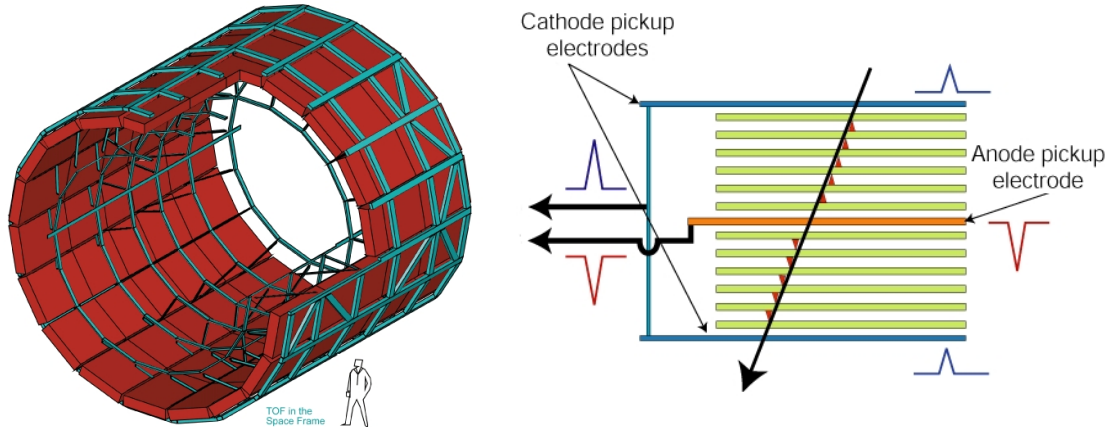

Figure 3.6: TOF and its support structure (left) and the principle of TOF's particle detection(right) [43].

electrodes. In this kind of detector there is no drift of charge to the electrodes and thus the time resolution is only limited by fluctuations in the growth of the avalanche. There are some more advantages of this technology: the chambers are operated at atmospheric pressure; since the signal is the analogue sum of the signals from many gaps there are no tails and the shape has a high narrow peak allowing precise timing; the resistive plates make the creation of sparks impossible and thus operation with higher gain is possible. The request for occupancy not higher than 10-15% and the large charged-track density in central Pb–Pb collisions led to more than 10^5 readout channels in TOF. The TOF modules are built out of 10-gap double-stack MRPC strips. The schematic cross-section of a strip and the principle of the particle detection with a MRPC is shown in Fig. 3.6 (right). The strips with 122 cm length and 13 cm width are placed perpendicular to the beam axis inside the gas-tight modules. The strips are overlapping in order to avoid dead areas and have tilted positions inside the chambers to be perpendicular for incoming tracks and so reduce the amount of traversed material and the charge sharing between the pads in which a strip is separated. The tilt goes from 0° at the center to 45° at the external part of the module. The thickness of the material corresponds to 30% of a radiation length.

The TOF PID is performed in the following way: first in the last pass of the Kalman tracking a set of times the particle would need along its trajectory is calculated assuming different particle-species. Here also the energy loss during the flight through the material is taken into account. Then the time of the collision is taken as measured by the T0 detector independently from the vertex position. This time from T0 does not have to be the starting time of the particle since it might be a secondary from strange decays

or a product of interactions with the detector's material. The real start time can be approximated by taking the momentum and the trajectory of the particle into account. Subtracting the starting time from the arrival time measured by TOF we can now compare it to the set of times for the different hypotheses. This comparison can be then translated into a set of probabilities for the Bayesian method or as in the case of our analysis one can just reject tracks that are more than five sigma away from the electron hypothesis. This way we have a loss-free method to improve the purity of our electron/positron sample.

3.3.3 V0 detector and Centrality Measurement

The V0 detector consists of two discus-shaped scintillator counters situated around the beam pipe on both sides of the interaction point. The main function of the V0 detector is to supply a minimum bias trigger for the central barrel part of the ALICE detector in both pp and Pb–Pb collisions. It can also be used as an estimator for the multiplicity since the number of particles registered with the detector array is monotonically dependent on the total number of produced primaries. This way it can be used to determine the centrality of a nucleus-nucleus collision. The definition of centrality classes used in ALICE [44] is presented in Fig. 3.7 which shows the distribution of events vs the V0 amplitude together with a Glauber fit and the class borders, containing the corresponding fraction of events.
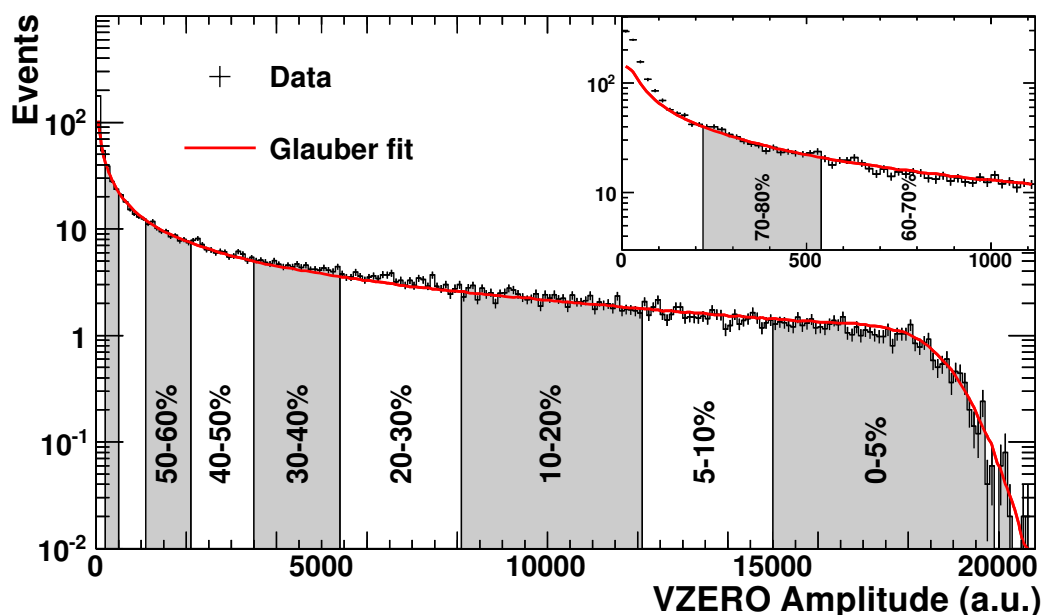
Figure 3.7: Distribution of events vs the V0 amplitude in ALICE together with a Glauber fit and the definition of the centrality classes like it is used in this analysis [44].

The V0 detector can be also used as a multiplicity trigger in pp or for triggering of central and semi-central Pb–Pb collisions if cuts on the total charge and on the number of fired counters are applied. The trigger can be operated in AND mode, where a signal in both V0A and V0C is required or in OR mode where one side is sufficient. The efficiency of the trigger for pp is ∼84% [39] if the effect of secondaries from the beam pipe material

is taken into account. For Pb–Pb collisions with 0-80% centrality the efficiency is close to 100%. Beam-gas events can be identified and this way a large number of false events can be rejected. Using the absence of the V0C trigger can help to significantly reduce the number of background triggers in the muon chambers. The V0 detector also takes part in the measurement of the pp luminosity.
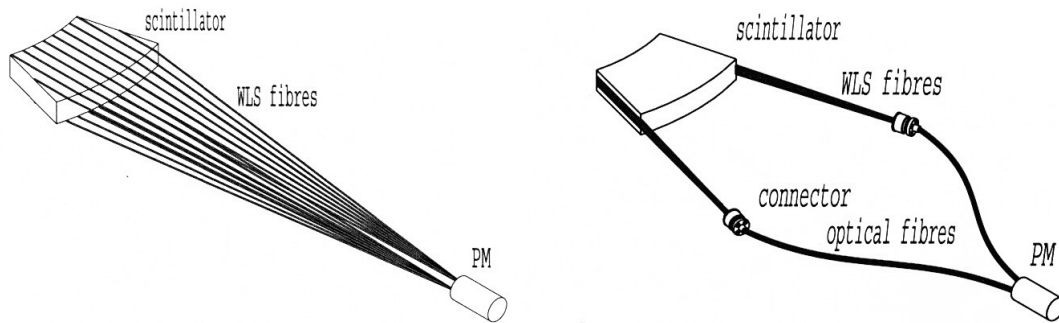

Figure 3.8: Design of the V0A (left) and V0C (right) detector elements [39].

The design of the V0 elements is presented schematically in Fig. 3.8. These elements are made of scintillating materials of 2.5 cm and 2.0 cm thickness for the A and C sides respectively. The signals are brought out with 1 mm diameter wave-length shifting fibers which are placed with 1 cm spacing on the transverse face of the 32 V0A segments. These segments are arranged in 4 rings with 8 segments each. For the V0C detector which is segmented into 48 elementary counters in 4 rings the wave-length shifting fibers are grouped into layers of 9 and glued to the radial edge of the segments. The V0C detector is located right before the hadronic absorber for the muonic spectrometer 90 cm from the interaction point. It covers a pseudo-rapidity range of -3.7 $< \eta <$ -1.7 which is further away from the beam than the 2.8 $< \eta <$ 5.1 range of the V0A detector placed at 340 cm from the vertex. The fibers guide the light to a system of photo-multipliers whose signals are delivered to the front-end electronics where the different triggers are created.

3.3.4 PHOS and EMCal

Photons are a very interesting probe in heavy-ion collisions since a considerable fraction of the soft component of their spectrum is produced by thermal radiation. The γ's of the hard component of the spectrum which are produced by the initial hard processes do not interact strongly with the medium when they transverse it.

In ALICE photons can be measured with PHOS which is a small single-arm electro-magnetic spectrometer at mid-rapidity with high energy resolution and granularity. Also neutral pions can be reconstructed from the PHOS photons and their correlations with jets studied. Being located 4.6 m away from the interaction point PHOS still has to cope with the rather large particle density of central Pb–Pb collisions since the maximum occupancy is required to be between 10 and 20% [39]. It uses therefore dense scintillating crystals made of $PbWO_4$ that have both a small Molière radius and sufficient light output giving

the detector the ability to measure particles with low energies. The depth of the detector is 20 radiation lengths suitable for the absorption of the full shower signal. PHOS has multi-wire proportional chambers in front as a charged-particle veto which help for the photon PID. Background from neutrons can be reduced by time-of-flight measurements and topological studies of the shower development. A PHOS module with $PbWO_4$ crystals and photon detectors mounted on cooling plates is shown in Fig. 3.9 (left).
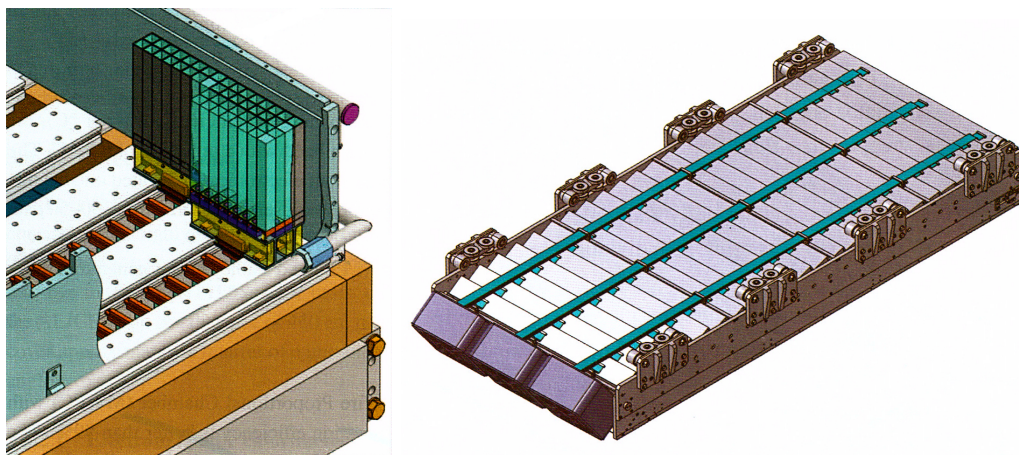

Figure 3.9: PHOS module with $PW0_4$ crystals (left) and an EMCal super module (right) [39].

In the same figure on the right a super module of the the EMCal detector is presented. This electromagnetic calorimeter is using a Pb-scintillator sampling technology and is much larger than the PHOS detector. It uses longitudinal wavelength-shifting fibers and avalanche photo diodes for the creation of the signal. EMCal has lower granularity and energy resolution than PHOS which decreases the resolutions of the photon energy measurement. But its large coverage will be crucial for ALICE's capability to study jet properties and thus the interaction of energetic hadrons with the dense matter. The EMCal is positioned opposite to PHOS and covers an angle of $107°$ in ϕ and a pseudo-rapidity range of $|\eta| < 0.7$. It can provide a fast and efficient trigger for photons, electrons and hard jets, important for the exploration of rare processes. The EMCal can also measure the neutral components of jets and together with the TPC allows ALICE to study the full range of jet-quenching effects that are expected at the LHC.

The π^0 results of PHOS and EMCal will be compared to the results of the analysis presented in this Thesis in section 6.1.

3.4 Triggering, Data Acquisition and Data Reconstruction

The event selection in ALICE is handled by the Central Trigger Processor (CTP) which can trigger on various features and at rates that can be adjusted (scaled down) to suit physics requirements or to be compatible with the bandwidth of the Data Acquisition (DAQ) system. The different "busy" times of the detector components after a valid trigger and the different collision systems with interaction rates that vary by two orders of magnitude are the main challenges that need to be faced by the ALICE triggering. The

fast trigger is divided into two separate stages: the L0 trigger with a latency of 1.2 μs and the L1 trigger 6.5 μs after the collision. This staging is needed because of the large amount of data that needs to be buffered in some of the ALICE detectors during Pb–Pb operation at 8 kHz but leads to an only partial trigger input for the L0 trigger. The input of the remaining trigger detectors is used by the L1 trigger. The CTP needs only 100 ns out of the 1.2 μs of the L0 delay time for decision taking, the rest is coming from the input generation and traveling of the signals along the cables. The environment created in ALICE by a central heavy-ion collision is characterized by high multiplicity that does not allow the reconstruction of events with more than one such collision. A "past-future protection" mechanism is therefore a substantial part of the triggering. The final triggering level L2 waits until the end of the 88 μs protection interval and only afterward decides whether the event can be taken. The waiting time can be used to run other trigger algorithms and to make a more complex decision. For pp runs with high luminosity where pile-up is inevitable but also tolerable up to a certain extent because of the lower multiplicity the limiting factor is the read-out time of the ITS pixel detectors (10 μs). In order to control the simultaneous running of different triggers and to insure that triggers important for the analysis are read out with sufficient rates two mechanisms can be applied. Taking only every nth event of a certain trigger (down-scaling) is one possibility which is not always the best since its adjustments cannot be changed during a run and thus it is not possible to react to changes of the luminosity which occur naturally during an LHC fill. Therefore a second method is also in use. It is the temporary storage of the DAQ that can be saturated and is the bottleneck of the readout this way. In this case especially rare processes can be effected stronger as the more frequent ones. Therefore all the triggers are divided into two groups: rare and common. If the occupied storage exceeds a predefined value the read-out of common-trigger events is stopped until the saturation reaches another lower value.

The task of the DAQ system in ALICE is to insure that both rare and frequent or large-size triggers get a fair share of the bandwidth, to provide the high-level trigger (HLT) with efficient access to the data and to archive the data for permanent storage. The final bandwidth to mass storage was estimated to be 1.25 GB/s. Although the Tier-0 of CERN's Computing Grid project is providing higher bandwidths and a bandwidth higher than 1.25 GB/s might be needed due to the increase of the number of triggers there are still efforts to satisfy the physics requirements with the original resources by an increase of trigger selectivity, data compression and partial readout. When the different detectors receive the trigger signal and the associated information they send the data through the ALICE-standard Detector Data Links (DDL) all using the same protocol. This transmission is performed by pairs of about hundred meter long optical fibers creating a 200 MB/s connection in both directions. The data is picked up by standard PCs called Local Data Concentrators (LDC) that then ship the received data packets to the Global Data Collectors (GDC). These are responsible for the building of the whole event from sub-events tagged with the same trigger. An Event Building and Distribution protocol is run on the whole system in order to balance the load on the single GDCs creating an overhead as small as possible at the same time. The data is archived in files of the same size which are registered in the ALICE Grid software (AliEn) and then moved to the Permanent Data Storage. The data flow from all detectors and triggers can reach values of 25 GB/s for high-luminosity heavy-ion runs but the highest rate that can be written to mass storage

is a factor 20 smaller. This problem calls for on-line processing in order to reduce the amount of needed storage which is possible because the physical content of many recorded events is rather small compared with their size. This task will be managed by the HLT, a computer farm with more than 1000 multi-core machines which can select relevant events or parts of events. Within five layers the HLT reconstructs global physical observables out of the raw data from each detector and takes a decision based on run specific selection criteria. For the TPC, compression factors of up to 9 are possible. For the 2010 data taking, HLT data selection and compression was not yet applied.

The data collected on tape this way needs to be analyzed in order to extract a physics message. This task including simulation, reconstruction, calibration, alignment, visualization and the analysis itself is managed by the Offline Project of ALICE. The main targets of this project are to insure a highly reliable storage of the data, wide access to it and make a timely physics discovery possible. The total computing power needed to achieve these objectives is so large that it is not possible to concentrate it in one place, but on the other hand it needs a common, centrally organized system in order to maintain all the data and to be able to guaranty its quality. To make the distributed and various resources that are available work as a single integrated computer center is the focus of the Grid project which although already functioning is still being further developed and optimized. The CERN computing center Tier-0 has the highest rank in this hierarchy and all the raw data coming from the experiment is first stored here. In the following steps the data is copied to the Tier-1 centers that are distributed around the world and are able to save the data on highly-reliable magnetic tapes just like Tier-0. The first pass of the reconstruction is done at CERN, later ones at the Tier-1 centers. The Event Summary Data (ESD) files created this way can be further distributed, analyzed and then used to give feedback for further improvement of the reconstruction. The analysis described in this thesis was performed on a copy of the data stored on the LUSTRE data servers at GSI, Darmstadt and using the GSI batch farm.

The ALICE offline framework, AliRoot, is implemented as an Object-Oriented supporting framework based on the ROOT system. It has been developed since 1998 and used for all the analysis tasks listed above. The tests and simulation studies for the sub-detector systems and the optimization of their design have being already done with AliRoot. For the Monte Carlo (MC) studies an event generator (Pythia [45], Phojet [46], HIJING (Heavy Ion Jet INteraction Generator) [47]) first creates a list of particles with information about type, momentum and mother-daughter relationship. These particles are then transported with GEANT 3.21 [48] through the detector with weak decays happening, hits being created and detector responses (digits) being calculated. From this point on the reconstruction happens the same way as for data with the only difference that the reconstructed tracks are labeled to know from which MC particle they were created. The final reconstructed data with information on tracks, decays, PID and more is then saved in the ESD file format for further analysis using the AliRoot framework.

Around 110 good runs (see Appendix 8.3) were recorded during the Pb–Pb 2010 data taking period. The run duration varied between tenths of minutes and several hours. The runs contain few hundred thousand events each collected at rates of up to 200 Hz. The bunch intensity increased from few 10^{10} to almost 10^{12}. Various triggers (SPD, TOF, V0, TRD, MUON) with different settings were in use.

4 π^0 Reconstruction

4.1 Analyzed Data and Monte Carlo

The analyzed data sample consisting of $\sim 18.4 \times 10^6$ minimum-bias events was collected by the ALICE experiment at the CERN Large Hadron Collider (LHC) in November and December 2010 with a center of mass energy per nucleon pair of $\sqrt{s_{\mathrm{NN}}} = 2.76$ TeV. In order to ensure the good quality of the analysis and to be able to select photons coming from the primary vertex we applied very strict conditions for the event selection. Only fully calibrated data (Pass 2) and the designated Monte Carlo productions were used in this analysis. Events with a centrality beyond 80% are not used due to not fully understood trigger efficiency issues. The centrality selection is done using the V0 detector (see subsection 3.3.3). We decided to have only four centrality bins in our analysis: 0-20%, 20-40%, 40-60% and 60-80% since smaller centrality classes are not possible with the currently available statistics. Two Monte Carlo samples LHC11a10a (incl. LHC11a10a_bis) and LHC11a10b with $\sim 1.2/1.1 \times 10^6$ minimum-bias events were used for the π^0 acceptance and reconstruction efficiency studies. These MC samples were generated with a HIJING version tuned to reproduce the charged-particle multiplicity as measured by ALICE. The LHC11a10b MC has additional signals (also π^0 and η) with flat p_{T} distributions added to enrich rare particle samples. The reconstruction of the MC samples was done with the same software framework as the real data tuned to reproduce the actual conditions during each data taking run. The event numbers presented above are for events that have already passed the ALICE Physics Selection (PS). The events taken for the π^0 analysis and efficiency calculation are additionally required to:

1. Have a reconstructed collision vertex with global tracks, or with SPD tracklets.

2. The z position of the collision vertex has to be within ± 10 cm of the nominal value.

The fraction of events without a vertex is negligible at least up to a centrality of 80%. The exclusion of events with $|z_{vtx}| > 10$ cm is necessary due to differences in the acceptance for such events. The results of the event selection are summarized in Table 4.1 for different centrality bins. The presented numbers may differ from the expected values (based on the definition of centrality) since $\sim 15\%$ of the PS events have a vertex with $|z_{vtx}| > 10$ cm and are not analyzed at all. In MC there is additionally the problem that the number of events is not equal for the different centrality bins, tending to be lower in the central classes. This is caused already at the event generation level and forces us to keep the centrality bin size low in order to avoid incorrect weighting towards lower centrality, which would result in an overestimation of the efficiency. The normalization of the neutral meson spectra is done separately in each centrality class. The event numbers used hereby are for events accepted by the Physics Selection and having a vertex within ± 10 cm of the nominal value in the corresponding centrality bin.

	$\sqrt{s_{NN}}$	Events with (PS+Vtx+$|z_{vtx}|$ <10)
Data (h) (Pass2, centrality 0-20%)	2.76 TeV	3.2e+06
Data (h) (Pass2, centrality 20-40%)	2.76 TeV	3.2e+06
Data (h) (Pass2, centrality 40-60%)	2.76 TeV	3.2e+06
Data (h) (Pass2, centrality 60-80%)	2.76 TeV	3.2e+06
MC LHC11a10a (h) HIJING 0-20%	2.76 TeV	1.5e+05
MC LHC11a10b (h) HIJING 0-20%	2.76 TeV	1.6e+05
MC LHC11a10a (h) HIJING 20-40%	2.76 TeV	1.9e+05
MC LHC11a10b (h) HIJING 20-40%	2.76 TeV	1.9e+05
MC LHC11a10a (h) HIJING 40-60%	2.76 TeV	2.2e+05
MC LHC11a10b (h) HIJING 40-60%	2.76 TeV	2.4e+05
MC LHC11a10a (h) HIJING 60-80%	2.76 TeV	2.5e+05
MC LHC11a10b (h) HIJING 60-80%	2.76 TeV	3.1e+05

Table 4.1: Number of events passing the event selection conditions (PS+Vtx+$|z_{vtx}|$ <10) that are used in the analysis for data and MC in all different centrality classes.

4.2 π^0 Reconstruction and Yield Extraction

The reconstruction of the π^0 meson is performed in two stages. First, tracks which pass the electron/positron selection cuts (see section 4.4) are combined to γ candidates, which have to pass additional cuts. Using pairs of surviving photon candidates, in the second stage, we calculate invariant mass distributions in different p_T intervals according to the binning of the final π^0 yield. The combinatorial background is also calculated in p_T bins using an event mixing technique with event classes based on the charged track or gamma candidate multiplicity and the z-position of the primary vertex. For the Pb–Pb analysis all these classes were optimized to contain similar number of events by evaluating the corresponding distributions for minimum-bias event selection after the quality cuts. For the multiplicity classes we also needed to check the compatibility with the centrality classes by making sure that there are no poorly populated but still not empty multiplicity classes in any of the used centrality classes. The distributions of accepted charged tracks (the conditions for a track to be accepted are presented in 4.4), the gamma candidate multiplicity and the z-position of the vertex for data and the LHC11a10a MC sample are presented in Fig. 4.1 and Fig. 4.2 for all centralities. For the accepted tracks it was easy to choose the classes in a way that each centrality occupies two multiplicity classes. The task was more complicated for the gamma multiplicity classes since there is much more overlapping of the centralities. A compromise between equally filled and centrality compatible classes was made. For the classes based on the z-coordinate of the primary vertex we took the shift between the data and MC distributions into account by averaging the results. The the event classes used for the background calculation via event mixing can be seen below:

- Charged Track Multiplicity: 0 / 55 / 210 / 550 / 1200 / 3000

- Gamma Candidate Multiplicity: 2 / 8 / 15 / 25 / 9999

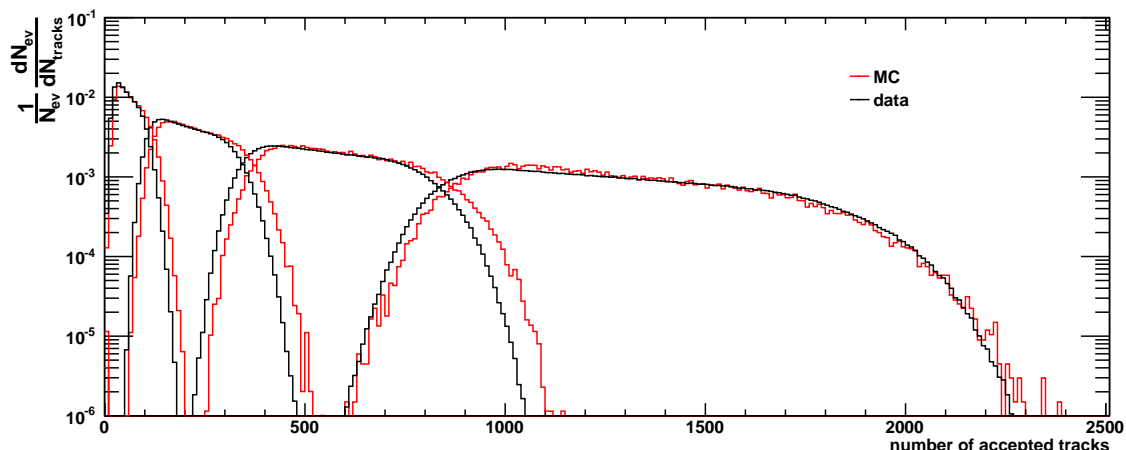- Z-Coordinate Vertex: -50 / -5.6 / -3.0 / -0.8 / 1.2 / 3.3 / 5.8 / 50

Figure 4.1: Number of accepted charged tracks for different centralities in data and MC LHC11a10a. (Each distribution is normalized to the total number of events in the centrality bin it represents.)
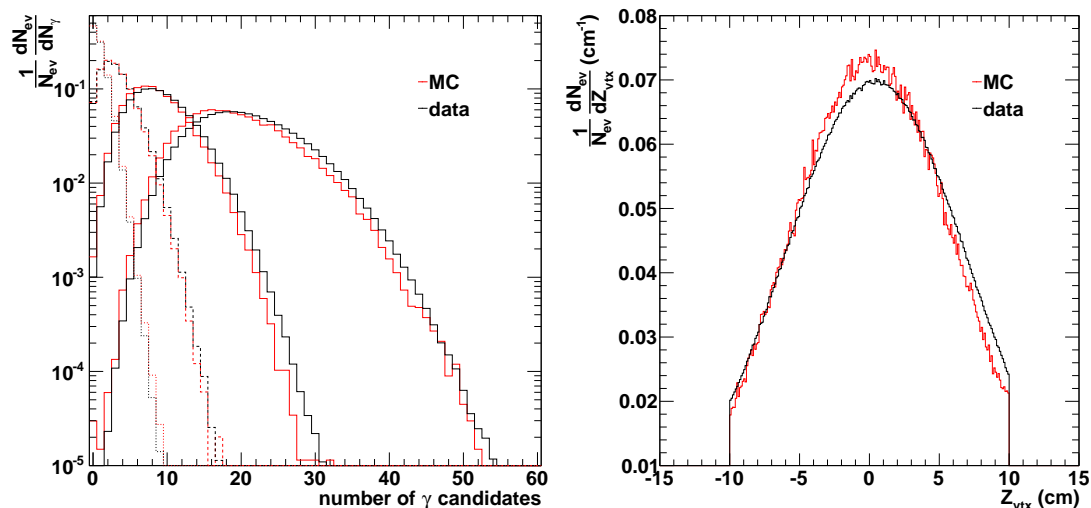

Figure 4.2: γ-candidate multiplicity for different centralities and the distribution of the z-coordinate of the primary vertex for data and MC LHC11a10a. (Each distribution is normalized to 1 by itself.)

In Fig. 4.3 (left) the $\gamma\gamma$ invariant mass distribution and the scaled background for one p_T bin are presented. A peak is clearly visible around the expected π^0 mass and one can see the quality of the mixed event background, that nicely describes the actual background, above 50 MeV/c^2. The peak at low invariant mass although not fully understood is well separated from the π^0 peak and will not influence the results. The background is scaled to the signal away from the π^0 peak and subtracted from the invariant mass distribution, which is then fitted by a Gaussian function with an exponential tail to account for bremsstrahlung energy loss of the electron/positron and a linear part to handle any remaining background (Eq. 4.1, Eq. 4.2; Fig. 4.3, right).
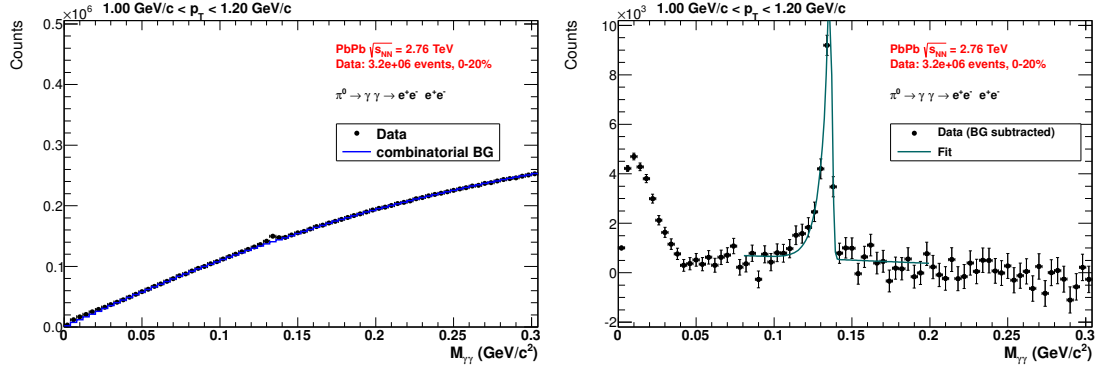
Figure 4.3: Invariant mass distribution of photon candidate pairs before (left) and after (right) background subtraction for the 0-20% centrality class in the 1.0-1.2 GeV/c transverse-momentum bin (black points). The blue histogram on the left is the combinatorial background obtained via event mixing. The cyan curve on the right is a fit to the π^0 peak.

$$y = A \cdot \left(G(M_{\gamma\gamma}) + \exp\left(\frac{M_{\gamma\gamma} - M_{\pi^0}}{\lambda}\right) \cdot \left(1 - G(M_{\gamma\gamma})\right) \cdot \Theta\left(M_{\gamma\gamma} - M_{\pi^0}\right) \right) + b + c \cdot M_{\gamma\gamma} \quad (4.1)$$

$$G(M_{\gamma\gamma}) = \exp\left(-0.5 \cdot \left(\frac{M_{\gamma\gamma} - M_{\pi^0}}{\sigma_{M_{\gamma\gamma}}}\right)^2 \right) \quad (4.2)$$

$$N_{raw}^{\pi^0} = \sum_{m_{reco}^{\pi^0} - 35 MeV/c^2}^{m_{reco}^{\pi^0} + 10 MeV/c^2} \left(N^{\gamma\gamma} - N_{scaled}^{bck} \right) - \int_{m_{reco}^{\pi^0} - 35 MeV/c^2}^{m_{reco}^{\pi^0} + 10 MeV/c^2} \left(c \cdot p_T - b \right) dp_T \quad (4.3)$$

The raw signal is then extracted by summing up the histogram between 35 MeV/c^2 below and 10 MeV/c^2 above the reconstructed π^0 mass position obtained from the fit. Additionally the remaining background calculated as the integral of the linear part of the fit over the same mass interval is subtracted from the raw signal. The calculation of the raw signal is summarized in Eq. 4.3. The raw yields resulting from this method are presented in Fig. 4.4 for each centrality. One can observe a nice ordering here despite the difference in reconstruction efficiency (see Fig. 4.6) for the different centralities which would push the raw yields together.The reconstructed π^0 mass positions (left) and peak widths (right) as a function of p_T can be observed in Fig. 4.5 for the 0-20% centrality bin. The gamma conversion method gives very narrow peaks with a FWHM/2.36 lower than 3 MeV/c^2 for low p_T and the reconstructed mass positions are very close to the PDG value of $\sim$135 MeV/c^2 even for these central events with very high track density. The peak widths of the reconstructed π^0 in data and the true reconstructed π^0 in MC are close to each other which is important for the π^0 reconstruction efficiency calculated in MC to describe properly the situation in data. The invariant mass distributions before and after background subtraction used for the extraction of the raw yields and the extracted peak positions and widths for all p_T bins, all centralities and for both data and MC can be found in the Appendix (see 8.2).
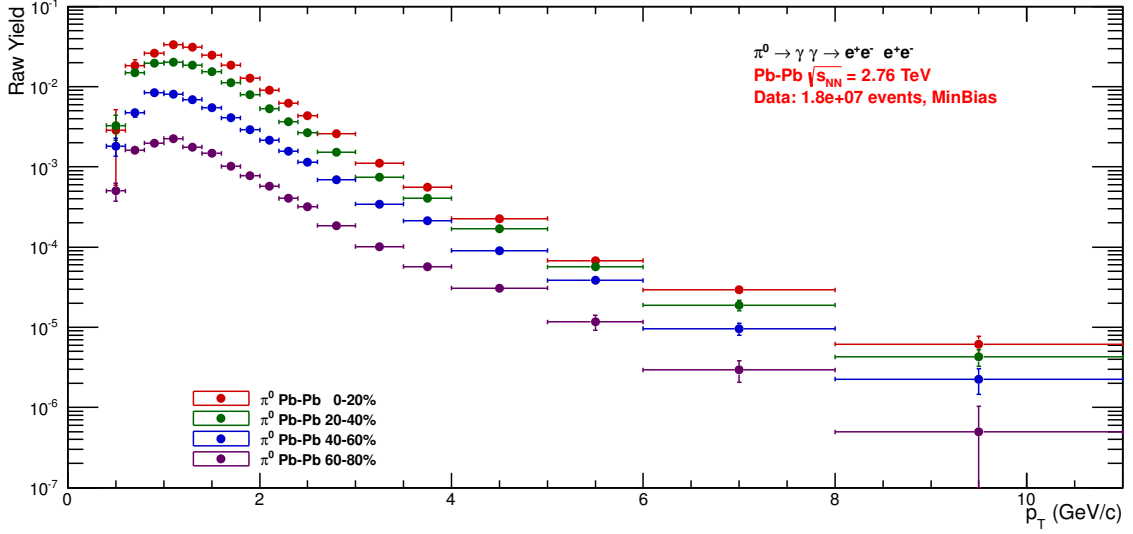
Figure 4.4: π^0 raw yields for each centrality bin as a function of the transverse momentum.
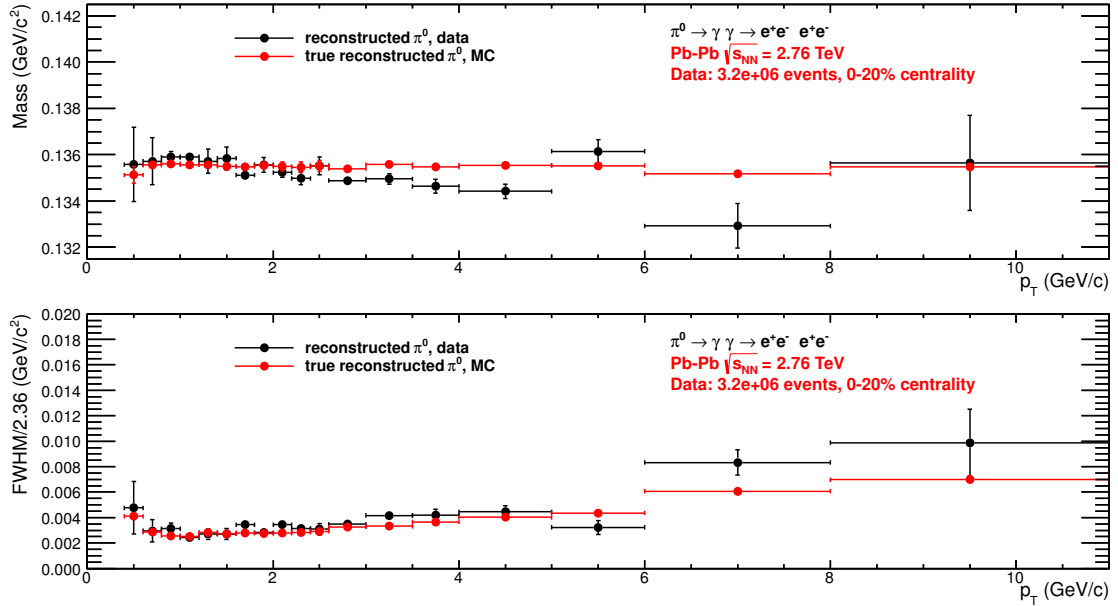

Figure 4.5: Mass (top) and FWHM/2.36 (bottom) of the reconstructed π^0 meson for data and the true reconstructed π^0 meson for MC for the 0-20% centrality bin obtained from the fit (Eq. 4.1).

The Pb–Pb π^0 analysis presented in this thesis is based on the software framework of the ALICE photon conversion group [49]. The framework which already contained the γ and π^0 reconstruction and yield extraction was optimized and extended for the heavy-ion analysis. The TOF PID was added and the TPC dE/dx cut was adjusted to optimize the e^+/e^- selection. On the photon level the purity was improved by the use of the q_T cut and on the meson level a study for the optimization of the decay asymmetry was performed.

4.3 Efficiency Calculation

The π^0 meson acceptance and reconstruction efficiency are calculated in Monte Carlo simulations where HIJING is used as event generator. The created particles are transported through the detector using GEANT 3.21 which also generates the detector response signals. These signals are then reconstructed using the same software as for real data (see 3.4 and 4.1). Since we are using converted photons for the π^0 reconstruction it is of great importance for us that the material budget of the ALICE detector is well implemented in GEANT, so that the real conversion probability and with it the π^0 reconstruction efficiency is reproduced properly in the MC simulations. The description of the material budget of ALICE was checked and improved by comparing the conversion density in data and MC for pp collisions by the photon conversion group [30] using the same γ reconstruction software as for the π^0 analysis.

The acceptance is defined as the ratio of the number of π^0 mesons within $|y| < 0.7$ whose decay products are in $|\eta| < 0.75$ over all π^0 mesons within $|y| < 0.7$. In both cases only π^0 with 2 γ daughters are considered, so the final π^0 yield has to be corrected for the $\pi^0 \rightarrow \gamma\gamma$ decay branching ratio. The transverse-momentum dependent acceptance for π^0 mesons is shown for all centralities in Fig. 4.6 (top). The deviation between different centralities at low momenta is caused by the additional π^0 signals added in the LHC11a10b MC sample which have a different rapidity distribution than the HIJING neutral pions. In addition the relative amount of such π^0s is not the same for the different centrality bins. Since the effect is less than 1% and only present at low momenta it is negligible compared to the statistical and systematic uncertainties that are of order 10% and 20% respectively.

In order to determine the meson reconstruction efficiency the same analysis chain as for real data was applied to the reconstructed Monte Carlo simulations. In addition, it was required that the two photon candidates are really photons that come from the same π^0 meson and have converted. We also check that the two track pairs associated to the two conversions consist of a real electron and positron from the converted gamma. In this way it is possible to obtain a background free meson sample. The efficiency obtained this way we call "true efficiency" as it contains no (combinatorial) background. The number of neutral pions that fulfill all these conditions is divided by the number of π^0s within the acceptance. The π^0 transverse-momentum dependent efficiency (shown in Fig. 4.6 (bottom) for all centralities) contains the γ conversion probability and reconstruction efficiency. These are shown in Fig 4.13 where one can see that they are quite low (0.6 and 0.08 for high p_{T}) which explains the low π^0 reconstruction efficiency if one considers the fact the both contribute quadratically.

There are two more issues with the used MC samples that needed investigation in order to ensure that the calculated π^0 efficiency was properly reproducing the situation in real data. First of all, as already reported, we observed that the number of events was not equal for different centrality bins although they all had the same width of 20%. The problem was rather large since the number of events in the 60-80% centrality bin was roughly double as large as the one for the 0-20% bin (see Table 4.1). Here we needed to check if there was a non-proper weighting already within a single centrality bin. First we divided each 20% centrality bin into two 10% centrality bins and obtained that the number of events in these two bins differs by not more than 10%. If we now consider the fact that the difference in efficiency for two neighboring 20% wide centrality bins is not
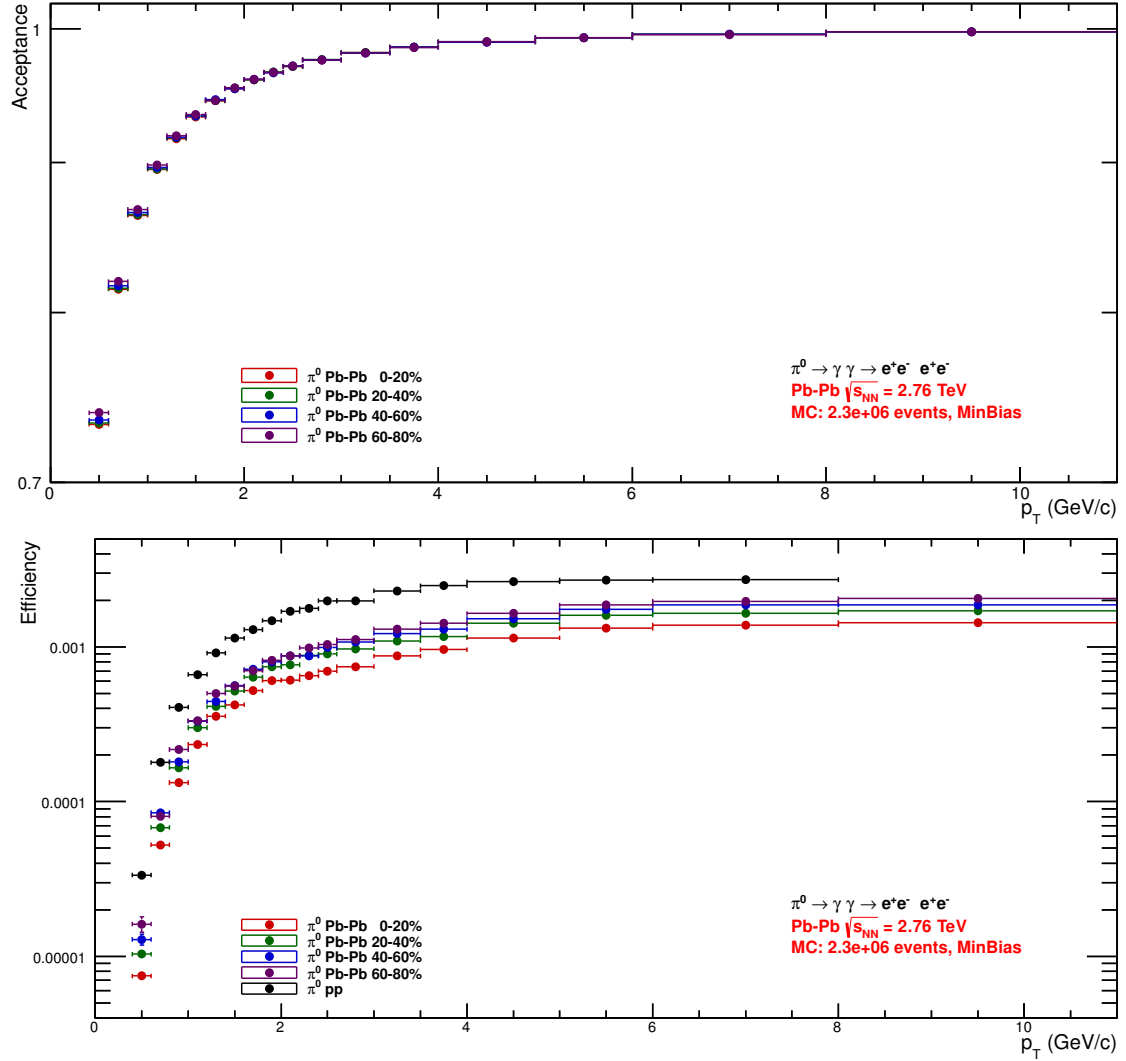
Figure 4.6: π^0 acceptance (top) and efficiency (bottom) vs p_T for $|\Delta y| < 0.7$ and for each centrality.

more than 50% (see Fig. 4.6) it is a valid assumption that the difference in efficiency for two neighboring 10% wide centrality bins is not more than 30%. This results into an efficiency for the 20% wide centrality bins that is less than 1% too high due to the rising number of events towards lower centralities. As an additional check we studied the distributions of the number of accepted charged tracks for different centrality classes for data and Monte Carlo (Fig. 4.1). This number is related to the number of primary tracks of a collision and is therefore a good measure of the track density in the detector on which the π^0 reconstruction efficiency depends. Here one can observe a different problem: although the MC matches qualitatively the shape of the data distributions we see an overall shift of the MC distributions compared to data towards higher number of tracks. This effect is well visible in the 20-40% bin. The shift is of the order of 10% of the mean track density for a centrality bin. Comparing this to the total difference in efficiency between two neighboring

centrality bins and using the same arguments as above we can conclude that the effect on the efficiency should be small (∼2%) and since it goes in the other direction as the one from above the total effect should be even smaller.

As we already mentioned we use two types of MC for the efficiency calculation: a pure HIJING one and one with added flat p_T π^0 signals (the distribution of the added signal is not exactly flat, but much less steep than the pure HIJING one). Having a steeply falling π^0 spectrum in data means that the efficiency of a p_T bin is actually the efficiency at a p_T which is more to the left of the bin due to the weighting towards lower p_T . If the MC π^0 spectrum is flat as in the LHC11a10b we obtain the efficiency at the p_T of the middle of the bin, which is bigger than the properly weighted one. To study this effect we assume that the efficiency of a certain bin is the one at the mean p_T of this bin calculated from the MC π^0 spectrum. This mean p_T is better suited for the efficiency determination in terms of properly describing the data in the MC LHC11a10a, where we have a falling spectrum, and not correct for MC LHC11a10b, which we have to use in order to reduce the statistical uncertainties of the efficiency especially at high $p_{mathrmT}$. For a certain p_T bin we interpolate the efficiency calculated from the LHC11a10b MC sample (placed at the mid p_T calculated from the MC LHC11a10b) between this and the previous bin to the mid p_T calculated from the LHC11a10a MC sample. We compare the resulting efficiency to the one from MC LHC11a10b for each bin. We use a linear interpolation, which gives us a higher limit for the effect since the efficiency follows a concave function. The maximum deviation turned out to be not larger then 2% and even much smaller for most on the p_T bins. This means that this effect is negligible at this stage of the analysis where our systematic uncertainties are of the order of 20% and higher. Fig. 4.7 shows a comparison of the LHC11a10a and LHC11a10b efficiencies and their ratio which agrees with unity within the uncertainties.
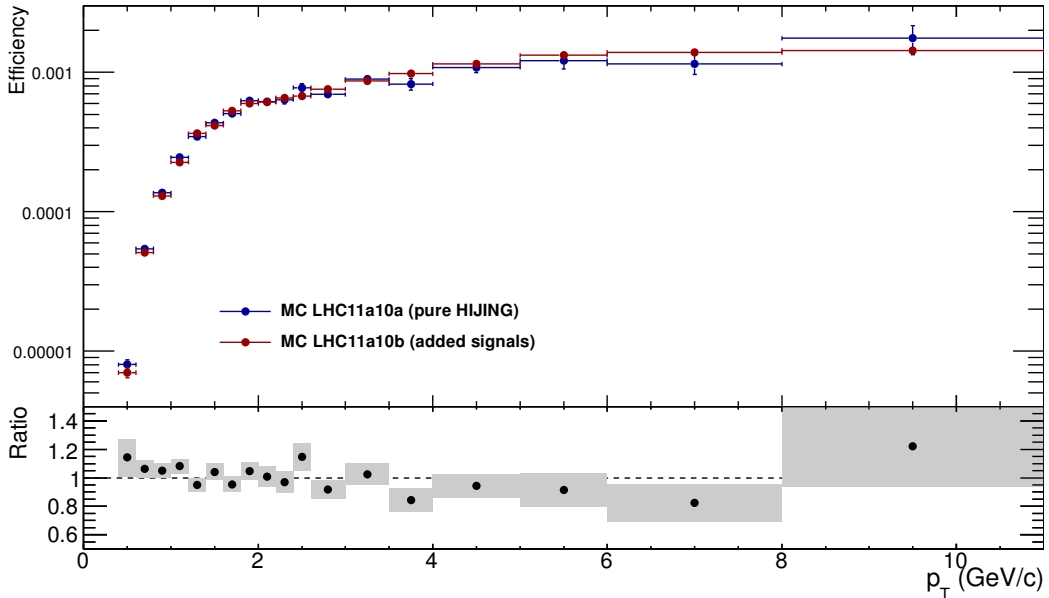
Figure 4.7: Two different π^0 efficiencies calculated separately with the LHC11a10a and LHC11a10b MC samples for the 0-20% centrality bin.

4.4 Cut Studies

The π^0 mesons reconstructed with the conversions method have two main sources of background: the V0s that are not true γ particles but pass the selection, and the pure photon combinatorial background, which would be always there, independently from the γ sample purity. Both contributions are increasing with the particle multiplicity in an event, so in Pb–Pb collisions the problem is much more eminent than in pp. In order to reduce the background we apply a series of cuts to enhance the signal at different stages of the reconstruction. First we try to identify electrons and positrons among all other tracks by PID with some of the ALICE detectors. Then we try to reject the false photon candidates by using the typical kinematic characteristics of a gamma conversion. And at the end we also apply some cuts on the π^0 candidates. Finally we subtract the background to obtain the number of reconstructed π^0 mesons as described in section 4.2. In order to have a good cut selection for the meson analysis a series of factors had to be taken into account. High significance was of course important to achieve. But considering the fact that tighter cuts were needed in Pb–Pb than in pp due to the higher background there was an even more important issue to be taken care of. The cuts applied had to have the same effect in the Monte Carlo as in the data, since otherwise a proper calculation of the efficiency would not be possible. A selection of distributions presented in the Appendix (see 8.1) was studied in order to ensure that no systematic errors are introduced by cutting on observables whose distributions deviate from each other in data and MC. Furthermore, two different V0 finders are used as they have very different efficiencies. The on-the-fly V0-finder is run during the reconstruction of the data and has access to more information that is in the raw data, which is later not available in the ESDs. This makes it more efficient and precise, but the off-line V0 finder, which can be run on the ESD data has the advantage that it can be optimized and rerun without redoing the whole reconstruction of the data. More details on the V0 finders can be found in [49]. The on-the-fly V0-finder is used as default due to its better performance:

- The reconstructed π^0 peak positions are closer to the expected one.

- The reconstructed peaks are narrower.

The standard cut selection chosen following the ideas from above is summarized here:

1. Inclusion of tracks within $[-4;5]\sigma$ around electron dE/dx line in the TPC.

2. Exclusion of tracks (with momenta between at 0.4GeV/c and 5GeV/c) below 3σ above the charged pion dE/dx line in TPC.

3. Exclusion of tracks outside $[-5;5]\sigma$ around electron line in TOF. (This cut is applied only on tracks that have a TOF signal).

4. Single $e^{\pm}$ $p_T > 0.05$ GeV/c.

5. Photon $\chi^2/NDF < 30$.

6. $|\eta| < 0.75$ for photons and $e^{\pm}$.

7. Line cut: $R_{conv} > rz_{slope} \cdot (|Z_{conv}| - Z_{vxt,max})$, $Z_{vxt,max} = 10$ cm, rz_{slope} depends on η cut. This cut is needed to ensure that γ from secondary particles which convert outside the acceptance are not accepted (important for photon analysis).

8. $q_T < 0.02$ GeV/c for photon with $p_T < 2.5$ GeV/c and
   $q_T < 0.06$ GeV/c for $p_T > 2.5$ GeV/c.

9. 5 cm $< R < 180$ cm for photon conversions (for exclusion of Dalitz decays).

10. $|y| < 0.7$ for π^0 mesons.

11. π^0 meson:
    $0.0 < \alpha < 0.65$ for the 0-20% centrality bin
    $0.0 < \alpha < 0.75$ for the 20-40% centrality bin
    $0.0 < \alpha < 0.80$ for the 40-60% centrality bin
    $0.0 < \alpha < 0.85$ for the 60-80% centrality bin

12. Charged track multiplicity event classes were used for background event mixing.

4.5 Optimization of the Cut on π^0 Decay Asymmetry

The asymmetry of the π^0 $\gamma\gamma$-decay is defined as $\alpha = |E_1 - E_2|/(E_1 + E_2)$ where E_1 and E_2 are the energies of the two gamma particles. As already mentioned in section 2.1 the distribution the decay asymmetry α is flat, but if we consider that both the conversion probability and the reconstruction efficiency of photons fall steeply from 1 GeV/c on towards lower transverse momenta (Fig. 4.13) it is clear that neutral pions with high asymmetry are disfavored by the reconstruction, especially at low momenta. At higher momenta the α distribution of the reconstructed π^0s gets flatter. In Fig 4.8 one can see the α distributions of true reconstructed neutral pions from MC and the combinatorial background from data that are scaled to each other to reproduce the actual situation in real data for two different p_T bins.
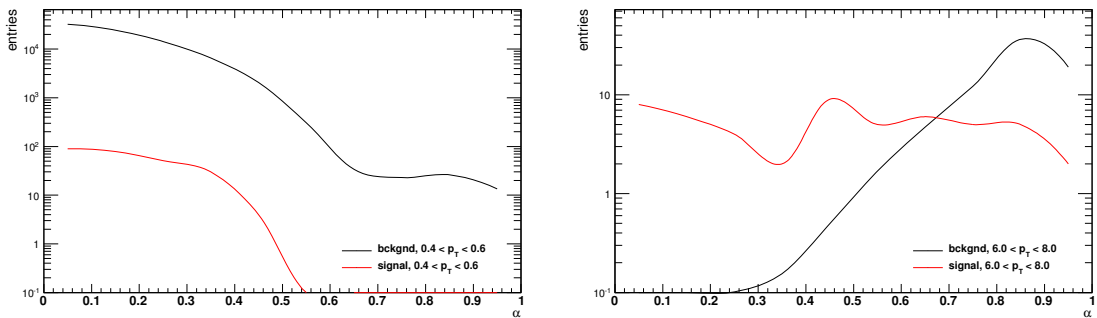
Figure 4.8: α distribution of true π^0 and combinatorial background for two p_T bins and 0-20% centrality.

It is clear that in the 0-20% centrality bin at low and high transverse momenta the significance can be optimized if we cut on the α distribution excluding pion candidates with high asymmetry. In the intermediate p_T region the α parameter has less separation power. In

order to find an optimal value for the cut parameter we fill two two-dimensional histograms with true reconstructed neutral pions from MC and with combinatorial background from data obtained via the event mixing technique as a function of p_T and α, both in the mass region of the π^0 meson from 0.1 to 0.15 MeV/c^2. We use the background calculated in real data because we believe that it will be much closer to the real background in data than the combinatorial background from MC. The reconstructed π^0s in MC should describe the data well since the α distribution at production level is flat and the α dependence of the π^0 reconstruction efficiency is defined by the p_T dependence of the γ reconstruction efficiency which is well described in MC. These histograms are then sliced in p_T using the binning for the final π^0 spectrum and for each p_T bin we calculate the values for the α_{min} and α_{max} parameters that correspond to the maximum significance ($\sigma = \frac{signal}{\sqrt{background+signal}}$) for the π^0 meson. This is done by varying both borders in 0.05 or 0.1 steps, covering all possible intervals and choosing the one with highest significance. As already mentioned the involved histograms were properly scaled so the results of this optimization can be applied to real data. The optimization for the π^0 meson gave an $\alpha_{min} = 0$ just as expected and the results for α_{max} are shown in Fig. 4.9 together with the results for the η meson as a function of the transverse momentum for the 0-20% centrality bin (for the η meson we used the same algorithm in the 0.5 to 0.57 GeV/c^2 mass region). The results for the π^0 meson suggest a value for α_{max} around 0.7 for intermediate and high p_T and a lower value (0.4-0.5) for low transverse momenta. Since we do not want to have steps in our π^0 efficiency which would be caused by different α cuts in different p_T regions we decided to apply an α_{max} cut of 0.6 for the π^0 meson which is a good compromise since it reduces the significance only in the intermediate p_T region where we can afford it. The same optimization was applied also for the other centrality bins. The individual results are presented in the Appendix (see 8.4). The optimal α_{max} cut for the 20-40% centrality bin was determined to be 0.75, for the 40-60% and 60-80% we obtained 0.8 and 0.85 respectively.
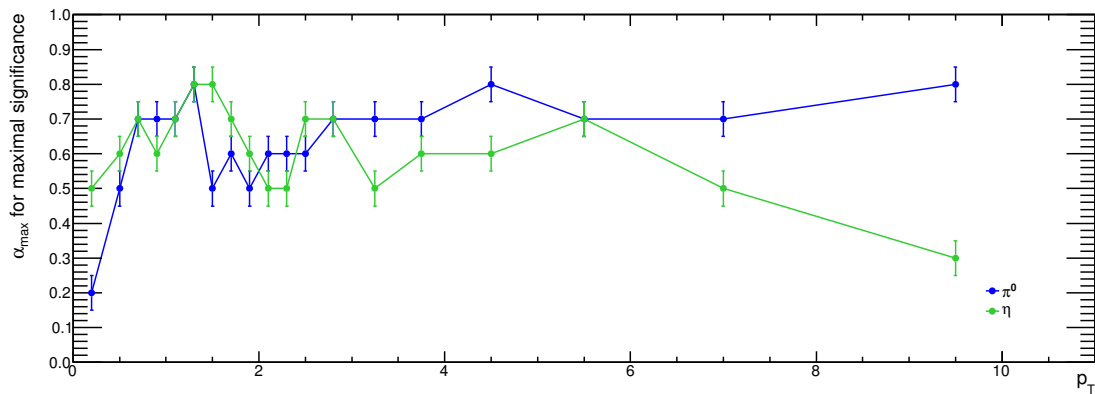
Figure 4.9: Optimal π^0 and η α-cut vs p_T ; 0-20%.

4.6 Identification of γ Candidates

The following plots show some of the quantities that were used for the identification of γ candidates and the electron/positron PID. They are for 0-20% centrality and created for the LHC11a10a MC sample only.
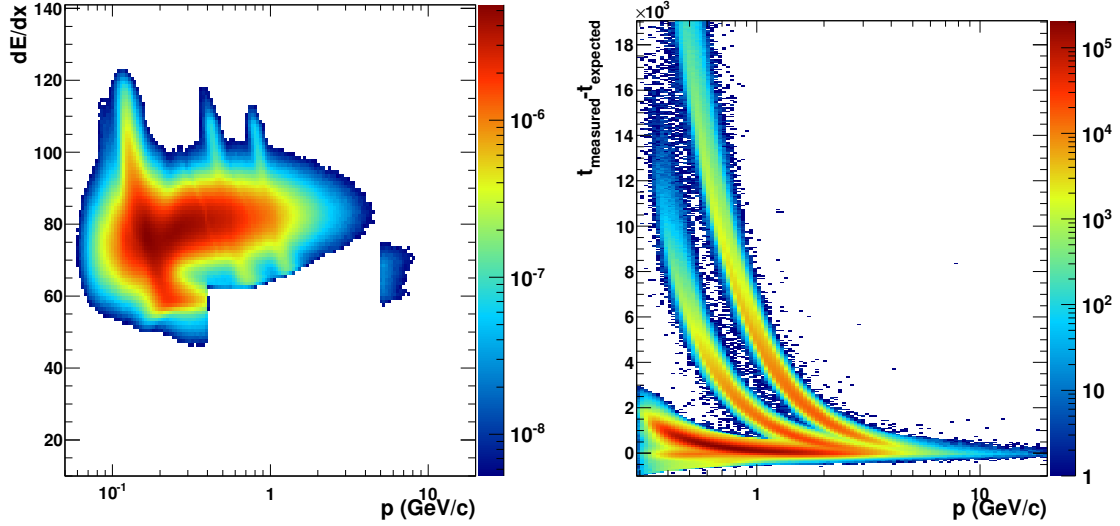
Figure 4.10: Distribution of electrons from γ candidates vs the TPC dE/dx and their momentum (left). Distribution of all negative tracks with TOF signal associated to a V0 candidate vs TOF time difference to electron expectation and their momentum (right). Both distributions are for data.

Each charged particle ionizes the medium it transverses. The charge created this way is proportional to the lost energy. This energy depends on the momentum and the mass of the particle. This way in a dE/dx vs. momentum plot each particle type follows a different Bethe-Bloch curve [50] allowing us to distinguish between different particles. The time of flight of a particle depends on its mass and momentum. Knowing the total distance the particle traveled and its momentum from the track and measuring the time with the TOF detector we can identify it. The dE/dx distribution of electron candidates and the TOF time distribution of all negative V0 tracks that have a TOF signal are shown in Fig. 4.10. The q_T (transverse component of the electron momentum relative to the γ momentum (from the lab frame) in the center of mass system of the electron and the positron) is a very powerful cut that can strongly improve the purity of the γ sample and this way is one of the main handles for background reduction and significance optimization for the π^0 yield extraction. But it also reduces the γ reconstruction efficiency (Fig. 4.13 middle) since it is very tight for low transverse momenta in the Pb–Pb analysis. The Armenteros plots are shown in Fig. 4.11 for V0 candidates before (left) and after (right) the γ identification cuts. On the left picture on top of the large combinatorial background one can even recognize the lines of the Λ baryon and K_S^0 meson which form V0s too, but populate different regions in the plot. In this analysis we apply different q_T cuts for low and for high p_T gamma candidates which explains the step in the right plot.
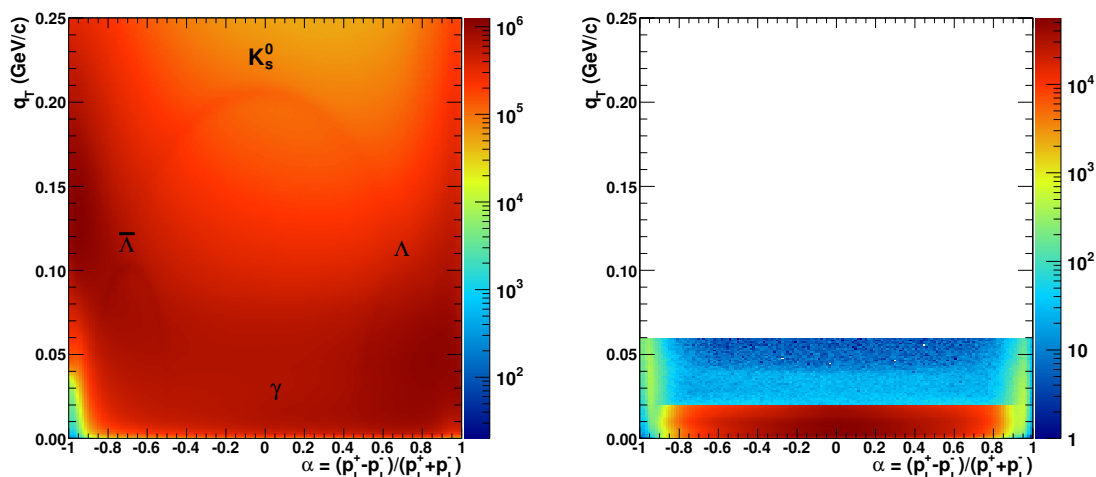
Figure 4.11: Distribution of all V0 candidates (left) and of all γ candidates (right) vs. the q_T and the asymmetry $\alpha = (p_L^+ - p_L^-)/(p_L^+ + p_L^-)$ of the γ conversion or particle decay (Armenteros plot) for data in the 0-20% centrality bin. p_L is the (back to the lab frame Lorentz transformed) longitudinal component of the electron momentum relative to the γ momentum (from lab frame) in the center of mass system of the electron and the positron.

In Fig. 4.12 the p_T spectrum of electrons from γ candidates (right) and the χ^2 (see below) distribution of γ candidates (left) are presented for both data and MC. The TPC can reconstruct tracks only down to a certain p_T limit due to the otherwise too large curvature caused by the magnetic field of 0.5 T. Therefore we set a lower p_T limit for the electron/positron selection of 50 MeV/c. The data and MC distributions differ at intermediate p_T and are also not identical at low p_T where we apply the cut. Therefore we need to study the effect of this on the final π^0 yield by varying the cut and including any deviations in the systematic uncertainties (see section 4.7). The photons are reconstructed using the AliRoot KFParticle package which calculates a χ^2 value telling us the "quality" of the created γ candidate. We apply a cut on the maximum allowed χ^2 of 120 which is in a region where the distributions are similar but differ at least in terms of the overall normalization. The final effect on the π^0 spectrum is studied during the evaluation of the systematic errors. This cut is also very important for the reduction of the background and plays an even more important role in the direct photon analysis, where a highly pure photon sample is required.

The cuts presented so far determine the reconstruction efficiency and the purity (Fig. 4.13 middle and right) of the selected γ sample. It is of course desirable to have both quantities as high as possible. But unfortunately it is always a trade-off of between them and for the π^0 analysis we need high reconstruction efficiency for the high-p_T photons in order to reconstruct as many high-p_T neutral pions from the falling spectrum as possible which results into a very low purity in this region. The step in both distributions at $p_T =$ 2.5 GeV/c is caused by the release of the photon q_T cut. The strong decrease of purity that takes place around 5 GeV/c is caused by the release of the TPC dE/dx cut at p = 5 GeV/c for electrons and positrons from γ candidates and by the fact that already before the charged pion and electron dE/dx lines are becoming closer to each other.

45
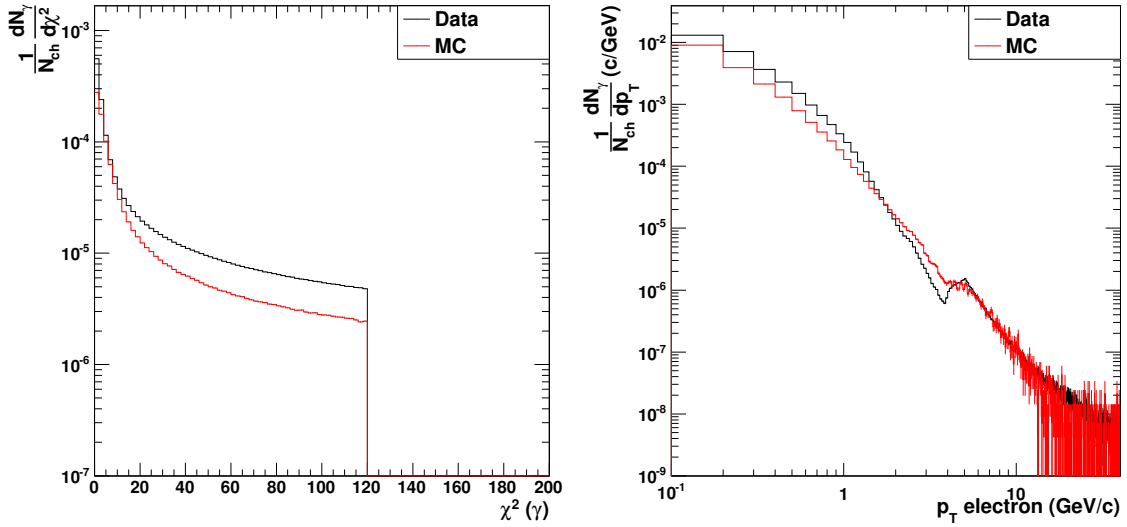
Figure 4.12: χ^2 distribution of photon candidates (left) and p_T distribution of electrons from photon candidates (right), both for data (black) and MC (red).
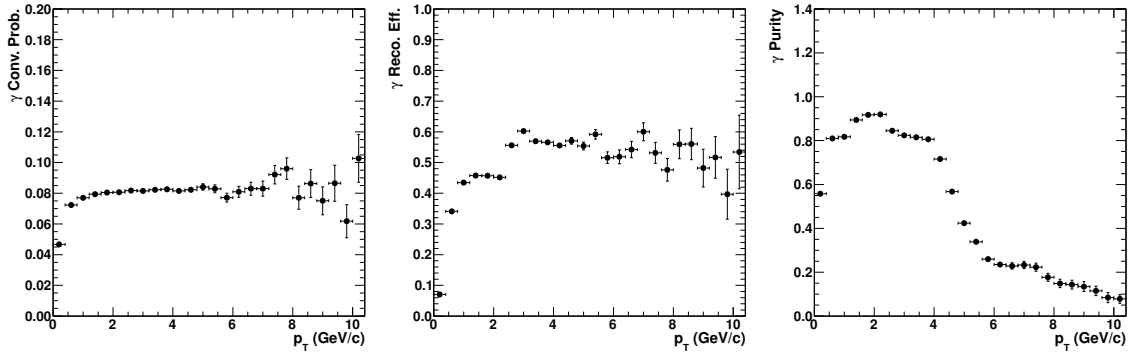
Figure 4.13: conversion probability (left), reconstruction efficiency (middle) and purity (right) as a function of the transverse momentum for γ candidates in the 0-20% centrality bin.

4.7 Evaluation of the Systematic Uncertainties

During the analysis and especially for the selection of the cuts we tried not to introduce any systematic errors in our measurement. But this is only possible up to a certain extent, since on the one hand the Monte Carlo describes the data with a finite precision and therefore distributions we cut on are not perfectly identical in data and MC and on the other hand we need to have rather tight cuts in order to reduce the high background in the Pb–Pb collisions and to make a significant measurement possible in the first place. In the following we describe the different sources of systematic uncertainties and determine their contribution to the total systematic error. The evaluation of the systematic errors has been therefore factorized in different components:

1. Signal extraction: variation of the background scaling which was done left from the peak here (stand.: right) and of the integration window for the signal extraction which was chosen wider as in the standard cut. This variation is needed to account for possible differences in the background shape and on the width of the π^0 peak.

2. Minimum p_T of the single electrons/positrons: the standard cut of 50 MeV/c needed to be increased to $p_{T,min} = 0.075$ GeV/c to ensure that the quality of the track reconstruction and TPC PID is still o.k. at this low p_T (0.05 GeV/c).

3. dE/dx: we opened the cut to only exclude tracks with dE/dx below 1σ above the charged pion dE/dx line in the TPC making sure that no e^+/e^- were excluded in this cut variation. This way we could check if the tighter cut led to a wrongly estimated efficiency due to differences between data and MC.

4. AliKFParticle $\chi^2(\gamma)$: $\chi^2/NDF < 100$; we include the final yield effect of the difference of the distributions in data and MC (Fig. 4.12) in the systematic uncertainties.

5. Background: γ candidate multiplicity for background event classification; since the signal to background ratio is low in Pb–Pb we are very sensitive to fluctuations and the shape of the background. We therefore explore the effect of a second method.

6. Off-line V0 finder: Getting the same result with the two methods with very different efficiencies is very important for the verification of these results.

7. γ q_T cut: $q_T < 0.06$ GeV/c; Opening the q_T cut to check if the drop in efficiency due to the tight cut at low p_T is properly reproduced in MC.

8. Different MC: LHC11a10a only, to see if the added signals have an effect on the efficiency and therefore on the corrected π^0 p_T spectrum.

The systematic error of the material budget determined with pp data and MC and added two times quadratically to the total uncertainties is shown below:

$$-6.21\% \text{ and } +3.44\% \qquad [30]$$

To account for these different contributions we take the standard cut selection described in section 4.4, vary one cut at a time according to the list above and run the complete analysis. We then compare the resulting π^0 invariant yields. For each cut variation the relative difference of the yield Δ_{rel} to the standard cut selection yield was calculated using Eq. 4.4. As the data sets are correlated the error of Δ_{rel} has to be calculated as shown in Eq. 4.5. Here we need to make sure that the sample of selected neutral pions in one of the cuts (modified/standard) fully contains the π^0 sample of the other cut. With other words it is not allowed that both samples include π^0 mesons that are not in the correspondingly other sample. For more details see [51].

$$\Delta_{rel} = (\text{Yield}_{\text{mod}} - \text{Yield}_{\text{stand}}) \, / \, \text{Yield}_{\text{stand}} \qquad (4.4)$$

$$\sigma(\Delta_{rel}) = \sqrt{|\sigma^2(\text{Yield}_{\text{mod}}) - \sigma^2(\text{Yield}_{\text{stand}})|} \, / \, \text{Yield}_{\text{stand}} \qquad (4.5)$$

Deviations are only taken into the systematic uncertainties if their statistical significance is high enough: $\Delta_{rel} > 0.9 \cdot \sigma(\Delta_{rel})$. In this case they are added quadratically to the
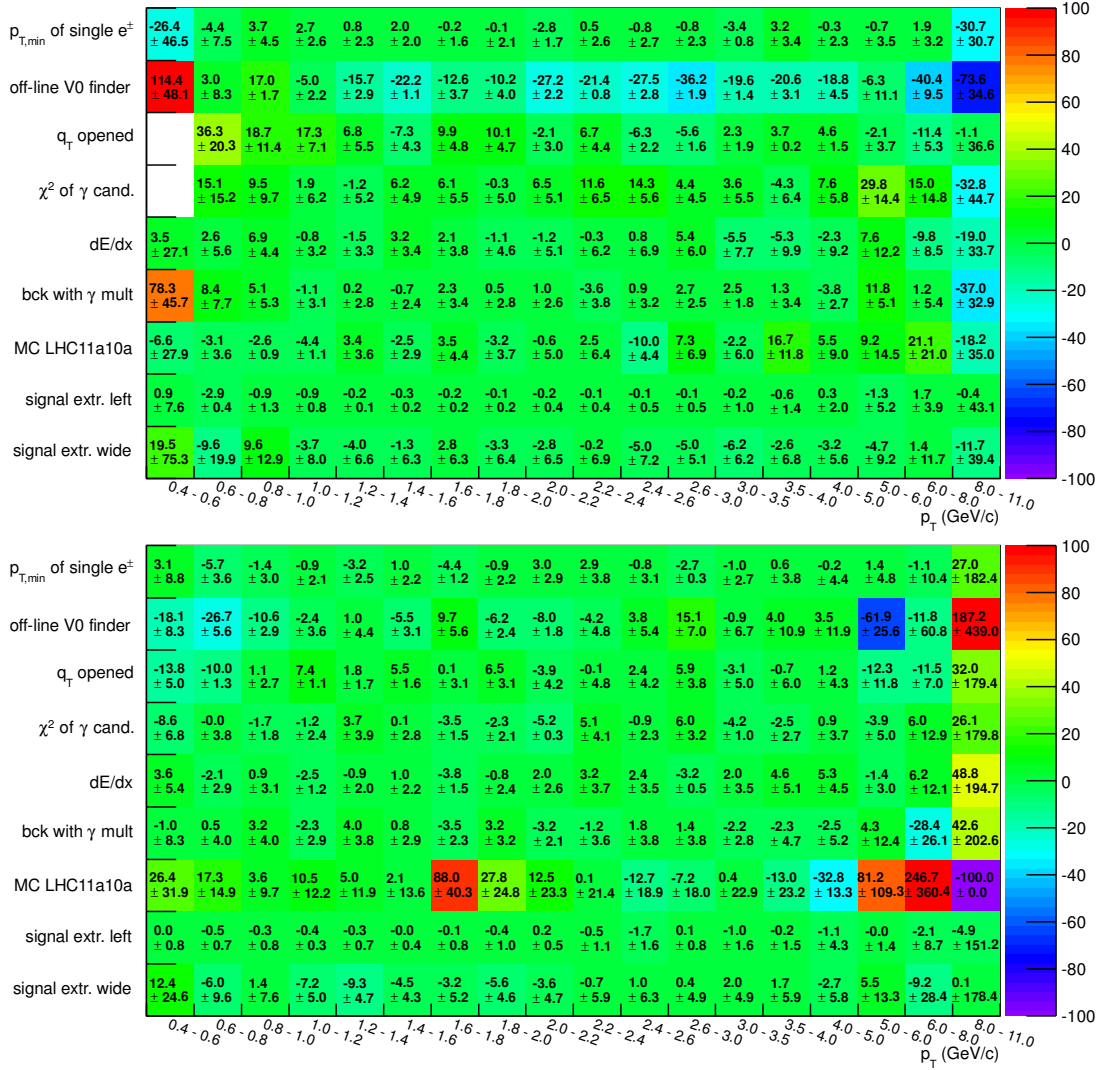
Figure 4.14: Different contributions to the systematic uncertainties shown as relative deviations of the cut-varied yields to the standard cut yield in per-cent for the 0-20%(up) and 60-80%(down) centrality bins.

total errors. Some of the (large) contributions for the first and last p_T bins are coming from bad fits or totally missing signal in those bins (opened cuts → low significance) and were therefore excluded from the final uncertainties. The final errors coming from the contributions so far except the material budget were symmetrized. In Fig. 4.14 the contributions of the different cut variations are presented in p_T bins for the 0-20% and 60-80% centrality bin. The systematics for the 20-40% and 40-60% centrality bins were obtained by a linear interpolation between the centralities. An additional variation (opening) of the α cut for $\pi^0 s$ was done for each centrality separately and then added to the total uncertainties quadratically. The final systematics can be found in Table 4.2.

p_T (GeV/c) / Centrality	0-20% (neg/pos)	20-40% (neg/pos)	40-60% (neg/pos)	60-80% (neg/pos)
0.400-0.600	0.793 / 0.786	0.620 / 0.608	0.446 / 0.430	0.273 / 0.253
0.600-0.800	0.421 / 0.408	0.388 / 0.372	0.351 / 0.335	0.320 / 0.299
0.800-1.000	0.309 / 0.295	0.261 / 0.238	0.214 / 0.182	0.164 / 0.128
1.000-1.200	0.214 / 0.188	0.192 / 0.160	0.169 / 0.131	0.146 / 0.103
1.200-1.400	0.200 / 0.171	0.186 / 0.154	0.172 / 0.137	0.158 / 0.120
1.400-1.600	0.265 / 0.248	0.224 / 0.195	0.185 / 0.147	0.143 / 0.099
1.600-1.800	0.177 / 0.144	0.171 / 0.140	0.164 / 0.127	0.159 / 0.119
1.800-2.000	0.161 / 0.123	0.211 / 0.180	0.262 / 0.238	0.313 / 0.296
2.000-2.200	0.310 / 0.282	0.255 / 0.235	0.210 / 0.179	0.165 / 0.134
2.200-2.400	0.250 / 0.235	0.211 / 0.187	0.173 / 0.133	0.134 / 0.092
2.400-2.600	0.328 / 0.307	0.258 / 0.231	0.192 / 0.150	0.128 / 0.071
2.600-3.000	0.392 / 0.376	0.331 / 0.313	0.272 / 0.250	0.217 / 0.187
3.000-3.500	0.242 / 0.219	0.205 / 0.173	0.173 / 0.127	0.131 / 0.080
3.500-4.000	0.240 / 0.217	0.203 / 0.169	0.165 / 0.121	0.130 / 0.073
4.000-5.000	0.238 / 0.204	0.269 / 0.247	0.323 / 0.291	0.350 / 0.335
5.000-6.000	0.344 / 0.328	0.288 / 0.266	0.231 / 0.254	0.175 / 0.141
6.000-8.000	0.449 / 0.436	0.409 / 0.396	0.370 / 0.355	0.331 / 0.314
8.000-11.000	0.888 / 0.882	0.702 / 0.693	0.516 / 0.503	0.331 / 0.314

Table 4.2: Final relative systematic uncertainties (not symmetric: negative and positive errors separately) for each centrality bin and for each p_T bin.

4.8 Reconstruction of the η Meson

The η meson is, like the π^0 meson, one of the eight Goldstone Bosons mentioned in section 2.1. Having a mass of 547.85 MeV/c^2 it is a superposition of the $u\bar{u}$, $d\bar{d}$ and $s\bar{s}$ bound states of quarks. The $\gamma\gamma$ decay channel which we use for its reconstruction has a branching ratio of 39.31%. Here we present some results from the η meson analysis which is in a "work in progress" status. No systematic uncertainties were estimated so far. We want to demonstrate the performance of our method which is able to reconstruct the η meson in the high multiplicity environment of central Pb–Pb collision where the combinatorial background is large. We reconstruct the η meson exactly in the same way as we do for the π^0 meson. All cuts except the asymmetry (α) cut are identical between both analyses. Using the same algorithm as for the π^0 (see section 4.5) we found that a cut with $0 < \alpha < 0.6$ was giving the highest significance for all centralities. The combinatorial background in the $\gamma\gamma$ invariant mass distribution is very large in the mass region of the η meson. This together with the fact that the currently available statistic is limited forced us to the choice of only one p_T bin between 2.0 and 4.0 GeV/c for the η analysis. Fig. 4.15 shows the $\gamma\gamma$ invariant mass distribution between 350 and 800 MeV/c^2 together with the combinatorial background calculated with an event mixing technique for each centrality bin. A peak is recognizable in all four plots but it is clear that the signal to background ratio is very small. In Fig. 4.16 we present the η signal peak after the subtraction of the background fitted with the function from Eq. 4.1 and Eq. 4.2. If one inspects the η peak from the $\gamma\gamma$ invariant mass for the 40-60% centrality bin shown in Fig. 4.16 one can see a big fluctuation of the background close to the η peak on its left side. Since it is in the integration window of the η that goes 50 MeV/c^2 down from the peak position it is included in the signal for the 40-60% centrality bin. We additionally calculated the π^0 invariant yield in the 2.0-4.0 GeV/c p_T bin in order to be able to extract the η/π^0 ratio.
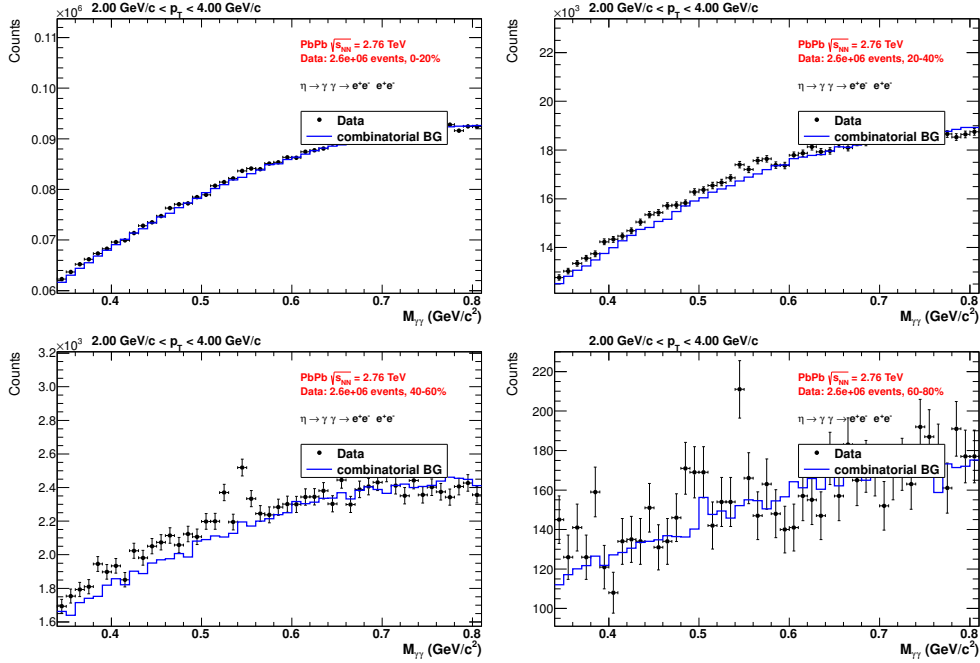
Figure 4.15: Invariant mass distributions of photon candidate pairs for all centrality classes in the 2.0-4.0 GeV/c transverse-momentum bin (black points). The blue histogram on is the combinatorial background obtained via event mixing and scaled to the data distribution away from the η peak.
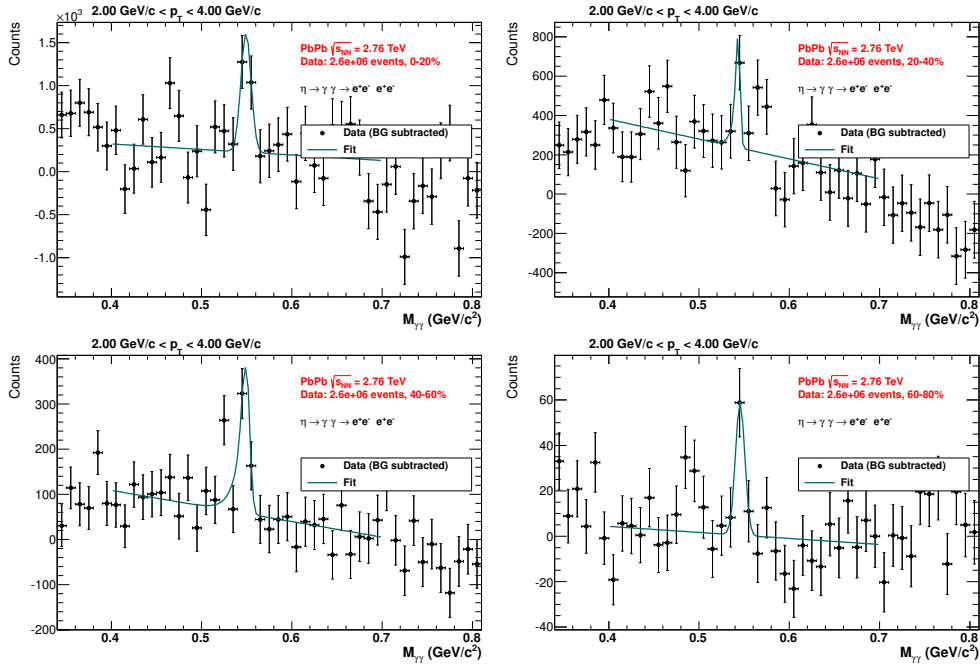
Figure 4.16: Invariant mass distribution of photon candidate pairs for all centrality classes in the 2.0-4.0 GeV/c transverse momentum bin after the subtraction of the combinatorial background. The cyan curve is a fit to the η peak.

5 Results

5.1 Differential π^0 Invariant Yield

5.1.1 Calculation

The differential invariant yield of the π^0 meson is calculated using Eq. 5.1

$$E\frac{d^3N}{dp^3} = \frac{d^3N}{p_T dp_T dy d\phi} = \frac{1}{2\pi}\frac{1}{p_T}\frac{d^2N}{dy dp_T} = \frac{1}{2\pi}\frac{1}{N_{ev}}\frac{1}{p_T^\star}\frac{1}{Eff}\frac{1}{Acc}\frac{1}{BR}\frac{N^{\pi^0}}{\Delta y \Delta p_T} \quad (5.1)$$

where N_{events} is the number of events which were used in the analysis for the corresponding centrality bin, Eff is the π^0 reconstruction efficiency, Acc the π^0 acceptance, BR is the branching ratio of the meson into the $\pi^0 \to \gamma\gamma$ decay channel, N^{π^0} is the number of reconstructed π^0 mesons in a given Δy and Δp_T, $p_T^\star$ is the transverse momentum obtained by the bin width correction algorithm that shifts the points along the transverse momentum axis (see 5.1.3). Decay contributions from $\eta \to \pi^+\pi^-\pi^0$, $\eta \to 3\pi^0$, $\rho^\pm \to \pi^\pm\pi^0$, $\omega \to \pi^+\pi^-\pi^0$ and $\omega \to \pi^0\gamma$ are not subtracted. The feed-down contribution from $K_S^0 \to \pi^0\pi^0$ should be small due to the request that the photons point to the primary vertex and the finite decay length of the K_S^0 meson ($c_\tau = 2.68$ cm).
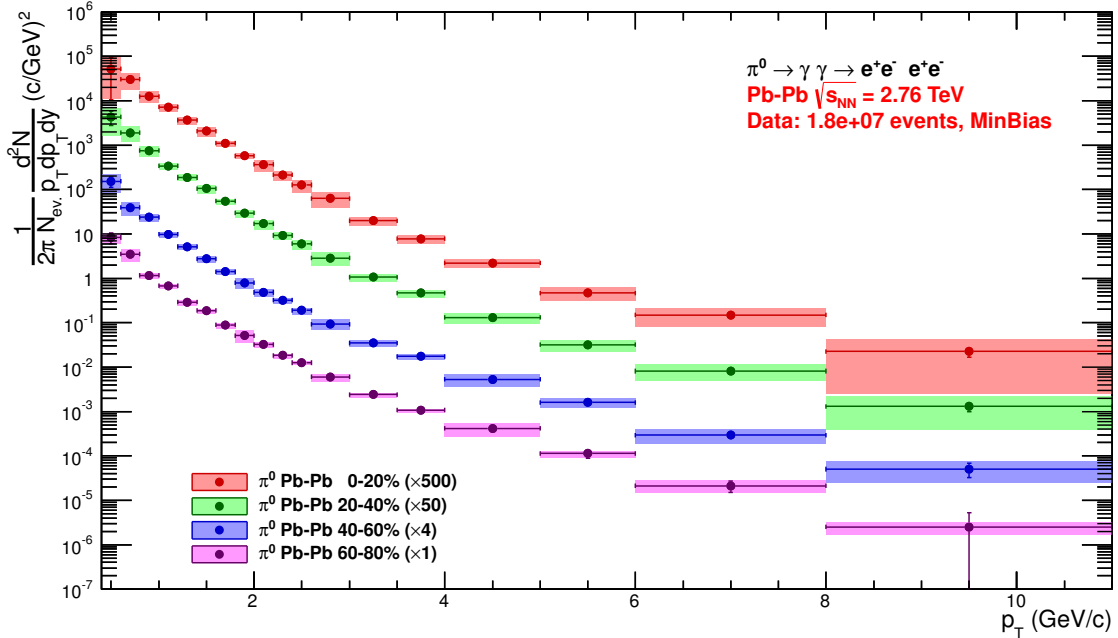
Figure 5.1: π^0 differential invariant yield for different centralities at $\sqrt{s_{NN}} = 2.76$ TeV. The different yields are scaled with different factors to separate the from each other for plotting.

The fully corrected spectra for each centrality are shown in Fig. 5.1. In Fig. 5.2 one can see all the spectra from the central to the peripheral bin (corrected for the p_T bin width by shifting along the p_T axis) in a log-log scale together with different lines corresponding to the pp reference at $\sqrt{s} = 2.76$ TeV (shifted along the y-axis as bin width correction) scaled with the proper $\langle N_{coll} \rangle$ (see table 5.2). Here we can already qualitatively compare the central and peripheral Pb–Pb spectra to the pp spectrum. The peripheral Pb–Pb spectrum and the accordingly scaled pp spectrum are close and parallel to each other. The distance between the central Pb–Pb spectrum and the correspondingly scaled pp spectrum is generally larger and not constant over the whole p_T range. This shows that in central Pb–Pb collisions there are mechanisms that not only suppress the production of neutral pions but also change the shape of the overall spectrum like it was described in sub-section 2.2.3.
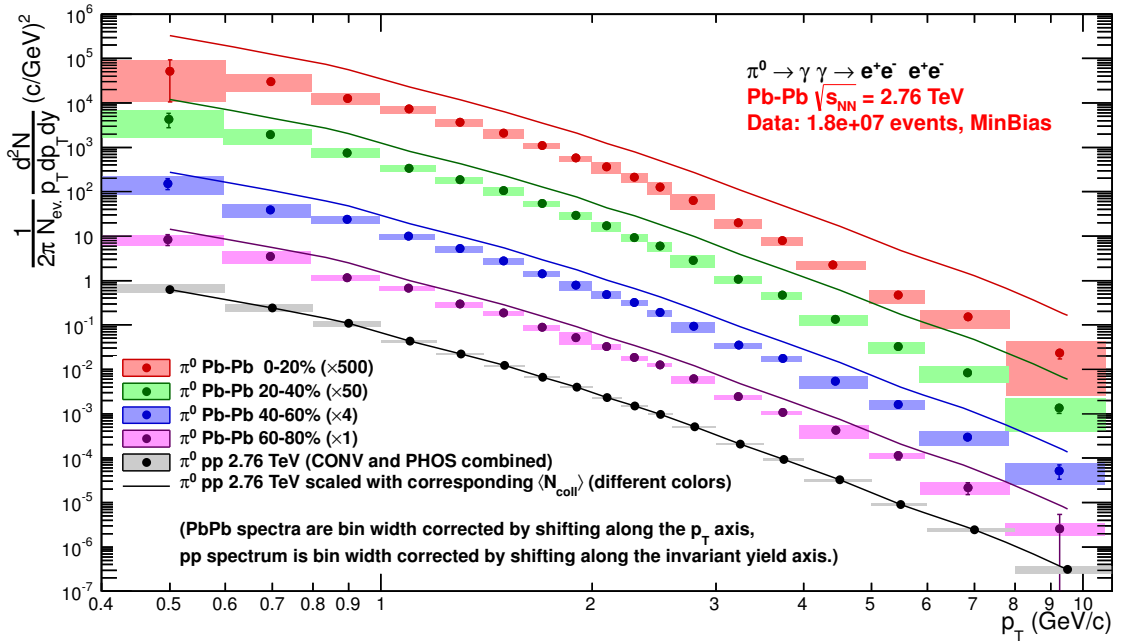
Figure 5.2: π^0 differential invariant yield in Pb–Pb at $\sqrt{s_{NN}} = 2.76$ TeV for different centralities and the reference pp differential invariant yield. Lines show the pp spectrum scaled with corresponding $\langle N_{coll} \rangle$ and 1.158 to account for pp trigger efficiency (see 5.2). They are drawn by ROOT and are not a fit. The different yields are scaled with different factors to separate them from each other for plotting.

5.1.2 Fit of the Invariant Yield

$$\frac{d^2N}{dydp_T} = \frac{(n_1-1)(n_1-2)}{n_1 T[n_1 T + m(n-2)]} \times \frac{dN}{dy} \times p_T \times \left(1 + \frac{m_T - m}{n_1 T}\right)^{-n_1} \tag{5.2}$$

$$\frac{d^2N}{dydp_T} = C \times p_T \times \left(\frac{1}{p_T}\right)^{n_2} \tag{5.3}$$

$$C = \frac{dN}{dy} \cdot \frac{(n_1-1)(n_1-2)}{n_1 T[n_1 T - m(n_1-2)]} \cdot \left(\frac{n_1 T}{p_{T,bound} + n_1 T - m}\right)^{n_1} \cdot p_{T,bound}^{n_2} \tag{5.4}$$

The transverse-momentum spectrum of the π^0 meson can be fitted using a combination of the Tsallis function [53] (Eq. 5.2) with a power law function (Eq. 5.3). This is needed since the spectrum has a rather complicated form in Pb–Pb, especially in the central collisions, and cannot be described by any of the functions that were used in pp. The Tsallis function is used in the low and intermediate p_T region since it is modified to be able to describe the thermal production at low transverse momenta. The power law function is fitted to the high-p_T part of the spectrum in order to describe the hard components of a collision. Both functions are fitted first separately to find the best junction region and then together with variable but constrained boundary. The parameter "C" of the power law function is actually a combination of all other parameters obtained using the fact that at the boundary the two functions need to meet (Eq. 5.4). Since the used spectra are actually histograms at this stage we fit to $d^2N/dydp_T$ and take the special integral fit option "I" in ROOT which uses integrals of the fit function over the bins normalized to the bin widths during the minimalization. In Fig. 5.3 the relative deviation of the histogram entries to the integrals of the fitted function over the p_T bins divided by the bin widths is presented and one can see how well the fit describes the data. The gray rectangles are the relative errors of the histogram entries. The extracted fit parameters for each centrality bin are summarized in Table 5.1.
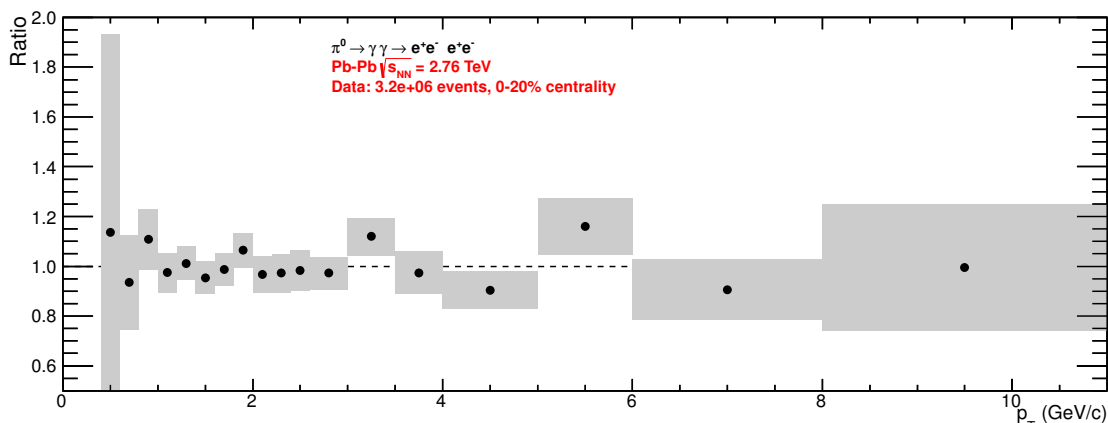
Figure 5.3: Relative deviation of integrals of fitted function over the p_T bins divided by bin widths to the histogram entries for 0-20%. The gray rectangles are the relative error of the histogram entries.

	0-20%	20-40%	40-60%	60-80%
dN/dy	414 ± 44	269 ± 29	110 ± 16	27.1 ± 4.3
n_1	13.9 ± 1.3	11.3 ± 1.0	8.58 ± 0.58	8.53 ± 0.86
T (GeV)	0.228 ± 0.014	0.194 ± 0.014	0.161 ± 0.015	0.162 ± 0.018
$p_{T,bound}$ (GeV/c)	4.50 ± 0.19	3.49 ± 0.01	4.20 ± 0.27	3.27 ± 0.25
n_2	5.97 ± 0.29	6.50 ± 0.18	6.33 ± 0.27	6.10 ± 0.25

Table 5.1: Results of the fit in terms of extracted parameter values for each centrality bin.

5.1.3 Bin Width Correction

As already mentioned the π^0 $d^2N/dydp_T$ measured and fitted so far is actually a histogram. Since many of the theoretical predictions are points of a function we need to modify our results to be able to compare to them. Putting the points just at the middle of the bins is not correct since we have a steeply falling spectrum here. A common approach is to shift the points in either x or y direction. The second one was disfavored by the conveners of the ALICE collaboration since we would modify the measurement itself. Therefore we developed a method, where we shift the points along the transverse momentum axis. In this method we take the function fitted to $d^2N/dydp_T$ described in the previous subsection and calculate the integral for each p_T bin divided by the bin width. Using the GetX(Y,a,b) function of the TF1 class in ROOT, which represents mathematical functions, we are able to find the p_T position that corresponds to the normalized integral of the bin. This way we are able to determine the bin shift from the shape of the spectrum and to calculate the proper position on the transverse momentum axis p_T^*. Since we fit to a histogram using the "I" option, which is supposed to treat everything properly, we do not need to iterate. The uncertainty of p_T^* can be calculated by varying the parameters of the fitted function within their errors and adding all deviations quadratically. This method follows the "natural" procedure during the filling of a histogram and is therefore delivering the proper p_T^* position. When we calculate the invariant yield we divide $d^2N/dydp_T$ by p_T^* and so the final result depends on the bin shifting. But knowing the position on the transverse momentum axis would allow anyone to extract back the original results. In order to calculate the π^0 R_{AA} where the pp reference is shifted in Y we divide the value of the fit function at the middle of the bins by the normalized integrals over the p_T bins and correct the spectrum with this factors. The original and bin shifted spectra are presented in Fig. 5.4.
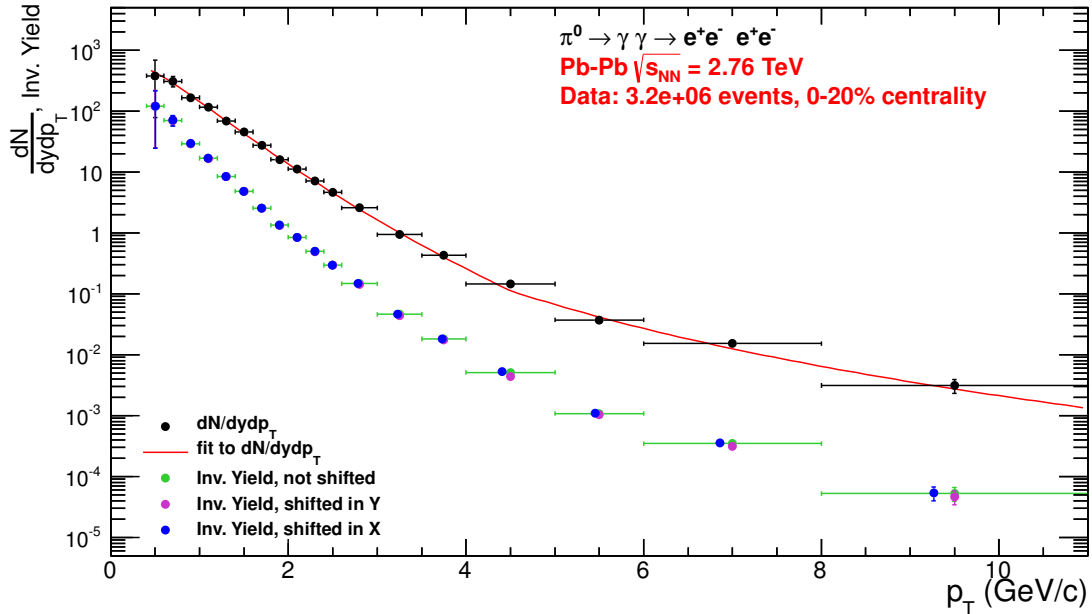
Figure 5.4: π^0 $d^2N/dydp_T$ and invariant yields, two bin shifted and one original.

5.2 The Nuclear Modification Factor R$_{AA}$

The ratio of the π^0 yield in Pb–Pb collisions over the π^0 yield in pp collisions scaled by the mean number of binary collisions $\langle N_{coll} \rangle$ for the respective centrality bin is an important observable for the study of the suppression of particle production at high p_T. The so-called R$_{AA}$ is calculated using the formula from Eq. 5.5.

$$R_{AA} \;=\; \frac{d^2 N_{Pb-Pb}/dy dp_T}{\langle N_{coll} \rangle \times \; d^2 N_{pp}/dy dp_T} \tag{5.5}$$

The systematic uncertainties are coming from the Pb–Pb spectrum, the pp reference and $\langle N_{coll} \rangle$. The contributions for both the pp and the Pb–Pb spectrum coming from the material budget cancel out. The minimum-bias event trigger in pp is sensitive only to a part ($\sim 86\%$) of the total inelastic cross section. In a (central) Pb–Pb collision, however, it is the inelastic pp cross section that is responsible for the particle production. Therefore we need to scale the π^0 pp invariant yield to the inelastic cross section to be able to compare the Pb–Pb and pp results. In the analysis presented in this thesis we scale the final R$_{AA}$ results by 1.158 to account for this problem.

5.2.1 The pp Reference for the R$_{AA}$ Calculation

The reference pp spectrum used for the calculation of the π^0 R$_{AA}$ is a combination of the spectra measured with the conversions method and with the PHOS detector. The results were averaged using as weight factors the inverse sum in quadrature of the statistical and systematic uncertainties [49]. Here we have both the Pb–Pb spectrum and the pp reference corrected for the bin width by shifting in y. As a comparison we also calculate the R$_{AA}$ with the not bin-shifted Pb–Pb spectrum and the not bin-shifted pp reference as measured by the conversions method where the last p_T bin is obtained by an extrapolation. It has the advantage that the systematic uncertainties on the material budget cancel out which improves the precision of the R$_{AA}$. The combined π^0 pp spectra for all LHC energies and the conversions spectrum for $\sqrt{s} = 2.76$ TeV are presented in Fig. 5.5.
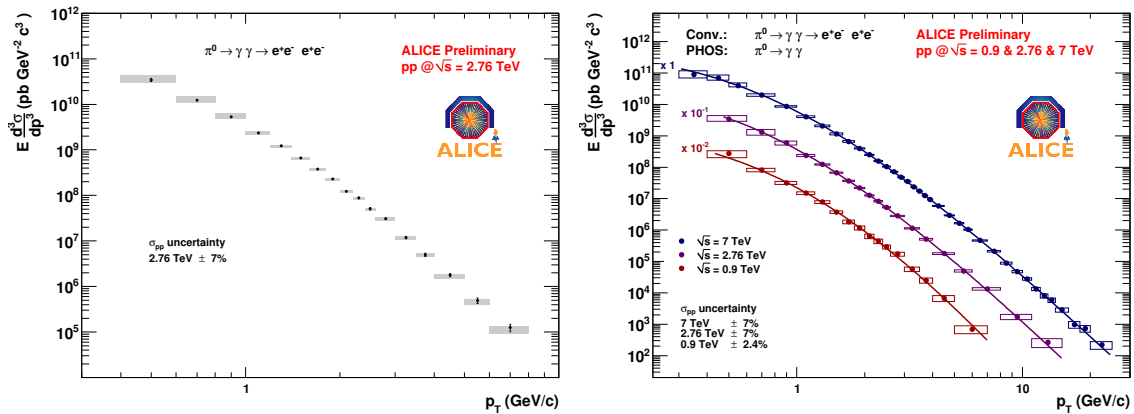
Figure 5.5: π^0 pp invariant cross-section measured by conversions at $\sqrt{s} = 2.76$ TeV (left) and combined conversions and PHOS π^0 pp invariant cross-sections for all LHC energies (right).

5.2.2 Number of Binary Collisions $\langle N_{coll} \rangle$

If we want to compare the Pb–Pb π^0 results to the spectrum from pp we need to know how the latter scales with centrality. The idea here is that the probability for hard interactions in a single nucleon-nucleon collision is small and thus if a nucleon traverses some other nucleons immediately after each other the probabilities should add. This way we can calculate the equivalent number of pp collisions $\langle N_{coll} \rangle$ for a single Pb–Pb collision at a certain centrality in terms of hard interactions. This number is higher than the number of nucleons participating in the Pb–Pb collision. The mean number of binary collisions $\langle N_{coll} \rangle$ used to scale the pp π^0 spectrum in order to obtain R_{AA} is calculated by a purely geometric Glauber model (see subsection 2.2.1). The numbers presented below (table 5.2) are the official ones published by ALICE [52]:

Centrality	$\langle N_{coll} \rangle$	$\langle N_{part} \rangle$	$\langle N_{part} \rangle / \langle N_{coll} \rangle$
0-20%	1211±131	308.2±3.4	0.2545 ± 0.0277
20-40%	439±44	157.3±3.4	0.3583 ± 0.0367
40-60%	128±13	68.8±2.4	0.5375 ± 0.0577
60-80%	26.8±2.5	22.55±1.05	0.8396 ± 0.0875

Table 5.2: Mean number of binary collisions $\langle N_{coll} \rangle$ and mean number of participating nucleons $\langle N_{part} \rangle$ from a Glauber model calculation for the used centrality bins. These are the ALICE official numbers [52] .

5.2.3 Results
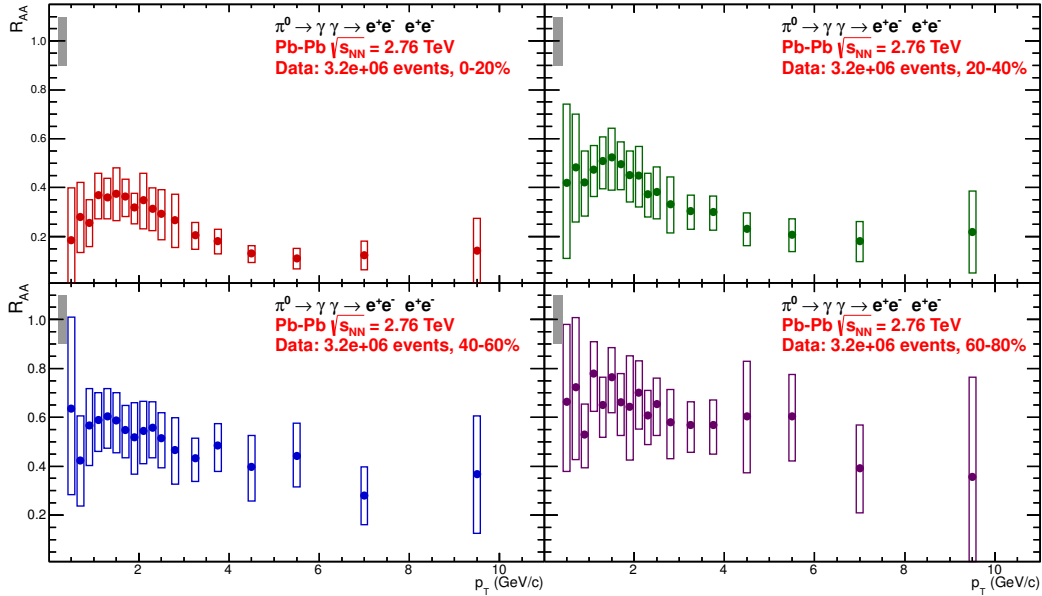
Figure 5.6: π^0 R_{AA} measured as a function of p_T for each centrality bin. The gray error band at the top left represents the uncertainty of the overall normalization of the π^0 pp invariant yield.

In Fig. 5.6 one can see the neutral pion R_{AA} obtained with the combined pp reference for each centrality bin used in this analysis. For this calculation the Pb–Pb differential invariant yields were bin width corrected by a shift along the yield axis (see 5.1.3) since the combined pp yield was available only with a bin shift along the yield axis. The ratio of this result to the R_{AA} with not bin shifted spectra (see 5.2.1) is shown in the Appendix (8.5). For all four centralities we observe that the π^0 R_{AA} is clearly below 1 which means that the π^0 production in Pb–Pb collisions for centralities up to 80% is suppressed compared to the π^0 production in pp collisions. For the 0-20% centrality bin we observe the strongest suppression of almost a factor 10 for the p_T bin between 5 and 6 GeV/c. For the same p_T range in the peripheral centrality bin (60-80%) we observe a suppression of almost a factor 2 ($R_{AA} \approx 0.6$). The last two p_T bins in both the 40-60% and 60-80% centrality bins seem to be lower than expected from the trend of the R_{AA} at lower p_T. This can be probably explained as a fluctuation due to low statistics for this two centrality bins and is not significant.

5.2.4 Energy Loss Models

We can try to interpret this results in terms of parton energy loss in a naive way using the models mentioned in sub-section 2.2.3. Here we can assume that the original nucleon-nucleon π^0 spectrum $\frac{dN_{nn}}{dp_T^*}(p_T^*)$ is transformed by the energy loss of the partons in the medium following: $p_T^* \rightarrow p_T = T(p_T^*)$, where T is a general transformation function, p_T^* is the particle transverse momentum before/without the energy loss and p_T is the observed transverse momentum after/with energy loss. The number of neutral pions in a Pb–Pb collision dN_{Pb-Pb} produced at the transverse momentum p_T within dp_T can be calculated with the following equation:

$$dN_{Pb-Pb}(p_T) = \langle N_{coll} \rangle \cdot \frac{dN_{pp}}{dp_T}(p_T^*) \cdot dp_T^* \tag{5.6}$$

where instead of the nucleon-nucleon spectrum $\frac{dN_{nn}}{dp_T}$ we use the measured pp spectrum $\frac{dN_{pp}}{dp_T}$, which is scaled by $\langle N_{coll} \rangle$, evaluated at the transverse momentum before the transformation p_T^* and multiplied with the original interval width dp_T^*. If we divide both sides of Eq. 5.6 by dp_T and use $p_T^* = T^{-1}(p_T)$ we get:

$$\frac{dN_{Pb-Pb}}{dp_T}(p_T) = \langle N_{coll} \rangle \cdot \frac{dN_{pp}}{dp_T}\big(T^{-1}(p_T)\big) \cdot \frac{dT^{-1}(p_T)}{dp_T} \tag{5.7}$$

Plugging Eq. 5.7 into the definition of the R_{AA} (Eq. 5.5) we obtain:

$$R_{AA}(p_T) = \frac{\frac{dN_{pp}}{dp_T}\big(T^{-1}(p_T)\big)}{\frac{dN_{pp}}{dp_T}(p_T)} \cdot \frac{dT^{-1}(p_T)}{dp_T} \tag{5.8}$$

As already mentioned in 2.2.3, R_{AA} is governed by the energy loss models at high p_T, where the contributions from initial state effects or from other medium effects can be considered negligible. At high transverse momenta the spectra have a power law shape, i.e., $\frac{dN_{pp}}{dp_T}(p_T) = C \cdot p_T \cdot \left(\frac{1}{p_T}\right)^n$ (like in Eq 5.3). If we plug this into Eq. 5.8 and simplify

we get:

$$R_{AA}(p_T) = \left(\frac{p_T}{T^{-1}(p_T)}\right)^{n-1} \cdot \frac{dT^{-1}(p_T)}{dp_T} \tag{5.9}$$

Using Eq. 5.9 we can calculate the expected R_{AA} for each transformation $T : p_T^* \to p_T = T(p_T^*)$, *i.e.*, for each energy loss model if we can calculate the inverse transformation T^{-1}. For the naive case where $T(p_T^*) = (1-\epsilon) \cdot p_T^*$, *i.e.*, for a constant fractional energy loss, we get $T^{-1}(p_T) = \frac{1}{(1-\epsilon)} \cdot p_T$ and:

$$R_{AA}(p_T) = \left(\frac{p_T}{\frac{1}{1-\epsilon} \cdot p_T}\right)^{n-1} \cdot \frac{1}{1-\epsilon}, \quad or \quad \epsilon = 1 - R_{AA}^{1/(n-2)} \tag{5.10}$$

The model predicts a flat R_{AA} at high p_T as measured by PHENIX at RHIC (Fig. 1.1). With a more realistic model inspired by pQCD we can use: $\Delta p_T \sim \langle N_{part}\rangle^{2/3} \cdot \ln(p_T)$ [29]. For an R_{AA} averaged in a p_T interval the dependence of the energy loss on the momentum drops out and we can calculate the relative energy loss $\epsilon = \Delta p_T / p_T$ with the formula from Eq. 5.10 [29]. The parameter $n = 6.02 \pm 0.12$ (stat⊕syst) was obtained by fitting the combined (conversions and PHOS) π^0 pp dN/dp_T with the power law function $C \cdot p_T \cdot \left(\frac{1}{p_T}\right)^n$. The relative energy loss ϵ was calculated for each of the four centrality bins using the measured R_{AA} averaged between 4 and 6 GeV/c. The results are plotted in Fig. 5.7 vs the mean number of participating nucleons $\langle N_{part}\rangle$. The distribution was first fitted with the function $\epsilon = c \cdot \langle N_{part}\rangle^{2/3}$ to check the model suggested in [29]. The function was not able to reproduce the data so we decided to use $\epsilon = c \cdot \langle N_{part}\rangle^m$ to study the exact dependence of the energy loss on the mean number of participating nucleons. The power of $\langle N_{part}\rangle$ obtained from the fit was with $m = 0.47 \pm 0.07$, more than two standard deviations away from the 2/3 expectation. Therefore a third function with the power of $\langle N_{part}\rangle$ fixed to 2/3 but with an additional term proportional to $\langle N_{part}\rangle^{4/3}$, which can be interpreted as a second-order correction of the $\langle N_{part}\rangle$ dependence of the energy loss, was also used for fitting. It describes the data as well as can be seen in Fig. 5.7.

If we now go to the p_T dependent part of the model where the energy loss is proportional to the logarithm of the energy we can use: $T(p_T^*) = p_T^* - \epsilon \cdot \ln(p_T^*)$. The inversion of this transformation function T is not trivial and we used Maple® to calculate T^{-1} and its derivative dT^{-1}/dp_T:

$$T^{-1}(p_T) = \exp\left(-\frac{p_T + \epsilon \cdot W_{-1}\left(-\frac{1}{\epsilon} \cdot e^{-p_T/\epsilon}\right)}{\epsilon}\right) \tag{5.11}$$

$$\frac{dT^{-1}(p_T)}{dp_T} = -\frac{1}{\epsilon} \cdot T^{-1}(p_T) \cdot \frac{1}{1 + W_{-1}\left(-\frac{1}{\epsilon} \cdot e^{-p_T/\epsilon}\right)} \tag{5.12}$$

Here W_{-1} is the lower branch of the Lambert W function that is the inverse function of $x \cdot e^x$. An analytical simplification for the R_{AA} with this input was not found but if we insert Eq. 5.11 and Eq. 5.12 in Eq. 5.9 it is possible to handle the R_{AA} function numerically and to obtain a value for ϵ using Maple® by plugging in one high-p_T point from the R_{AA} distribution. We used the averaged $p_T = 8.25$ GeV/c and averaged $R_{AA} = 0.135^{+0.060}_{-0.070}$ from the last two points of the π^0 R_{AA} for 0-20% centrality and n $= 6.02 \pm 0.12$(stat⊕syst). We take the highest measured p_T for the calculation of ϵ since it is the only one high
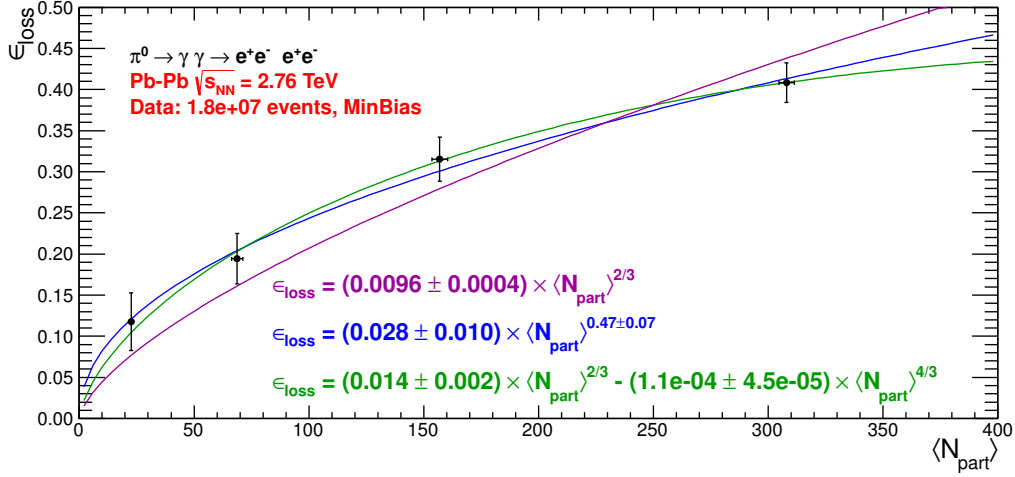
Figure 5.7: Parton energy loss calculated from the π^0 R_{AA} (averaged in the p_T interval 4-6 GeV/c) for each centrality bin vs $\langle N_{part}\rangle$. Of the three fits which were applied ($\epsilon = c \cdot \langle N_{part}\rangle^{2/3}$ (violet), $\epsilon = c \cdot \langle N_{part}\rangle^m$ (blue) and $\epsilon = c_1 \cdot \langle N_{part}\rangle^{2/3} - c_2 \cdot \langle N_{part}\rangle^{4/3}$ (green)) only the last two describe the data.

enough to be sure that the R_{AA} is ruled by an energy loss model. With this we get $\epsilon = 1.738^{+0.477}_{-0.233}$ (stat$\oplus$syst) which can be used to extrapolate our π^0 R_{AA} measurement towards higher p_T. The uncertainty of ϵ was calculated by varying the R_{AA} and n parameters by their uncertainties and then adding separately the resulting two positive and two negative deviations of ϵ quadratically and dividing them additionally by $\sqrt{2}$. With this result we create an extrapolation for the π^0 R_{AA} in the 0-20% centrality bin, which is shown in Fig. 5.8 together with the measured R_{AA} of neutral pions.
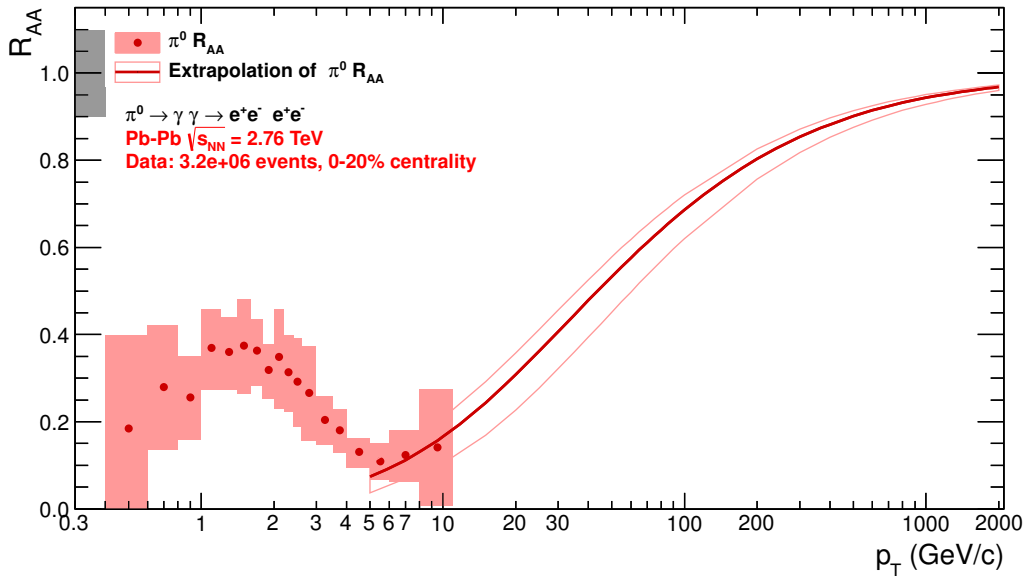
Figure 5.8: Measured π^0 R_{AA} for 0-20% centrality with extrapolation for higher p_T.

5.3 η Meson Results

Here we summarize the results of the η analysis that was described in section 4.8. The acceptance, efficiency and raw yield for the η meson are presented in table 5.3 for each of the four centrality bins. The difference of the acceptance for different centralities comes from the added η signals in the LHC11a10b MC sample (see section 4.3). One can also see that the efficiency rises slightly from the central to the peripheral bin. The raw yields are nevertheless nicely ordered increasing with the centrality. Table 5.3 shows also the differential invariant yield for the η meson calculated using Eq. 5.1. The uncertainties of the invariant yields are only statistical. A study of the systematic effects of the applied cuts on the final results has not been performed yet.

Centrality	Acceptance	Efficiency	$1/N_{ev} \cdot dN_{raw}^{\pi^0}/dp_T$	invariant differential yield
0-20%	0.97 ± 0.00	7.1e-04 ± 1.0e-05	2.8e-03 ± 1.1e-04	1.5e-01 ± 6.3e-03
20-40%	0.97 ± 0.00	8.4e-04 ± 1.3e-05	1.5e-03 ± 5.1e-05	7.1e-02 ± 2.6e-03
40-60%	0.97 ± 0.00	9.1e-04 ± 1.5e-05	6.5e-04 ± 2.2e-05	2.8e-02 ± 1.1e-03
60-80%	0.98 ± 0.00	9.6e-04 ± 1.7e-05	1.7e-04 ± 7.8e-06	6.9e-03 ± 3.4e-04

Table 5.3: Acceptance, efficiency, raw yield and the differential invariant yield of the η meson in the 2.0-4.0 GeV/c p_T bin for each centrality (statistical uncertainties only).

Using the differential invariant yields of the η and π^0 mesons for the 2.0-4.0 GeV/c p_T bin we calculated the η/π^0 ratios for each centrality bin. They are presented in table 5.4. The pp differential invariant yields of the η and π^0 mesons for the 2.0-4.0 GeV/c p_T bin were obtained by a fit of the Tsallis function (see Eq. 5.2) to the bin width corrected spectra combined from the PHOS and conversions measurements [49]. The fitted function was transformed into dN/dydp_T by multiplying with 2π and p_T and then integrated between 2.0 and 4.0 GeV/c. The result was divided by the bin width of 2 GeV/c and transformed back to differential invariant yield by dividing by 2π and the p_T at the bin middle (3GeV/c). This way we obtained non bin width corrected pp spectra which we can use for the calculation of the η/π^0 ratio in pp and as a reference for the π^0 and η R$_{AA}$ in the 2.0-4.0 p_T bin. Since all the spectra are similarly steeply falling any effect coming from their finite bin width should cancel out in their ratios. We obtained an ratio for pp collision of $\eta/\pi^0 = 0.40 \pm 0.06$ (stat⊕syst). The η/π^0 ratios for all centralities except for 40-60% (see section 4.8) agree with value from pp nicely. The 40-60% ratio is compatible with pp ratio within the uncertainties. The uncertainties are in general very large so it is not possible to make any conclusions from this result. The R$_{AA}$ results are shown in table 5.4. Here the same conclusions as for the η/π^0 ratio are valid: nice agreement between the η and π^0 results except for the 40-60% centrality, large uncertainties.

Centrality	η/π^0	η R$_{AA}$	π^0 R$_{AA}$
0-20%	0.40 ± 0.23	0.27 ± 0.15	0.27 ± 0.03
20-40%	0.45 ± 0.19	0.38 ± 0.16	0.34 ± 0.04
40-60%	0.63 ± 0.19	0.73 ± 0.23	0.47 ± 0.05
60-80%	0.37 ± 0.16	0.50 ± 0.22	0.55 ± 0.06

Table 5.4: η/π^0 ratio and η and π^0 R$_{AA}$ for the 2.0-4.0 p_T bin for each centrality bin (stat. errors only).

6 Comparison to Other Measurements and to Theoretical Predictions

In this chapter we compare the results of the π^0 measurement with conversions in ALICE at $\sqrt{s_{NN}} = 2.76$ TeV to another neutral pion measurement by the ALICE PHOS detector and also to the measurements of charged pions and unidentified charged particles in ALICE. A comparison to the PHENIX neutral pion measurement at $\sqrt{s_{NN}} = 200$ GeV will be presented, too. At the end we show two sets of theoretical predictions of the neutral pion R_{AA} at the LHC energy and discuss the comparison to the measured R_{AA}.

6.1 Comparison to PHOS Results

In ALICE there are three different techniques or detector systems available for the reconstruction of π^0 mesons. The calorimeters PHOS and EMCal provide two individual measurements which can be compared to the results obtained by the conversions method. There are no π^0 results in Pb–Pb available from the EMCal detector so far, so we are not able to show any comparison here. For the PHOS detector we will present a comparison of the π^0 invariant yield and R_{AA}. Fig. 6.1 shows the ratios of the measured π^0 invariant yields which agree with unity within the uncertainties (stat⊕syst) except the 20-40% bin where the disagreement slightly exceeds the errors. If one considers the fact that the uncertainties of the conversions measurement are not included due to the use of a fit the agreement is even better but there is a general trend that the PHOS results are ∼20% higher than our results. In Fig. 6.2 the R_{AA} as measured by the PHOS detector is shown together with the R_{AA} from conversions for all centralities. The very good agreement between the two measurements is due to the missing correction factor 1.158 to the inelastic pp cross section in the PHOS R_{AA}. If applied the results should show similar (dis)agreement as in Fig. 6.1.
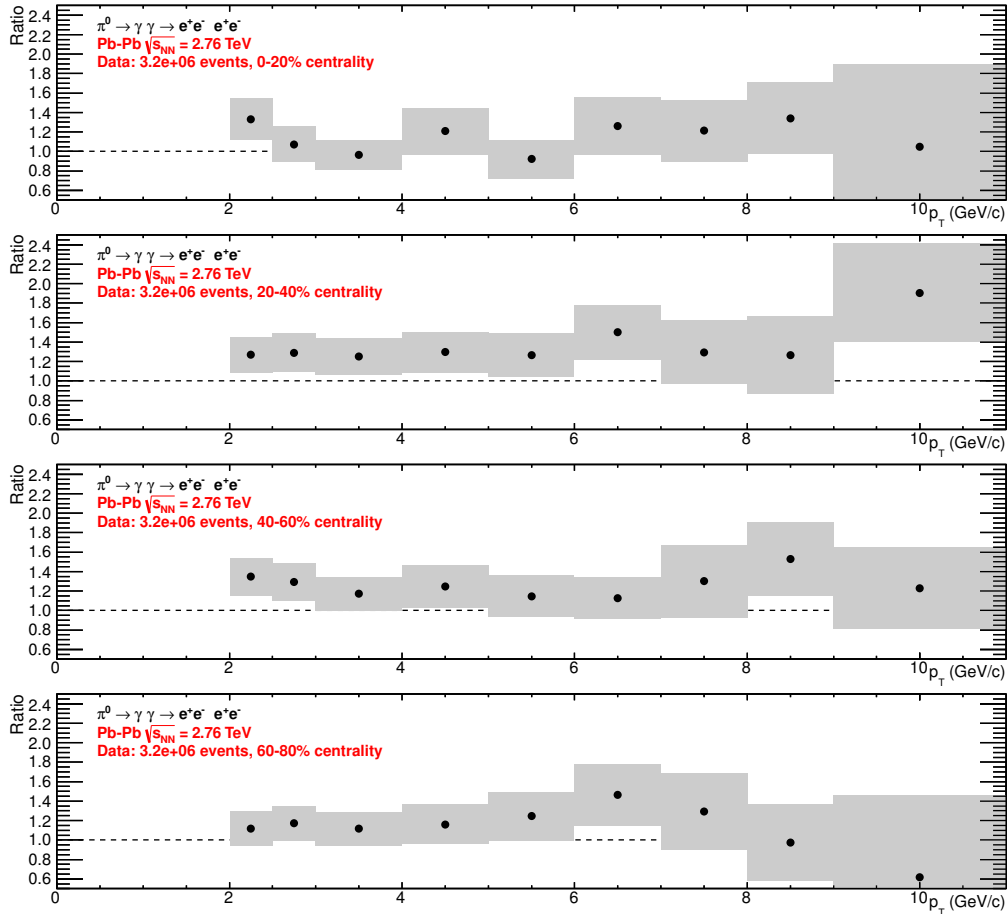
Figure 6.1: Ratios of π^0 spectrum measured by PHOS to a fit of the conversions spectrum for all centrality bins. The error bands are calculated out of the stat. and syst. uncertainties of the PHOS spectrum.
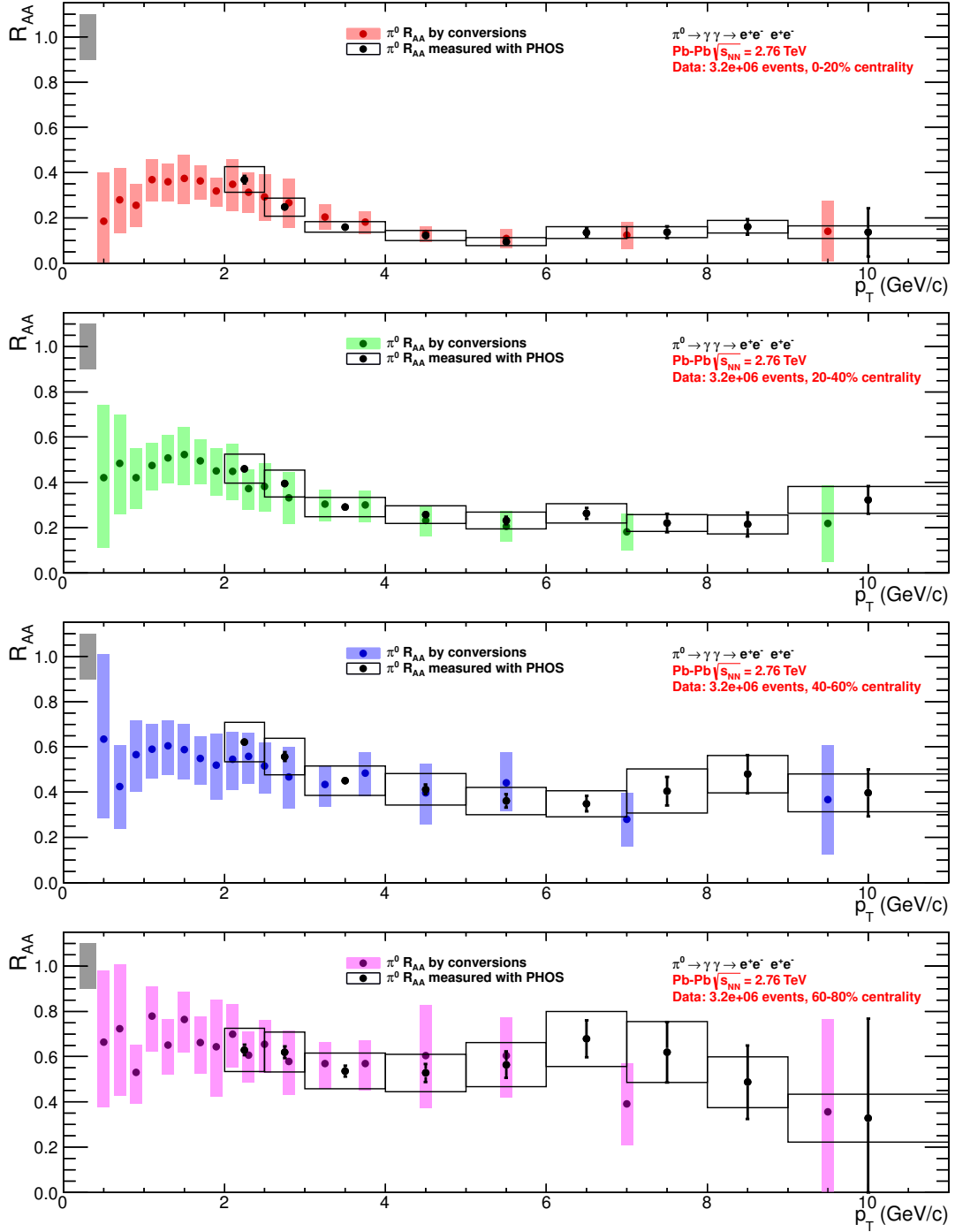
Figure 6.2: Comparison of π^0 R_{AA} measured with the conversions method to π^0 R_{AA} measured by PHOS for each centrality bin. The PHOS measurement is "work in progress".

6.2 Comparison to Charged Pions and Charged Particles

In this section we present the comparison of our π^0 measurement to the charged-pion results. These results for the charged-pion spectra are a combination of the ITS/TPC/TOF ($p_{\mathrm{T}} < 3$ GeV/c) and TPC dE/dx ($p_{\mathrm{T}} > 3$ GeV/c) measurements. In Fig. 6.3 one can see the ratios of the π^0 spectra measured with the conversions method to the combined charged-pion spectra. The results for the neutral pions are below the charged-pion results but within the systematical uncertainties there is an overall good agreement.
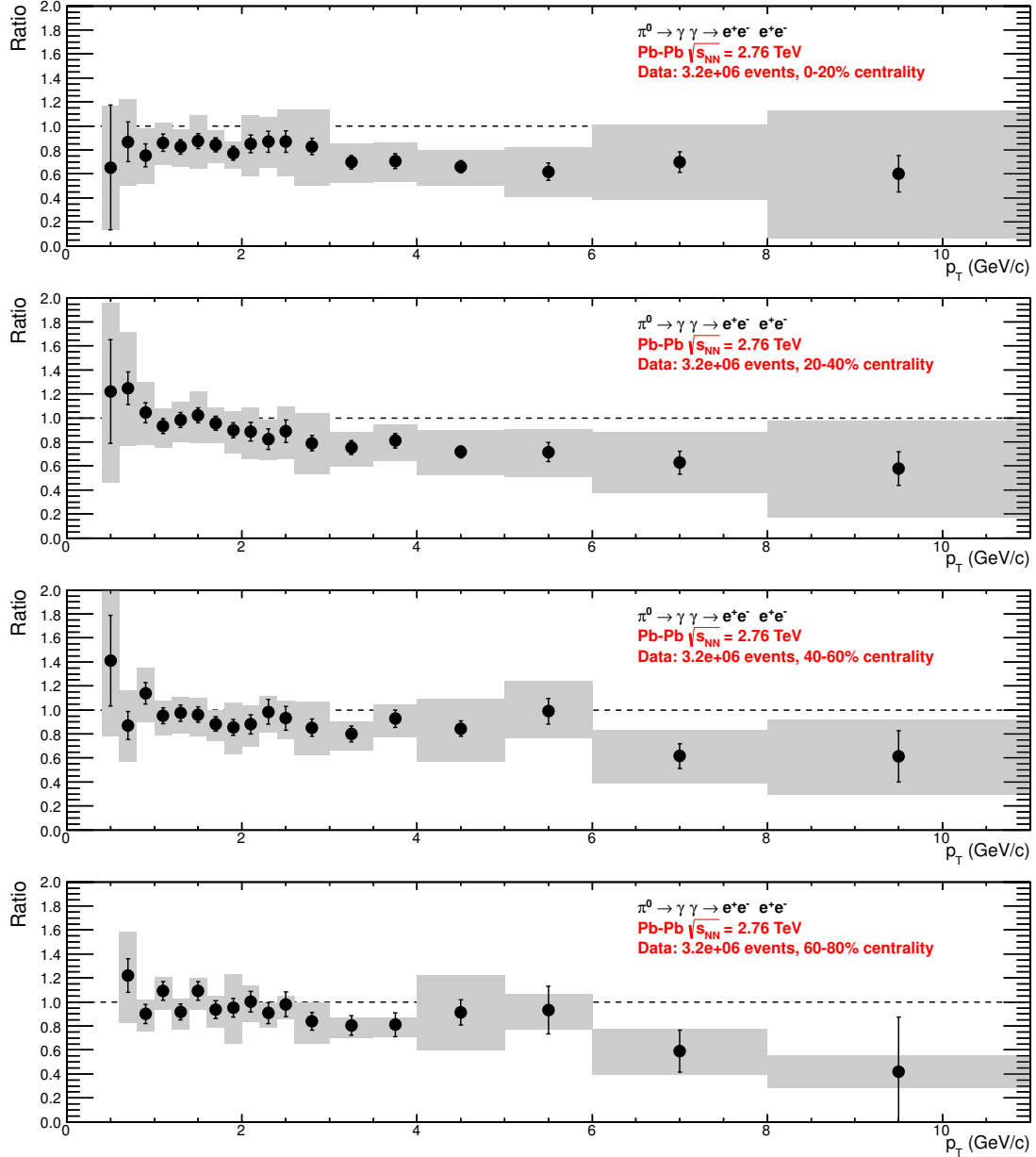
Figure 6.3: Ratio of π^0 spectrum by conversions to the charged-pion spectrum for all centrality bins.

In Fig. 6.4 we present the comparison of the neutral pion R_{AA} to the charged-pion R_{AA}. For the this comparison there is a similar trend as for the comparison of the spectra: neutral-pion R_{AA} is a bit lower than the charged-pion results, but within the uncertainties they are compatible. The main advantage of the π^0 R_{AA}, although it suffers from low statistics due to the low efficiency of the reconstruction, is that here we measure down to 0.4 GeV/c where the charged pion R_{AA} start only at 3 GeV/c.
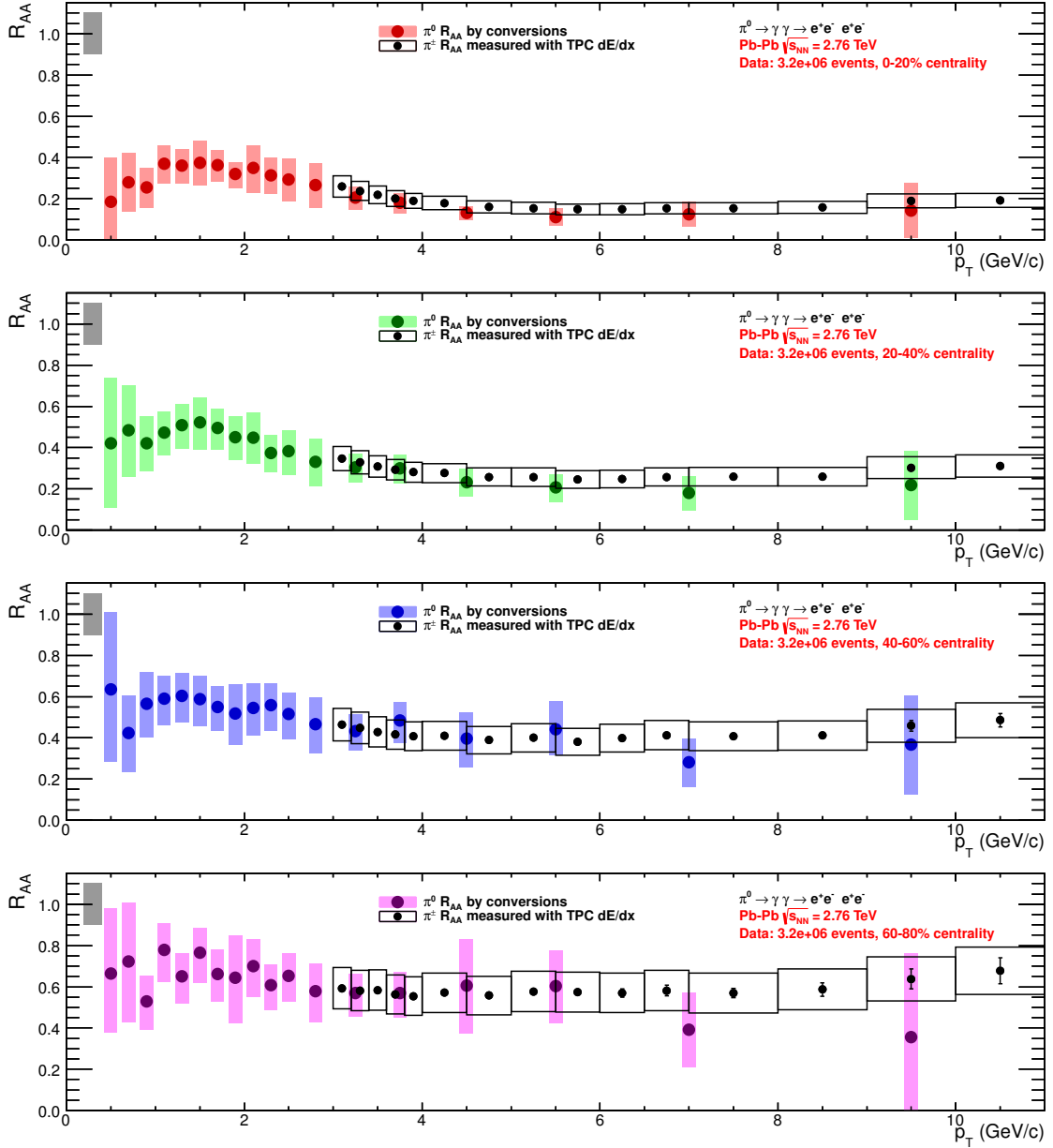
Figure 6.4: π^0 R_{AA} measured by conversions and charged pion for all centrality bins.

If we now compare the π^0 R_{AA} to the $h^\pm$ R_{AA} (see Fig. 6.5) we see that for the peripheral centrality bin both agree very well. Here the R_{AA} is quite high and rather flat when compared to the central bin. For the central bin there is a significant difference between the two results in the intermediate p_T region between 1 GeV/c and 6 GeV/c. It can be explained by the higher fraction of protons in the charged particle sample in this p_T region and by the fact that protons have a different R_{AA} since they are baryons. At high p_T the fraction of charged pions becomes dominant and it is in general expected that pions and protons have the same R_{AA}. We use this to check the π^0 R_{AA} p_T extrapolation presented in sub-section 5.2.4. The comparison of the measured π^0 R_{AA} and its extrapolation to the measured charged particle R_{AA} up to 45 GeV/c is presented in Fig. 6.6 and shows a very good agreement between the measurement and the extrapolation within the uncertainties. Although the slope seems to be not perfectly matched by the extrapolation we can still conclude that the model has good description power compared with the data.
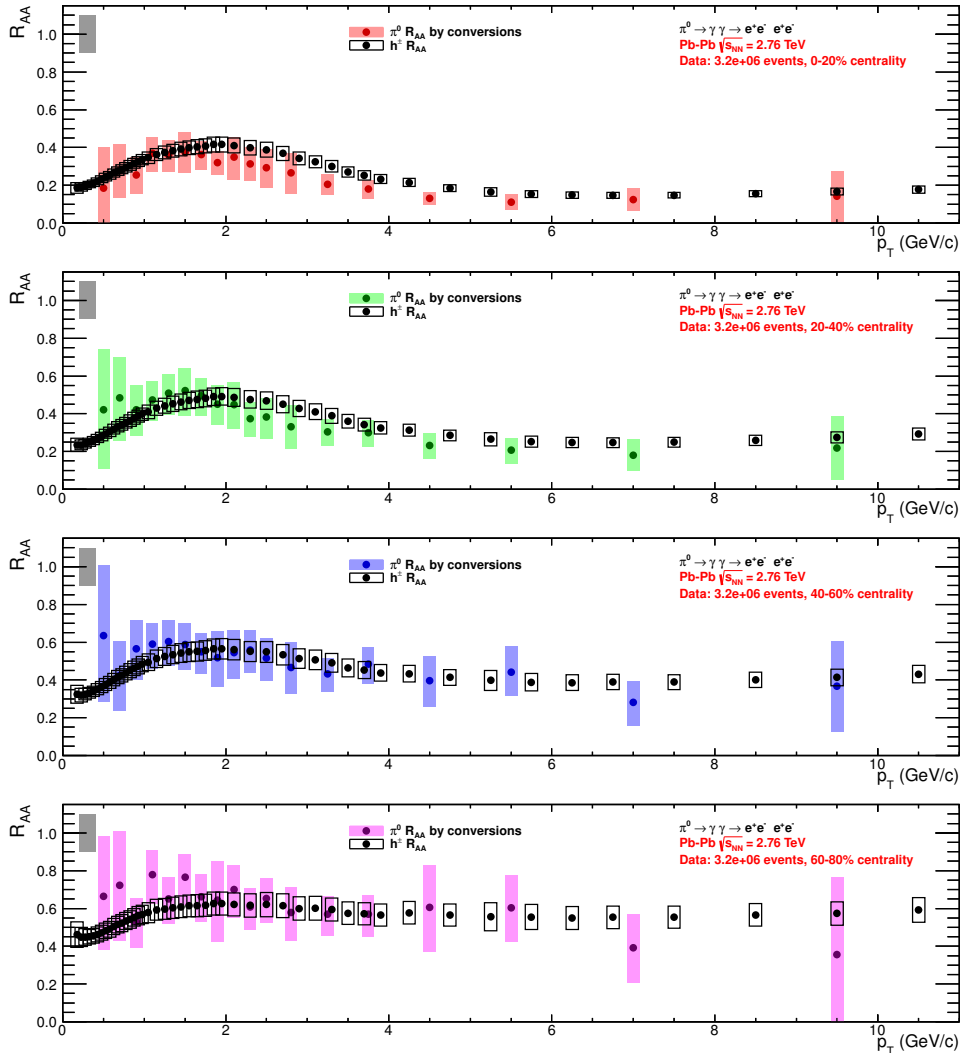
Figure 6.5: π^0 R_{AA} for 0-20% and 60-80% centrality compared to $h^\pm$ R_{AA}.
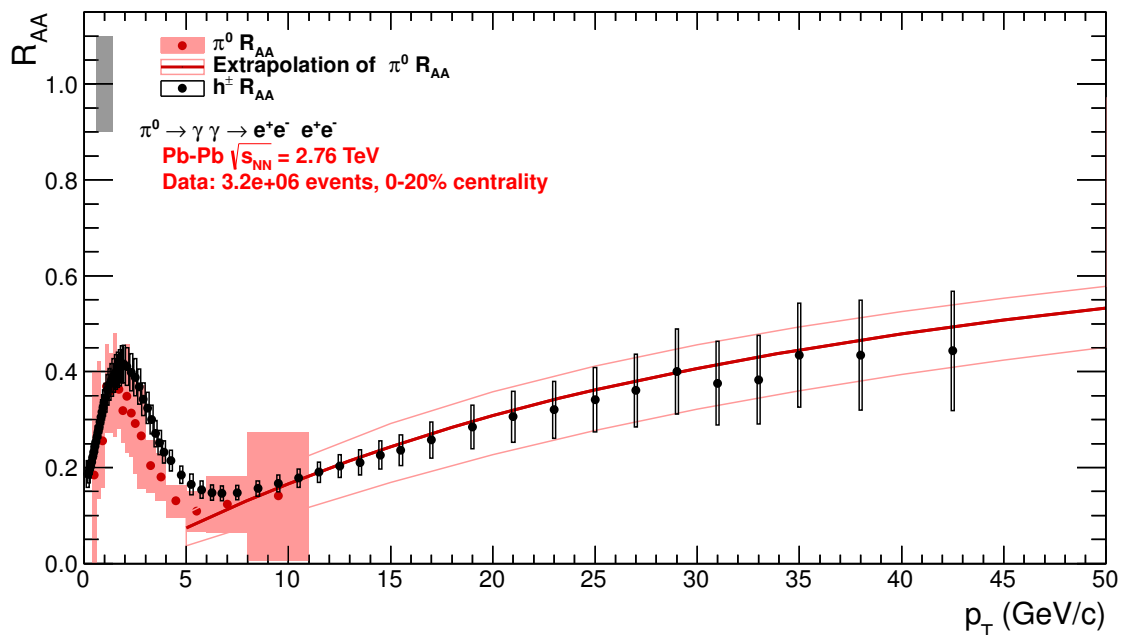
Figure 6.6: π^0 R_{AA} for 0-20% centrality with extrapolation in p_T (red line) compared to $h^{\pm}$ R_{AA}.

6.3 Comparison to PHENIX Results
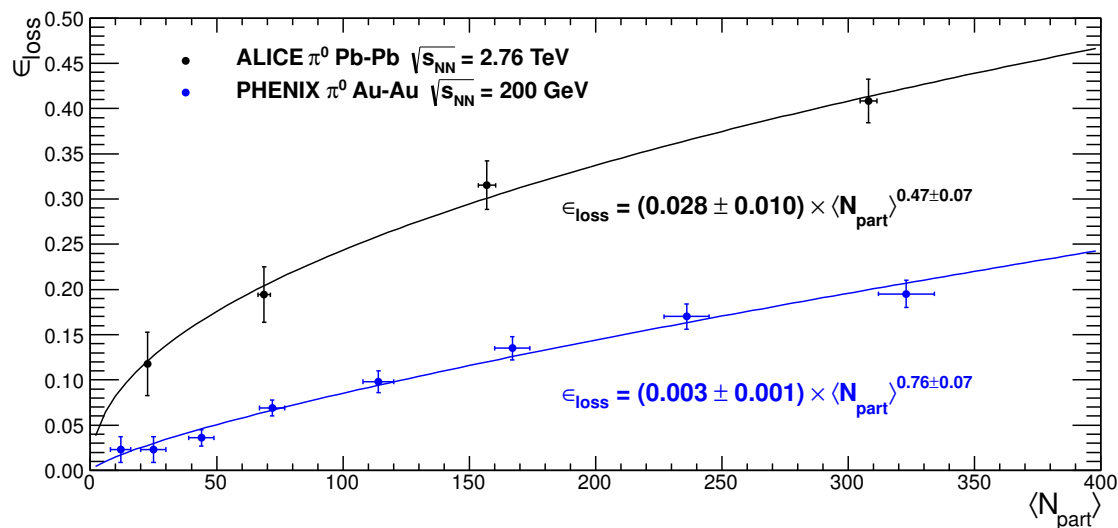
Figure 6.7: π^0 energy loss vs $\langle N_{part} \rangle$ measured with conversions for Pb–Pb at $\sqrt{s_{NN}} = 2.76$ TeV and the PHENIX results for Au–Au at $\sqrt{s_{NN}} = 200$ GeV. Both measurements are fitted with $\epsilon = c \cdot \langle N_{part} \rangle^m$.

In this chapter we want to compare the energy loss ϵ obtained from the neutral pion R_{AA} (see sub-section 5.2.4) measured with ALICE at $\sqrt{s_{NN}} = 2.76$ TeV to the energy loss

from the PHENIX π^0 measurement at $\sqrt{s_{NN}} = 200$ GeV [54]. In Fig. 6.7 the results of both measurements are presented vs the mean number of participating nucleons $\langle N_{part} \rangle$ together with their respective fits of $\epsilon = c \cdot \langle N_{part} \rangle^m$. For PHENIX we obtained m = 0.76 ± 0.07 which is only 1.3σ away from the 2/3 expectation from [29] while the ALICE result is with m = 0.47 ± 0.07 more than 2.8σ away from 2/3. This shows that there is a qualitative difference in the energy loss if one compares RHIC and LHC energies which can be interpreted as a second order correction that goes as $\langle N_{part} \rangle^{4/3}$ for the results at $\sqrt{s_{NN}} = 2.76$ TeV (see sub-section 5.2.4).

6.4 Comparison to Theoretical Predictions

Eventually we present the comparison of the measured π^0 R_{AA} to two theoretical predictions that use the RHIC experimental results for Au–Au at $\sqrt{s_{NN}} = 200$ GeV as starting point. The first one is the WHDG [55, 56] (S. Wicks, W. Horowitz, M Djordjevic, M. Gyulassy) model. It includes inelastic and elastic scattering and path length fluctuations. Once the parton flavour, energy (E), length (L) and α_s are fixed the only remaining free parameter of the model is the density of the medium scattering centers. The temperature is related to the density via the assumption of a thermalized medium of ultra-relativistic massless gluons. The R_{AA} is calculated with:

$$R_{AA} = \langle \int d\epsilon (1-\epsilon)^{n(p_T) \cdot} \cdot P(\epsilon) \rangle_{geom} \tag{6.1}$$

where $P(\epsilon)$ is the distribution of probability for the energy loss ϵ. It can be calculated using the number distribution of emitted gluons dN_g/dx which is obtained with the DGLV [57] generalization of the GLV [58] model for the radiative energy loss. The elastic scattering included is most important for the heavy quarks but is not completely negligible for the light quarks. $\langle ... \rangle_{geom}$ is the mean over the geometry of the medium which can be described either by choosing a characteristic length L or better by using a probability distribution P(L) found with a Glauber thickness function from a Woods-Saxon base geometry [55]. The comparison of the measured π^0 R_{AA} to the WHDG prediction which was kindly provided to us by W. Horowitz (wa.horowitz@uct.ac.za) is shown in Fig. 6.8. Within the uncertainties the data agrees with the predictions but it seems that the theory underestimates the data for the two most peripheral centralities especially if we consider the fact that the last two points in both might be too low when compared to the $\pi^\pm$ R_{AA}. The second model presented here describes the nucleus-nucleus collision as a convolution of parton distribution functions inside the nuclei, elementary parton-parton scattering cross sections and an effective parton fragmentation function modified to describe the high p_T parton energy loss in medium [59]. The energy loss and the effective fragmentation function are calculated within the higher-twist approach (HT) [60, 61] where a high p_T parton produced via a hard process travels through the medium and looses energy by multiple scattering and induced gluon bremsstrahlung. One important parameter here is the jet transport parameter $\hat{q}$ [62] which is the medium property on which the energy loss depends in this model. The energy loss model needs through this information about the space time evolution of the temperature and flow velocity in the bulk medium [59]. They are obtained from a full three-dimensional 3+1D ideal hydrodynamics model by T. Hirano
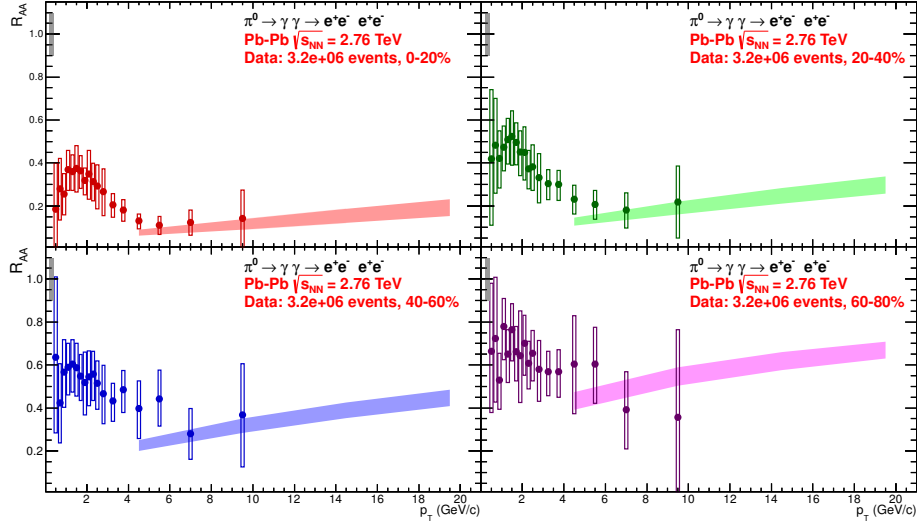
Figure 6.8: Measured π^0 R_{AA} Pb–Pb at $\sqrt{s_{NN}} = 2.76$ TeV (points) and a theoretical prediction by the WHDG model based on experimental data from RHIC at $\sqrt{s_{NN}} = 200$ GeV (shaded areas).

[63]. The q̂ parameter is related to the charged particle density $dN_{ch}/d\eta$ which is obtained by a fit to the RHIC data for most central collisions. We received the predictions for the π^0 R_{AA} for all centrality bins in our analysis from Xiao-Fang Chen (chenxf@iopp.ccnu.edu.cn). The comparison is shown in Fig. 6.9. The two most central R_{AA} measurements are described very well by the theoretical predictions as low as 4 GeV/c in p_T . For the two more peripheral bins the agreement is not that good even if one considers that the last two points (with highest p_T) of the measured π^0 R_{AA} might be too low. Here the theoretical predictions seem to overestimate the data.
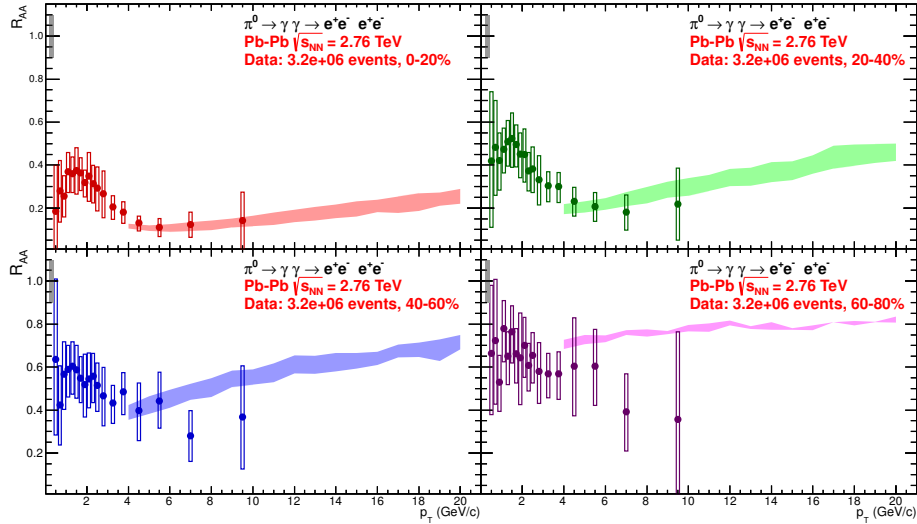
Figure 6.9: Measured π^0 R_{AA} for Pb–Pb at $\sqrt{s_{NN}} = 2.76$ TeV (points) and a theoretical prediction by a HT/Hydro model based on experimental data from RHIC at $\sqrt{s_{NN}} = 200$ GeV (shaded areas).

69

7 Summary and Outlook

In this Thesis we presented a study of the neutral pion and η meson differential invariant yields and nuclear modification factors. The analyzed data was collected with the ALICE detector during the LHC 2010 heavy-ion run at $\sqrt{s_{NN}} = 2.76$ TeV. This center-of-mass energy is more than thirteen times higher than any other energy reached at a heavy-ion collider so far. The medium created hereby is hotter, denser and lives longer giving us the opportunity to study the properties of the QPG formed in such an environment.

The method used for the analysis of the two neutral mesons is based on the reconstruction of photons converted in the detector material with the ALICE ITS and TPC tracking detectors. It allows us to measure the neutral pion down to a transverse momentum of 0.4 GeV/c where we can probe the thermodynamic particle production in the medium and up to a p_T of 11 GeV/c giving us the possibility to study the particle production suppression due to the energy loss of high energetic partons in the medium. The meson reconstruction and yield extraction were optimized for the conditions of the heavy-ion collisions and the effects of the specialties of the Pb–Pb MC samples were analyzed. An extensive study on the systematic effects of the applied cuts was performed to ensure that no false results were obtained due to inappropriate cuts. The π^0 differential invariant yields were fitted with a combination of the Tsallis and power law functions and a bin width correction via a shift of the data points along either the p_T or yield axis was applied. The R_{AA} was calculated for each centrality and all the results were compared to the measurements of the neutral pions by PHOS and to the charged pions with the TPC dE/dx showing a good agreement. An energy loss model was studied using the measured π^0 data and showed a good description power when comparing the extrapolation of the π^0 R_{AA} obtained with the model to the R_{AA} of unidentified charged particles up to momenta of 45 GeV/c. When used for a comparison to the PHENIX results the model showed also that there is a qualitative difference between the energy loss at LHC and RHIC energies. Comparison of the measured data to two individual theoretical predictions showed a generally good agreement but also proposed the need of more precise measurement in order to be more distinguishable between the different models.

The η meson analysis was performed for all centrality bins but for only one bin in p_T due to the large background and limited statistics. The obtained results suffer from large statistical uncertainties and no study of the systematics has been performed yet. Nevertheless it was important to show that our method is able to reconstruct the η meson and the obtained results show an η to π^0 ratio that agrees with the pp measurement and an η R_{AA} that is similar to the results for the π^0 like it is expected from the PHENIX measurement. However we must point out that the conclusions made above have to be considered taking seriously the large statistical errors that are at the order of 50%.

The 2011 LHC Pb–Pb run is expected to collect a higher number of events than the 2010 run and special centrality triggers are planned in order to enhance the sample of the most central events. This will allow a more precise measurement of the π^0 meson differential

invariant yield and R_{AA} and will also increase the p_T reach. The measurement of the η meson with smaller statistical uncertainties and with a higher number of p_T bins will also become possible.

8 Appendix

8.1 γ and e^+/e^- Plots
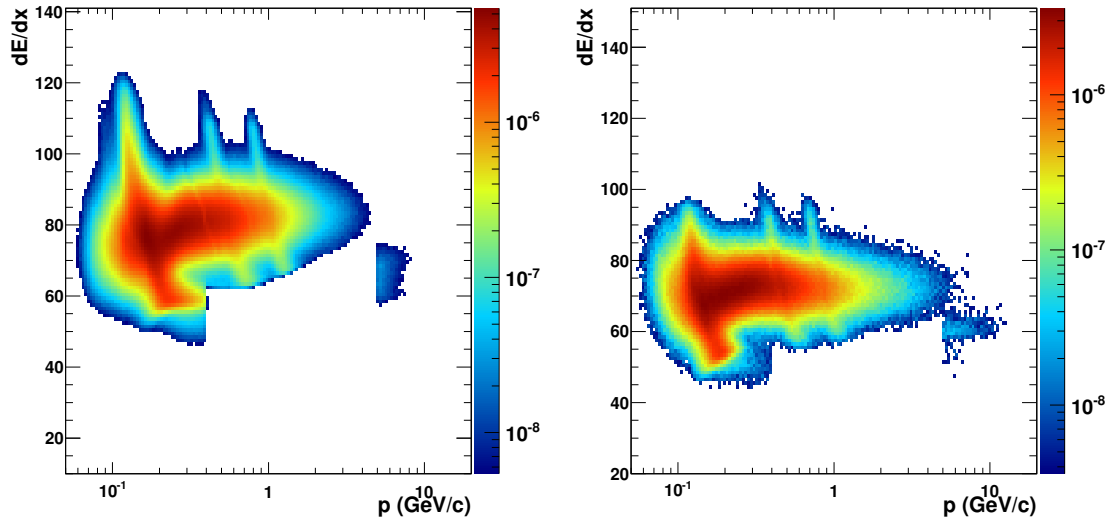
Figure 8.1: dE/dx of electrons from selected photon candidates for data (left) and MC (right); 0-20%
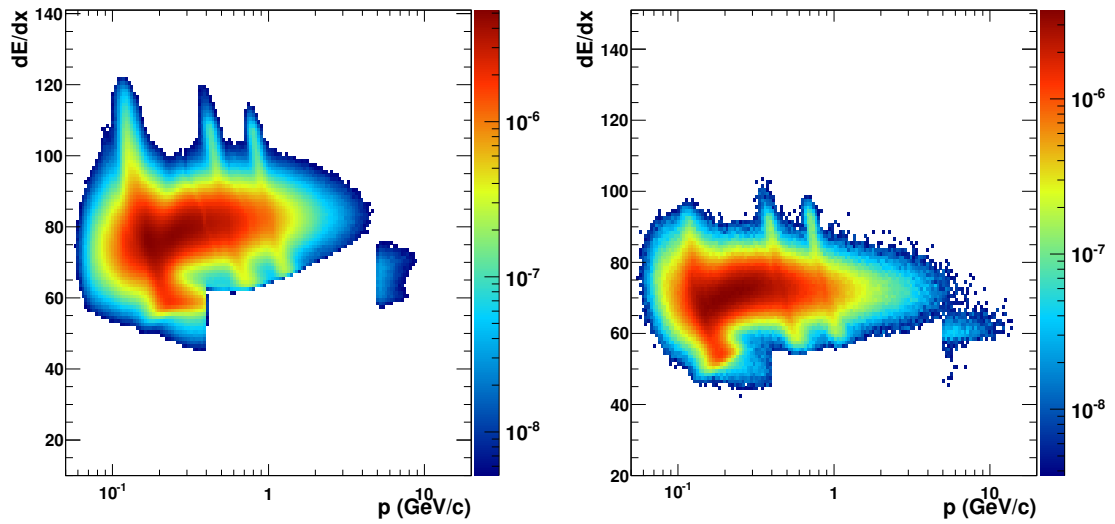
Figure 8.2: dE/dx of positrons from selected photon candidates for data (left) and MC (right); 0-20%
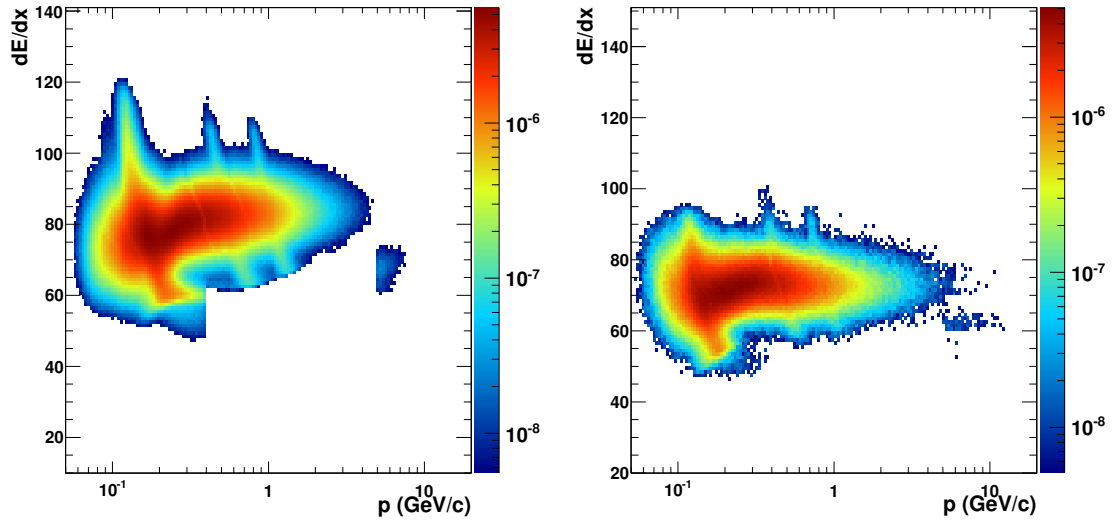
Figure 8.3: dE/dx of electrons from selected photon candidates for data (left) and MC (right); 20-40%
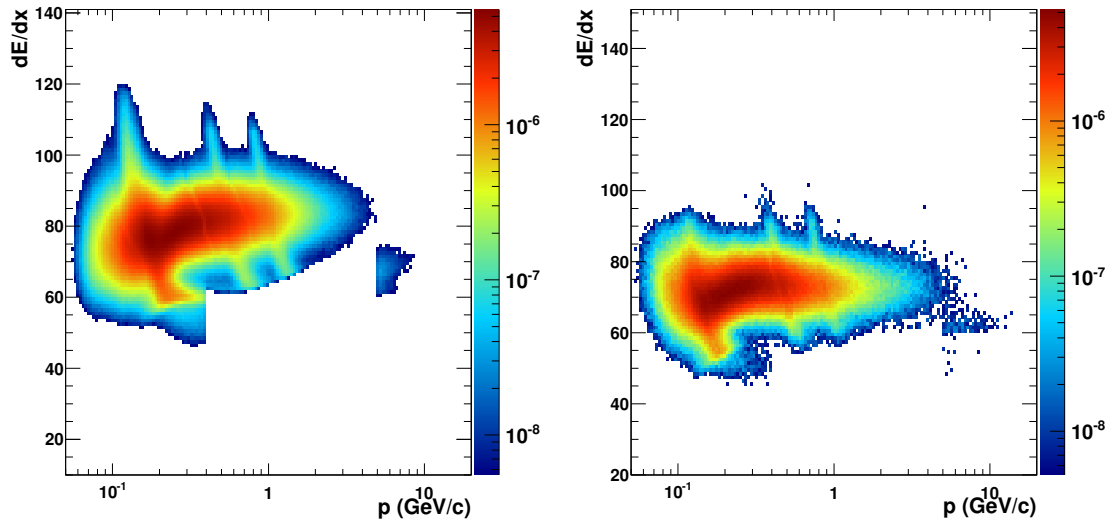
Figure 8.4: dE/dx of positrons from selected photon candidates for data (left) and MC (right); 20-40%
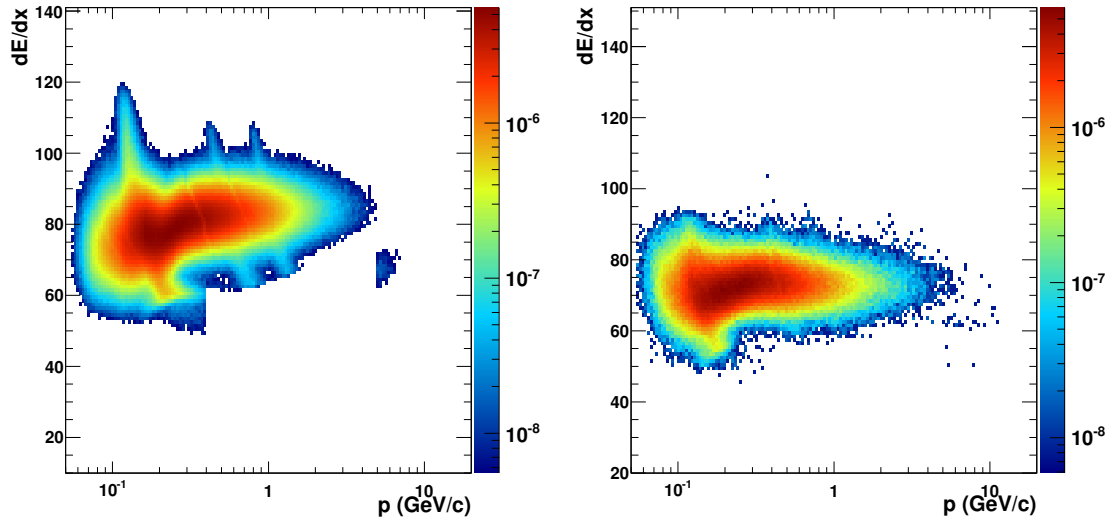
Figure 8.5: dE/dx of electrons from selected photon candidates for data (left) and MC (right); 40-60%
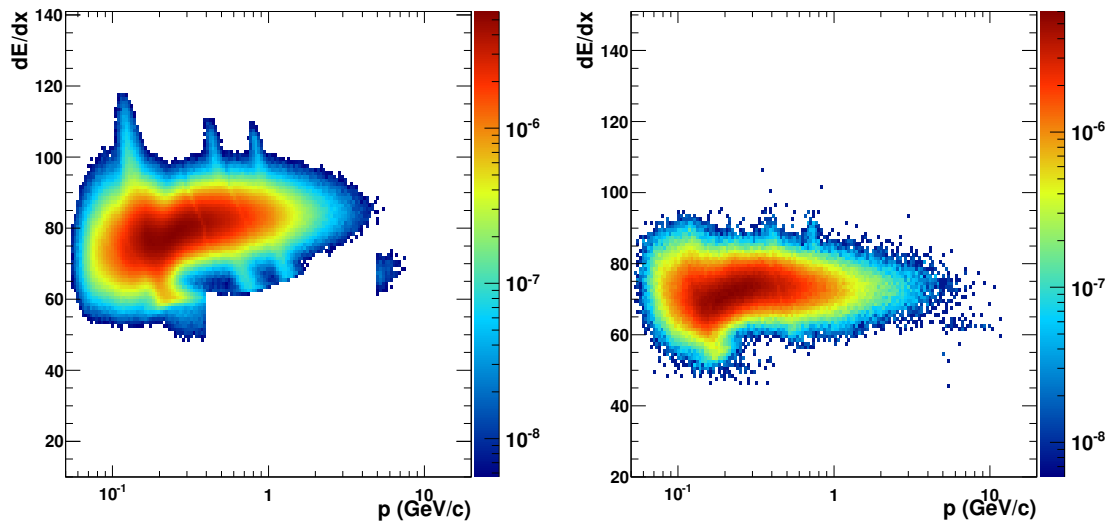
Figure 8.6: dE/dx of positrons from selected photon candidates for data (left) and MC (right); 40-60%
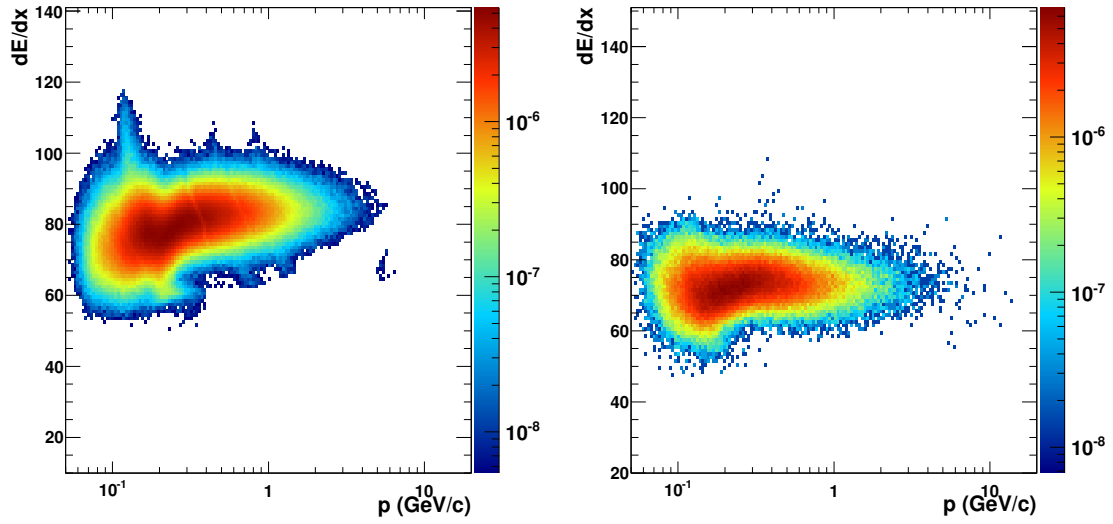
Figure 8.7: dE/dx of electrons from selected photon candidates for data (left) and MC (right); 60-80%
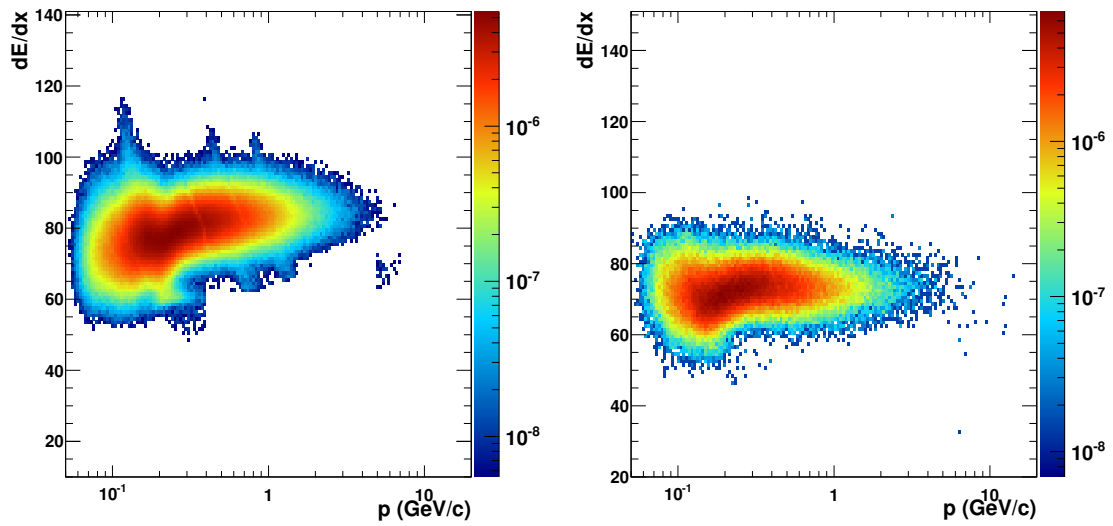
Figure 8.8: dE/dx of positrons from selected photon candidates for data (left) and MC (right); 60-80%
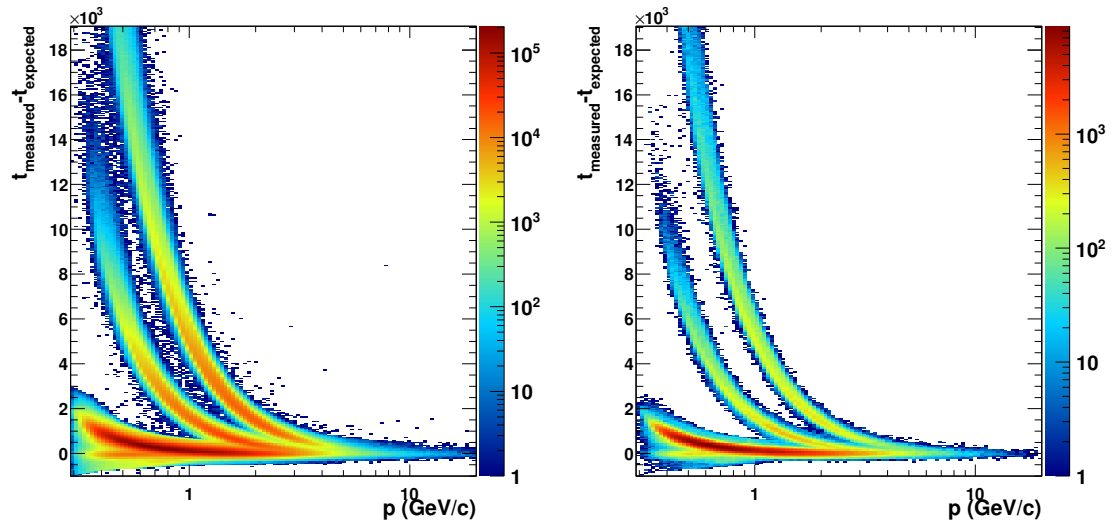
Figure 8.9: TOF $t_{measured} - t_{expected}$ of $e^{\pm}$ before cuts for data (left) and MC (right); 0-20%
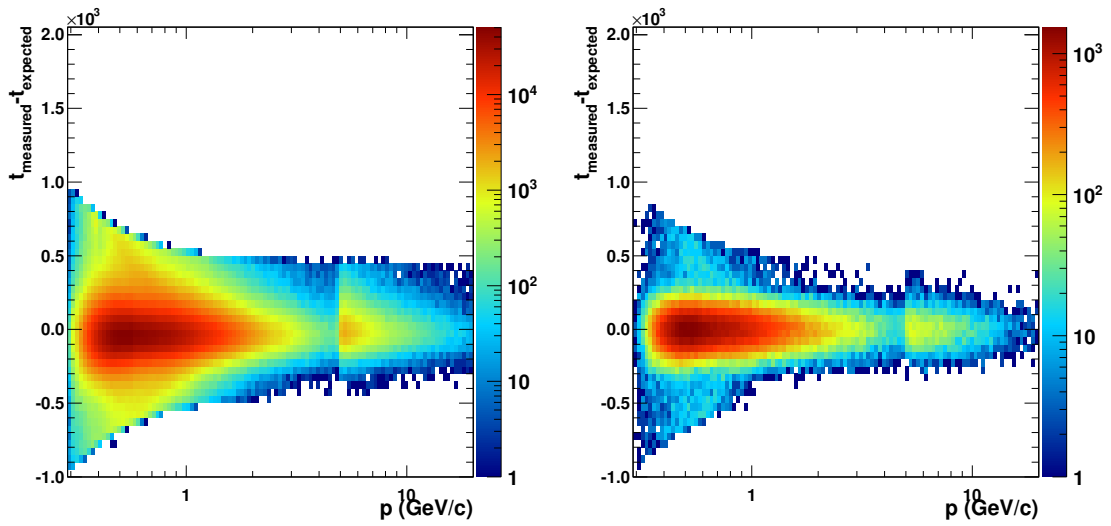
Figure 8.10: TOF $t_{measured} - t_{expected}$ of $e^{\pm}$ after cuts for data (left) and MC (right); 0-20%
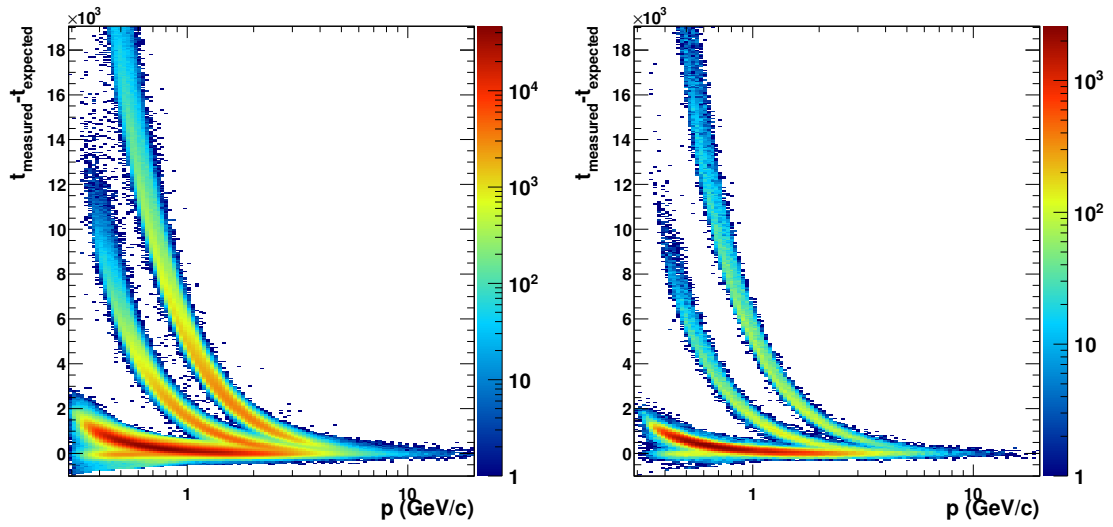
Figure 8.11: TOF $t_{measured} - t_{expected}$ of $e^{\pm}$ before cuts for data (left) and MC (right); 20-40%
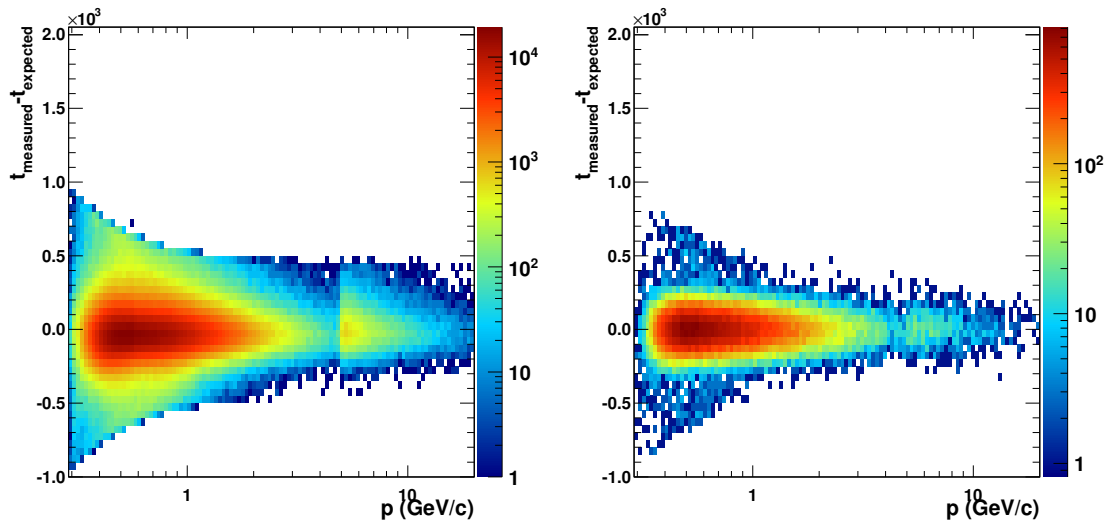
Figure 8.12: TOF $t_{measured} - t_{expected}$ of $e^{\pm}$ after cuts for data (left) and MC (right); 20-40%
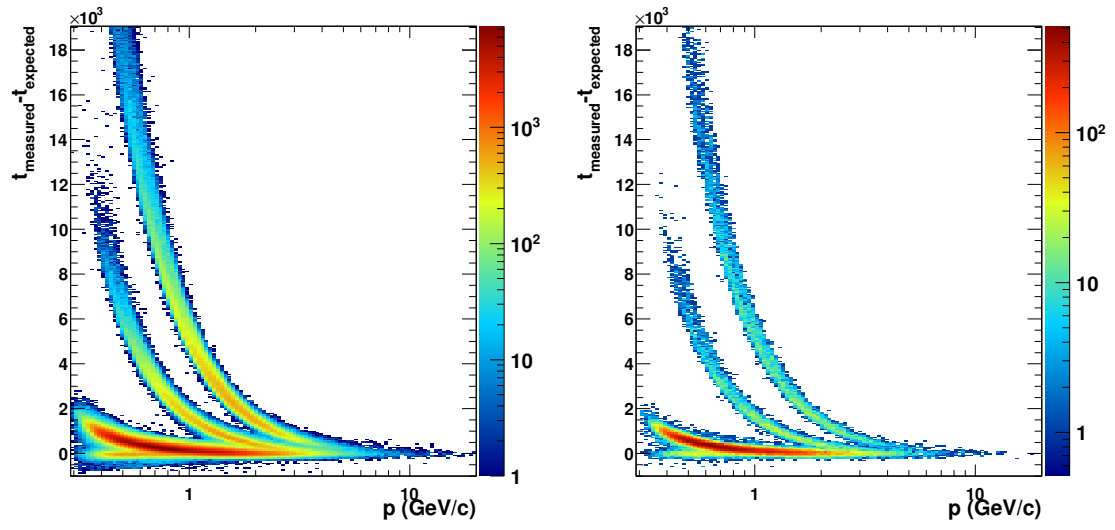
Figure 8.13: TOF $t_{measured} - t_{expected}$ of $e^{\pm}$ before cuts for data (left) and MC (right); 40-60%
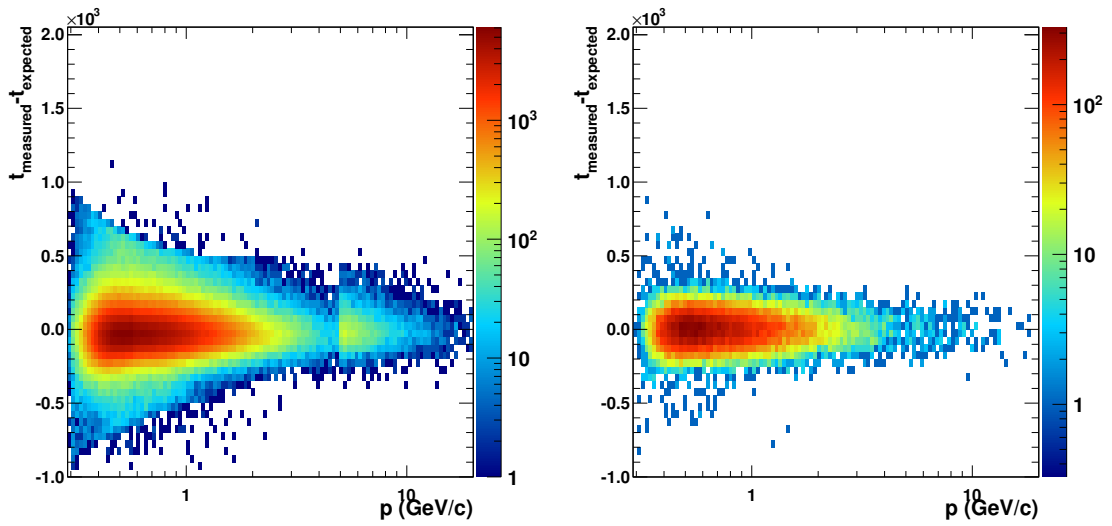
Figure 8.14: TOF $t_{measured} - t_{expected}$ of $e^{\pm}$ after cuts for data (left) and MC (right); 40-60%
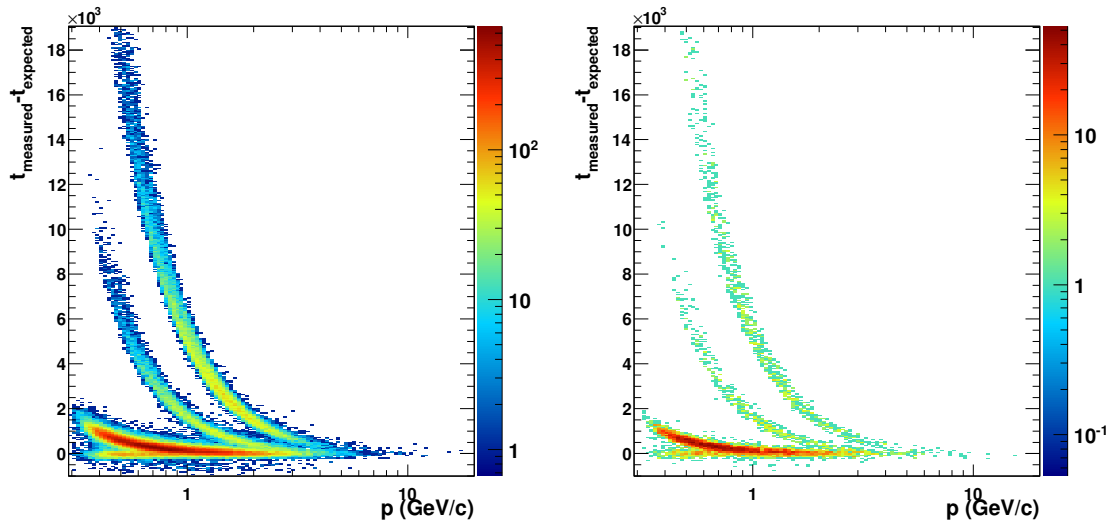
Figure 8.15: TOF $t_{measured} - t_{expected}$ of $e^{\pm}$ before cuts for data (left) and MC (right); 60-80%
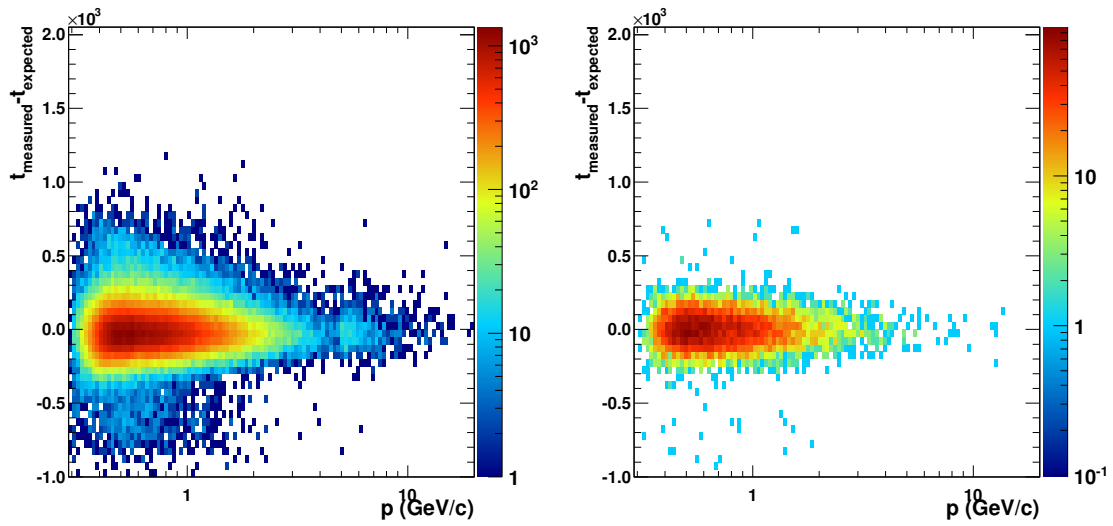
Figure 8.16: TOF $t_{measured} - t_{expected}$ of $e^{\pm}$ after cuts for data (left) and MC (right); 60-80%
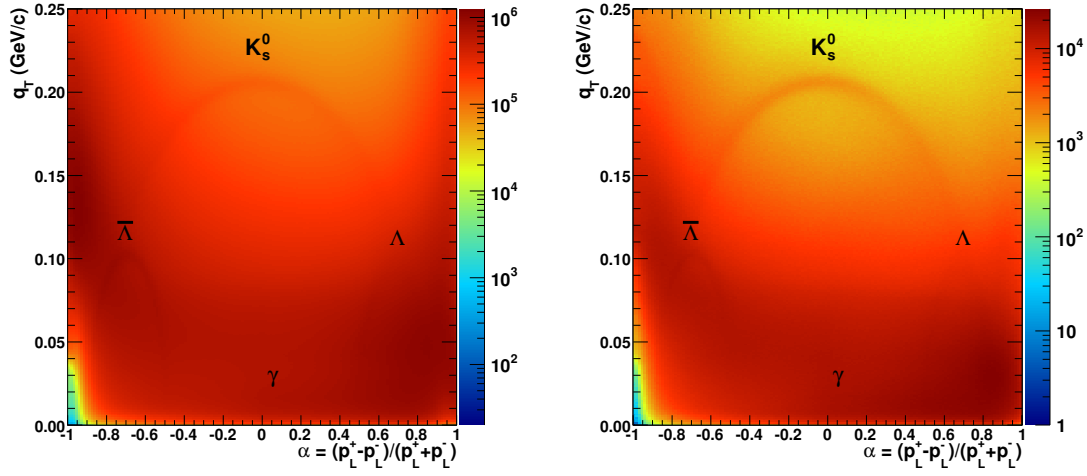
Figure 8.17: Armenteros plots for data (left) and MC (right) before cuts; 0-20%
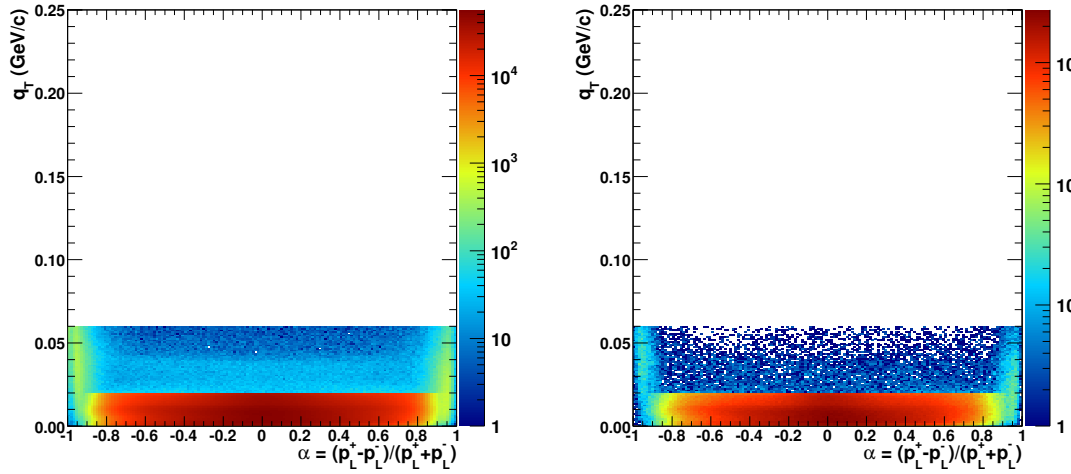
Figure 8.18: Armenteros plots for data(left) and MC(right) after cuts; 0-20%
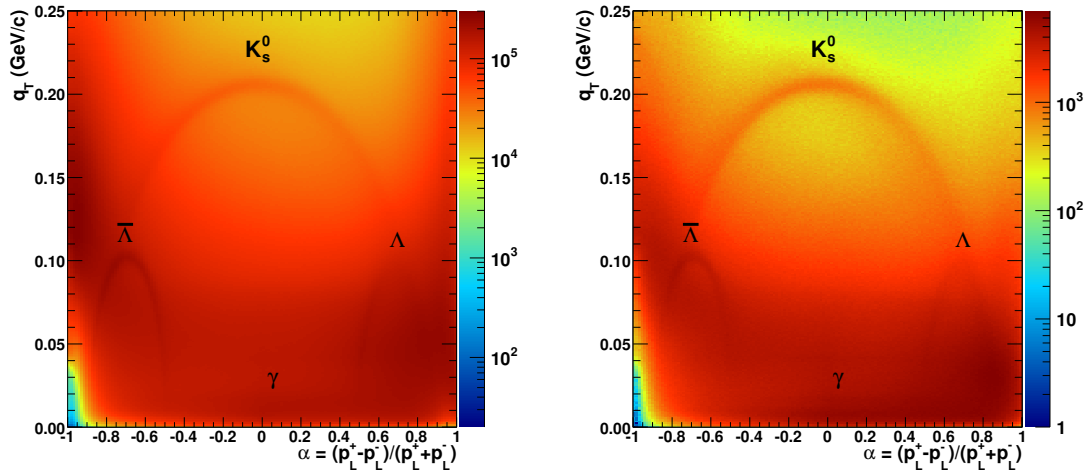
Figure 8.19: Armenteros plots for data (left) and MC (right) before cuts; 20-40%
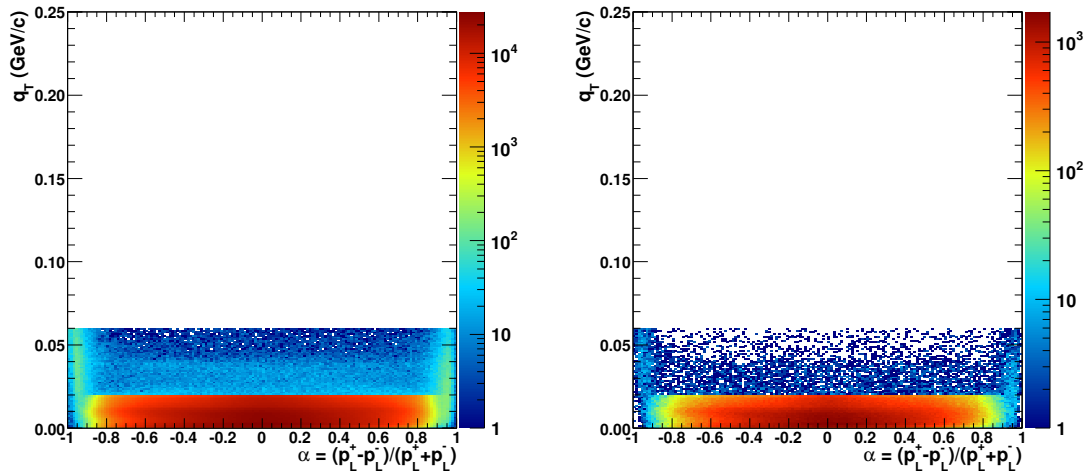
Figure 8.20: Armenteros plots for data(left) and MC(right) after cuts; 20-40%
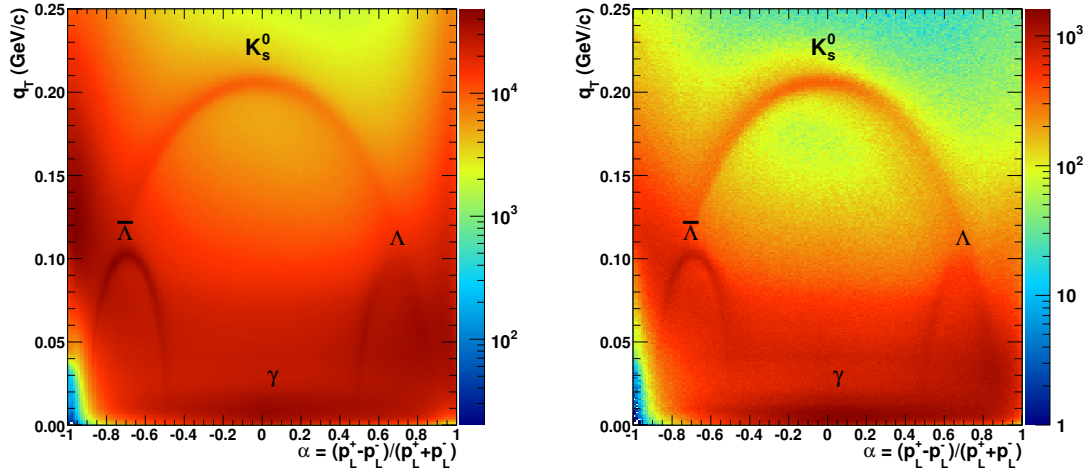
Figure 8.21: Armenteros plots for data (left) and MC (right) before cuts; 40-60%
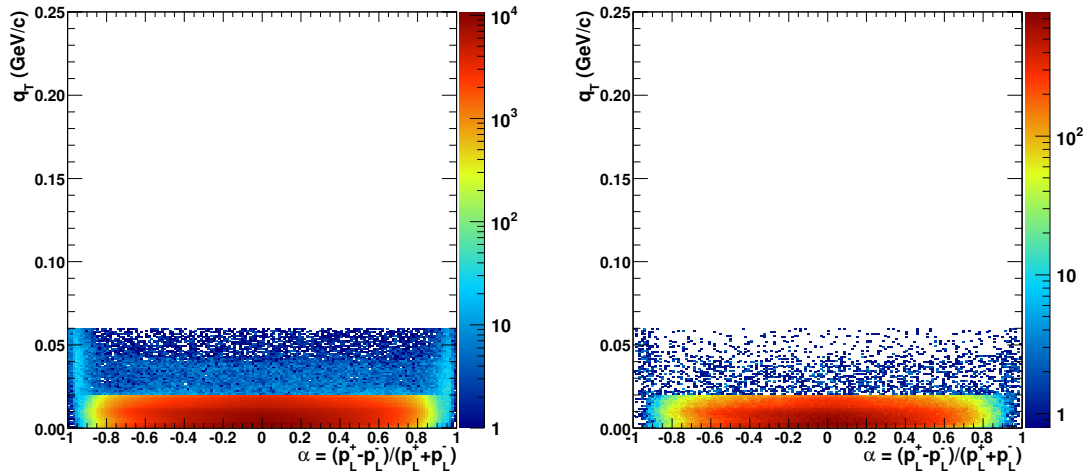
Figure 8.22: Armenteros plots for data(left) and MC(right) after cuts; 40-60%
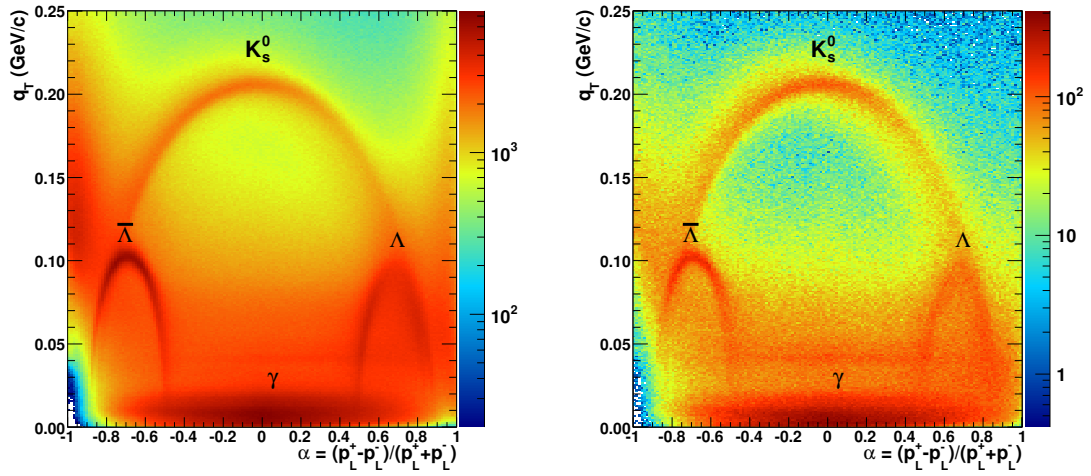
Figure 8.23: Armenteros plots for data (left) and MC (right) before cuts; 60-80%
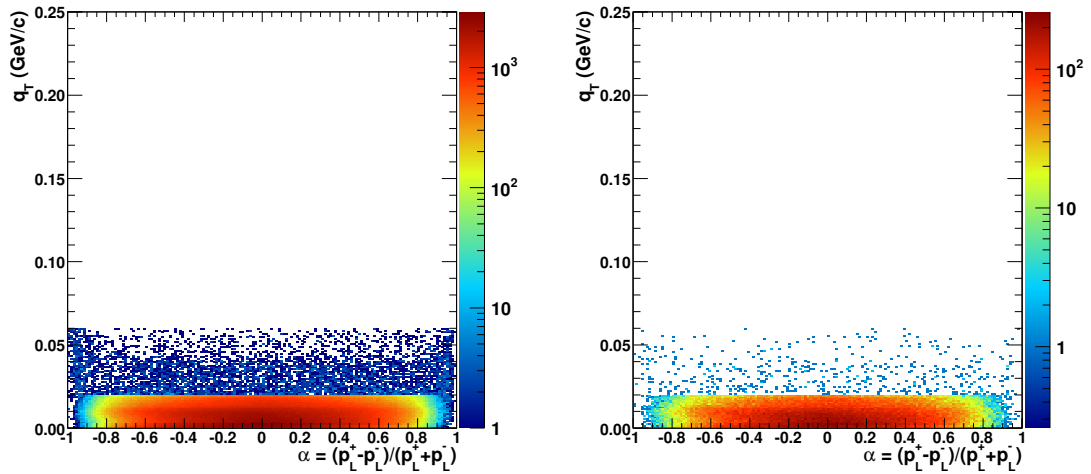
Figure 8.24: Armenteros plots for data(left) and MC(right) after cuts; 60-80%
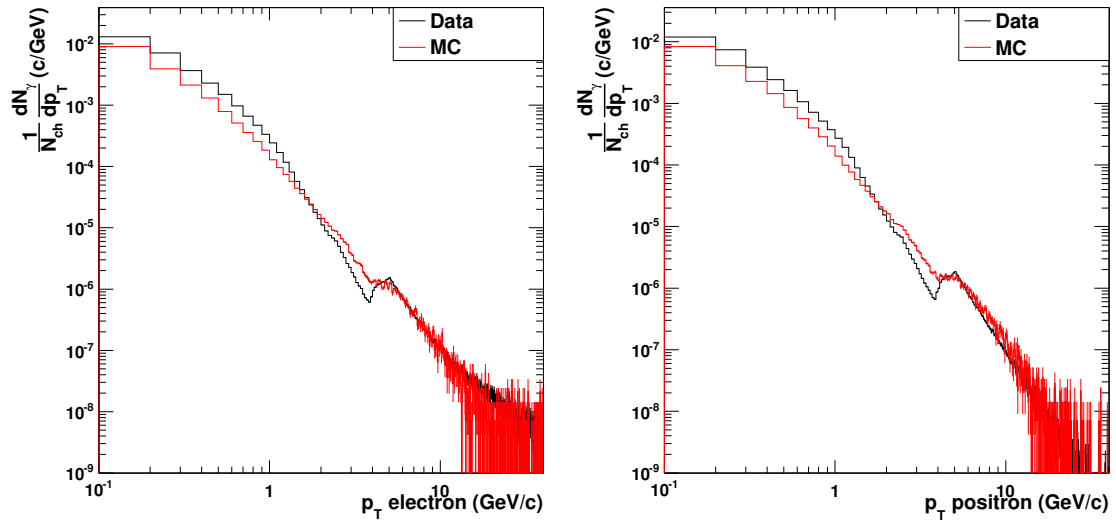
Figure 8.25: electron (left) and positron (right) p_T distributions in data (black) and MC (red); 0-20%
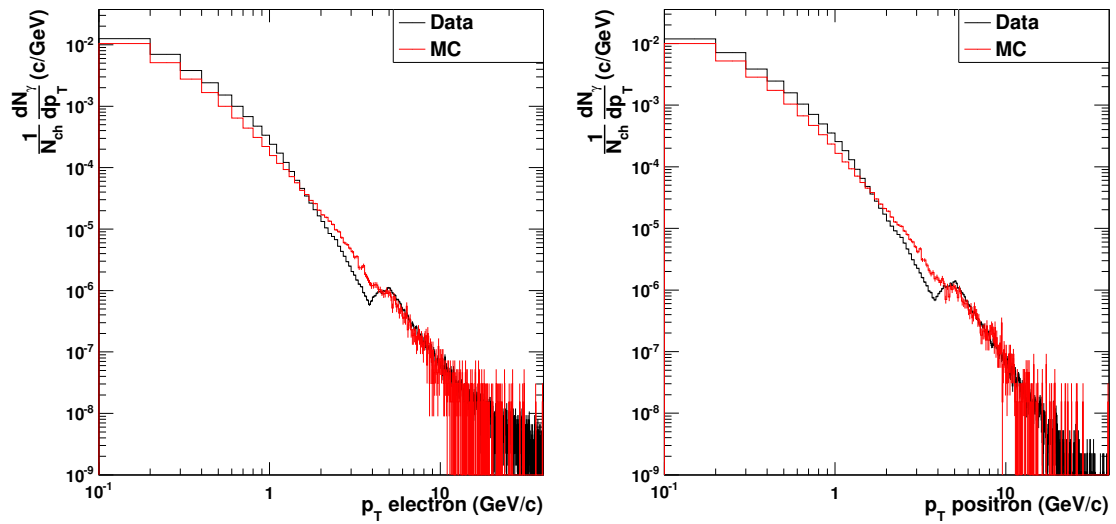
Figure 8.26: electron (left) and positron (right) p_T distributions in data (black) and MC (red); 20-40%
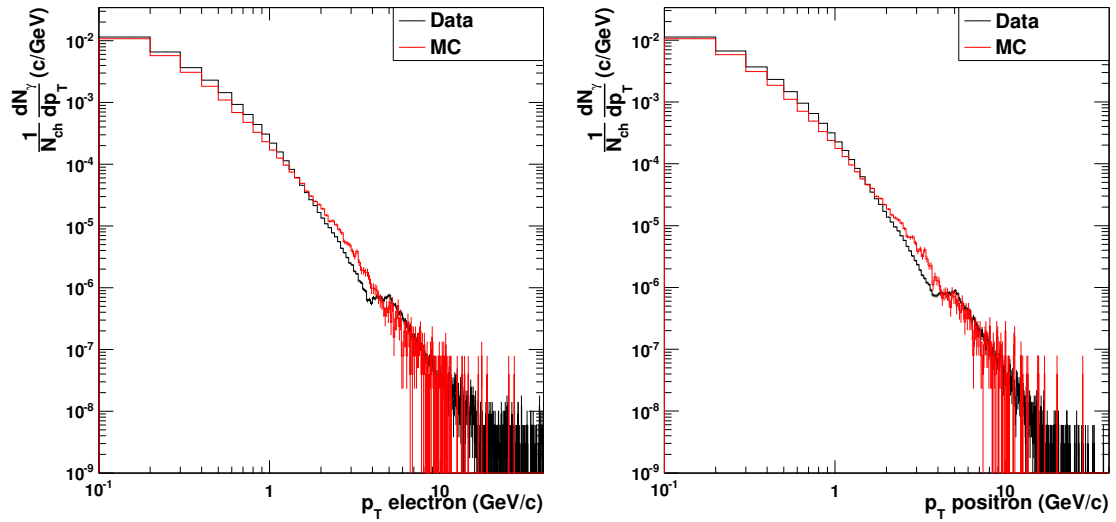
Figure 8.27: electron (left) and positron (right) p_T distributions in data (black) and MC (red); 40-60%
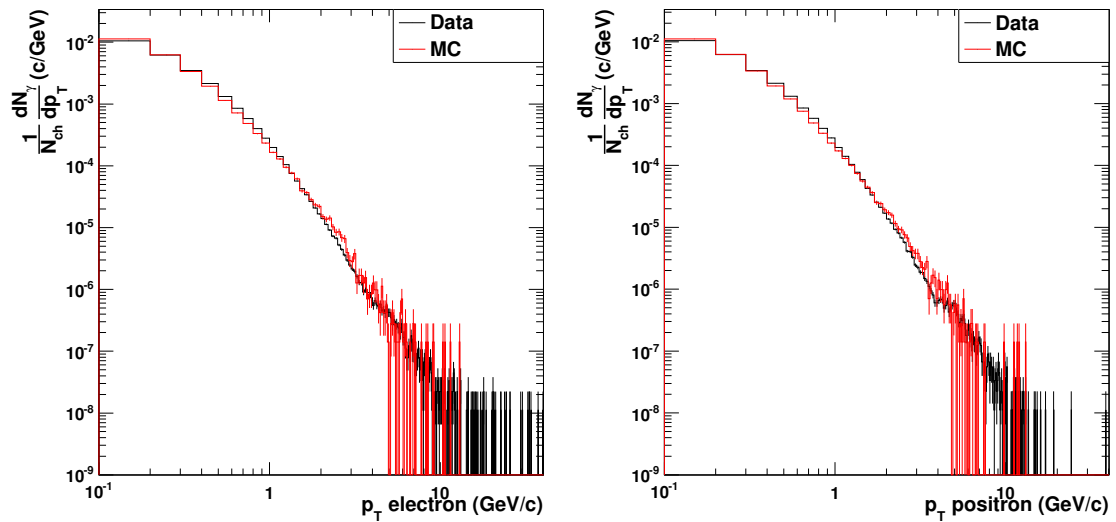
Figure 8.28: electron (left) and positron (right) p_T distributions in data (black) and MC (red); 60-80%
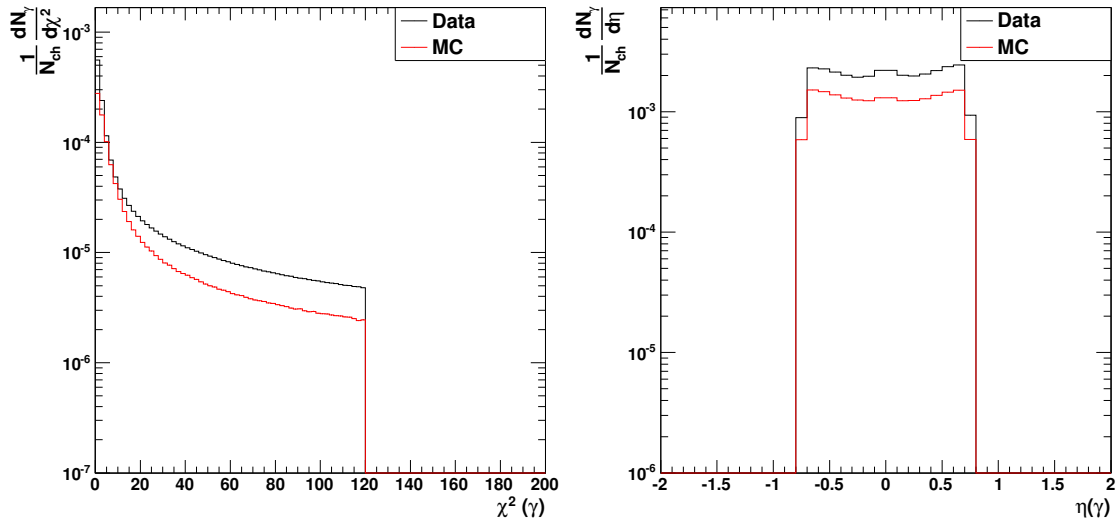
Figure 8.29: χ^2 (left) and η (right) distributions for photon candidates; 0-20%
(Step at the edges comes for $|\eta| < 0.75$ cut and 0.1 bin width.)
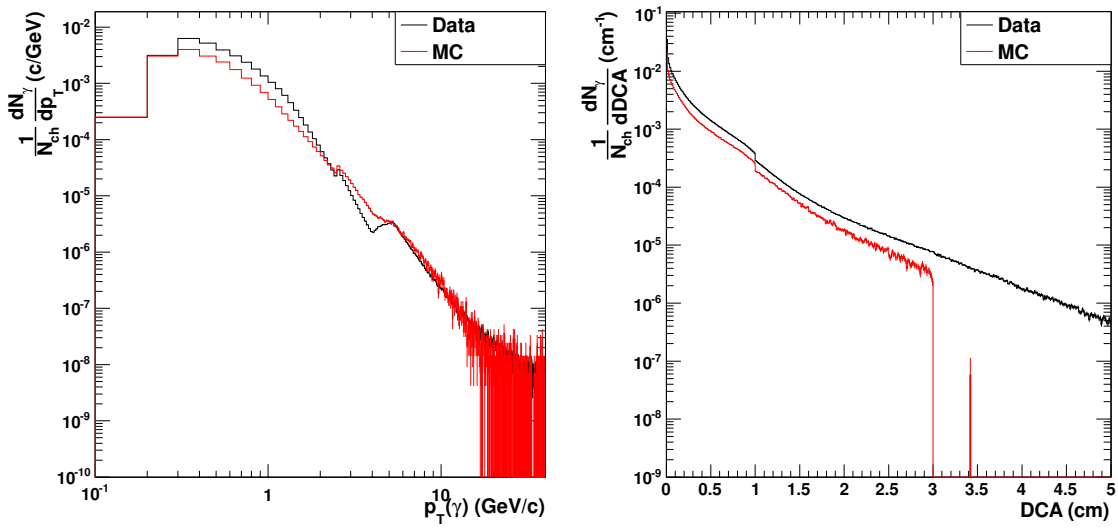
Figure 8.30: p_{T} distribution of photon candidates and DCA distributions of their daughters; 0-20%
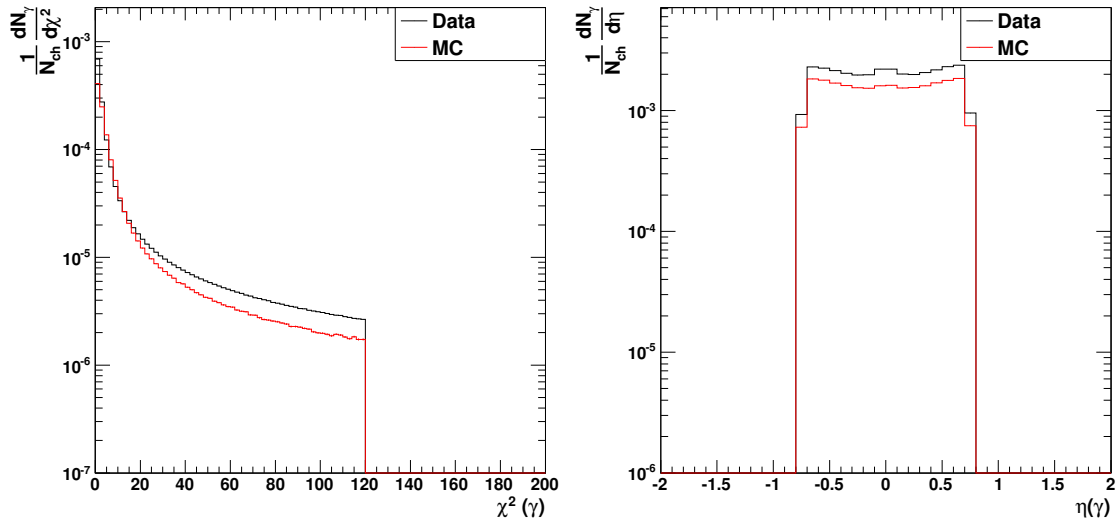
Figure 8.31: χ^2 (left) and η (right) distributions for photon candidates; 20-40% (Step at the edges comes for $|\eta| < 0.75$ cut and 0.1 bin width.)
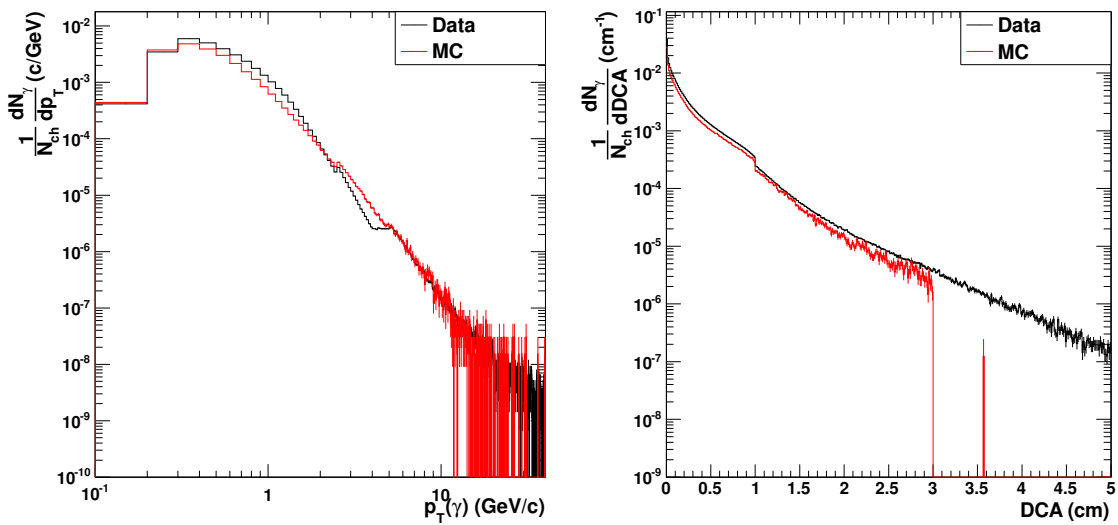
Figure 8.32: p_T distribution of photon candidates and DCA distributions of their daughters; 20-40%
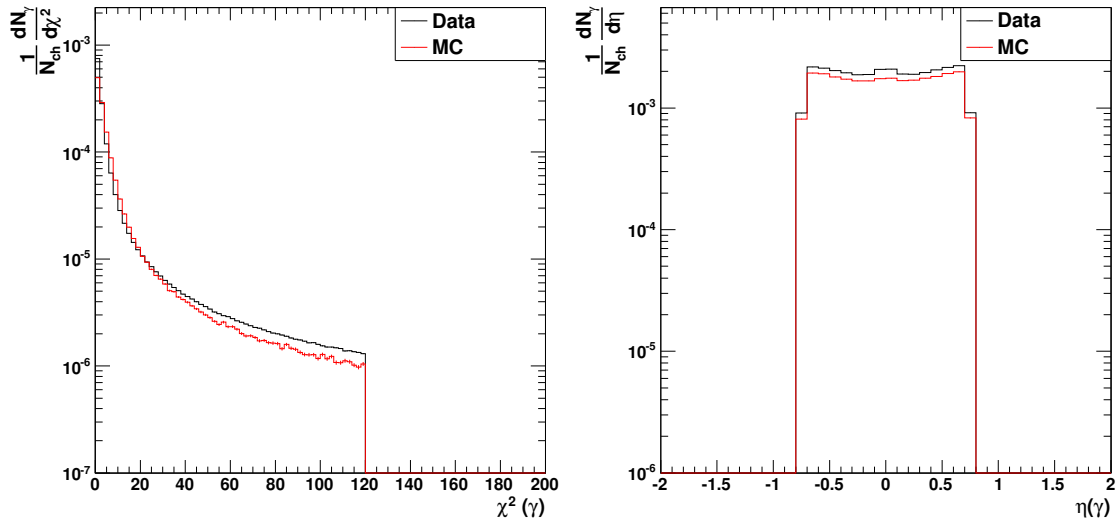
Figure 8.33: χ^2 (left) and η (right) distributions for photon candidates; 40-60% (Step at the edges comes for $|\eta| < 0.75$ cut and 0.1 bin width.)
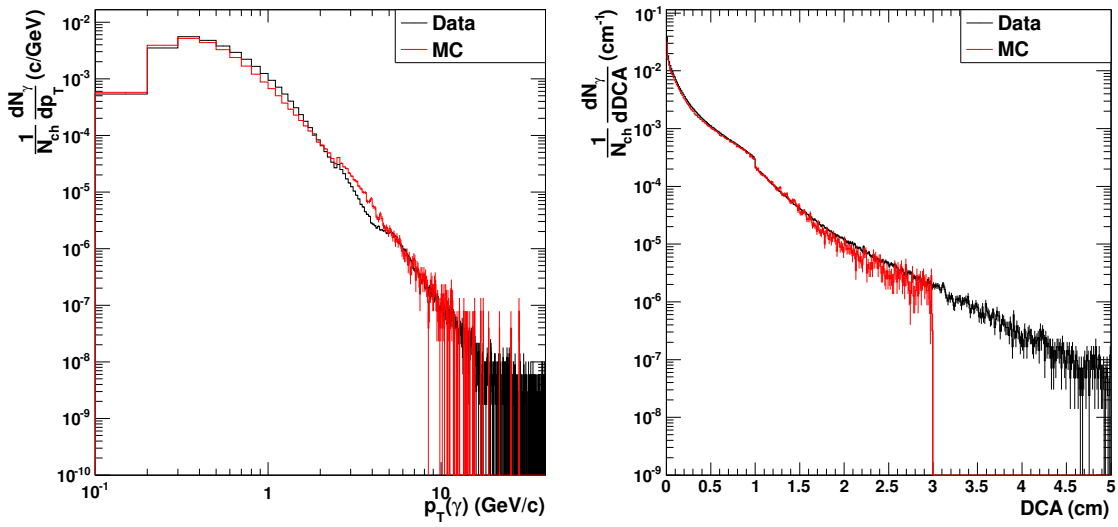
Figure 8.34: p_T distribution of photon candidates and DCA distributions of their daughters; 40-60%
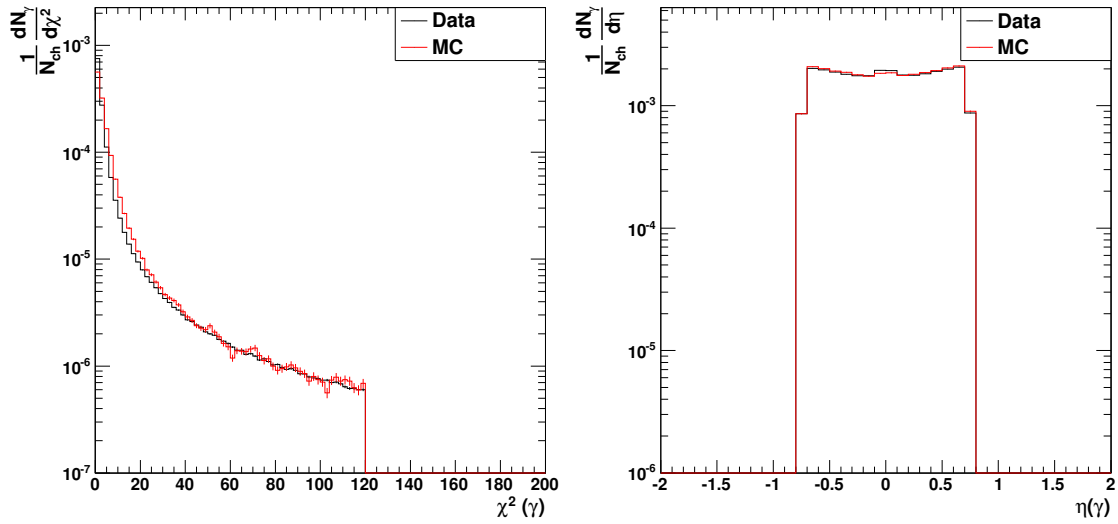
Figure 8.35: χ^2 (left) and η (right) distributions for photon candidates; 60-80% (Step at the edges comes for $|\eta| < 0.75$ cut and 0.1 bin width.)
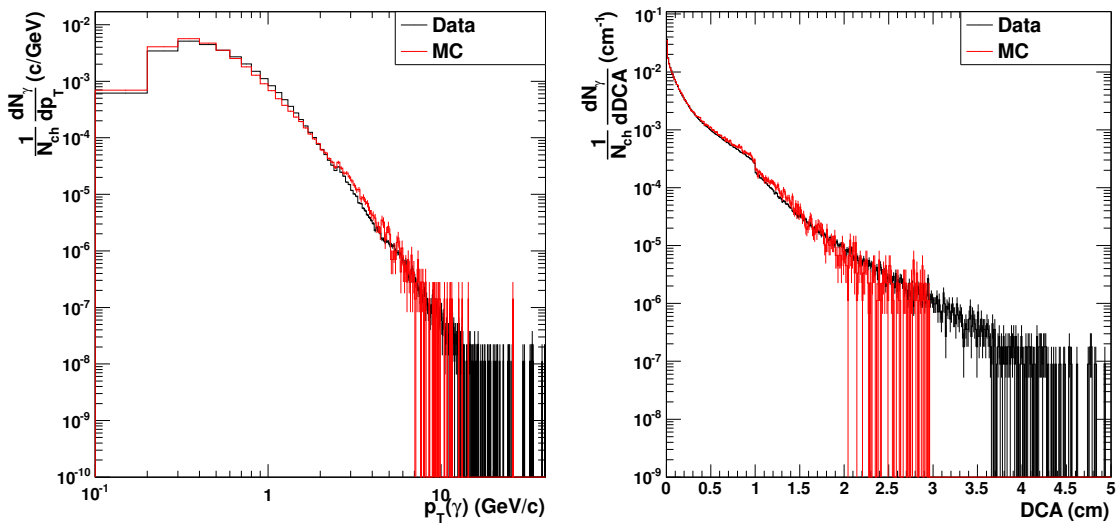
Figure 8.36: p_T distribution of photon candidates and DCA distributions of their daughters; 60-80%
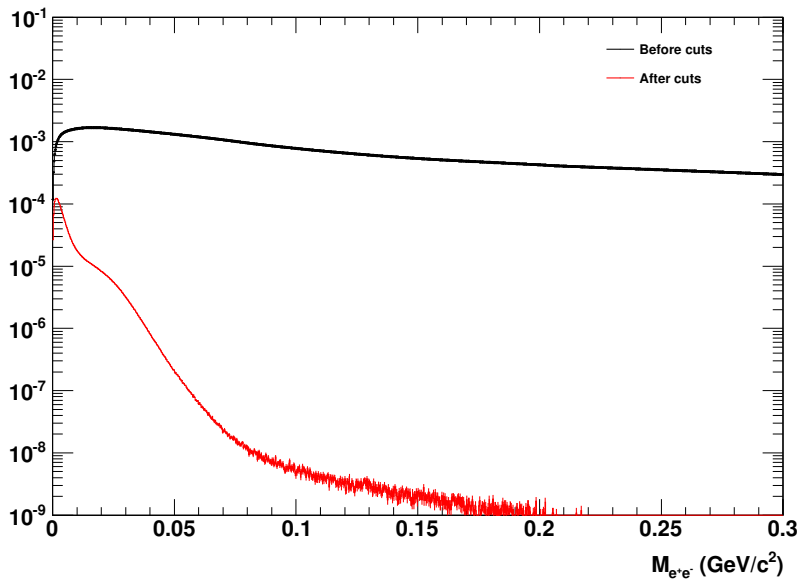
Figure 8.37: Invariant mass of gamma candidates before (black) and after (red) the cuts; 0-20%
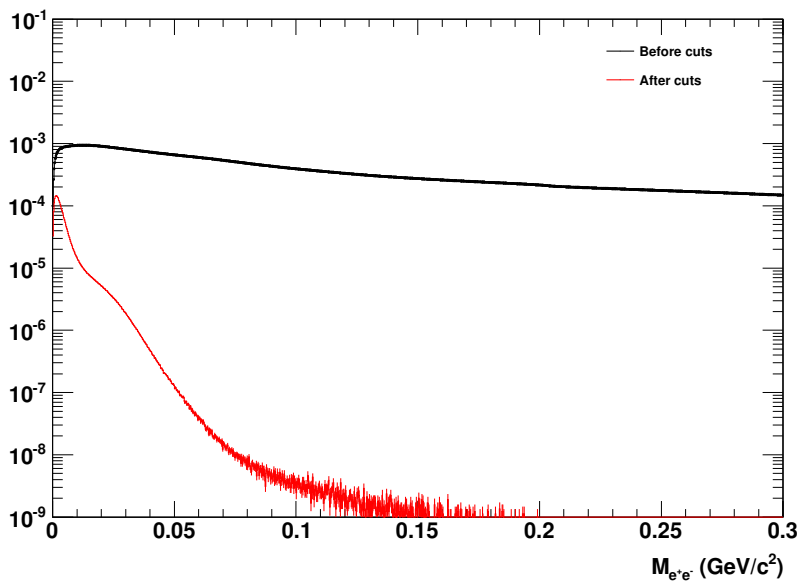
Figure 8.38: Invariant mass of gamma candidates before (black) and after (red) the cuts; 20-40%
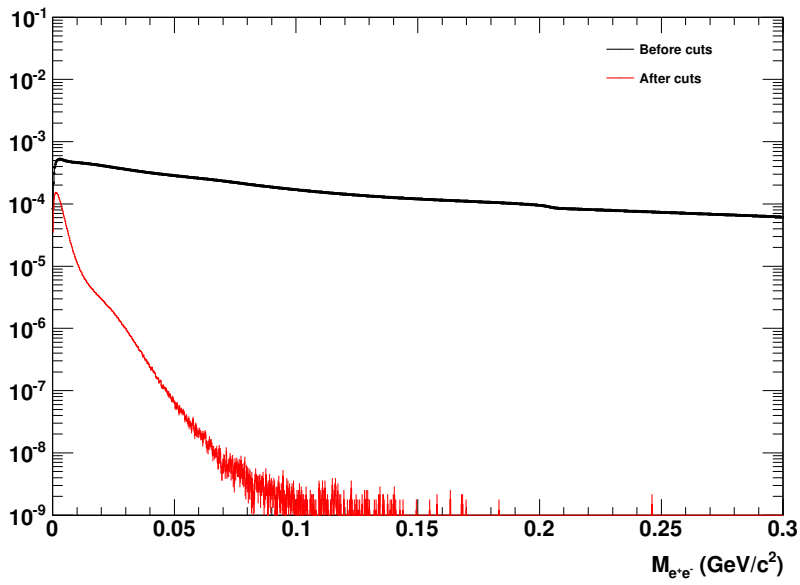
Figure 8.39: Invariant mass of gamma candidates before (black) and after (red) the cuts; 40-60%
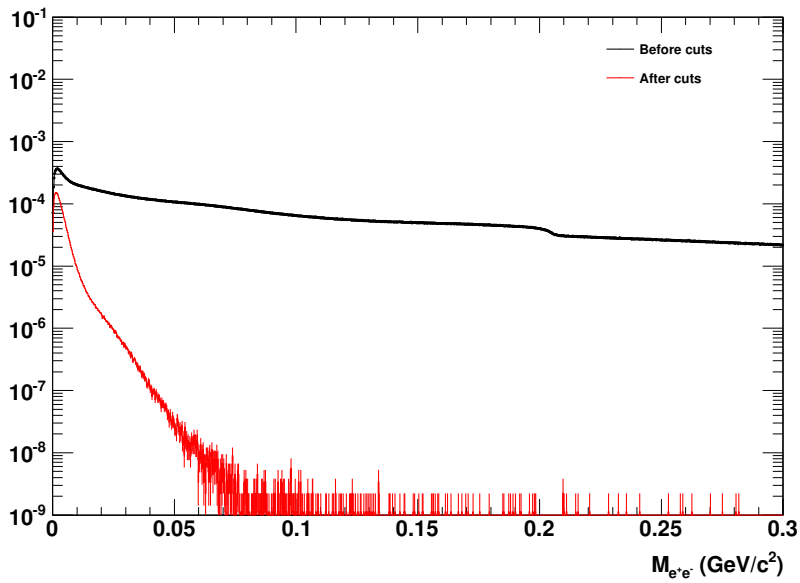
Figure 8.40: Invariant mass of gamma candidates before (black) and after (red) the cuts; 60-80%

8.2 π^0 Plots
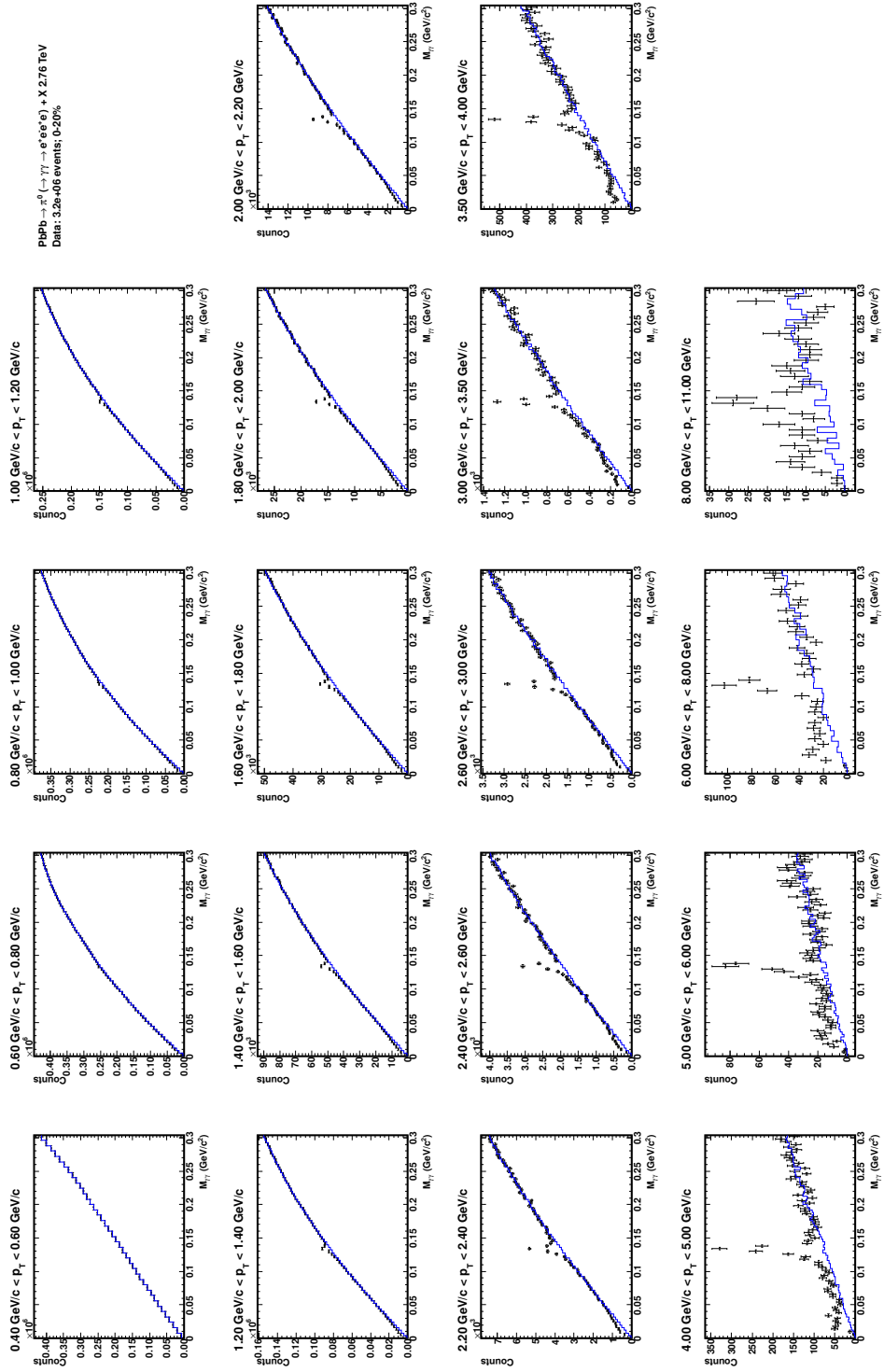
Figure 8.41: $\gamma\gamma$ invariant mass distributions in p_{T} bins with scaled background (blue); 0-20% centrality.
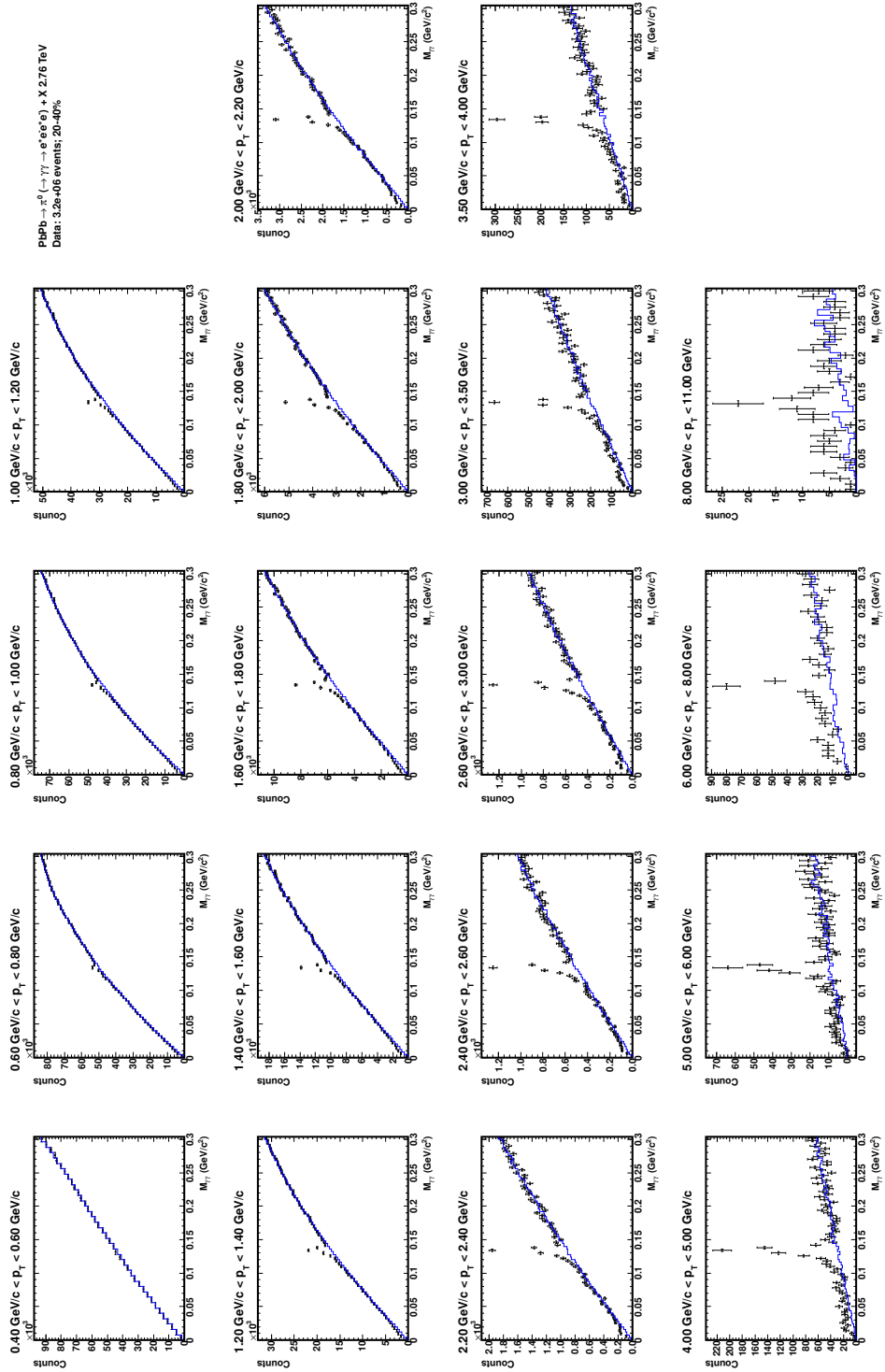
Figure 8.42: $\gamma\gamma$ invariant mass distributions in p_{T} bins with scaled background (blue); 20-40% centrality.
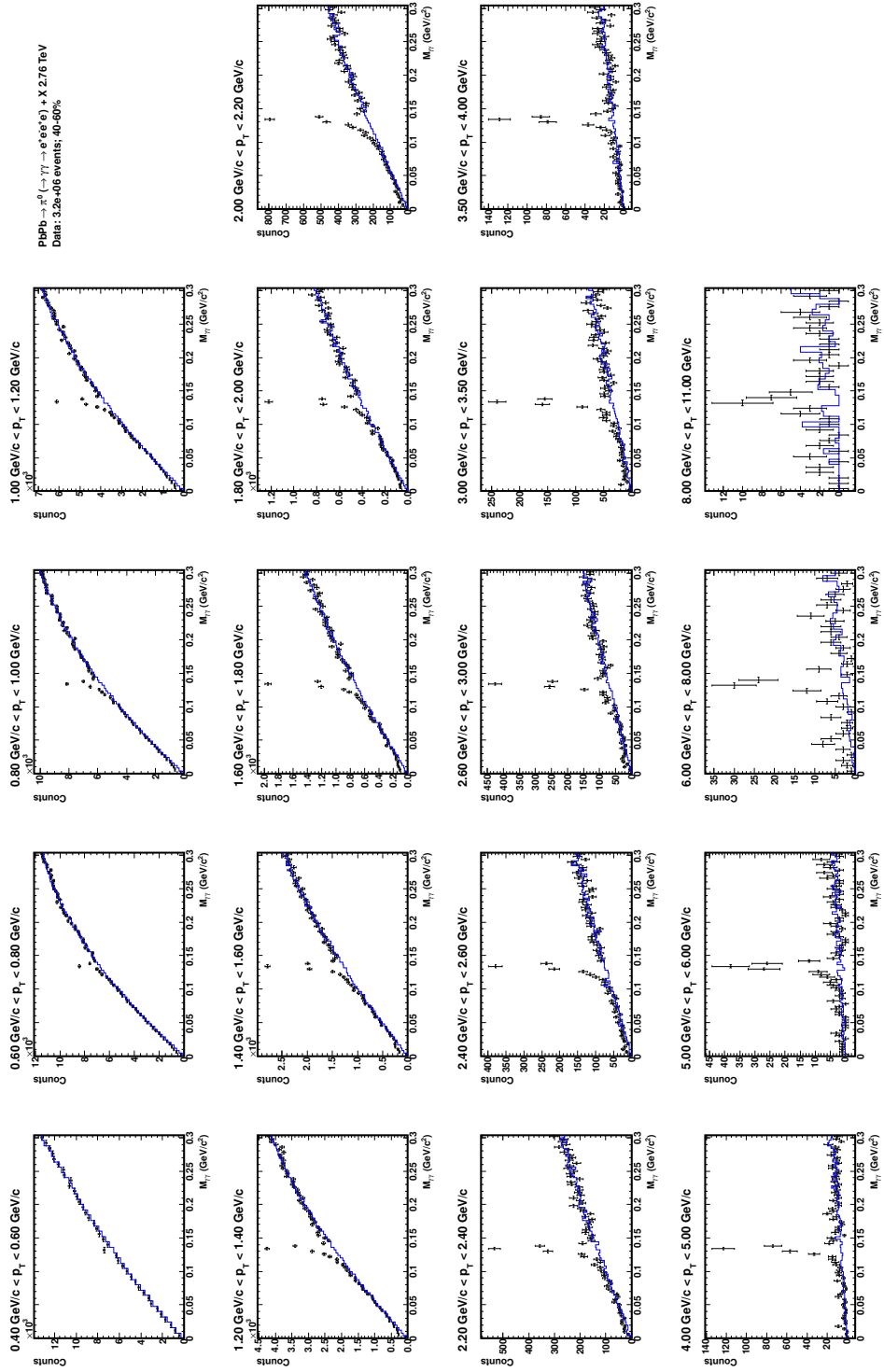
Figure 8.43: $\gamma\gamma$ invariant mass distributions in p_{T} bins with scaled background (blue); 40-60% centrality.
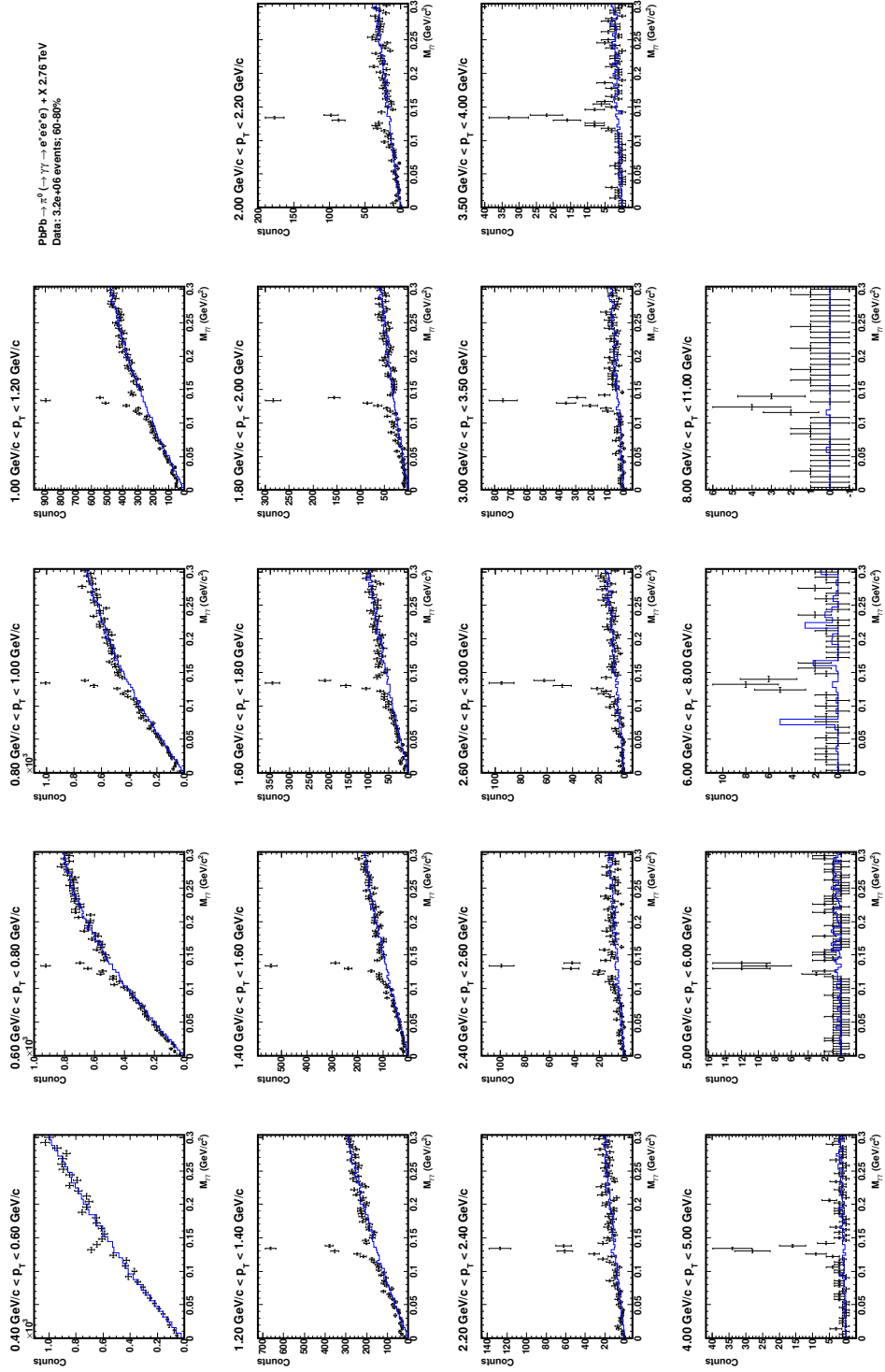
Figure 8.44: $\gamma\gamma$ invariant mass distributions in p_{T} bins with scaled background (blue); 60-80% centrality.
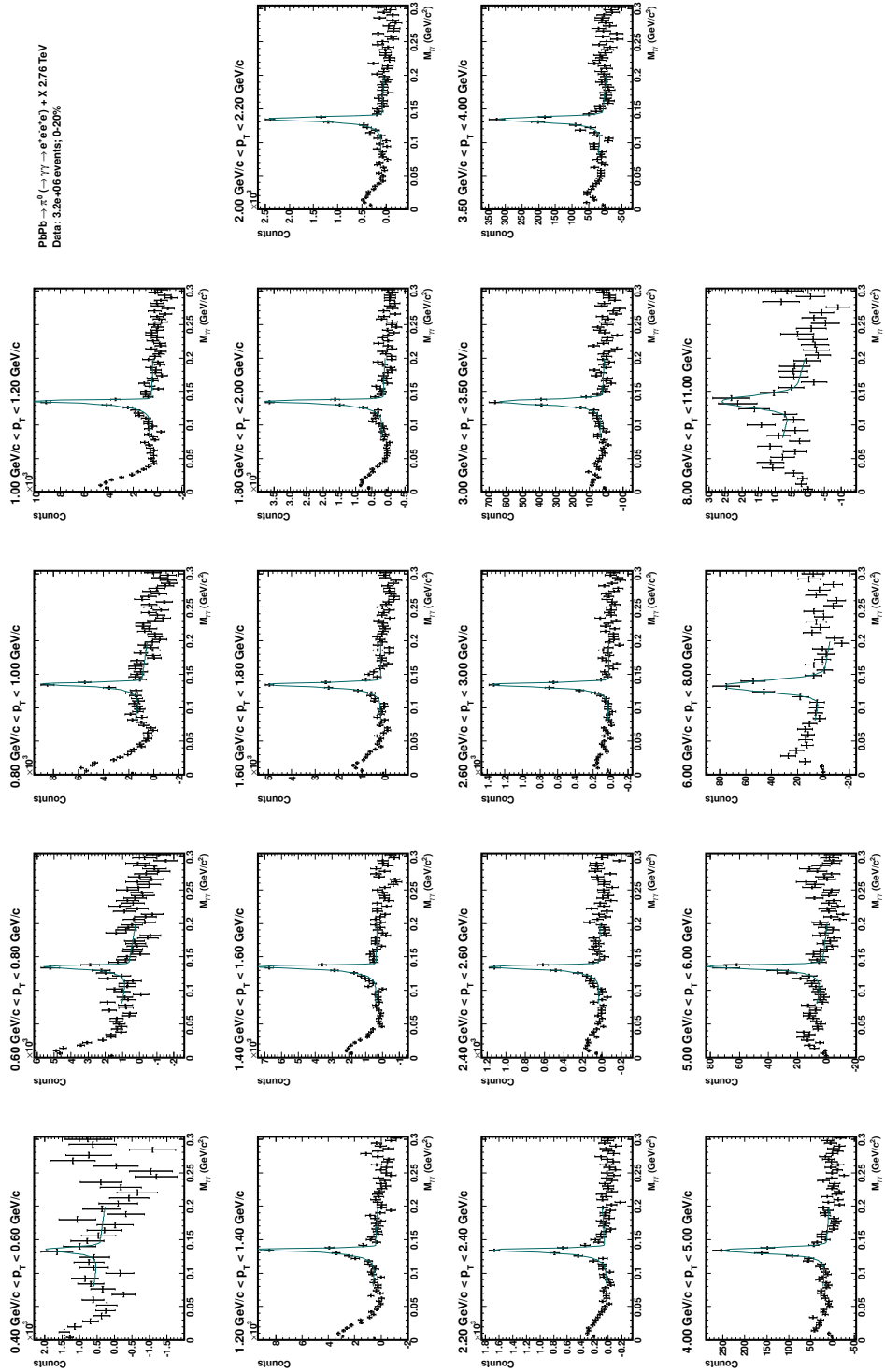
Figure 8.45: Fitted $\gamma\gamma$ invariant mass distributions in p_T bins after bck subtraction; 0-20% centrality.
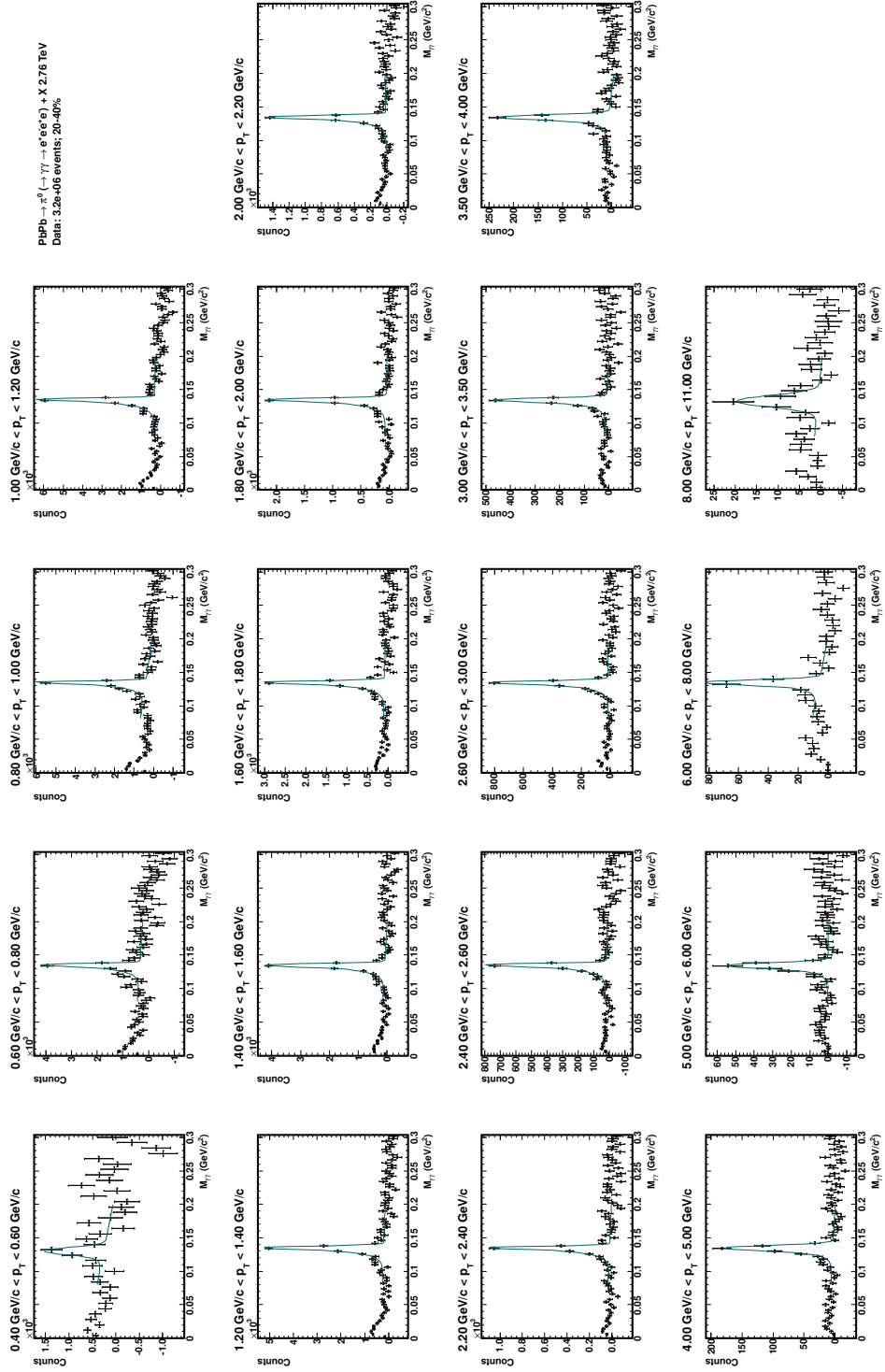
Figure 8.46: Fitted $\gamma\gamma$ invariant mass distributions in p_T bins after bck subtraction; 20-40% centrality.
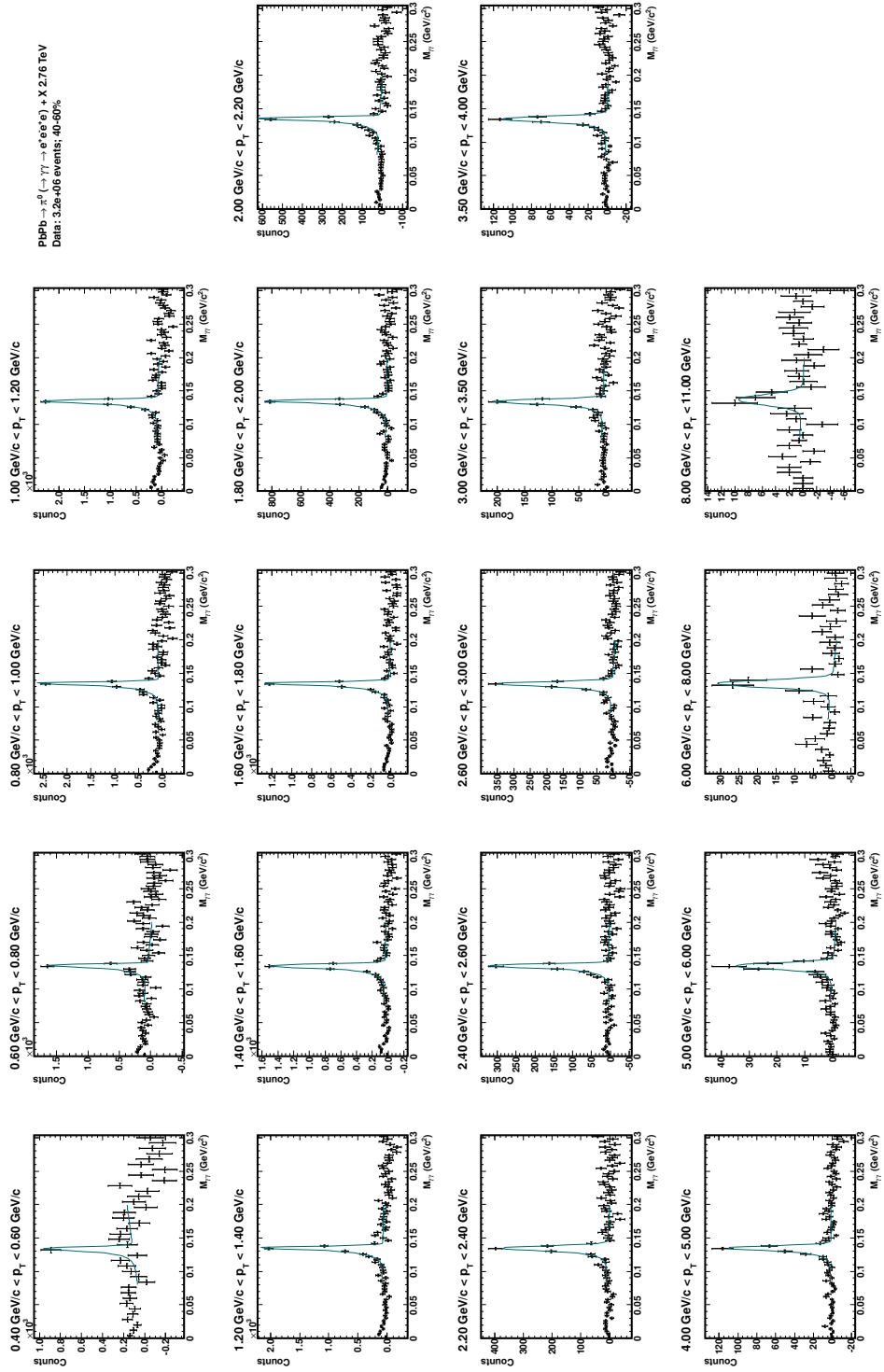
Figure 8.47: Fitted $\gamma\gamma$ invariant mass distributions in p_T bins after bck subtraction; 40-60% centrality.
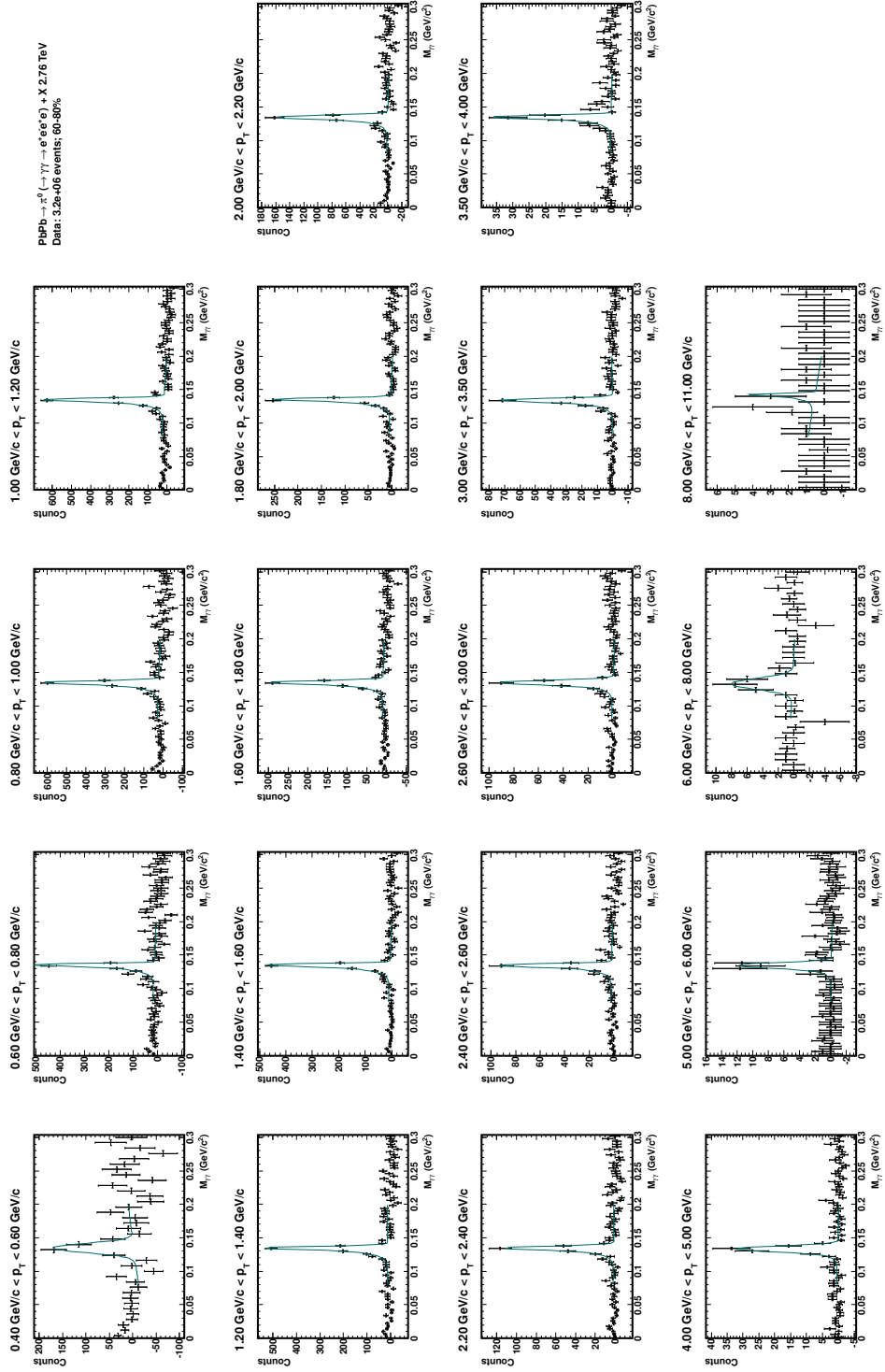
Figure 8.48: Fitted $\gamma\gamma$ invariant mass distributions in p_T bins after bck subtraction; 60-80% centrality.
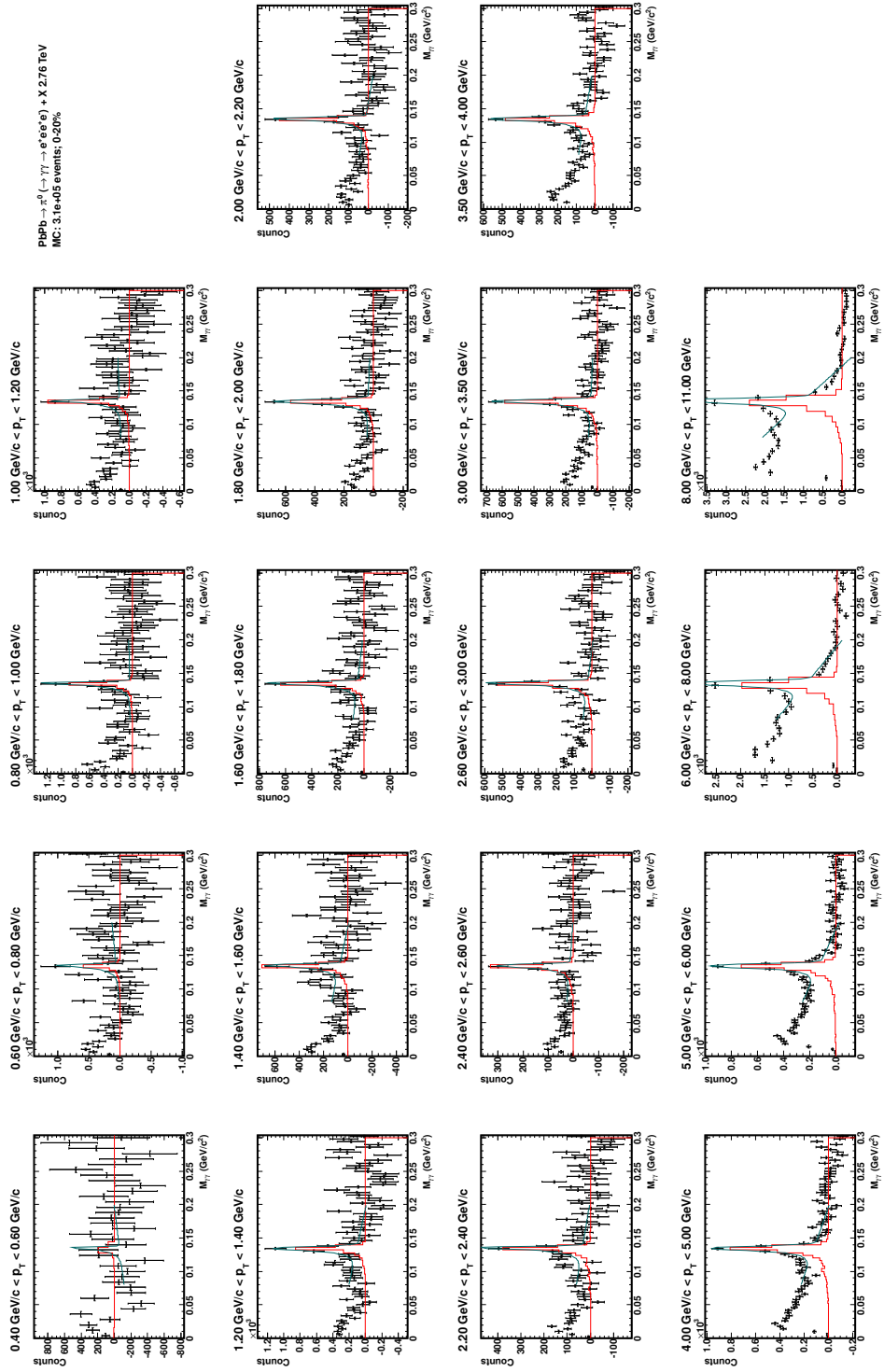
Figure 8.49: MC $\gamma\gamma$ invariant mass after bck subtraction and true reconstructed π^0s; 0-20% centrality.
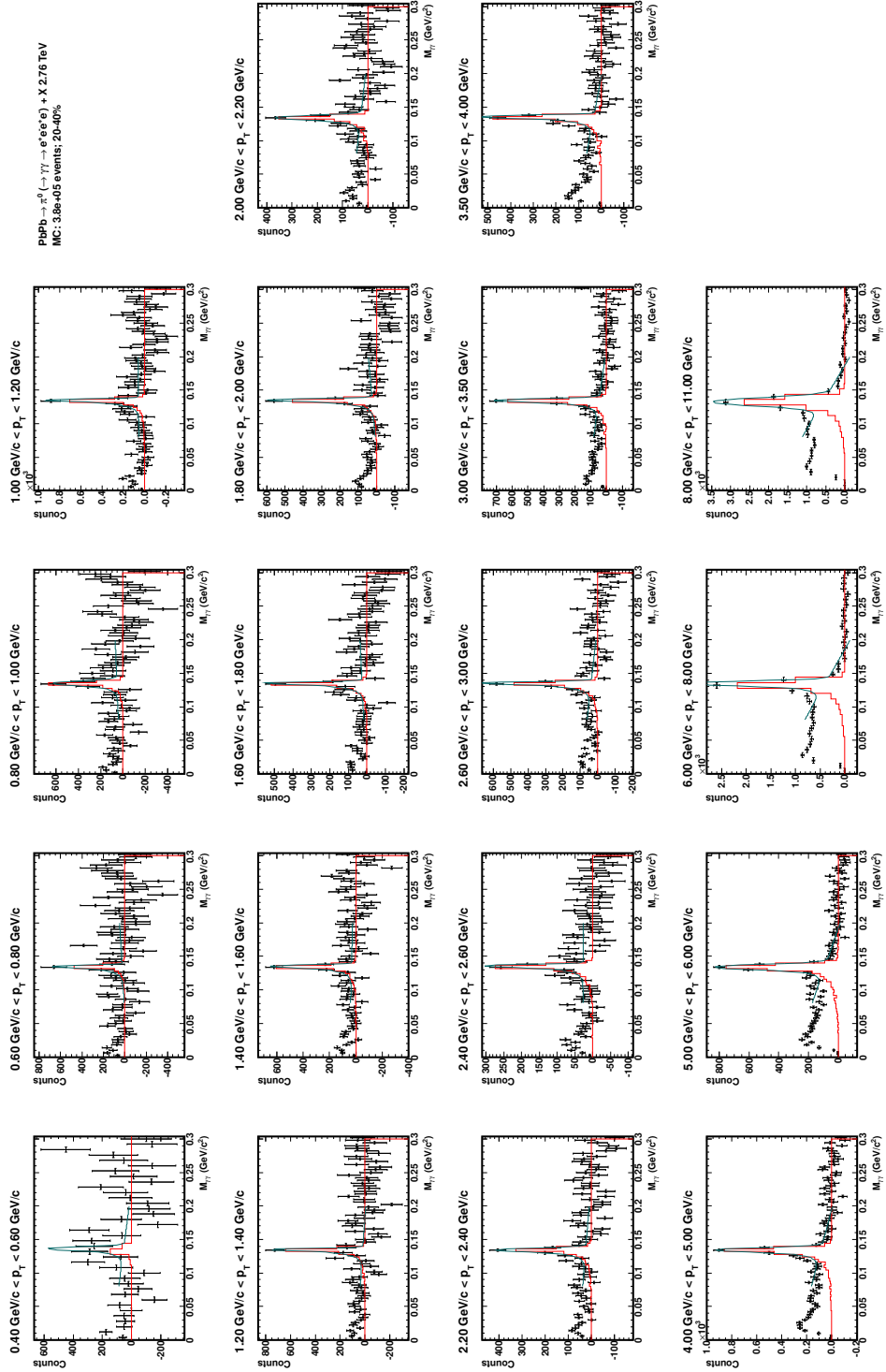
Figure 8.50: MC $\gamma\gamma$ invariant mass after bck subtraction and true reconstructed π^0s; 20-40% centrality.
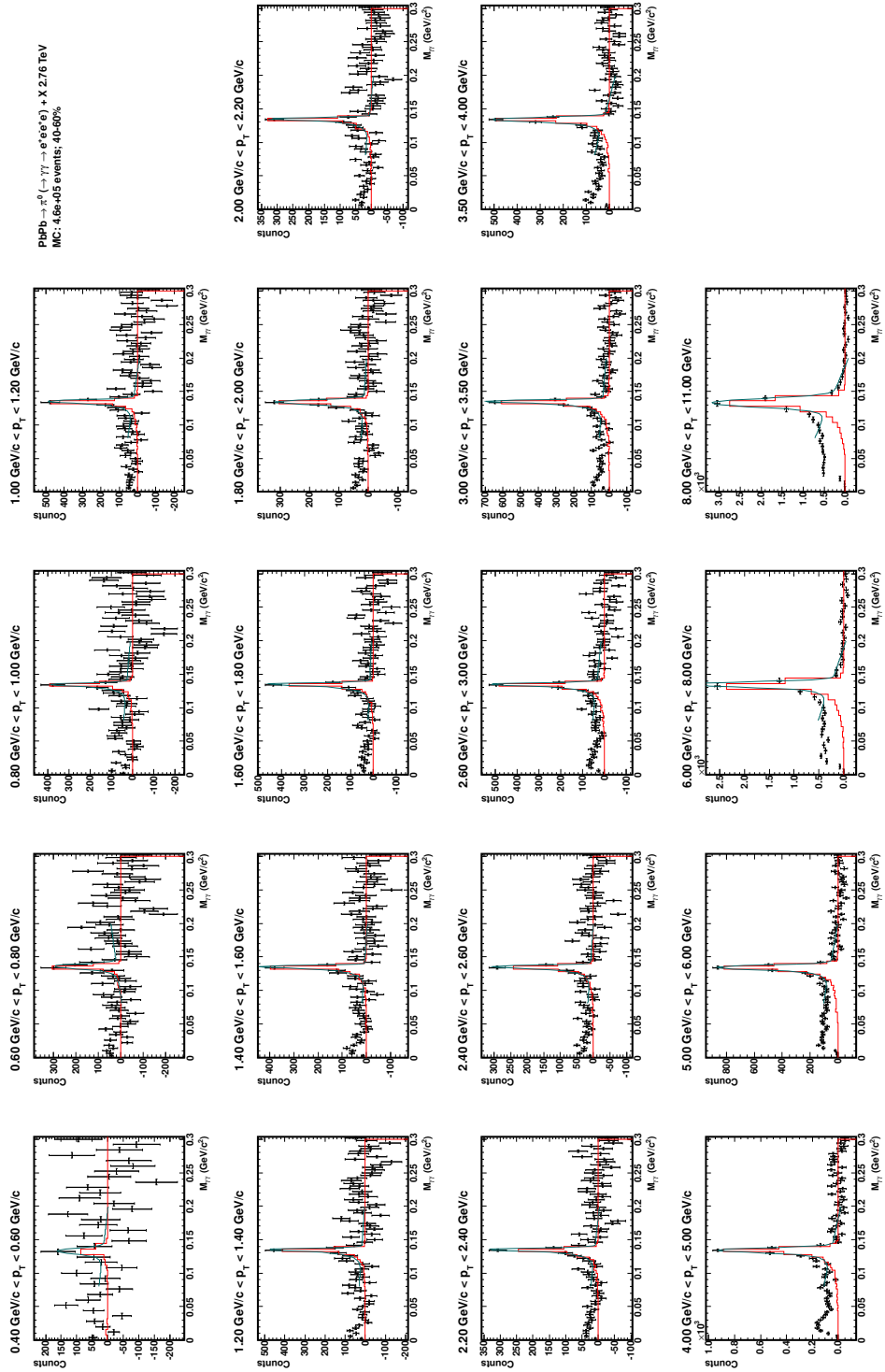
Figure 8.51: MC $\gamma\gamma$ invariant mass after bck subtraction and true reconstructed π^0s; 40-60% centrality.
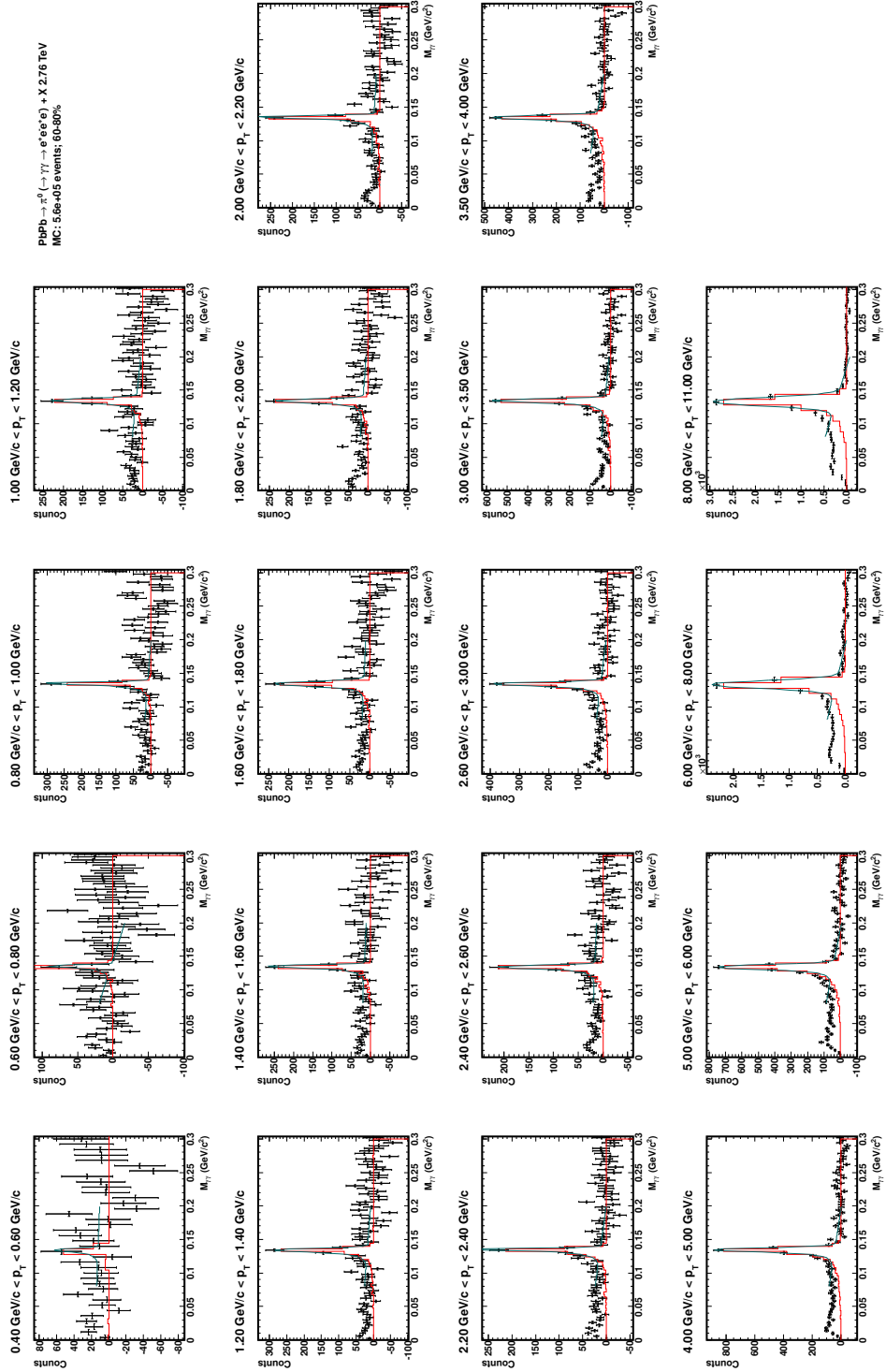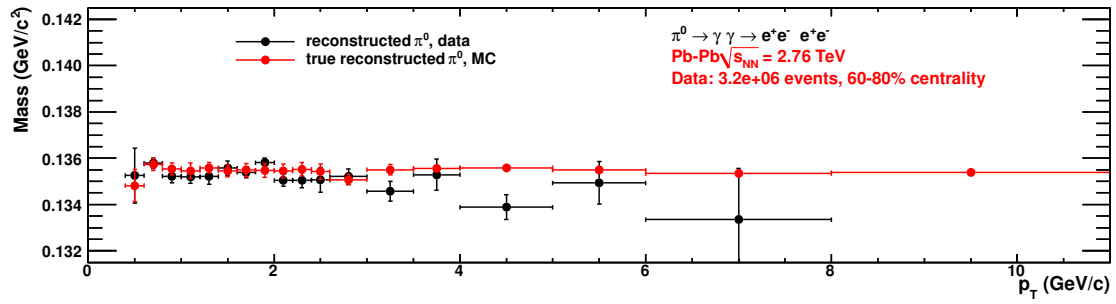
Figure 8.52: MC $\gamma\gamma$ invariant mass after bck subtraction and true reconstructed π^0s; 60-80% centrality.
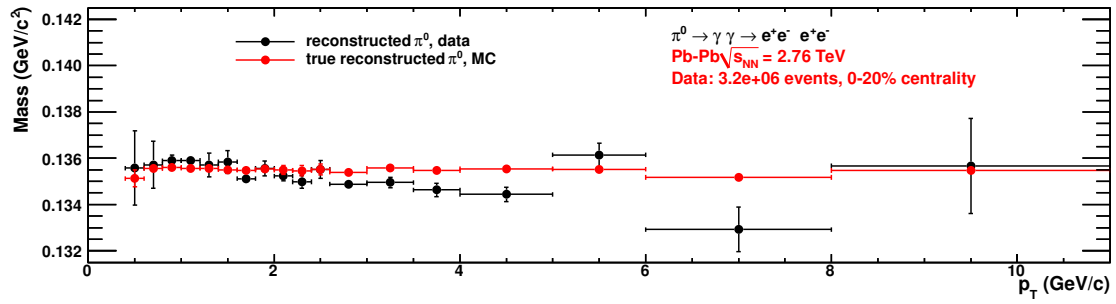
Figure 8.53: π^0 mass position for data and MC; 0-20%
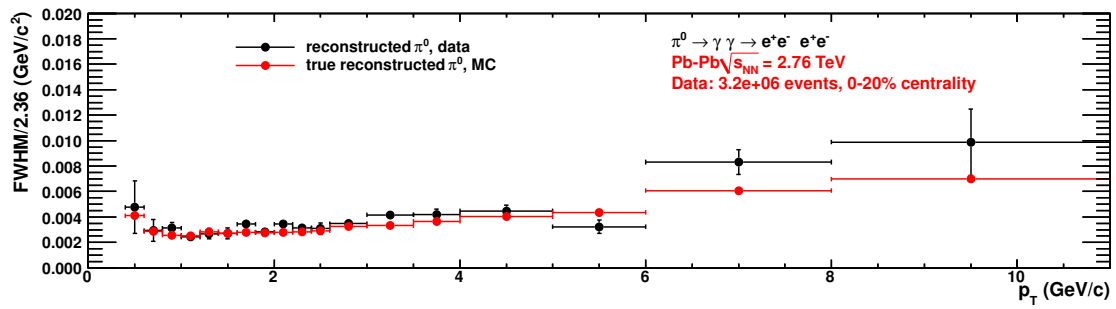
Figure 8.54: π^0 FWHM for data and MC; 0-20%
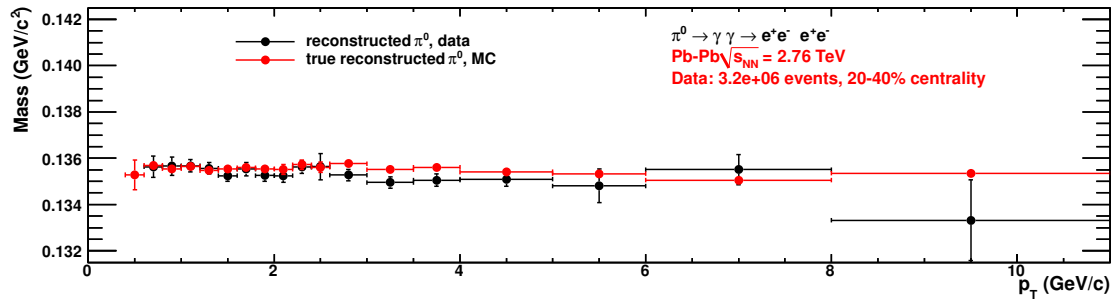
Figure 8.55: π^0 mass position for data and MC; 20-40%
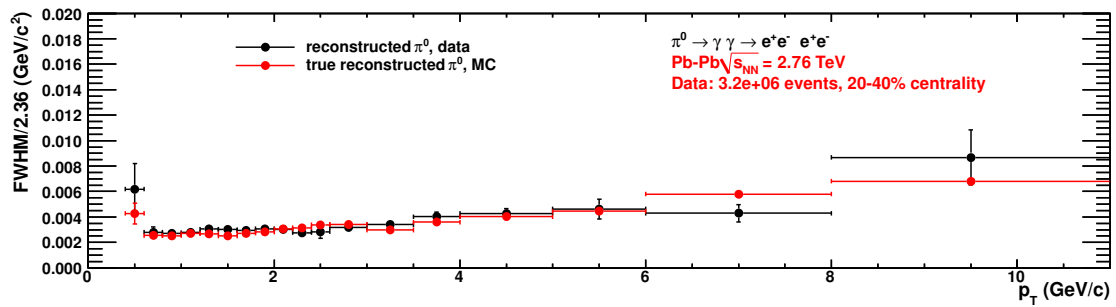
Figure 8.56: π^0 FWHM for data and MC; 20-40%
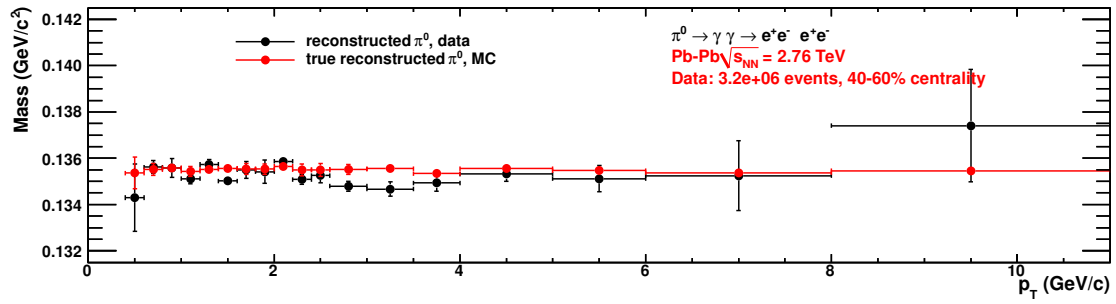
Figure 8.57: π^0 mass position for data and MC; 40-60%
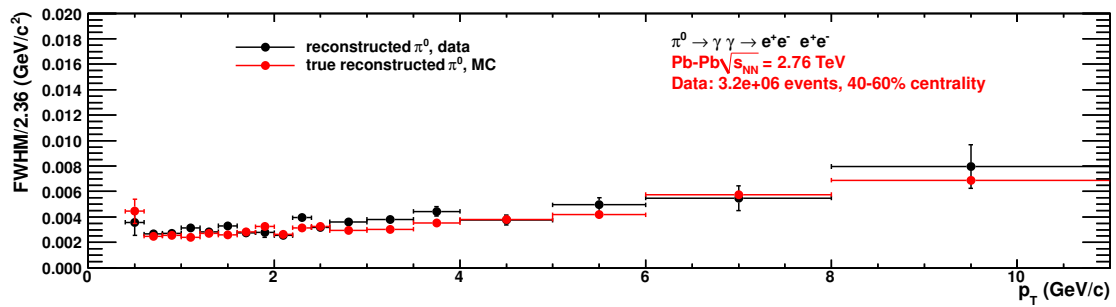
Figure 8.58: π^0 FWHM for data and MC; 40-60%

Figure 8.59: π^0 mass position for data and MC; 60-80%
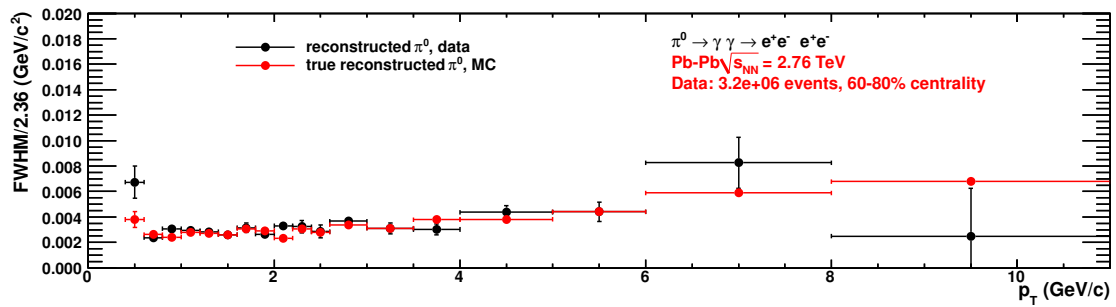
Figure 8.60: π^0 FWHM for data and MC; 60-80%
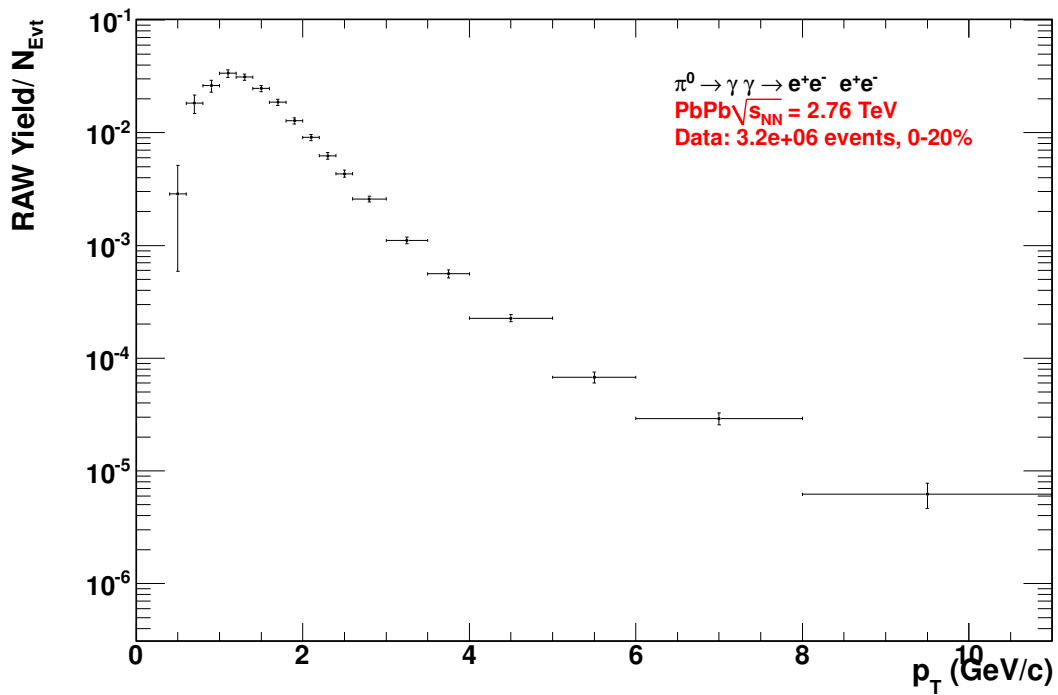
Figure 8.61: π^0 meson raw yield for the 0-20% centrality bin
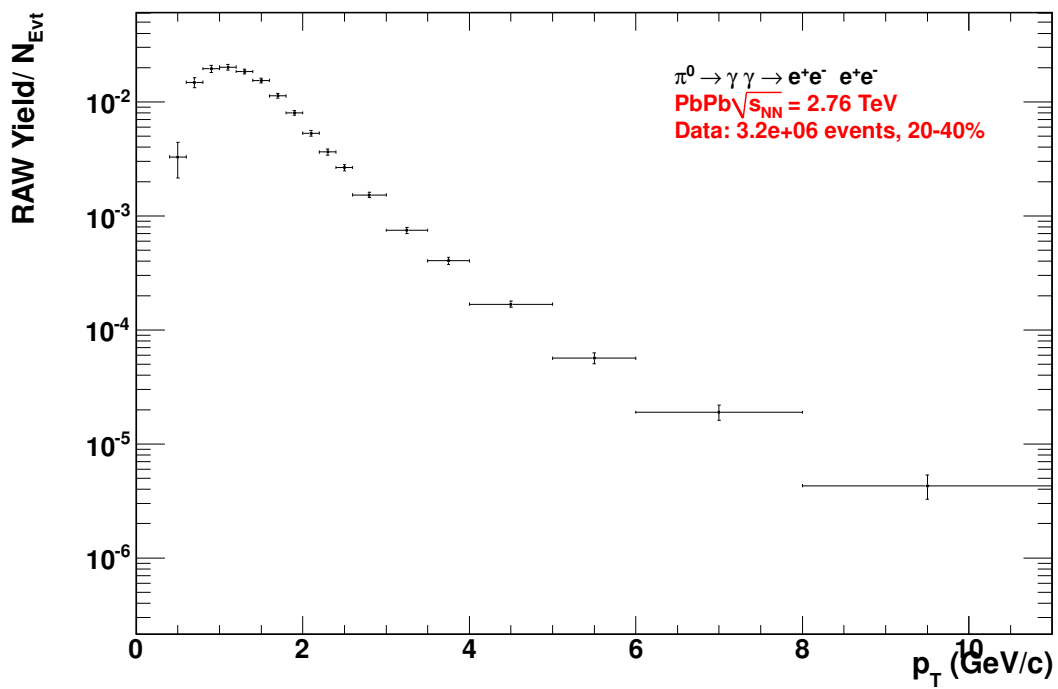
Figure 8.62: π^0 meson raw yield for the 20-40% centrality bin
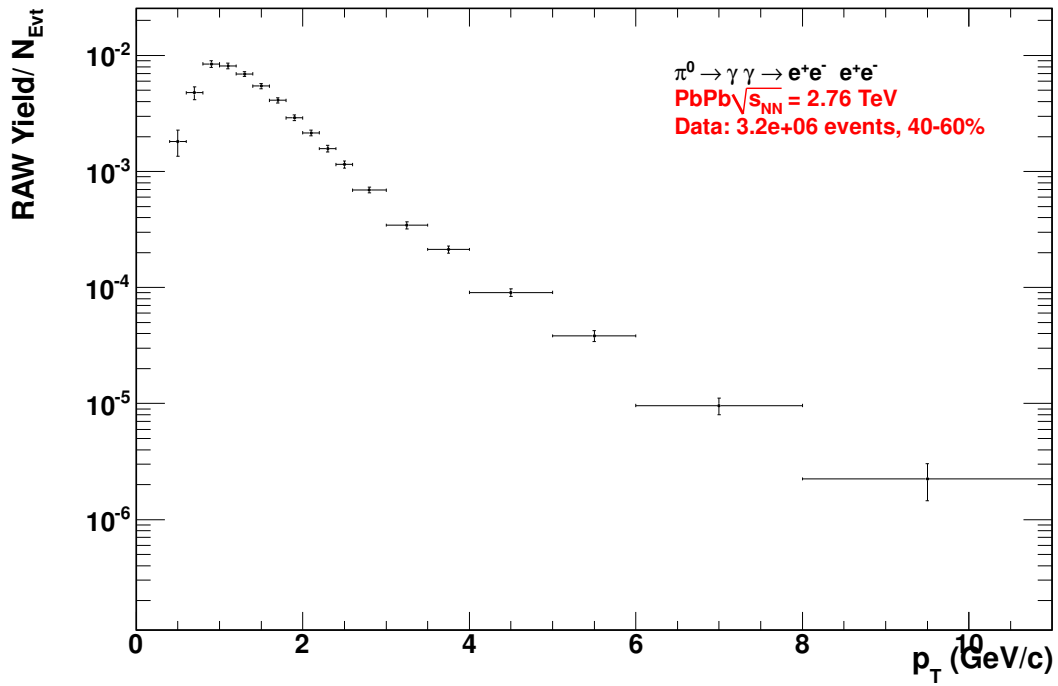
Figure 8.63: π^0 meson raw yield for the 40-60% centrality bin
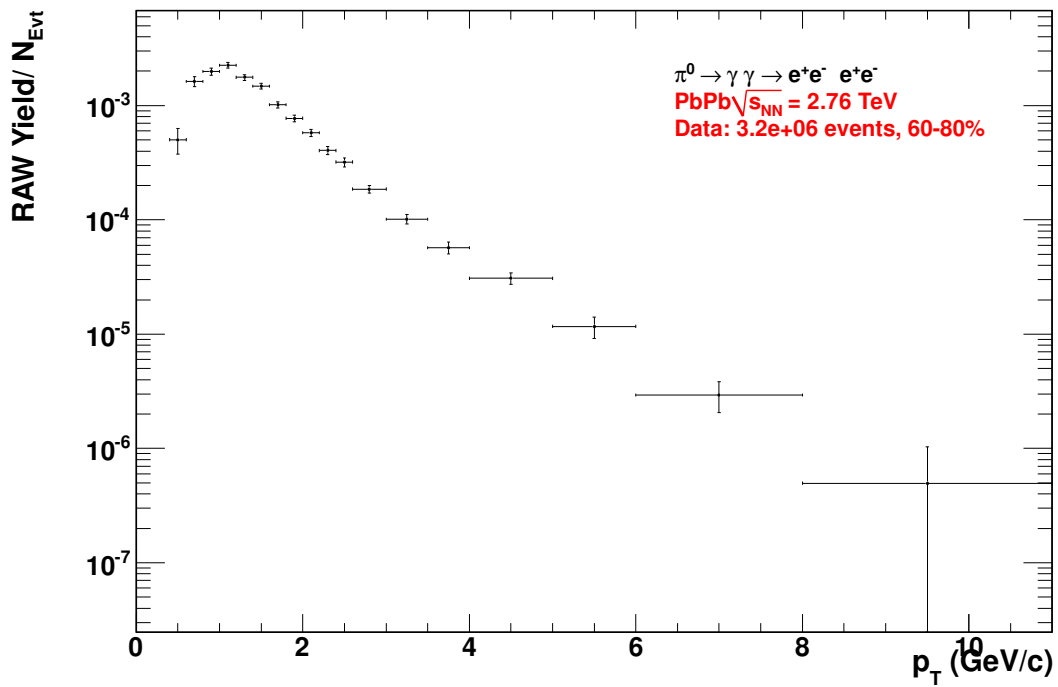
Figure 8.64: π^0 meson raw yield for the 60-80% centrality bin
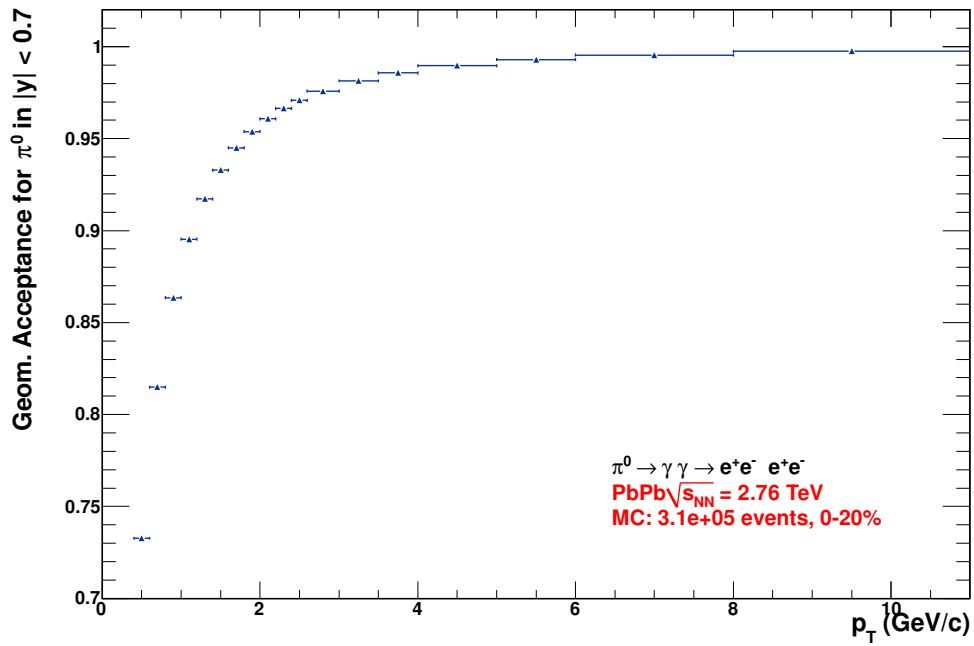
Figure 8.65: π^0 acceptance vs p_T for $|\Delta y| < 0.7$ and centrality 0-20%.
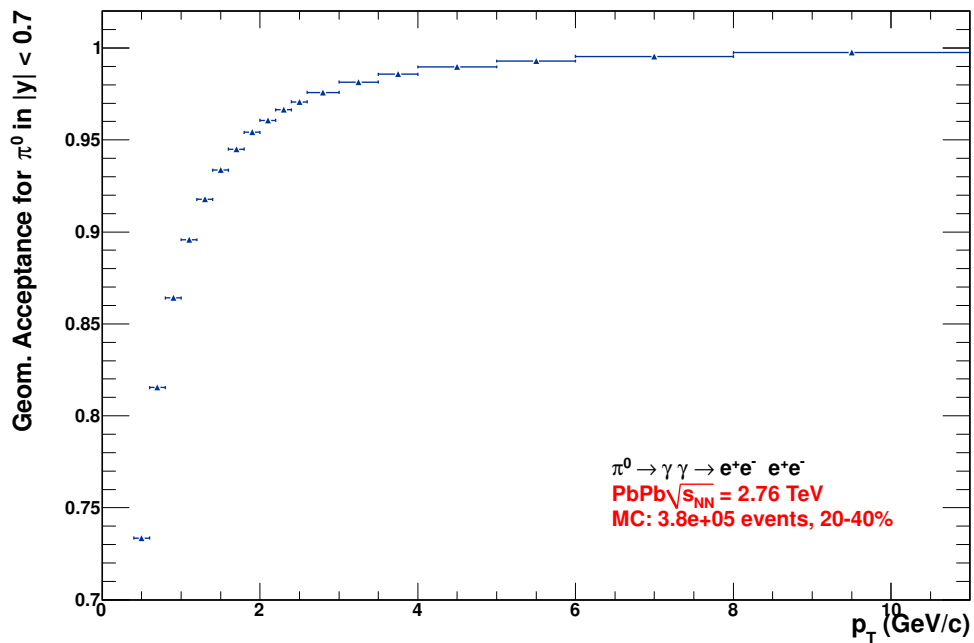
Figure 8.66: π^0 acceptance vs p_T for $|\Delta y| < 0.7$ and centrality 20-40%.
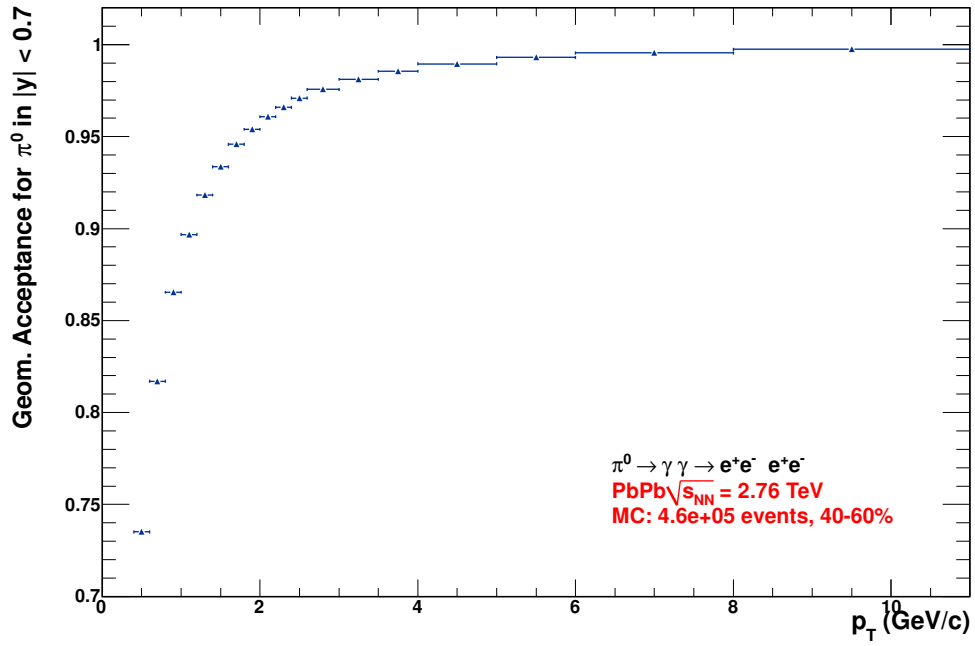
Figure 8.67: π^0 acceptance vs p_{T} for $|\Delta y| < 0.7$ and centrality 40-60%.
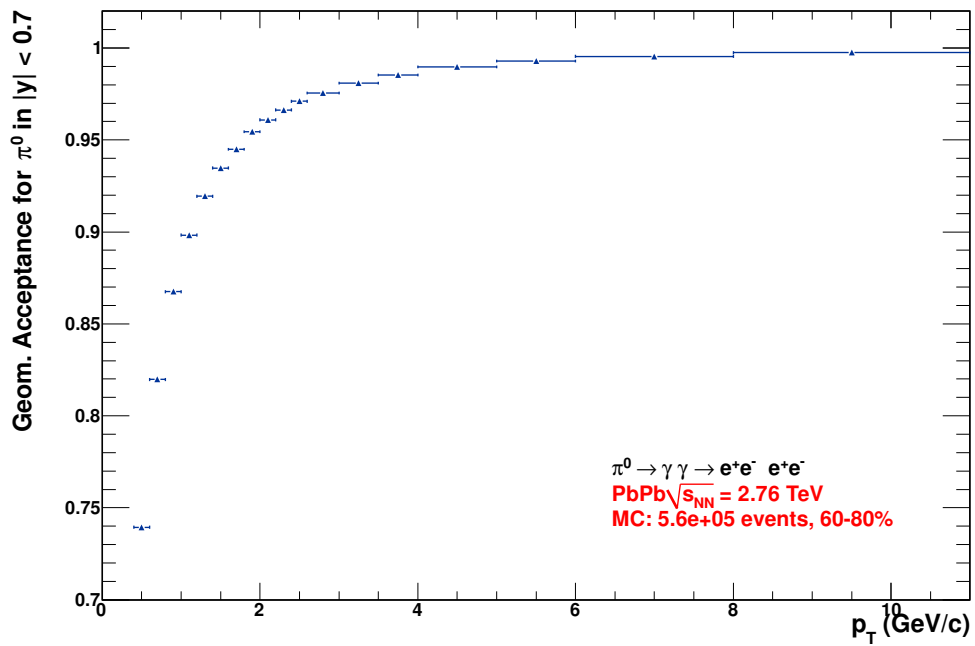
Figure 8.68: π^0 acceptance vs p_{T} for $|\Delta y| < 0.7$ and centrality 60-80%.
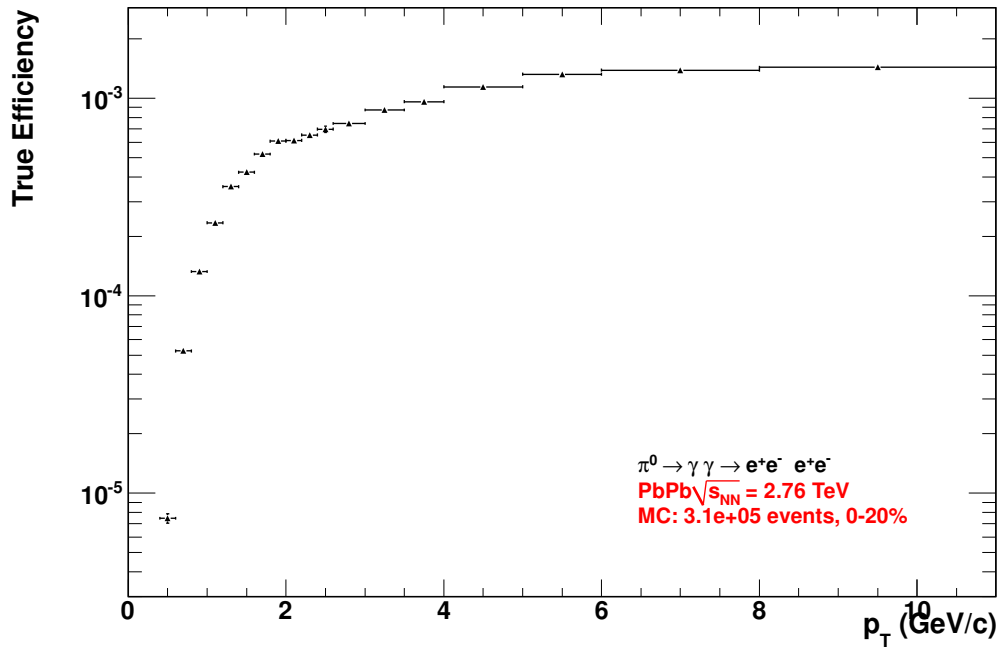
Figure 8.69: π^0 efficiency vs p_T for $|\Delta y| < 0.7$ and centrality 0-20%.
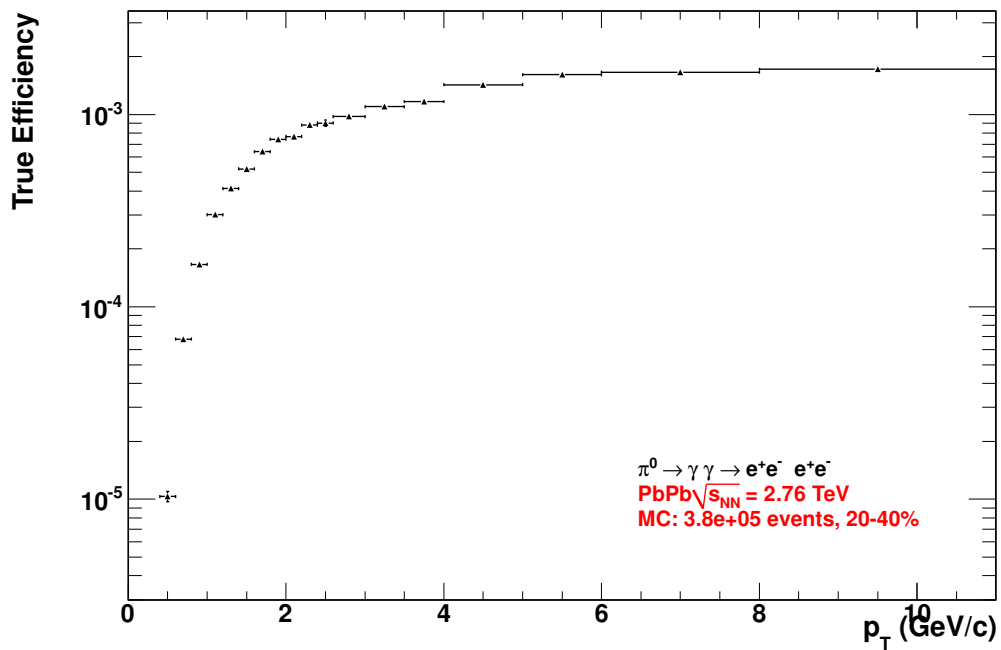
Figure 8.70: π^0 efficiency vs p_T for $|\Delta y| < 0.7$ and centrality 20-40%.
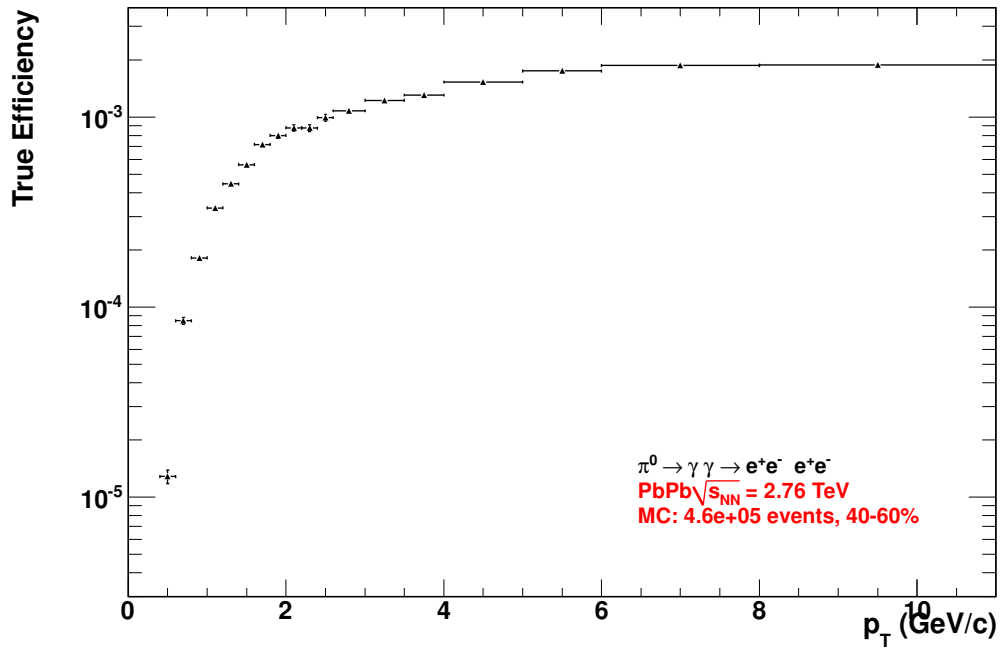
Figure 8.71: π^0 efficiency vs p_T for $|\Delta y| <0.7$ and centrality 40-60%.
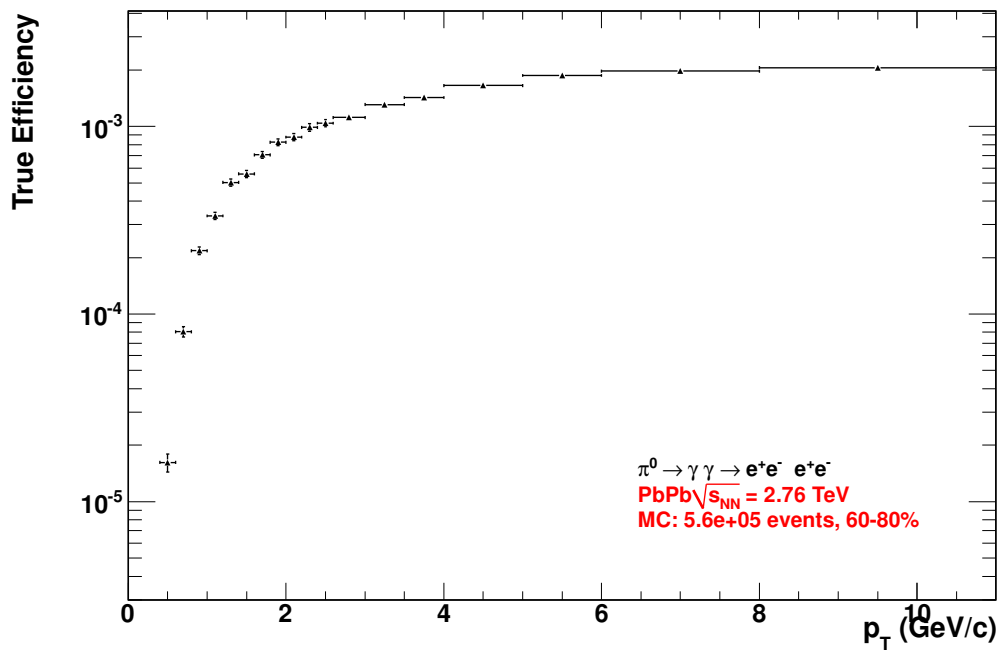
Figure 8.72: π^0 efficiency vs p_T for $|\Delta y| <0.7$ and centrality 60-80%.

8.3 List of Analyzed Runs

run	PS	no Vtx.	ratio	$\|Z_{vtx}\| >10$ cm	ratio	analyzed	ratio
137161	6.19e+04	81	0.00131	5.95e+03	0.0962	5.58e+04	0.902
137162	4.96e+04	44	0.000886	7.19e+03	0.145	4.24e+04	0.854
137231	1.53e+05	182	0.00119	1.54e+04	0.101	1.37e+05	0.898
137232	5.75e+04	65	0.00113	7.22e+03	0.126	5.02e+04	0.873
137235	1.49e+04	15	0.00101	2.06e+03	0.139	1.28e+04	0.86
137236	3.29e+04	42	0.00128	4.46e+03	0.136	2.84e+04	0.863
137243	3.26e+04	33	0.00101	4.62e+03	0.142	2.8e+04	0.857
137366	2.07e+05	521	0.00251	1.28e+04	0.0616	1.94e+05	0.936
137430	4.26e+04	81	0.0019	2.83e+03	0.0665	3.97e+04	0.932
137431	1.98e+05	430	0.00217	1.59e+04	0.08	1.82e+05	0.918
137432	8.58e+04	218	0.00254	8.05e+03	0.0938	7.75e+04	0.904
137434	7.34e+04	200	0.00272	7.41e+03	0.101	6.58e+04	0.896
137439	9.66e+03	29	0.003	1.01e+03	0.105	8.62e+03	0.892
137440	4.03e+04	96	0.00238	4.3e+03	0.107	3.59e+04	0.891
137441	8.97e+04	193	0.00215	9.99e+03	0.111	7.95e+04	0.887
137443	2.11e+04	41	0.00194	2.52e+03	0.119	1.86e+04	0.879
137530	2.63e+03	9	0.00342	108	0.0411	2.51e+03	0.955
137531	2.85e+03	2	0.000702	130	0.0456	2.72e+03	0.954
137539	3.41e+05	761	0.00223	2.88e+04	0.0843	3.12e+05	0.913
137541	1.91e+05	468	0.00244	1.99e+04	0.104	1.71e+05	0.893
137544	1.76e+05	427	0.00243	2.08e+04	0.118	1.54e+05	0.879
137546	1.1e+03	5	0.00456	128	0.117	963	0.879
137549	3.26e+05	758	0.00232	4.22e+04	0.129	2.84e+05	0.868
137595	2.56e+05	592	0.00231	2.76e+04	0.108	2.28e+05	0.89
137608	2.64e+05	356	0.00135	3.28e+04	0.125	2.3e+05	0.874
137638	1.43e+05	207	0.00144	1.72e+04	0.12	1.26e+05	0.879
137639	3.32e+04	39	0.00117	4.2e+03	0.127	2.9e+04	0.872
137685	8.31e+03	16	0.00193	986	0.119	7.31e+03	0.879
137686	2.52e+05	365	0.00145	3.36e+04	0.133	2.18e+05	0.865
137691	2.23e+05	310	0.00139	3.37e+04	0.151	1.89e+05	0.848
137692	1.18e+05	172	0.00146	1.85e+04	0.157	9.93e+04	0.841
137693	1.44e+04	25	0.00174	2.23e+03	0.155	1.21e+04	0.843
137704	1.59e+05	228	0.00143	2.59e+04	0.163	1.33e+05	0.836
137718	5.48e+04	82	0.0015	9.13e+03	0.167	4.55e+04	0.832
137722	3.77e+05	520	0.00138	6.22e+04	0.165	3.14e+05	0.834
137724	5.9e+04	82	0.00139	9.86e+03	0.167	4.91e+04	0.831
137751	1.43e+05	159	0.00111	1.95e+04	0.136	1.24e+05	0.863
137752	2.08e+05	274	0.00132	2.91e+04	0.14	1.78e+05	0.859
137848	7.54e+04	108	0.00143	1.14e+04	0.151	6.39e+04	0.847

Table 8.1: run statistics for the analyzed data.

run	PS	no Vtx.	ratio	$|Z_{vtx}| > 10$ cm	ratio	analyzed	ratio
138150	5.03e+04	4	7.95e-05	4.84e+03	0.0962	4.55e+04	0.904
138154	2.48e+04	5	0.000202	3.11e+03	0.125	2.17e+04	0.874
138190	1.79e+05	250	0.0014	2.22e+04	0.124	1.56e+05	0.875
138192	4.41e+05	614	0.00139	6.4e+04	0.145	3.76e+05	0.854
138197	1.52e+05	217	0.00143	2.44e+04	0.161	1.27e+05	0.837
138201	2.49e+05	366	0.00147	4.38e+04	0.176	2.05e+05	0.823
138225	2.52e+05	337	0.00134	3.11e+04	0.123	2.21e+05	0.875
138275	1.66e+06	2.14e+03	0.00129	2.51e+05	0.151	1.41e+06	0.848
138359	3.39e+05	375	0.00111	3.11e+04	0.0916	3.08e+05	0.907
138364	4.6e+05	582	0.00126	5.6e+04	0.122	4.04e+05	0.877
138396	4.84e+05	636	0.00131	6.36e+04	0.131	4.2e+05	0.867
138438	6.72e+04	91	0.00135	6.69e+03	0.0996	6.04e+04	0.899
138439	2.03e+05	251	0.00123	2.36e+04	0.116	1.8e+05	0.883
138442	4.43e+05	594	0.00134	5.88e+04	0.133	3.83e+05	0.866
138469	1.64e+05	187	0.00114	1.49e+04	0.091	1.49e+05	0.908
138534	1.53e+06	1.88e+03	0.00123	2.05e+05	0.134	1.33e+06	0.865
138578	2.94e+05	353	0.0012	2.62e+04	0.0891	2.67e+05	0.91
138579	2.69e+05	313	0.00116	3.01e+04	0.112	2.39e+05	0.887
138582	4.62e+04	51	0.0011	5.79e+03	0.125	4.03e+04	0.874
138583	2.25e+05	258	0.00114	3.03e+04	0.134	1.95e+05	0.865
138621	1.83e+05	283	0.00155	2.07e+04	0.113	1.62e+05	0.886
138624	1.72e+05	240	0.00139	2.16e+04	0.125	1.5e+05	0.873
138638	2.17e+05	297	0.00137	3e+04	0.138	1.87e+05	0.86
138652	2.42e+04	28	0.00116	3.53e+03	0.145	2.07e+04	0.853
138653	4.15e+05	591	0.00142	6.32e+04	0.152	3.51e+05	0.846
138662	2.37e+05	356	0.0015	3.82e+04	0.161	1.98e+05	0.837
138666	2.66e+05	385	0.00145	4.39e+04	0.165	2.22e+05	0.834
138730	4.79e+04	82	0.00171	6e+03	0.125	4.18e+04	0.873
138731	1.87e+04	36	0.00192	2.45e+03	0.131	1.62e+04	0.867
138732	1.87e+04	25	0.00134	2.63e+03	0.141	1.6e+04	0.858
138837	2.78e+05	354	0.00127	4.36e+04	0.157	2.34e+05	0.842
138870	8.2e+04	42	0.000512	8.58e+03	0.105	7.34e+04	0.895
138871	4.03e+04	22	0.000546	4.45e+03	0.11	3.58e+04	0.889
138872	1.65e+04	20	0.00121	2.08e+03	0.126	1.44e+04	0.873

Table 8.2: run statistics for the analyzed data.

run	PS	no Vtx.	ratio	$|Z_{vtx}|>10$ cm	ratio	analyzed	ratio
139028	3.74e+04	44	0.00118	4.83e+03	0.129	3.26e+04	0.87
139036	1.44e+05	186	0.00129	2.31e+04	0.161	1.21e+05	0.838
139037	1.23e+05	175	0.00142	2.04e+04	0.166	1.02e+05	0.833
139038	4.03e+05	553	0.00137	6.82e+04	0.17	3.34e+05	0.829
139042	1.18e+05	171	0.00145	2.05e+04	0.175	9.69e+04	0.824
139105	3.82e+04	57	0.00149	4.36e+03	0.114	3.38e+04	0.885
139107	5.29e+05	744	0.00141	7.11e+04	0.134	4.57e+05	0.864
139173	3.29e+05	452	0.00137	4.43e+04	0.135	2.84e+05	0.864
139308	267	1	0.00375	32	0.12	234	0.876
139309	1.26e+05	178	0.00142	1.46e+04	0.116	1.11e+05	0.883
139310	1.09e+05	148	0.00135	1.35e+04	0.124	9.58e+04	0.875
139311	6.36e+03	8	0.00126	807	0.127	5.55e+03	0.872
139314	2.36e+05	292	0.00124	3.27e+04	0.139	2.03e+05	0.86
139316	4.96e+03	4	0.000806	709	0.143	4.25e+03	0.856
139328	1.64e+05	205	0.00125	2.56e+04	0.156	1.39e+05	0.843
139329	2.67e+05	368	0.00138	4.29e+04	0.161	2.23e+05	0.838
139360	2.81e+04	34	0.00121	2.52e+03	0.0896	2.55e+04	0.909
139437	4.96e+05	612	0.00123	4.71e+04	0.0948	4.48e+05	0.904
139438	1.39e+05	211	0.00152	1.55e+04	0.112	1.23e+05	0.887
139439	7.15e+03	10	0.0014	861	0.12	6.28e+03	0.878
139440	7.03e+04	90	0.00128	8.48e+03	0.121	6.17e+04	0.878
139465	6.6e+05	818	0.00124	8.41e+04	0.127	5.75e+05	0.871
139503	2.5e+04	26	0.00104	2.04e+03	0.0813	2.3e+04	0.918
139504	422	0	0	34	0.0806	388	0.919
139505	4.42e+04	70	0.00158	4.02e+03	0.0908	4.02e+04	0.908
139507	3.41e+05	573	0.00168	3.52e+04	0.103	3.06e+05	0.895
139510	1.51e+05	273	0.00181	1.77e+04	0.117	1.33e+05	0.881

Table 8.3: run statistics for the analyzed data.

8.4 Optimization of α Cut for the π^0 and η Mesons
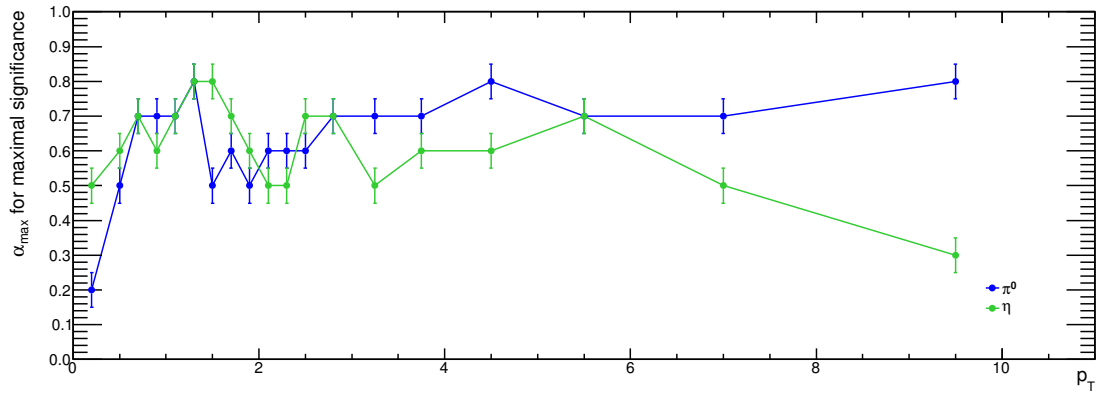
Figure 8.73: π^0/η α_{max} cut for maximal significance; 0-20%.
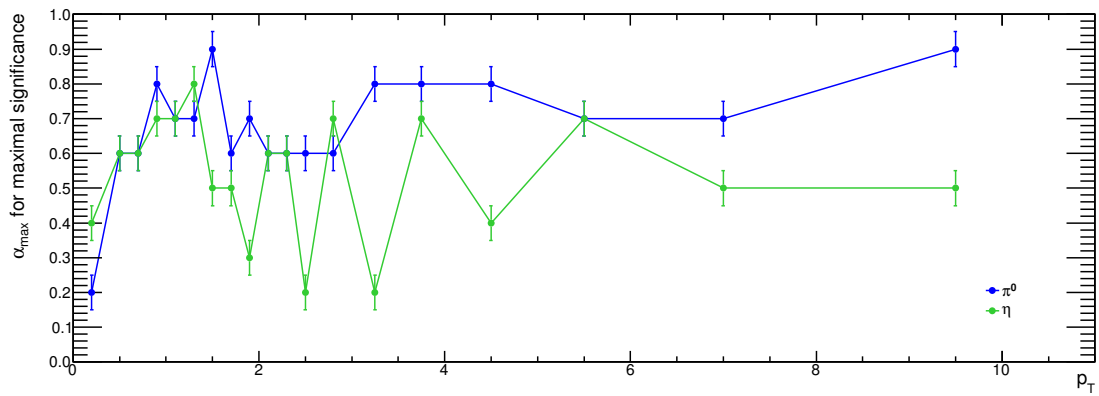
Figure 8.74: π^0/η α_{max} cut for maximal significance; 20-40%.
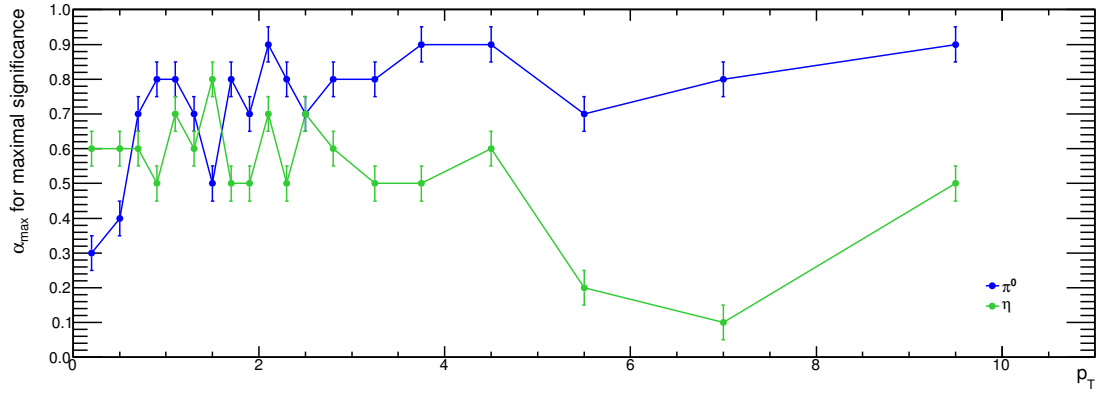
Figure 8.75: π^0/η α_{max} cut for maximal significance; 40-60%.
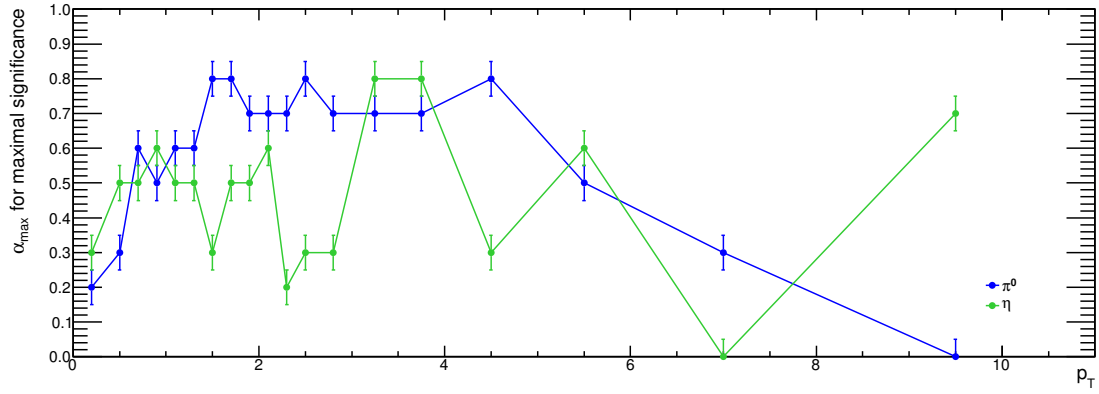
Figure 8.76: π^0/η α_{max} cut for maximal significance; 60-80%.

8.5 Comparison of π^0 $\mathrm{R_{AA}}$ with Conversions and Combined Reference
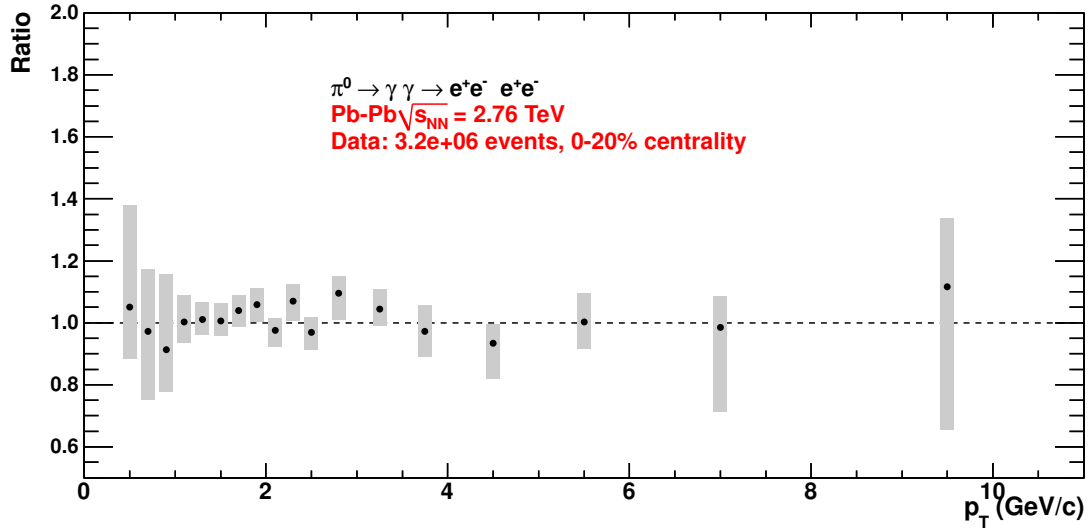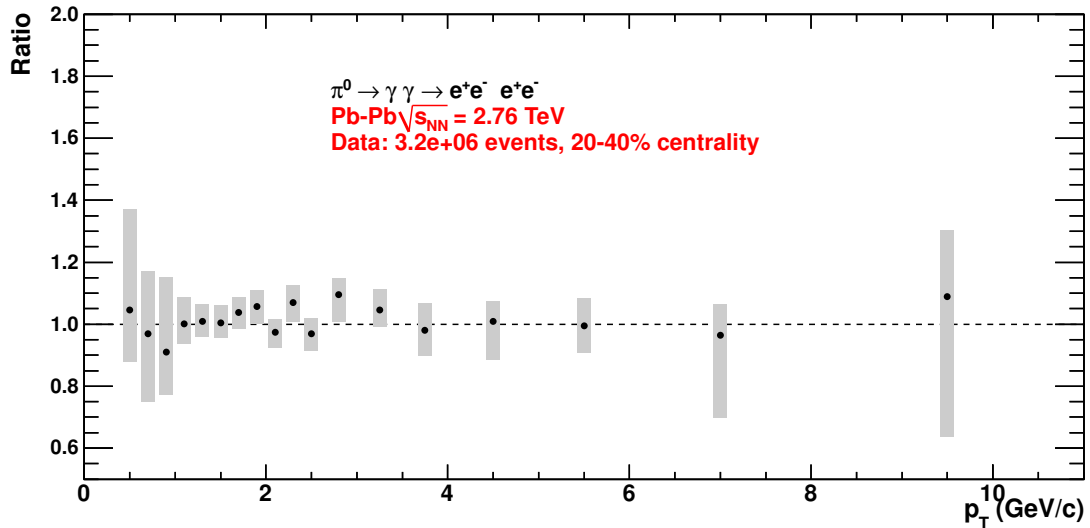

Figure 8.77: Comparison of the π^0 $\mathrm{R_{AA}}$ calculated without a bin width correction and with the conversions pp reference only to the π^0 $\mathrm{R_{AA}}$ with bin width correction and with the combined pp reference; 0-20%

Figure 8.78: Comparison of the π^0 $\mathrm{R_{AA}}$ calculated without a bin width correction and with the conversions pp reference only to the π^0 $\mathrm{R_{AA}}$ with bin width correction and with the combined pp reference; 20-40%

Figure 8.79: Comparison of the π^0 R$_{AA}$ calculated without a bin width correction and with the conversions pp reference only to the π^0 R$_{AA}$ with bin width correction and with the combined pp reference; 40-60%
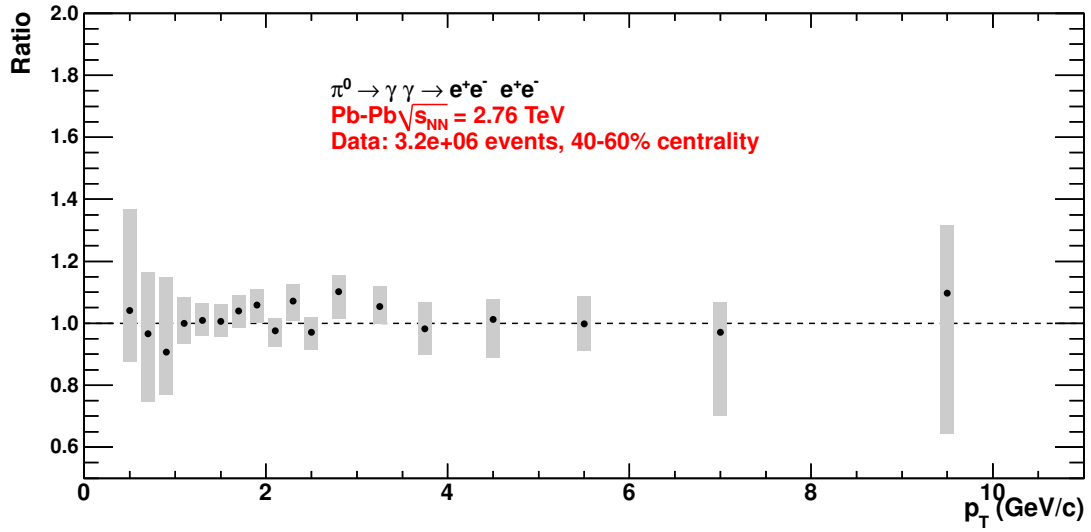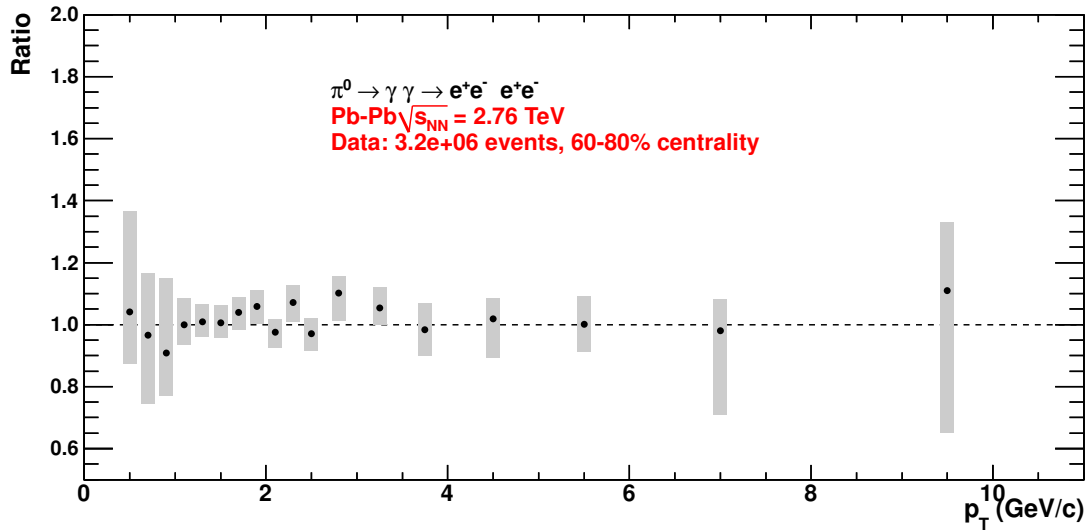

Figure 8.80: Comparison of the π^0 R$_{AA}$ calculated without a bin width correction and with the conversions pp reference only to the π^0 R$_{AA}$ with bin width correction and with the combined pp reference; 60-80%

Bibliography

[1] Nobel Prize in Physics 2004; The Royal Swedish Academy of Sciences; Press Release
http://www.nobelprize.org/nobel_prizes/physics/laureates/2004/press.html

[2] Superdense Matter: Neutrons or Asymptotically Free Quarks?; J. C. Collins and M. J. Perry; Phys. Rev. Lett. 34, 1353-1356 (1975).

[3] The quest for the quark-gluon plasma; P. Braun-Munzingen, J.Stachel; Nature 2007 Vol.449.

[4] Hadron Production in Ultra-relativistic Nuclear Collisions: Quarkyonic Matter and a Triple Point in the Phase Diagram of QCD; A. Andronic *et al.*; Nucl. Phys. A837 (2010) 65-86.

[5] Suppression pattern of neutral pions at high transverse momentum in Au + Au collisions at $\sqrt{s_{NN}}$ = 200 GeV and constraints on medium transport coefficients; PHENIX Collaboration (A. Adare *et al.*); Phys. Rev. Lett. 101 (2008) 232301.

[6] PHENIX Data Plot (id p0820)
http://www.phenix.bnl.gov/WWW/plots/show_plot.php?editkey=p0820

[7] Chemical Freeze-out and the QCD Phase Transition Temperature; P. Braum-Munzinger, J. Stachel, C. Wetterich; Phys. Lett. B596 (2004) 61-69.

[8] Review of Particle Physics; Particle Data Group; J. Phys. G: Nucl. Part. Phys. 37 (2010) 075021; page 320ff.

[9] Measurement of the neutrino-nucleon and antineutrino-nucleon total cross sections; T. Eichten *et al.*; Phys. Lett. 46B, 138 (1973).

[10] Experimental Observation of a Heavy Particle J; J. J. Aubert *et al.*; Phys. Rev. Lett. 33, 1404-1406 (1974).

[11] Discovery of a Narrow Resonance in e^+e^- Annihilation; J. -E. Augustin *etal.*; Phys. Rev. Lett. 33, 1406-1408 (1974).

[12] Experimental observation of the intermediate vector bosons W^+, W^-, and Z^0; Carlo Rubbia; Rev. Mod. Phys. 57, 699-722 (1985).

[13] Observation of Top Quark Production in Pbar-P Collisions; The CDF Collaboration; Phys. Rev. Lett. 74, 2626-2631 (1995).

[14] Spontaneous Symmetry Breakdown without Massless Bosons; Peter W. Higgs; Phys. Rev. 145, 1156-1163 (1966)

[15] Standard Model: An Introduction; S.F.Novaes; arXiv:hep-ph/0001283v1 (27 Jan 2000)

[16] Implications of combined solar-neutrino observations and their theoretical uncertainties; S. A. Bludman, N. Hata, D. C. Kennedy and P. G. Langacker; Phys. Rev. D 47, 2220-2233 (1993).

[17] http://commons.wikimedia.org/wiki/File:Standard_Model_of_Elementary_Particles.svg?uselang=de

[18] http://www.nature.com/nphys/journal/v7/n1/images/nphys1874-f1.jpg

[19] Approximate symmetries and pseudoGoldstone bosons; Steven Weinberg; Phys. Rev. Lett. 29, 1698-1701 (1972).

[20] Midrapidity neutral pion production in proton proton collisions at $\sqrt{s_{NN}} = 200$ GeV; PHENIX Collaboration (S.S. Adler (Brookhaven) *et al.*); Phys. Rev. Lett. 91, 241803 (2003).

[21] Review of Particle Physics; Particle Data Group; J. Phys. G: Nucl. Part. Phys. 37 (2010) 075021, page 277.

[22] Systematic Study of the Centrality and $\sqrt{s_{NN}}$ Dependence of the $dE_T/d\eta$ and $dN_{ch}/d\eta$ in Heavy ion collisions at Mid-Rapidity; S.S.Adler *et al.*, (including A.Milov); Phys. Rev. C71 034908 (2005).

[23] Glauber Modeling in High Energy Nuclear Collisions; Michael L. Miller, Klaus Reygers, Stephen J. Sanders, Peter Steinberg; Ann.Rev.Nucl.Part.Sci.57:205-243,2007

[24] http://www.gsi.de/forschung/fair_experiments/CBM/Phasendiagram.jpg.

[25] Quark mass and flavour dependence of the QCD phase transition; Karsch, F., Laermann, E. & Peikert, A.; Nucl. Phys. B 605, 579-599 (2001).

[26] Evidence for a new state of matter: an assessment of the results from the CERN lead beam programme; Heinz, U. & Jacob, M.; arXiv:nucl-th/0002042v2 (16 Feb 2000)

[27] R. Arnaldi lecture(1): http://personalpages.to.infn.it/ nardi/QGPSchool/5th/welc11.html.

[28] Suppression of charged particle production at large transverse momentum in central Pb–Pb collisions at $\sqrt{s_{NN}}$= 2.76 TeV; K. Aamodt *et al.*; Phys. Lett. B 696, 1-2, (2011), 30-39.

[29] Testing the theory of QGP-induced energy loss at RHIC and the LHC; I. Vitev; Phys. Lett. B639, 38-45, (2006).

[30] ALICE NOTE. Material Budget of ALICE.

[31] http://217.91.25.33/eng/deeper_insight/physics.htm

[32] Bachelor Thesis Friederike Bock: http://www.physi.uni-heidelberg.de/ fbock/

[33] Review of Particle Physics; Particle Data Group; J. Phys. G: Nucl. Part. Phys. 37 (2010) 075021; page 291.

[34] Review of Particle Physics; Particle Data Group; J. Phys. G: Nucl. Part. Phys. 37 (2010) 075021, page 291.

[35] E. Lohrmann - Hochenergiephysik - ISBN 3-519-33043-1 (page 99).

[36] http://public.web.cern.ch/public/en/LHC/LHC-en.html

[37] http://www.weltmaschine.de/sites/site_weltmaschine/content/e92/e70729/e70810/ imageobject70817/9906026-A4-at-144-dpi.jpg

[38] Image found under http://lhc-machine-outreach.web.cern.ch /lhc-machine-outreach/images/cryodipole.jpg

[39] The ALICE Experiment at the LHC. 2008 JINST 3 S08002 (ISBN: 978-92-9083-347-5)

[40] http://aliceinfo.cern.ch/Public/en/Chapter2/Chap2Experiment-en.html

[41] http://www.gsi.helmholtz.de/forschung/kp/kp1/ experimente/alice/tpc/TPC_overview_e.html

[42] The ALICE TPC, a large 3-dimensional tracking device with fast readout for ultra-high multiplicity events, Nucl. Instrum. Meth. A622 (2010) 316-367.

[43] http://aliceinfo.cern.ch/Public/en/Chapter2/Chap2Experiment-en.html

[44] Centrality Dependence of the Charged-Particle Multiplicity Density at Midrapidity in Pb-Pb Collisions at $\sqrt{s_{\mathrm{NN}}} = 2.76$ TeV; K. Aamodt et al. (ALICE Collaboration); Phys. Rev. Lett. 106, 032301 (2011).

[45] Short writeup, describing status and new physics as of PYTHIA 6.154; T. Sjöstrand, P. Edèn, C. Friberg, L. Lönnblad, G. Miu, S. Mrenna and E. Norrbin; Computer Phys. Commun. 135 (2001) 238 (LU TP 00-30, hep-ph/0010017).

[46] R. Engel, J. Ranft, S. Roesler, Phys. Rev. D 52 (1995) 1459.

[47] HIJING: A Monte Carlo model for multiple jet production in p p, p A and A A collisions; Xin-Nian Wang and Miklos Gyulassy; Phys. Rev. D 44, 3501 (1991).

[48] GEANT, Application Software Group, GEANT 3.21, CERN programm Library Long Writeup W5013, 1994.

[49] Photon Conversion Group: Analysis Note: π^0 and η meson measurement with conversions in ALICE in proton-proton collisions at $\sqrt{s} = 7$ TeV, $\sqrt{s} = 2.76$ TeV and at $\sqrt{s} = 900$ GeV at the CERN LHC.

[50] Nuclear Physics C. Nuclear Dynamics, Experimental; M. Stanley Livingston and H. A. Bethe; Rev. Mod. Phys. 9, 245â390 (1937).

[51] Script of R. Barlow lectures on Statistics and Numerical Methods in HEP (lecture5): http://www-group.slac.stanford.edu/sluo/lectures/Stat_Lectures.html.

[52] https://twiki.cern.ch/twiki/bin/viewauth/ALICE/CentStudies

[53] C. Tsallis; J. Stat. Phys. 52, (1988) 479.

[54] Detailed study of high-p_{T} neutral pion suppression and azimuthal anisotropy in Au+Au collisions at $\sqrt{s_{\mathrm{NN}}} = 200$ GeV; S. S. Adler et al. PHENIX Collaboration; Phys. Rev. C 76, 034904 (2007).

[55] LHC Predictions from an extended theory with Elastic, Inelastic, and Path Length Fluctuating Energy Loss; William A. Horowitz; Int. J. Mod. Phys. E16, 2193-2199 (2007).

[56] Elastic, Inelastic, and Path Length Fluctuations in Jet Tomography; Simon Wicks, William Horowitz, Magdalena Djordjevic, Miklos Gyulassy; Nucl. Phys. A784, 426-442 (2007).

[57] Heavy quark radiative energy loss in QCD matter; Magdalena Djordjevic, Miklos Gyulassy; Nucl. Phys. A733, 265-298 (2004).

[58] The Ter-Mikayelian effect on QCD radiative energy loss; M. Gyulassy, P. Levai, I. Vitev; Phys. Rev. C68, 034914 (2003).

[59] Suppression of high-p_{T} hadrons in Pb+Pb collisions at energies available at the CERN Large Hadron Collider; Xiao-Fang Chen, Tetsufumi Hirano, Enke Wang, Xin-Nian Wang, and Hanzhong Zhang; Phys. Rev. C 84, 034902 (2011).

[60] Multiple Scattering, Parton Energy Loss and Modified Fragmentation Functions in Deeply Inelastic eA Scattering; Xiaofeng Guo, Xin-Nian Wang; Phys. Rev. Lett 85 3591-3594 (2000).

[61] Multiple Parton Scattering in Nuclei: Parton Energy Loss; Xin-Nian Wang, Xiaofeng Guo; Nucl. Phys. A696 (2001) 788-832.

[62] Energy dependence of jet transport parameter and parton saturation in quark-gluon plasma; Jorge Casalderrey-Solana and Xin-Nian Wang; Phys. Rev. C 77, 024902 (2008).

[63] Is early thermalization achieved only near midrapidity in Au + Au collisions at $\sqrt{s_{\mathrm{NN}}} = 130$âGeV; T. Hirano; Phys. Rev. C 65, 011901 (2001).

Acknowledgements

Erklärung

Ich versichere, dass ich diese Arbeit selbständig verfasst und keine anderen als die angegebenen Quellen und Hilfsmittel benutzt habe.

Heidelberg, den 29.09.2011

. . . .

Radoslav Rusanov